Study of the dynamic properties of perovskite solar cells for visible light communication

Hesham Hawashin

Thèse de doctorat

Laboratoire XLIM – Axe RF-ELITE

Thèse pour obtenir le grade de

Docteur de l'Université de Limoges

Electronique des hautes fréquences, photonique et systèmes

Présentée et soutenue par

Hesham Hawashin

Le 7 décembre 2021

Etude des propriétés dynamiques de cellules solaires pérovskites pour la réception de données par voie optique dans le visible

Rapporteurs

M. Yvan Bonnassieux, Professeur des Universités, LPMCI, Ecole Polytechnique

M. Jean-Jacques Simon, Professeur des Universités, IM2NP, Université Aix-Marseille

Examinateurs

M. François Tran-Van, Professeur des Universités, PCM2E, Université de Tours

M. Bernard Ratier, Professeur des Universités, XLIM, Université de Limoges

Directeurs

M. Johann Bouclé, Maître de Conférences, XLIM, Université de Limoges

M. Thierry Trigaud, Maître de Conférences, XLIM, Université de Limoges

Droits d’auteurs

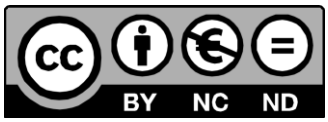

Abstract

The advent of new telecommunication technologies such as 5G and 6G, as well as the strong development of the Internet of Things (IoT) require more efficient communication systems that are able to provide high data rates and high service quality. These developments are coupled with an ever-increasing need for electrical energy supply. In this context, integrating a low cost solar cell as simultaneous data receiver and energy harvester in optical wireless communication systems (OWC) is one of the most relevant approaches to address this challenge.

Emergent solar cell technologies such as perovskite solar cells can be well-adapted for such applications, considering their low cost, high efficiencies in indoor environment, light weight and flexibility. This thesis work aims at studying the dynamic behavior of perovskite solar cells, using impedance spectroscopy, and at discussing its relation with their photovoltaic performances.

We especially study the dynamic response of various mixed cations and mixed halide perovskite absorbers, thanks to their outstanding power conversion efficiency, their relatively easy processing from solution, and their suitable stability in ambient conditions. In particular, based on the simulation of the experimental impedance of the devices, we discuss the specific physical process governing their low frequency and high frequency response, and the relation with the achievable bandwidths when used as receiver for OWC applications. We more directly illustrate the possibility to tune the response time of the devices through the architectures (interfacial and active layer properties). Significant improvement in bandwidth can be achieved, suggesting strong potentialities for future applications.

Keywords: Optical wireless communication, visible light communication, perovskite solar cells, impedance spectroscopy, triple cation perovskite solar cells.

Résumé en français

Les nouvelles technologies dans les domaines des télécommunications sans fils et de l'Internet des objets (IoT) nécessitent des solutions efficaces capables d'assurer des transmissions à des débits élevés tout en assurant une bonne qualité de service mais aussi l'autonomie énergétique des dispositifs. Dans ce contexte, l'intégration d'une cellule solaire en tant que récepteur de données et récupérateur d'énergie dans les systèmes de communication optique sans fil est une approche très pertinente, récemment proposée dans la littérature.

Les technologies émergentes de cellules solaires, telles que les cellules solaires pérovskites, sont de bonnes candidates pour cette application, en raison de performances élevées, de coûts réduits, et d'une facilité d'intégration importante. Ce travail de thèse s'inscrit dans cette problématique, en visant à étudier de façon systématique le comportement dynamique de cellules photovoltaïques pérovskites à l'aide de la spectroscopie d'impédance, pour mettre en évidence les relations entre performances pour la récupération d'énergie et la réception de données par voie optique. Nous nous focalisons pour cela sur des couches actives à cations mixtes, choisies en raison de leurs excellentes performances et de leur bonne stabilité. Sur la base des phénomènes physiques mis en jeu, nous proposons un modèle électrique équivalent des dispositifs compte-tenu de cette application. Nous montrons finalement qu'une modification des architectures permet de moduler la bande passante des composants permettant de démontrer le fort potentiel de la filière pérovskite pour la récupération simultanée d'énergie et la réception de données par voie optique.

ACKNOWLEDGEMENT

Firstly I would like to thank my thesis supervisors Johann Bouclé and Thierry Trigaud for their support and guidance throughout my PhD, and for the enriching discussions that we have had which were always constructive and have always led me towards new ideas for my research. Special thanks to Bernard Ratier, he always took the time to discuss the scientific concepts around my thesis work which allowed me to expand my knowledge of the various aspects and areas of photovoltaic solar cells.

I would like to thank Yvan Bonnassieux, Jean-Jacques Simon, and François Tran-Van for reviewing this work and for their valuable suggestions.

In addition, I am grateful to all the ELITE permanent members Rémi Antony, Sylvain Vedraine, Bruno Lucas, Nicolas Parou, and Marie-Laure Guillat for helping me through my lab work in XLIM laboratory.

A special thanks to my colleagues who have become good friends over the course of this thesis: Malika, Issoufou, Karthik, Youssef, Salim, Alexandre, Ceren, and Hamza.

Finally, I would like to thank all my friends and family members for their support and care. I have no words to show my gratitude to my parents, that I dedicate this thesis for them, who have encouraged me and provided their love and all forms of unconditional support, and without their sacrifices, I would never be who I am today.

Table of contents

General introduction..... 12

Chapter I – Context of solar cells for VLC

I.1 Introduction of Visible light communication.....17

I.1.1 Overview and history of VLC 17

I.1.2 VLC Applications.....20

I.1.2.1 RF restricted areas.....21

I.1.2.2 Vehicular Networks 21

I.1.2.3 Smart Home/ Office.....22

I.1.2.4 VLC System for Under Water Applications.....23

I.2 Visible light Communication State of art and the working principle 24

I.2.1 Overview 24

I.2.2 Transmitter: 24

I.2.2.1 Phosphor-Converted LED (PC-LED):.....26

I.2.2.2 Red-Green-Blue LED (RGB-LED): 26

I.2.3 VLC channel and modulation schemes: 27

I.2.3.1 VLC channel 27

I.2.3.2 Modulation schemes 28

I.2.3.2.1 OOK (On-Off Keying) 28

I.2.3.2.2 OFDM (Orthogonal Frequency Division Multiplexing) 29

I.2.4 Receivers 30

I.2.4.1 Cameras.....30

I.2.4.2 Photodiodes.....30

I.2.4.3 Solar cells.....32

I.2.4.4 Photodiodes vs Solar cells as OWC photodetectors 34

I.3 Conclusion (Motivation and objectives).....36

Chapter II – Introduction to perovskite solar cells

II.1 Introduction to Perovskite Solar cells 39
II.1.1 Overview 39
II.1.2 Cristal structure 40
II.1.3 Device architecture 44
II.1.4 Absorption and charge generation: 45
II.1.5 Charge separation: 48
II.1.6 Recombination: 49
II.1.6.1 Band-to-band or radiative recombination 49
II.1.6.2 Trap-assisted recombination or Shockley-Read-Hall (SRH) recombination 50
II.1.6.3 Auger recombination 50
II.1.7 Equivalent Circuit of a Solar Cell: 50
II.1.8 Conclusion 52
II.2 Experimental methods 53
II.2.1 Device fabrication 53
II.2.1.1 Materials: 53
II.2.1.2 Device architecture: 53
II.2.1.3 Transparent electrode: 54
II.2.1.4 Electron transporting layer 55
II.2.1.5 Perovskite layer: 57
II.2.1.6 Hole transporting layer (Spiro-OMeTAD) 58
II.2.1.7 Top electrode (Au) 60
II.2.2 Solar cell Current density-Voltage (J-V) measurement 61
II.2.2.1 Short circuit current (Jsc) 62
II.2.2.2 Open circuit voltage (V_{oc}) 62
II.2.2.3 Fill factor (FF) 63
II.2.2.4 Power conversion efficiency 63
II.2.2.5 Series resistance R_S and the shunt resistance R_{SH} 63
II.2.3 Conclusion 66

Chapter III- Toward efficient and reproducible perovskite solar cells

III.1 Introduction 68
III.2 Toward efficient and reproducible perovskite solar cells 68
III.2.1 SnO_2 optimization 69
III.2.1.1 SnO_2 Aggregation 69
III.2.1.2 SnO2 wettability 72
III.2.2 Perovskite layer optimization 79

III.2.2.1 Solvent diffusion 79
III.2.2.2 The effect of the antisolvent on the reproducibility of PCS 81
III.2.2.3 Inside Vs Outside of the glove box 86
III.3 The stability of perovskite solar cells 89
III.4 Conclusion 91

Chapter IV - Principle of impedance spectroscopy and application in the context of visible light communications

IV.1 Introduction 93
IV.2 Basics of Impedance spectroscopy 94
IV.3 The impedance of basic circuit elements 96
IV.3.1 Resistor 97
IV.3.2 Capacitor 97
IV.3.3 Inductor 99
IV.4 Equivalent circuits 99
IV.5 Experimental measurements by impedance spectroscopy 102
IV.5.1 Impedance spectroscopy experimental setup: 102
IV.5.2 Finiteness 102
IV.5.3 Linearity 103
IV.5.4 Causality 104
IV.5.5 Stability 107
IV.6 Impedance data fitting 108
IV.6.1 The inductive part 111
IV.6.2 Towards a better equivalent circuit for IS data fitting 113
IV.7 Understanding the device physics from impedance spectroscopy 117
IV.8 The relation between the bandwidth and equivalent circuit of the solar cell 120
IV.9 Conclusion 130

Chapter V - Dynamic response of perovskite solar cells

V.1 The effect of the voltage on the PV and VLC parameters of the solar cell 133
V.2 Perovskite solar cell as a band-pass filter 139
V.2.1 Conclusion 142
V.3 Triple cation perovskite solar cells, planar VS mesoporous structure 143
V.3.1 Conclusion 150
V.4 Double Vs triple cation perovskite solar cells 150
V.4.1 XRD 151

V.4.2 JV characteristics of devices....152
V.4.3 Impedance spectroscopy....153
V.4.4 Conclusion....156
V.5 Effect of the perovskite thickness on the dynamic response of the perovskite solar cell 157
V.5.1 XRD....157
V.5.2 Morphology investigated by SEM....158
V.5.3 UV-visible absorption....159
V.5.4 JV....160
V.5.5 Dynamic properties probed by impedance spectroscopy....161
V.5.6 Conclusion....165
V.6 Effect of the SnO_2 electron transporting layer....165
V.6.1 Structural properties of the perovskite active layer on top SnO_2 ETLs....166
V.6.2 UV-visible absorption....167
V.6.3 JV....168
V.6.4 Impedance spectroscopy....169
V.6.5 Conclusion....171
General conclusion....172
Annex....173

General introduction

The tremendous growth of wireless communications is revolutionizing our modern society. Related technologies such as the fifth-generation of wireless networks 5G, machine to machine (M2M) communications, internet of things (IoT) contribute strongly to this development by connecting our ubiquitous devices. The communications in the near future will spread from ’human-human’ to ’human-thing’, and ’thing-thing’ especially with the appearance of the IoT where every object or thing (e.g., coffee machines, cars..), will be connected to the internet (more than 50 billion of objects are planned to be connected in the next few years) [1]. Therefore, the proliferation of smart connected devices will cause a significant increase in data traffic demand, whereas the existing networks are not well suited for responding to this sustained and increasing need.

According to Cisco Systems which is a major network systems company, the global mobile data traffic representing the global amount of data sent and received by mobile devices(e.g., smartphones, tablets, PCs, M2M…) is growing exceedingly. The annual growth rate is around 46%, and it goes from 12 exabytes per month in 2017 to 77 exabytes per month in 2022 as shown in Figure I.1.

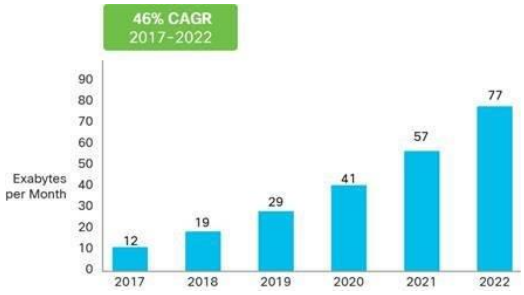

Figure I.1: Cisco forecast for mobile data traffic by 2022 [1]

In fact, 80% of the actual global mobile data traffic is consumed in indoor environments, and according to Cisco’s VNI prediction, this rate is expected to increase, until it reaches this 96% when the 5G gets deployed [2].

The existing wireless communication systems are operating in radio frequency RF bands, however, the radio frequency spectrum is a scarce resource. The massive use of radio frequency bands by our existing communication devices has caused the congestion of the available RF bandwidth which is known as radio-frequency spectrum crunch [3]. This RF spectrum crunch has prompted the research community to seek alternatives for RF

communications in the large electromagnetic spectrum. Hence, optical wireless communications (OWC), and especially visible light communications (VLC), have gained a rising interest in the few last years.

The VLC is operating in the visible part of the electromagnetic spectrum between 380-780nm, which leads to a huge available communication bandwidth, 10000 times larger than the entire RF bandwidth [4]. Moreover, the VLC presents other advantages compared to RF such as the high level of communications security since the visible light is spatially confined between the walls of a room [5], the low electromagnetic interference which is interesting for applications in hospitals and airplanes, the low consumption of electricity especially with the dual use of LEDs for VLC systems and illumination rather than the halogen or incandescent lamps, the safety since the visible light is harmless for the human body unlike RF that is classified as possible to cause cancers according to the world health organization [6], and the very broad range of accessible data rates, from low values in the kbits/s domain, up to very high-speed rates (GBits/s) which can largely compete with conventional high-speed RF technologies [7].

	Spectrum	RF interference	Safety	Power consumption	Cost	Range	Data rates
RF	3-300GH (Limited)	Yes	Medium	High	High	100-200m	Hight
VLC	385-790THz (Immense)	No	High	Low	Low	<10m	Verry hight

Table 1: Comparison between RF and VLC Systems.

All these advantages make the VLC a very strong candidate especially for indoor applications (House, office..) such as the Light Fidelity (LiFi), and numerous applications in IoT and 5G technologies [4]. However, the emergence of all these new technologies will create an ever-increasing need for electricity and energy supply. Currently, communication technologies consume in the order of 10% of our global electricity production, However, this rate is expected to continue increasing, until it reaches 21% in 2030 as illustrated in Figure I.2 [8].

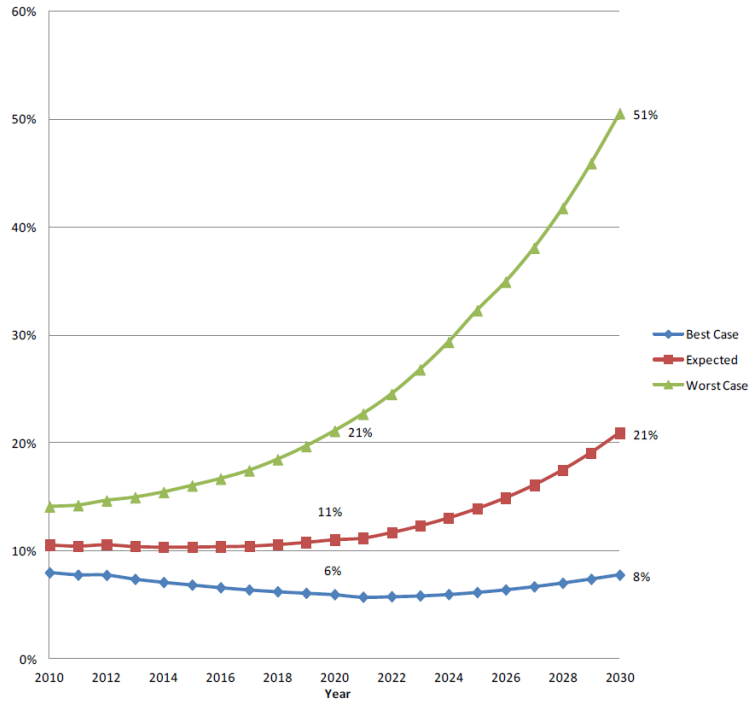

Figure I.2: Share of communication technology of global electricity usage 2010–2030 [8]

To tackle this challenge, a new concept appeared in the few last years which consists to integrate solar panels as receivers of VLC systems[9][10]. In such an approach, the solar cell is simultaneously used for data detection and energy harvesting. However, the choice of the type of solar cell is crucial for the success of such a concept. The third generation of solar cells, mainly organic and perovskite solar cells, are suitable and highly promising especially for VLC indoor applications due to their low cost and very high efficiencies under low lighting conditions (up to 40% of efficiency, far beyond silicon-based or inorganic photovoltaic technologies)[11] REF. In 2015, S. Zhang et al. have demonstrated for the first time a VLC link using PTB7:PCBM organic solar cell as a high-speed detector and energy harvester [3]. In 2020, triple cation perovskite solar cells have achieved a high data rate of 56 Mbps and a power conversion efficiency (PCE) of 18% [12]. This reflects the significant potential of perovskite solar cells to be used as energy harvesters and data receivers simultaneously. Moreover, such a type of solar cell can represent a strong candidate for indoor applications such as IoT due to its low cost, flexibility, and high PCE especially in indoor environments [13] [14].

The main goal of this thesis is to study the dynamic behavior of mixed cation perovskite solar cells using impedance spectroscopy. Therefore the first objective of this work is to fabricate efficient and stable perovskite solar cells in order to be used as receivers for OWC systems.

The second objective is to make a systematic analysis of the capacitive and resistive effects that can limit the bandwidth and the signal detection response using impedance spectroscopy.

Therefore in chapter I, we are introducing the field of visible light communication as well as the basics and the significant improvement of the field in the last decades. Thereafter we are focusing on the utilization of photovoltaic solar cells as data receivers in OWC systems.

In chapter II, we are giving more focus on the basic physics of PCSs As well as the fabrication and characterization methods. Understanding the different physical phenomenons occurring inside of the PSC (Photogeneration, recombination, etc.) is crucial for the understanding of the physical origin behind the solar cell behavior in a dynamic regime.

In chapter III, we are showing our methodology towards will optimized and reproducible PSCs, which is crucial to the comparative studies conducted in the next chapters.

In chapter IV, we are showing our methodology to investigate the dynamic response of the PSCs via impedance spectroscopy, and the proper way to extract significant parameters for OWC such as the bandwidth, the time constant, and its related capacitance and resistance.

In chapter V, we are presenting our results and conclusions that discuss the impact of the structural properties of the PCS (nature and thickness of the perovskite, quality of ETL) on its dynamic response, especially the dynamic resistance and capacitance as well as the bandwidth of the solar cells.

Chapter I – Context of solar cells for VLC

I.1 Introduction of Visible light communication

II.1.1 Overview and history of VLC

The mysterious visible light has fascinated humankind since time immemorial. This strange and magical nature of light, primarily made by the sun and fire, is what prompted humankind through history to try to understand, create, and use it.

The concept of using visible light for communication is not recent. Many early civilizations utilized fire, smoke, or sunlight reflection to transmit messages. In ancient China, in the 5th century BC, fire signals were widely employed by the great wall guardians as a fast way of communication. Furthermore, the ancient Romans and Greeks used polished metal as mirrors to transmit information by reflecting the sunlight [15]. Lighthouses also served, from ancient times up to the present day, as an aid to maritime coastal navigation, they emit an intermittent signal of visible light in order to help and guide ships sailing in risky coastal areas. The Pharos of Alexandria, constructed around 250 BC in Egypt, was the greatest lighthouse in antiquity and one of the Seven Wonders of the Ancient World [16].

Figure I.3: Left, The Pharos of Alexandria[17]***. Right, Man holds two signal fire SOS signal with hand flare*** [18]

Afterward, the American inventor Alexander Graham Bell and his assistant Charles Tainter invented a transceiver, which is a device that can transmit and receive information, called the photophone. This invention is considered the birth of modern wireless optical communication. The photophone uses the reflected sunlight to transmit voice messages over

a distance of 200 m [19]. The voice signals are transmitted by a vibrating mirror which reflects the sunlight and, his modulated sunlight is received by a selenium photocell as shown in Figure I. 4. However, the studies in this field were marginalized due to the outstanding success of radio waves wireless communications, and telegraphy conducted by brilliant scientists such as Guglielmo Marconi and Ferdinand Braun (they shared the 1909 Nobel prize in physics for their works on the development of wireless telegraphy), Heinrich Hertz, David Edward Hughes, Reginald Fessenden, Thomas Edison, Nikola Tesla, etc.[20][21].

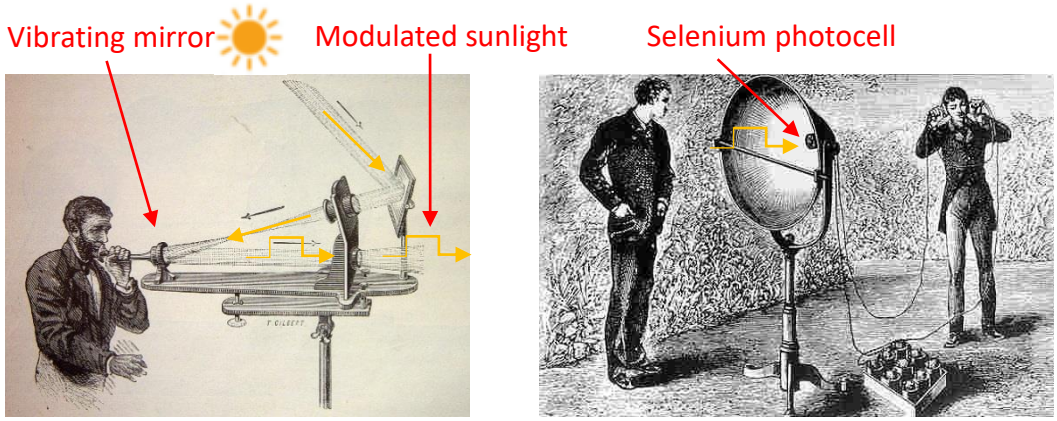

Figure I. 4: Alexander Graham Bell Photophone

The maturation of semiconductors technology, in the 1960s, led to the discovery of Laser and light-emitting diode (LED) which gives a rebirth to OWC. this technology employs three bands of the electromagnetic spectrum which are ultraviolet (UV), visible light (VL), and infrared (IR). For instance, in 1962 researchers from the MIT Lincoln laboratory spectacularly demonstrate the transmission of television signals over a distance of 48 km [22]. From that moment onwards, the number of research programs and projects in this emergent field, back at the time, had multiplied especially for deep-space applications notably the Mars Laser Communication Demonstration and the Semiconductor-laser Inter-satellite Link Experiment, conducted respectively by NASA and the European Space Agency[23][24] [22]. In the last few years, Visible light communications (VLC), which is a subclass of OWC, have achieved many relevant successes as shown in table I.2. In japan 1999, Pang et al. demonstrate for the first time the concept of VLC using LED for illumination and communication. In the following years, research and innovation were significantly thriving, driven by the establishment of active institutions such as the Visible Light Communication Consortium (VLCC) created in 2003[25] and the Li-Fi Consortium created in 2011[26] with a goal of pushing the boundaries of research (data rates, emission,

and detection bandwidth, modulation techniques, cost…) and bringing this innovation into the industry and the market.

Year	Development
1999	➢ LED Traffic Light as a Communications Device [27]
2003	➢ The establishment of the Visible Light Communications Consortium (VLCC), in Japan, aiming to publicize and standardize visible light communication technology.[28]
2007	➢ Visible optical communication system (JEITA: CP-1221) and Visible light ID system (JEITA:CP-1222) were standardized by Japan Electronics and Information Technology Industries Association (JEITA)[29]
2008	➢ Visible optical communication (VLCC), Infrared Data Association (IrDA) and Infrared Communication Systems Association (ICSA) corporate for the standardization activities[28]
2010	➢ The European Union-funded project hOME Gigabit Access (OMEGA) home-area-network achieved Visible-light communication system enabling 73 Mb/s data streaming
2013	➢ The first demonstration of typical silicon solar cell as Visible Light Communication signals receiver[30]
2014	➢ P. A. A. Haigh, Z. Ghassemlooy, S. Rajbhandari, I. Papakonstantinou, and W. Popoola, “Visible Light Communications: 170 Mb/s Using an Artificial Neural Network Equalizer in a Low Bandwidth White[31] ➢ 3-Gb/s Single-LED OFDM-Based Wireless VLC Link Using a Gallium Nitride μLED[32] ➢ 7.01 Mbit/s using commercial multicrystalline silicon solar panel as a receiver for VLC by orthogonal frequency division multiplexing [9].
2015	➢ 8-Gb/s RGBY LED-Based Wavelength Division Multiplexed (WDM) VLC

	System Employing High-Order CAP Modulation and Hybrid Post Equalizer[33] ➢ The first organic solar cells as high-speed data detectors data rate of 34.2 Mbps for visible light communication [3]
2016	LED-Based Wavelength Division Multiplexed (WDM) 10 Gb/s Visible Light Communications[34]
2017	"Gbps Long-Distance Real-Time Visible Light Communications Using a High-Bandwidth GaN-Based Micro-LED,".[35]
2019	➢ 15.73 Gb/s Visible Light Communication with off-the-shelf LEDs[36] ➢ A Wide-Area Coverage 35 Gb/s Visible Light Communications Link for Indoor Wireless Applications[37]
2020	➢ The first Perovskite (triple cation) solar cell with a data rate of 56 Mbps [12]
2021	➢ The record of organic solar cells with a data rate of 363 Mbps [38]

Table I. 2: The evolution of visible light communication technology.

II.1.2 VLC Applications

Recently, the VLC has shown great potential to offer a very high-speed data rate especially with the interesting development in VLC modulation techniques such as Orthogonal frequency division multiplexing (OFDM) wavelength division multiplexing (WDM). For instance, LED-based VLC systems achieved 10 Gb/s in 2016 [34] and 15.73 Gb/s in 2019[36]. To the best of our knowledge, the highest data-rate ever reported in the literature is 35Gb/s published in Nature scientific reports in2019[37]. The utilization of solar cells as a data receiver and energy harvester can be strategic in order to reduce electricity consumption especially in environments that do not require a high data rate, this concept was demonstrated in 2013 [30]. Solar panels were tested for the same purpose and showed a data rate of 7 Mbps and 2 mW under low light intensity (0.35 mW/cm²) [9]. Whereas, in 2020, J.Fakidis et al. have shown that the use of inorganic solar cells can increase the data rate up to 784 Mb/s while harvesting 1 mW from ambient light [39]. **This remarkable progress of the data rate reflects the high potential of solar cells as VLC receivers and the possibility to reach**

very high data rates in the few next years. The state of the art of VLC systems using solar cells as receivers is shown in the following part.

The specific physical properties of visible light give VLC systems numerous advantages compared to the RF communication systems. Therefore, the exploitation of these properties can allow the VLC to be present in a wide domain of diverse applications. Some of these applications are discussed below (**for all these applications, solar cells can be used as the receiver**).

I.1.1.1 RF restricted areas

The VLC can be widely deployed in environments where the RF is not recommended or even prohibited such as radio-quiet zones, which are areas where telescopes and earth-space communication stations are highly protected against RF interferences. Moreover, hospitals, airplanes, laboratories, industries, using sensitive equipment that can be affected by electromagnetic interferences caused by RF devices, thus the VLC shows no electromagnetic interference with sensitive electronic devices nor the existing RF communication systems. In airplanes, for instance, the VLC can be used as an on-board communication system, which can ensure high quality of communication between the Aircrew (Pilot, Navigator, Flight attendants, etc.) and ensures the internet for the passengers in commercial flights as well.

I.1.1.2 Vehicular Networks

The existing vehicle and traffic lights can provide the infrastructure for VLC deployment. VLC can be used to enable the communication between Vehicle-to-Vehicle and Infrastructure-to-Vehicles in order to improve the traffic flow by collecting real-time traffic information and coordinating the movement of vehicles accordingly as shown in Figure I.5. Furthermore, VLC vehicular networks can improve safety by predicting and avoiding potential collisions, using different techniques such as emergency automatic brake lights, speed, and traffic signal violation warnings.

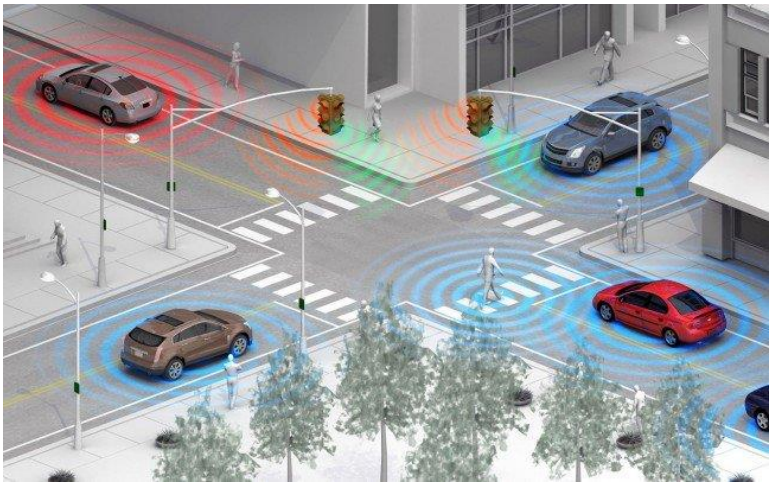

Figure I.5: Vehicle-to-vehicle technology [40]

I.1.1.3 Smart Home/ Office

VLC has a great potential to occupy an important position in the development of our future smart homes, offices, and cities due to its attractive features as illustrated in the following examples:

- The high data rate can provide high internet debit for our PCs, cell phones, TVs, etc. LiFi technology represents a concretization of such a feature. Furthermore, Li-fi can be also a well-suited platform that can incubate new smart concepts such as IoT and M2M.
- The RF waves can easily go through the walls causing numerous security issues. However, the VLC is more adapted for highly secured environment communications (e.g. military and government offices) since the visible light can be room confined and cannot go through the walls which pr very high protection to the local network against any network eavesdropping.
- VLC can perfectly be utilized for indoor localization services by setting a system that links each source of light (transmitter) to the exact position of the receiver in real-time.

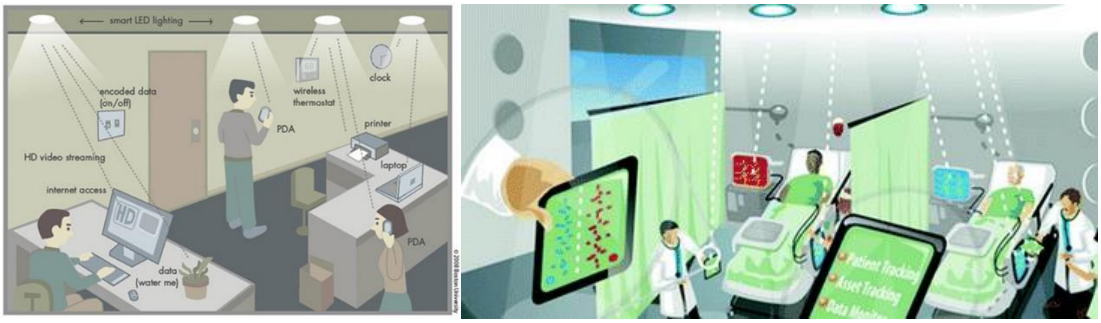

Figure I.6: Li-Fi technology in offices (left) and hospitals (right)[41]

I.1.1.4 VLC System for Under Water Applications

The significant growth of the human underwater activities offshore oil exploration and extraction, submarine communications, marine biology studies, ocean pollution, seismic and sea-level monitoring, etc. The existing RF and acoustic underwater communication are very limited in terms of slow speed and weak signals due to the high attenuation of RF and acoustic waves in seawater. However, the VLC has been recently proposed as a powerful alternative since visibleovide light can easily move in such an environment. Thus, VLC underwater systems can provide high data rates, 15 Gbit/s was reported in 2019 [42] and can be widely used for underwater applications as illustrated in Figure I.7.

Figure I.7: Illustration of human activities underwater demanding long-distance, high transmission speed, and large data rate wireless communications [43]**.**

I.2 Visible light Communication State of art and the working principle

II.1.3 Overview

The operating principle of any OWC system is based on the transmission and the detection of Intensity-modulated light as illustrated in Figure I.8. The modulator transforms the imputed data (image, video, text…) to a modulated electrical signal, afterward, the transmitter converts this electrical signal to an Intensity-modulated visible light that will be received by a receiver. The receiver converts back this visible light to a modulated electrical signal that will be demodulated and turned back into data. A schematic of a basic VLC system is shown in Figure I.8.

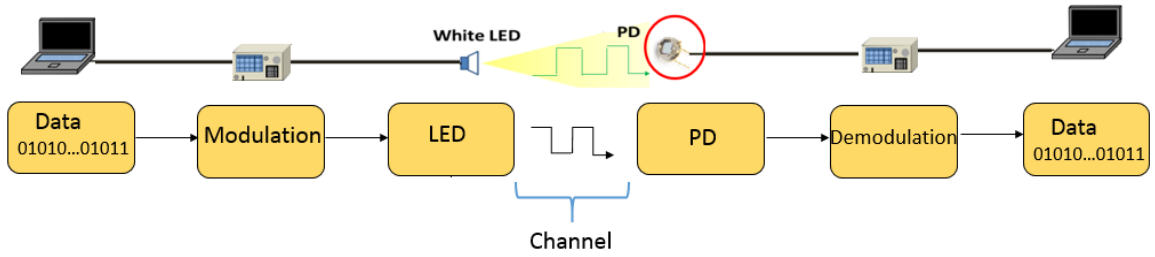

Figure I.8: Block diagram of a visible light communication (VLC) system where is the LED is the light-emitting diode and the PD is the photodetector

II.1.4 Transmitter:

The VLC transmitter, called also emitter, is the component mainly used to convert the modulated electrical signal into modulated light that contains the data.

Light Emitting Diode (LED) is considered as an excellent VLC transmitter since it can be dually used for transmission and illumination at the same time. To transmit the data, the LED is able to be light intensity-modulated which means that the LED lighting On/Off represents the binary code of any transmitted data (0/1). In VLC indoor applications, the changing of light intensity is undetectable for the human eyes, due to the fact that the human eye is not able to see any light intensity fluctuation above 80 Hz [44].

The LED is a solid-state semiconductor device, mainly a PN junction diode able to emit light when current flows into it. The PN junction represents the interface of two types of semiconductor materials deposited one on top of the other:

- N-type semiconductor: intrinsic semiconductor highly doped with electron donor impurities, creating negative majority carriers (electrons) and positive minority carriers (holes).
- P-type semiconductor: intrinsic semiconductor highly doped with electron acceptor impurities, creating positive majority carriers (holes) and negative minority carriers (electrons).
- Depletion region: when n semiconductor is in contact with p semiconductor (PN junction formation), electrons diffuse from n to p region and holes defuse from p to n region instantly which creates a new region free of any mobile charge carriers, it is also called space charge region.

When an external voltage is applied, electrons and holes flow from the electrodes of the LED into the PN junction and end up meeting each other (recombination) in the depletion region, this electron-hole recombination is associated with the emission of light. In fact, electrons lose energy by going from a higher to a lower energetic level (recombination), this loss of energy is manifested in LED as the release of a photon, this effect was discovered by the British engineer Henry Joseph Round in 1907 and called electroluminescence.

The energy of the photon can roughly be represented by the difference between the conduction and valence band levels known as the band-gap energy Eg. This energy is responsible for the color of the emitted light since the wavelength of the photons is related to the energy by Planck–Einstein relation.

$$\boldsymbol{E = h\nu = \frac{hc}{\lambda}} \qquad \textbf{(I. 1)}$$

Where E represents the photon energy, ν the frequency, h Planck constant, the wavelength, and c is the speed of light.

The color of the monochromatic LED depends on the nature and the physical properties of the used semiconductors. For example Blue LED($450 < \lambda < 500$) is made of InGaN semiconductor material and red LED ($610 < \lambda < 760$) is made of AlGaAs semiconductor

material. However, the color of the required LED for illumination is white. Thus, there are two major approaches to produce white color light LEDs.

I.2.1.1 Phosphor-Converted LED (PC-LED):

PC-LEDs are widely used for lighting applications due to their low price compared to the other type of LEDs. This type of LED consists to use blue (sometimes ultraviolet) light, emitted by monochromatic blue LED, that is converted to yellow light using a yellow phosphorescent material. The phosphor layer absorbs some of the blue LED photons (high energy) and emits lower energies photons (other colors), this combination of different light colors appears white to the human eyes. However, when the blue LED light is off the phosphorescent material continues emitting light for a relatively long amount of time (long decay or relaxation time). Consequently, the bandwidth off PC-LED under modulation (on, off) is reduced to be around 3MHz[45]. This slow modulation response can represent a limitation for the system, especially for high data rate VLC applications.

I.2.1.2 Red-Green-Blue LED (RGB-LED):

Known also as Trichromatic LED, this type of LED produces white light by combining red, green, and blue LED chips. In addition, RGB-LED can produce just one of the three primary colors or other different colors such as orange, yellow, by controlling and modulating the current intensity passing inside of each single LED chip, since the LED is a current-driven device.

The cost of fabrication of this multichip LED (a complex LED structure) is higher than the PC-LEDs. However, the modulation bandwidth is around 100 MHZ which is higher than PC-LED [46] [22]. Furthermore, the speed response of the RGB-LEDs can enhance the transmitted data rate, which can improve the performance of the whole VLC system. Moreover, the promising channel modulation WMD (wavelength division multiplexing) is enabled, due to the three separated chips that emit three different wavelengths (colors) in this kind of LED. WMD modulation leads to a high data rate of around 10 Gb/s as reported in H. Chun et al. paper. [34].

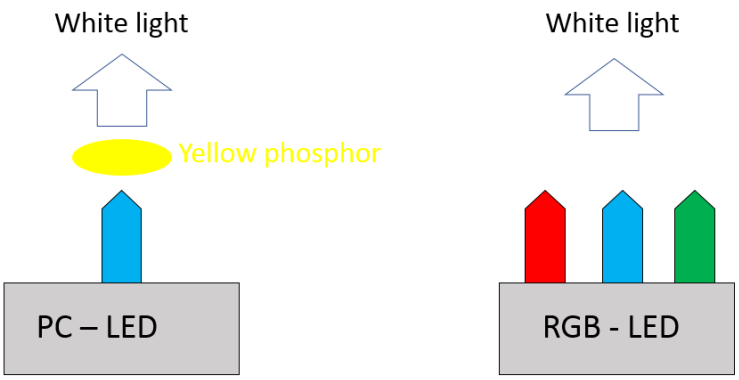

Figure I.9: Phosphor-Converted and Red-Green-Blue LED

II.1.5 VLC channel and modulation schemes:

I.2.1.3 VLC channel

The channel is one of the most important features in any communication system as it represents the wave propagation from the transmitter to the receiver through space. In VLC systems, the transmitted light has to go through the free space optical channel, however, this light signal could not be received as it was transmitted due the signal degradation. This degradation in the quality of the detected signal is caused by two physical phenomena.

First, signal power losses since the light intensity decreases, according to the Inverse-square law, with the square root of the distance between the transmitter and the receiver.

Second, the optical noises such us:

- The different present light sources causing interferences (for example, the artificial lights in indoor applications or the sunlight in outdoor applications).
- Multipath reflections created by indoor surfaces of walls, furniture, ceiling, etc.

In any digital communication system, the maximum data rate transmitted over a communication channel in the presence of noise is represented by Shannon–Hartley theorem as shown in the equation below:

$$C = B\,log_2(1 + \frac{S}{N}) \qquad (I.\ 2)$$

Where C is the capacity of the channel in bits per second (bps), which represents the highest data rate that can be achieved. B is the bandwidth in hertz (Hz), S is received signal power in

watt (W), N is the noise power in watt (W), S/N represents signal-to-noise ratio (SNR) which is often expressed in decibels.

According to Shannon–Hartley equation, a high data rate can be achieved by either increasing the bandwidth, which is limited by the nature of the used transmitter and receiver, or by increasing the signal-to-noise ratio S/N. In VLC indoor applications, the signal power cannot be increased without causing a problem for human eye safety, However, the noise power can be reduced by choosing the proper way of modulation. [47]

I.2.1.4 Modulation schemes

In VLC systems, the modulation schemes play an essential role in enhancing data rate. many of these methods were studied and developed in the last few years such as on-off keying (OOK), pulse width modulation (PWM), orthogonal frequency division multiplexing (OFDM), pulse position modulation (PPM), color shift keying (CSK). We emphasize in the following paragraphs two common modulation schemes for VLC.

I.2.1.4.1 OOK (On-Off Keying)

mainly used for simple and inexpensive systems, the OOK modulation scheme consists to convert the binary data (0,1) into amplitude modulated light beam signal by controlling the light intensity of the LEDs [48]. Hence, in this simple modulation technique, the higher amplitude signal corresponds to the LED light representing digit 1 from the binary data system. Whereas bit 0 is represented by the lower amplitude signal corresponding to the LED light off, Figure I.10 illustrates the OOK modulation mechanism. OOK modulation fits under the category of single-carrier modulation since OOK uses only one signal frequency to transmit the data. Figure I.10 shows the ideal signal shape modulated using the OOK scheme, this ideal square pulse requires fast rise and fall times of the transmitter (LED) and the receiver (example: photodiode).

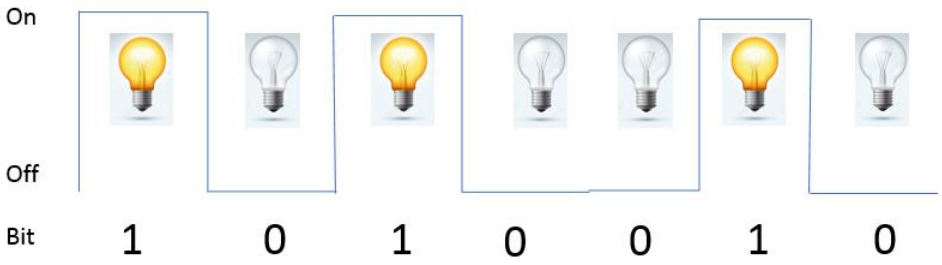

Figure I.10: On-Off Keying data modulation

I.2.1.4.2 OFDM (Orthogonal Frequency Division Multiplexing)

Initially developed for RF communication systems, OFDM is a more complex and advanced modulation scheme for VLC systems compared to OOK. OFDM can remarkably increase the data rate, however, these complex modulations can increase the final cost of the whole VLC system.

Contrary to OOK, OFDM is a multicarrier modulation scheme since it divides the frequency channel into many subchannels (subcarriers). The subcarriers transmit information bits simultaneously over the same channel, which increases the amount of transmitted data. Therefore, OFDM affords high spectral frequency compared to OOK or even conventional FDM. Frequency Division Multiplexing (FDM) is a multicarrier modulation technique, however, the main difference between FDM and OFDM is that the carriers in FDM must be separated and spaced to avoid any interference between the subchannels (or more precisely an inter-symbol interference ISI). However, the subchannels in OFDM can be overlapped in the frequency domain without any interference, which is due to the harmonic mathematical relationship between the subcarriers called the orthogonality [22]. Consequently, OFDM is more spectrally efficient than OOK and FDM because it saves a significant part of the bandwidth as illustrated in Figure I.11.

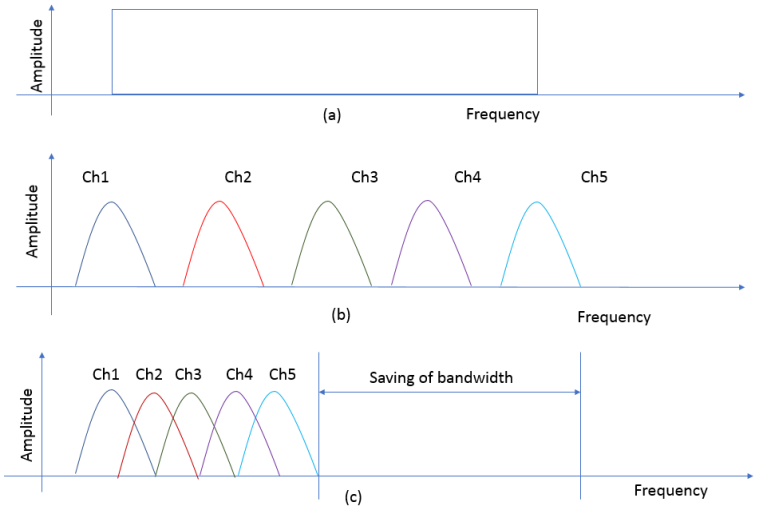

Figure I.11: a) Single carrier modulation, b) FDM, c) OFDM

II.1.6 Receivers

A VLC receiver is a photosensitive device that transforms the modulated visible light emitted by the transmitter into an electrical modulated signal. In this circumstance, the receiver bandwidth is a serious concern for VLC systems since it represents the speed at which the receiver responds to the optical signal variations, consequently, the limitation of the receiver bandwidth vis a vis the LED (when the LED bandwidth is higher) is a limitation of the bandwidth and data rate of the whole VLC system.

Several types of receivers can be utilized such as photodiodes, which are widely used, phototransistors, cameras, solar cells (that we are focusing on in this thesis), or even LEDs. In the following paragraphs, we highlight some of these concepts and with more focusing on solar cells and photodiodes since they belong to the same type of optoelectronic component.

I.2.1.5 Cameras

Cameras are widely used in many ubiquitous devices (e.g. mobile phones, PCs), they can easily detect the light intensity and the colors due to the array of coupled semiconductor capacitors in their image sensors as in charge-coupled device sensors (CCD) or the array of photodiodes and active transistors as in active-pixel sensors (APS). However, cameras need more image processing to interpret the VLC signal detected by the image sensors. Cameras are also able to focus on specific pixels from where the visible light signal is coming and ignore the reset of pixels, which can reduce the optical noise. However, the data rate is limited in conventional cameras due to the relatively low shutter speed (high-speed cameras are better but they are too big and expensive to be used in our everyday devices).

I.2.1.6 Photodiodes

The photodiode (PD) is a solid-state semiconductor device, mainly a PN junction able to absorb photons and generate an electrical current (photocurrent). Generally, this kind of PN junction can operate under two different modes:

- Photoconductive mode: when an external reverse bias is applied on the PN junction, it is also called photodiode mode.
- Photovoltaic mode: when there is no external bias applied on the PN junction, it is also called solar cell mode.

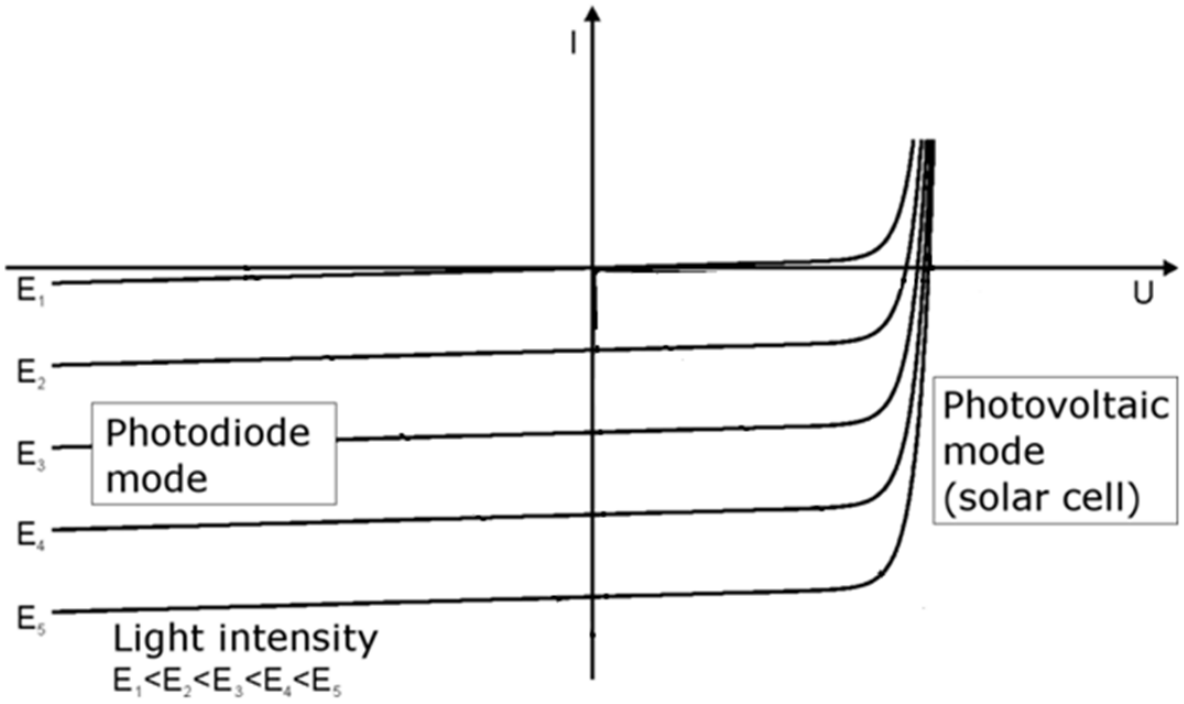

Figure I.12: I-V characteristic of the photodiode (the photoconductive and the photovoltaic modes)

The photodiodes (PDs) and conventional solar cells (SCs) belong to the same type of device (PN or PIN junction), however, the main difference is that they are not operating at the same working point (bias) as shown in Figure I.12.

Under reverse bias (the photodiode mode), the depletion region of the PN junction becomes wider, the built-in electric field stops the electrons going from N to P regions and the holes going from P to N regions. When the PN junction is under illumination the generated electrons and holes defuse to the N and P regions respectively, which is due to the presence of the electric field, afterward, electrons move toward the cathode and the holes move toward the anode producing a photocurrent. However, in the dark, some electrons and holes can be generated without any photon absorption causing a reverse bias leakage current (or dark current) this current represents a significant source of noise for the photodiode. Moreover, other types of current noises can also be present such as thermal noise. Obviously, the presence of noises can strongly affect the quality of the signal reception, however, in this study, we are not addressing this specific point.

I.2.1.7 Solar cells

The photovoltaic solar cell is an optoelectrical device that can convert visible light (sunlight or artificial light) to electricity due to the photovoltaic effect. Same as the photodiode, SC is basically a PN (or PIN) junction where the photoactive material absorbs photons and generates electrons. However, PD is not able to produce electricity as efficiently as a solar cell. This physical quantity (producing electricity) is expressed by the power conversion efficiency (PCE), which represents the ratio between the produced electrical power and the incident light power. PCE is the most significant parameter to describe the performance of a solar cell.

In the last decades, the power conversion efficiency (PCE) of SCs has been enhanced due to the appearance of revolutionary photosensitive semiconducting materials such as perovskite and organic materials, which can reduce also the cost of SCs as we will explain in detail in the next section. Moreover, SCs based on these materials can efficiently produce electricity even under low-intensity indoor light. Due to their tunable and high-energy bandgap and also their excellent spectral matching with the irradiance spectrum of the artificial source of light (e.g. LED).

In this context, SCs are mainly used for outdoor applications such as satellites, solar stations, electrical vehicles, etc. Whereas the rapid growth of IoT has pushed towards the evolution of solar cells destined for indoor applications. In indoor environments, the third generation solar cells, including perovskite solar cells, organic photovoltaics (OPV), and Dye-sensitized Solar Cells (DSSC) are the most promising peavey technologies due to their low cost and their higher indoor PCE compared to inorganic solar cells[13] [49]. In fact, perovskite solar cells have demonstrated very high indoor efficiencies up to 40 % under 1000 Lux [50] [14] whereas the amorphous silicon (a-Si) technology has failed to exceed the 9% of indoor PCE [13].

Solar cells have recently been proposed as VLC receivers combining an energy harvesting and a data receiving capability, giving the promise for autonomous communication devices for the Internet of Things (IoT) or Body Area Networks (BAN). Actually, Harald Haas's group demonstrated this concept using conventional solar panels (polycrystalline silicon) in 2014 [9]. The generated power was around 2 mW under low light intensity (0.35 mW/cm^2) while the generated data rate was around 7 Mbps using the OFDM modulation scheme. Afterward, different inorganic and thin-film photovoltaic technologies were assessed as VLC

receivers [51] [52] [53] [54] [55], for instance, the CIGS module of DisaSolar or a-Si module of SunPartner Technologies that both shows a data rate of around 8 Mbps [51]. In 2020, J.Fakidis et al. have demonstrated a data rate of up to 784 MBps while harvesting 1 mW from ambient light (300 mW/cm²) using inorganic off-the-shelf components (GaAs laser and PV cell) [39].

On the other hand, OSCs and PSCs seem to be particularly relevant since the VLC is deployed mainly in indoor environments. The groups of Harald Haas and Ifor Samuel demonstrate the first organic solar cell as a VLC receiver in 2015, using an organic solar cell based on the reference PTB7:PCBM active layer in a direct architecture. A PCE of 7% and data at rates up to 42 Mbps in a simple VLC chain were reported [3]. Furthermore, triple cation perovskite solar cells achieved in 2020 a high data rate of 56 Mbps with high efficiency of 18% [12], both demonstrations used the OFDM modulation technique. Mica et al. have demonstrated the effect of the thickness of the active layer on the bandwidth and the data rate since the bandwidth is limited by the RC time constant (R is the dynamic resistance and C is the dynamic capacitance). This study has shown that the dynamic capacitance C is the geometrical capacitance of the solar cells which is basically related to the geometry of the active layer however there is no further information about the physical origin of the dynamic resistance R, a complete comparison between the results and measurement methods reported in this paper and ours are shown in the annex. In 2020 Samuel's and Haas's groups have demonstrated a high-speed data rate of 363 Mb/s which is a record in this field using an organic solar cell that can generate a power conversion efficiency of 8.8% under 1 Sun (solar simulator) and 14% under indoor lighting conditions which correspond to10.9 mW [38].

Perovskite solar cells were recently used for visible light communication however the state of the art of this technology remains scarce. The first and the most relevant paper that explores the potential of using hybrid perovskite solar cells as energy and data harvesters in VLC is Mica's paper [12]. In this work, triple cation perovskite solar cells ($Cs_{0.06}MA_{0.15}FA_{0.79}PB(I_{0.85}Br_{0.15})_3$) were used with different thicknesses (60nm, 170nm, 250nm, 640nm, 840nm, 965nm), the photovoltaic and the dynamic performances were investigated based on the changing of the active layer thickness. This preliminary work has demonstrated that increasing the thickness of the perovskite layer can reduce the geometric capacitance and the time response and consequently increase the bandwidth and eventually the data rate of the VLC system. Therefore, the triple cation perovskite solar cells with an

appropriate design have achieved a power conversion efficiency of 20% and a data rate of 49 Mbps using OFDM modulation system.

These relevant results show the great perspective of perovskite solar cells to improve their signal detection as well as the power conversion efficiency via optimizing the device structure. However, the physics behind this behavior is still unclear and deserves a better in-depth understanding especially the physical origin of the dynamic capacitance and resistance (see next part). Therefore, we will try in this thesis work to cover these aspects using the impedance spectroscopy technique as described in Chapter IV and Chapter V.

I.2.1.8 Photodiodes vs Solar cells as OWC photodetectors

As mentioned previously, the main difference between PDs and SCs is that SCs produce electrical energy, where the PDs consume energy since the PD is an external driving power device working under reverse bias. On the other hand, the signal detection is better in the PD than the SC due to the physical nature (mainly the capacitance) of each device as explained below.

It should be pointed out that the PDs and SCs have the same behavior under a dynamic regime therefore they can be electrically modeled with the same equivalent circuit. shows a simplified electrical equivalent circuit that models the dynamic response of both PD and SC.

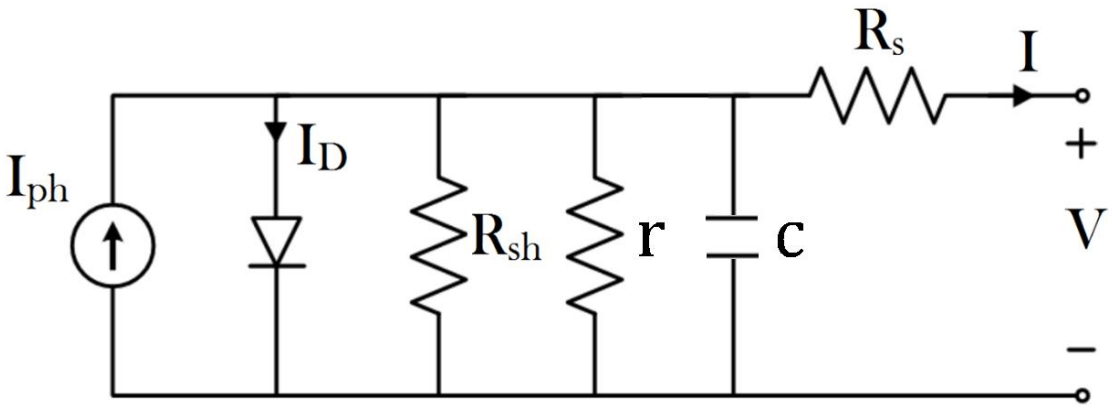

Figure I.13: A simplified electrical equivalent circuit of a solar cell under a dynamic regime

In the ideal case, PDs and SCs can be represented just by a diode and current source (the photocurrent I_{ph}). However, in a real device, there are many imperfections and parasitic physical phenomenon that can strongly affect the device such as the dark current, shunt and

series resistances, etc. Moreover, under a dynamic regime, the dynamic resistance (r) and capacitance (C) must be taken into consideration in order to model the dynamic behavior of the photodetector (PD or SC).

From the equivalent circuit, we can see that the photodetector (PD or SC) behaves as a low pass filter, where its bandwidth is governed by the RC time constant. Therefore, the photodetector bandwidth is limited by the capacitance C and the corresponding resistances (mainly the dynamic resistance r // the shunt resistance R_{sh}). This dynamic capacitance was attributed to the geometric capacitance which is basically related to the geometry of the device. This capacitance is similar to the capacitance of a simple capacitor, where its general formula is represented in the following equation:

$$\boldsymbol{C = \varepsilon \frac{A}{d}} \qquad \textbf{\textit{(I. 4)}}$$

- C is the capacitance (F) in the PN junction it represents the junction capacitance C_j
- A is the area of the two plates (m^2) in the PN junction
- d is the distance between the plates (m) in the PN junction
- ε is the dielectric permittivity (F/m) in PN.

In PN junction photodetectors type, the capacitance C of the device is related to the depletion region created in the interface between P and N semiconductors. Therefore, $\boldsymbol{d}$ represents the width of the depletion region and $\boldsymbol{A}$ represents the junction area of P and N regions (electrodes).

In a photoconductive mode, the PN junction is under reverse bias, which increases the width of the depletion region, leading to a decrease of the junction capacitance, and consequently enhances the bandwidth that makes the PD more efficient in signal detection compared to a conventional solar cell.

On the solar cell side, the capacitance of SCs is bigger than the photodetector (in the order of Nano farads for SCs compared to Pico farads for PDs), leading to a lower bandwidth (generally hundreds of kHz). However, this bandwidth is good enough for indoor applications such as IoT.

The dark current of the PN photodiode (under reverse bias) represents an important source of the noise. Whereas, solar cells are less affected by this problem since they are not working under reverse bias but some other types of nose current can still be present in both

solar cells and photodiodes such as the thermal or Johnson noise. Photodetectors can also be more sensitive to external sources of light noise compared to the solar cells however many solutions are proposed such as optical filters, that reduce the optical noise using specific modulation schemes.

The following table illustrates the major differences between SCs and PDs:

	Photodiode	Solar cell
Electrical energy	Consume	Produce
Bandwidth	MHz-GHz	KHz-MHz
Capacitance	Low (Pico farad)	High (Nano farad)
Signal detection	High	Low
Noise	High	Low

Table I. 3: Photodiode VS Solar cell

Besides the PN junction devices, other concepts such as PIN photodiodes, which contain an intrinsic semiconductor layer between the P and N layers, are very promising. This high resistance region increases the width of the depletion region and by consequence reduces the capacitance and improves the signal detection (bandwidth). However, this kind of photodiode has no significant effect on the noise current that reduces the signal-to-noise ratio, since it still operating under reversed bias. Despite the noise, the PIN photodiode is still well suited for very high bandwidth applications (GHz).

On the solar cell side, this concept is already present in perovskite and organic solar cells, where the I layer represents the absorber (the perovskite layer) and P and N present the two transporting layers as is explained in chapter II. Therefore, the capacitance of such kinds of solar cells can be controlled by the thickness of the absorber unlike in PN type solar cells where it is more difficult to control and increase the width of the depletion region.

I.3 Conclusion

In this chapter, we highlighted the potential of visible light communication and the important role that it can play in the future especially when new technologies such as 5G and IoT be more present in our daily life. This thesis focuses primarily on the data receiving part of the OWC system, particularly the photodetection. Photodiodes show a high potential to achieve

high data rates, whereas, solar cells can be a strong rival since they can be used as energy harvesters and signal detectors simultaneously. In our case, we are focusing on indoor applications to reduce electrical energy consumption, therefore we are studying the SCs as energy harvesters but also as data receivers. Perovskite solar cells are more adapted for such applications due to their good IPCE, low cost, and the promising VLC performances proved recently. Moreover, the PIN structure of PSCs can be a big advantage to improve signal detection via reducing the SC capacitance.

Chapter II – Introduction to perovskite solar cells

II.2 Introduction to Perovskite Solar cells

II.2.1 Overview

Perovskite solar cells are named according to the crystal structure of the absorber material called perovskite. The term perovskite was primarily attributed to the mineral calcium titanium oxide (CaTiO3); it was first discovered in 1839 by the German mineralogist Gustav Rose in the Ural mountains of Russia and named after the Russian mineralogist L.A.Perovski.

Hybrid inorganic-organic lead halide perovskites have been first reported as an absorber for solar cells in 2009 by Miyasaka groups, with an efficiency of around 3.8% [56]. However, the real perovskite breakthrough was in 2012 due to the enhancement of efficiency (more than 9%) achieved by Park and Snaith groups [57] [58]. This progress relies on the advances made by dye-sensitized solar cells (DSSCs), where the DSSC absorber was replaced by the perovskite, and the rest of the solar cell had remained the same (same HTL, ETL, and electrodes). The tremendous research efforts made by many research groups all over the world had strongly prompted the efficiency until reaching 25.5 in 2020 [59]. This efficiency is a bit higher than the whole efficiencies reported by the generation of thin-film solar cells and close to the best record of crystalline silicone generation as illustrated in the National Renewable Energy Laboratory (NERL) chart Figure II.1. The Si single crystal has recorded a high power efficiency however the process of fabrication requires very high temperature, which increases the cost of fabrication, the same problem is faced in thin-film solar cells that require a very high vacuum. On the other side, the cost of perovskite solar cells is less with the same excellent performance, due to the relatively simple fabrication processes moreover, the possibility of printing PSCs at a high scale can reduce even more the fabrication cost.

The outstanding performances of PSC put it as a strong rival of crystalline silicon and thin-film solar cell technologies, thus it is expected that the PSC will take an important part of the solar cells market. The high power conversion efficiency of PCS and its low fabrication cost are the key points to reduce the price of the kWh of electricity.

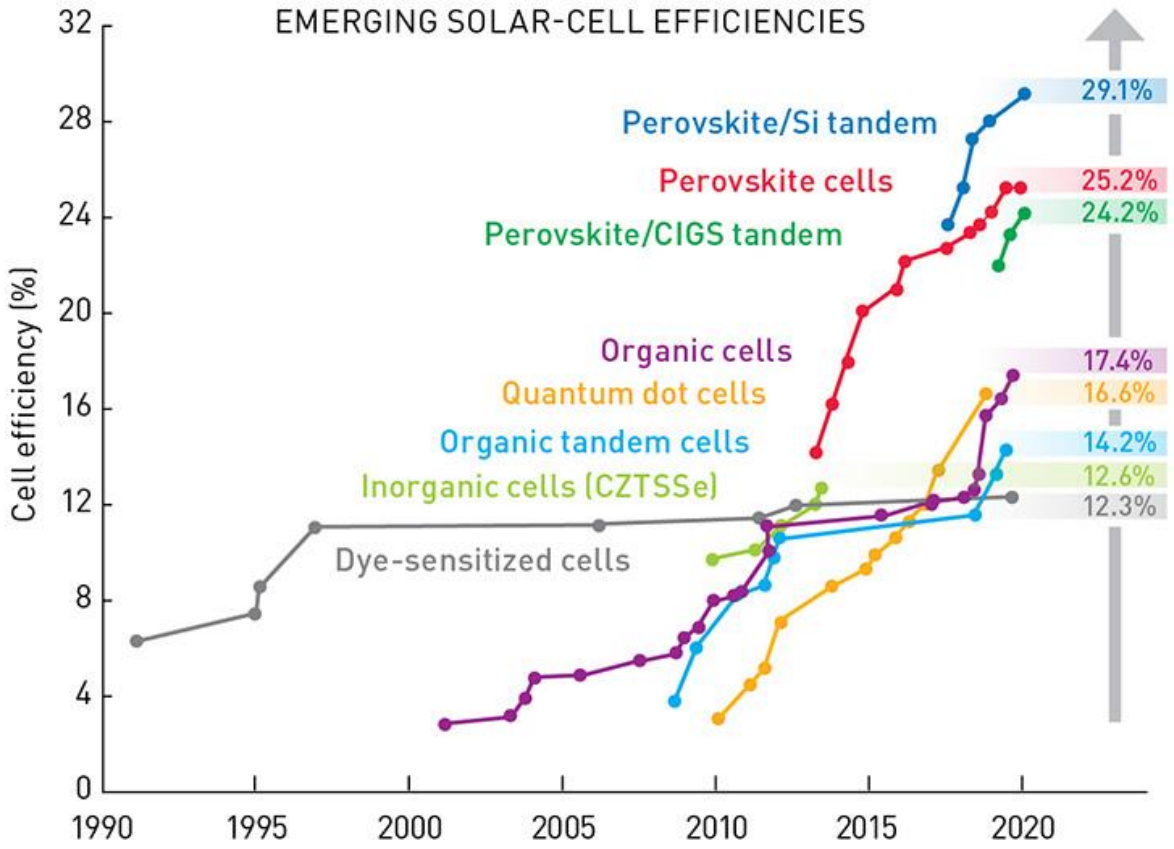

Figure II.1: Evolution of the world record efficiencies of the different photovoltaic SCs technologies obtained in laboratory conditions [60]**.**

II.2.2 Cristal structure

The general formula of Perovskites is ABX_3, where A and B are two cations and X is the anion as shown in.

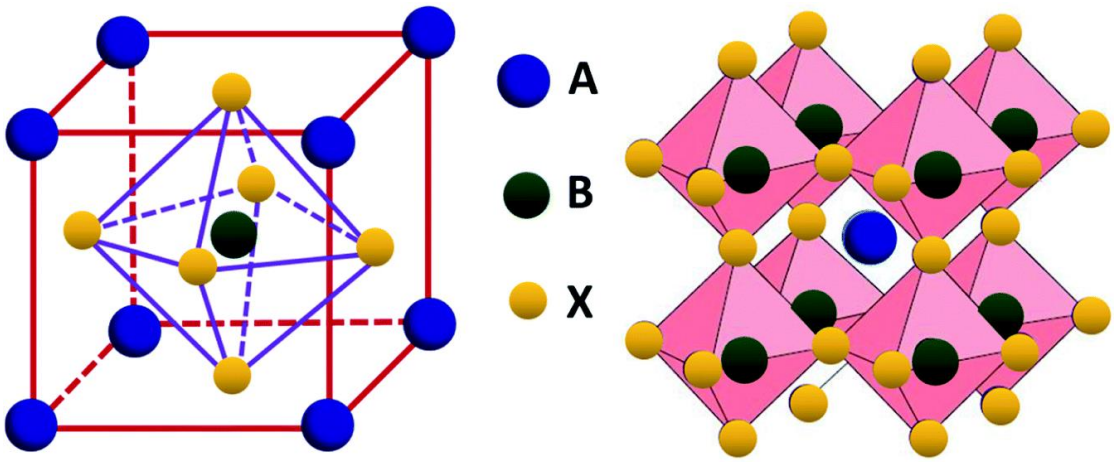

Figure II. 2: Structure of ideal ABX3 perovskites[61]

In hybrid organic-inorganic halide perovskite solar cells:

- X is a monovalent anion that forms the BX_6 octahedra with B in the center, X is typically a single or a mixture of halides such as Br^-, Cl^-, or I^-.
- B is a cation generally bivalent with an oxidation state of 2+, it is typically a metal such as Pb^{2+} or Sn^{2+}.
- A is a univalent cation located in the corners of a cube in an ideal perovskite structure, it is typically an organic molecule or an inorganic cation (cesium) or sometimes a mixture of both.

The choice of the type and the size of the A cation can be crucial since it can easily distort the crystalline structure (e.g. hexagonal rather than cubic structure) which have a considerable effect on the physical properties of the perovskite layer (e.g. yellow non-photoactive film rather than dark photoactive film).

In order to have a stable 3D halide perovskite structure the value of the tolerance factor t, also known as the Goldschmidt factor, must be between 0.8 and 1 [62]. The Goldschmidt factor is a dimensionless value that characterizes the stability and the distortion of the ABX3 crystal structure in regards to the ionic radius r (ionic radii) of A, B and X ions. It has been widely used to predict the stability of the 3D structure of the perovskite only by knowing its chemical formula and the A, B, X radius. The tolerance factor can be calculated from the following expression:

$$t = \frac{r_A + r_X}{\sqrt{2}(r_B + r_X)} \quad \text{(II. 1)},$$

Where r_A, r_B and r_X are the ionic radius of the A, B, and X sites respectively.

When the tolerance factor is between 0.8 and 1, the cubic crystal structure tends to be formed (The ideal ABX_3 cubic perovskite is formed around $t \approx 1$), the color of the perovskite is dark and this perovskite phase is well suited for photovoltaic applications, it is commonly named the α-phase. Other perovskite crystal structures can be also formed between 0.8 and 1, they are also considered as an α-phase such as the tetragonal structure. However, when t<0.8 an orthorhombic structure tends to be formed, and when t>1 a hexagonal structure tends to be formed. These non-perovskite structures, with a yellow color, are not suitable for photovoltaic applications and are commonly known as the δ-phase. δ_O-phase for the orthorhombic structure and δ_H-phase for the hexagonal structure. Furthermore, the use of a large A cation size can transform the 3D structure to a 2D structure with t>>1, which is not more convenient for LED applications than solar cells. When t<<0.8, caused by the small size of A cation, a trigonal structure tends to be formed and this phase is called the β phase. The perovskite material may change its structure or even its phase according to the changing of temperature that can cause torsion of the crystal structure, however, it is necessary for photovoltaic applications to have a stable α-phase around room temperature.

The torsion of the crystalline structure can also be caused by the preparation method and the storage conditions (degradation caused by moisture, light, temperature..) of the perovskite film, which explains the occasional appearance of the two faces in the same film for known chemical composition.

It is difficult sometimes to calculate the tolerance factor since it is hard to determine the organic cation size accurately, which is due to its non-spherical geometry and its constant rotation inside of the lattice [63]. However, it is possible and very helpful to estimate the size of organic cations and estimate the tolerance factor afterward, which can give the possibility of mixing high size and low size cations, in order to have an appropriate tolerance factor.

Many organic molecules have been investigated such as the methylammonium (MA^+ or CH3NH3$^+$) or the formamidinium (FA+ or $NH_2CH{=}NH_2^+$). MA^+ occupied the A cation site in typical methylammonium lead triiodide ($MAPbI_3$) perovskite structure widely used in halide perovskite solar cells. The tolerance factor of $MAPbI_3$ is around 0.95 with a stable dark alpha phase however $FAPbI_3$ have shown a higher tolerance factor of 1.03 with a δH-phase at room temperature which could be understandable considering the FA^+ ionic radius of 2.53 Å that is higher than the MA^+ ionic radius of 2.16 Å [64].

Organic cesium has been also investigated as perovskite A site cation, Cs^+ have a smaller size than MA^+ and FA^+ which gives a lower tolerance factor with a stable nonphotoactive δ_O-phase at room temperature for $CsPbI_3$, however, an α-CsPbI3 can be obtained at a temperature higher than 350 °C which is not interesting for photovoltaic applications [65].

The tolerance factor can be tuned by mixing high size cation FA^+ and low cation size Cs^+ in the same structure in order to have an effective tolerance factor between 0.8 and 1 as illustrated in Figure II. 3, this mixing can be also called doping.

Mixed or double cation $FACsPbI_3$ shows a stable black alpha phase with a cubic structure at room temperature, unlike pure $CsPbI_3$ and $FAPbI_3$ that show a yellow gamma phase. Moreover, double cation (Cs FA) and triple cation (Cs FA MA) solar cells have shown high thermal stability with high power conversion efficiency[66].

The correlation between the perovskite structure and the Goldschmidt factor is shown in Figure II. 3.

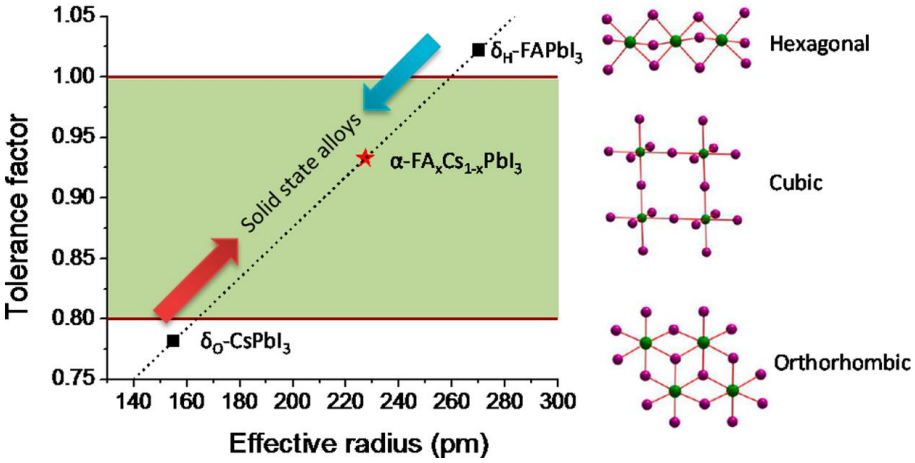

Figure II. 3: Correlations between tolerance factor and crystal structure of perovskite materials [11]

Correlations between tolerance factor and crystal structure of perovskite materials [62]

On the other side, the choice of the anion that occupied the X site is very important since it has a large effect on the optical bandgap of the perovskite. In $APb(I_xBr_{1-x})_3$ mixed-halide perovskites, the bandgap can be tuned from 1.48 eV to 2.35 eV just by mixing Iodide with bromide in the X site which can boost the PCE of the solar cells by increasing the absorption of the visible spectrum [67].

The BX_6 octahedra tend to be more stable, however, the choice of B and X sites should take into consideration the octahedral factor μ. It has been found that the perovskite tends to be more stable for μ values between 0.442 and 0.895 [64]. The octahedral factor is defined as:

$$\mu = \frac{r_B}{r_X} \text{ (II. 2)},$$

II.2.3 Device architecture

In perovskite solar cells, the photon absorption and the pair electron-hole generation occur in the perovskite layer, it is also called the active or absorber layer. It is situated between two transport layers that can efficiently extract charges (electrons and holes) from the active layer and inject them into the electrodes. The electron transporting layer (ETL) is an N-type semiconductor that blocks the holes and transports electrons from the active layer to the electrode whereas the Hole transporting layer (HTL) transports the holes and block the electrons. Unlike ETL and HTL the perovskite layer is intrinsic, thus it is neither N-doped nor P-doped. On the other hand, the electrical field created by the transport layers helps for the charge extraction by creating an electrical field that moves the generated electrons to the ETL and the generated holes to the HTL.

There are mainly two PSC structures as shown in Figure II. 4.:

- Direct structure (NIP) where the ETL is transparent and allows the visible light to go through it in order to reach the perovskite layer.
- Inverse structure (PIN) where the HTL is transparent and allows the visible light to go through the HTM in order to reach the perovskite layer.

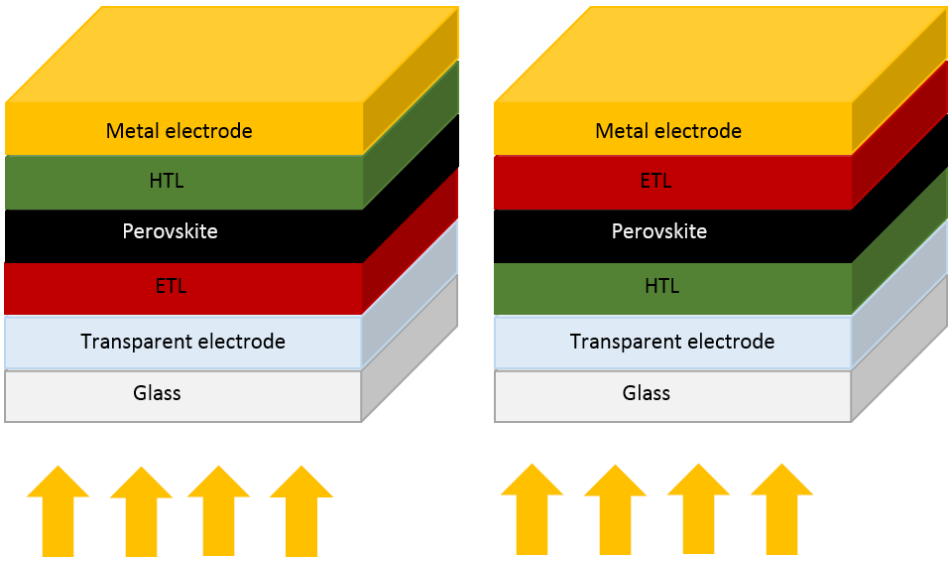

Figure II. 4: Perovskite solar cell direct structure NIP (on the left), inverse structure PIN (on the right)

Our perovskite solar cells have a direct structure with SnO_2 as a transparent ETL and Spiro-OMeTAD as HTL. The main physical phenomenons happening in the PSC are described in the following paragraphs.

II.2.4 Absorption and charge generation:

In PSCs the photogeneration is mainly happening in the perovskite layer that absorbs the light and generates pairs of electrons and holes. The absorption of any semiconductor depends on its bandgap (Eg), which is the difference between the valence band and the conductive band, and the wavelength of the light. Thus, the semiconductor can only absorb photons with equal or high energy than the bandgap energy, this energy is sufficient to move the electrons from the valence band to the conduction band, this transition is called band-to-band transition. Electrons that absorb higher photon energy will go to an energy state above the edge of the conduction band, but they will quickly lose the excess of energy ($hv - Eg$) generally by releasing thermal energy (by interacting with the lattice). Thus, the electrons end up settling down next to the band edge (electrons relaxation). Most of the photons with lower energy can not be absorbed so they are transmitted through the material. However, the presence of defect states within the bandgap such as tail states and midgap states can absorb a part of the photons with lower energy than the bandgap and generate charge carriers, this transition is called trap assisted transition.

The band-to-band transition can be whether direct if the semiconductor has a direct bandgap or indirect if the semiconductor has an indirect bandgap. When the maximal-energy state in the valence band and the minimal-energy state in the conduction band have the same crystal momentum (k-vector) in the Brillouin zone, the bandgap is called direct. Whereas, when the crystal momentum of the conductive band minima and the valence band maxima is different the bandgap is called indirect as illustrated in Figure II. 5. In other words, the direct bandgap transition implicates only the change of charge carrier energy, unlike the indirect bandgap transition that implicates the changing of the charge carrier energy and the momentum. In indirect transition, the conservation of crystal momentum imposes, when the momentum changes, the interaction with the lattice in the form of phonon absorption or emission.

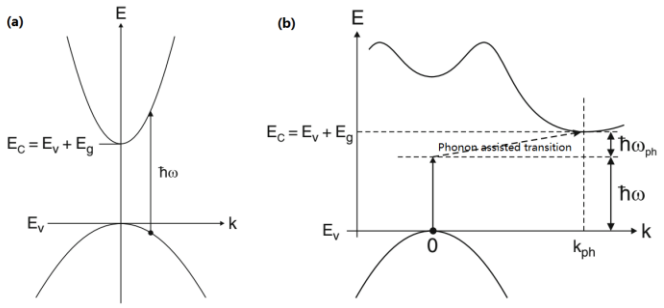

Figure II. 5: Electron transitions after light absorption in (a) direct bandgap semiconductors, and (b) indirect bandgap semiconductors [68]**.**

Semiconductors with either direct or indirect bandgap can be used as absorbers for photovoltaic applications. The absorption rate, which is defined by the absorption coefficient, of indirect bandgap materials (E.g. crystal silicon) is lower than direct bandgap materials, therefore a layer with a high thickness is required in order to absorb light efficiently. On the contrary, direct bandgap materials (E.g. perovskite, InAs, GaAs) are more suitable for thin-film photovoltaic applications since they have a high coefficient of absorption, which means that they can absorb light efficiently even with a low thickness layer.

The absorption coefficient α is an important optical parameter as it characterizes the ability to absorb light by material within a given thickness. It has a different formula depending on the type of transition[69].

For direct bandgap, the absorption coefficient is given by:

$$\alpha = A(\nu - E_g)^{\frac{1}{2}} \qquad (II.3),$$

The absorption coefficient of trap-assisted transition can also be calculated differently by including E_U the Urbach energy as a distribution function of tail and mid-gap defect states [70] [69]. This kind of absorption coefficient is very low because the density of the tail and mid-gap defect states is very low, therefore, this coefficient is not significant for the nature of the material but more its defects. The optical bandgap Eg can be estimated from the absorbance spectrum since the absorbance coefficient and the optical bandgap are linked by the Tauc equation [71] :

$$\alpha h\nu = B^2(h\nu - E_g)^r \qquad (II.5),$$

Where hυ is the incident photon energy, B is a parameter corresponding to the band tailing, and r a parameter that determines the nature of optical transition with specific values: r=2 for allowed indirect transitions, r=3 for forbidden indirect transitions, r=1/2 for allowed direct transitions, or r=1/3 for forbidden direct transitions.

Perovskites have generally a direct bandgap with a high absorption coefficient, the Figure II. 6 illustrates the absorption coefficient of different materials used as absorbing layers in photovoltaic solar cells [72]. From Figure II. 6 we can observe that $CH_3NH_3PbI_3$ perovskite has a bandgap around 1.7ev with a very high absorption coefficient that is competitive to the CIGS thin-film solar cells and way higher than the crystalline silicon c-Si, which means that the $CH_3NH_3PbI_3$ perovskite can absorb photons efficiently with a very thin film. $CH_3NH_3PbI_3$perovskite has a bandgap around 1.6 eV which is slightly larger than 1.34 eV the optimized bandgap value for a single-junction solar cell according to Shockley-Queisser limit (SQ)[73].

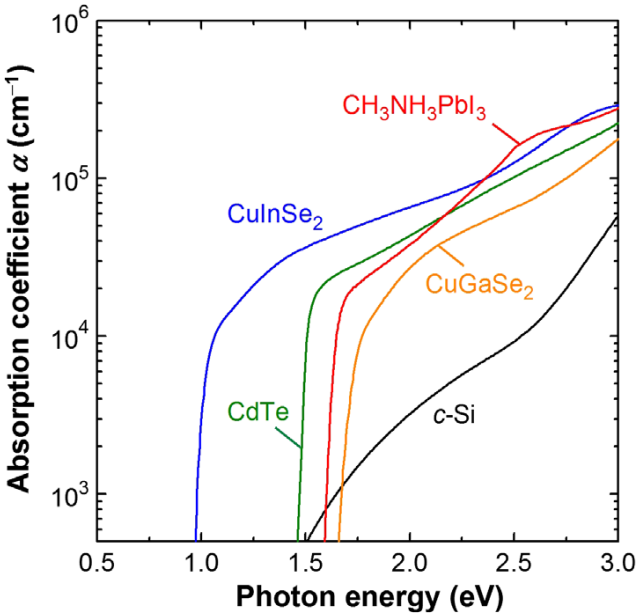

Figure II. 6: Absorption coefficient (α) spectra of various solar cell materials [18]

II.2.5 Charge separation:

The active layer generates an electron and hole that are bound together due to the Colomb force, known as electron-hole pair or exciton. The attractive Coulomb force will cause the recombination of electron and hole if the two charges are not separated, the charge separation, which is the creation of free electrons and holes, require extra energy that is higher than the exciton binding energy.

For solar cell applications, it is required to use absorbing material with low binding energy in order to achieve high power conversion efficiency, unlike LED that requires high binding energy material in order to favorite the radiative recombination (light emission). Perovskite solar cell materials, and crystalline silicon as well, mainly have binding energy lower than thermal energy K_BT where T is the temperature and K_B is the Boltzmann constant. For example, the binding energy at room temperature of $CH_3NH_3PbI_3$ ($MAPbI_3$) is around 10 meV which is lower than the available thermal energy kBT ~ 26 meV [74], which means that the generated electron and hole are instantly free (this is also the reason why we don't talk often about excitons for perovskite solar cells). However, some perovskite materials especially wide-bandgap perovskites can have binding energy way higher than thermal energy which makes them more suitable for LED applications [75].

On the other hand, organic solar cells have binding energy higher than thermal energy (typically between 100 meV and 500 meV [76]) which requires more energy to separate the charges. Donor/Acceptor heterojunction structure is generally used to resolve this problem.

II.2.6 Recombination:

The recombination is when the excited electron of the conduction band loses its energy and goes back to the valance band and recombine with a hole, this phenomenon is considered as the reverse process of the electron-hole excitation. Recombination is one of the key parameters that can extremely affect solar cells and highly reduce their performances, it can occur inside of each layer of the solar cell (inside the semiconductor bulk) and on the interfaces between two layers as well. Recombination takes place through three mechanisms, one radiative (Band-to-band recombination) and two nonradiative (Auger recombination and Trap-assisted recombination) as illustrated in Figure II. 7.

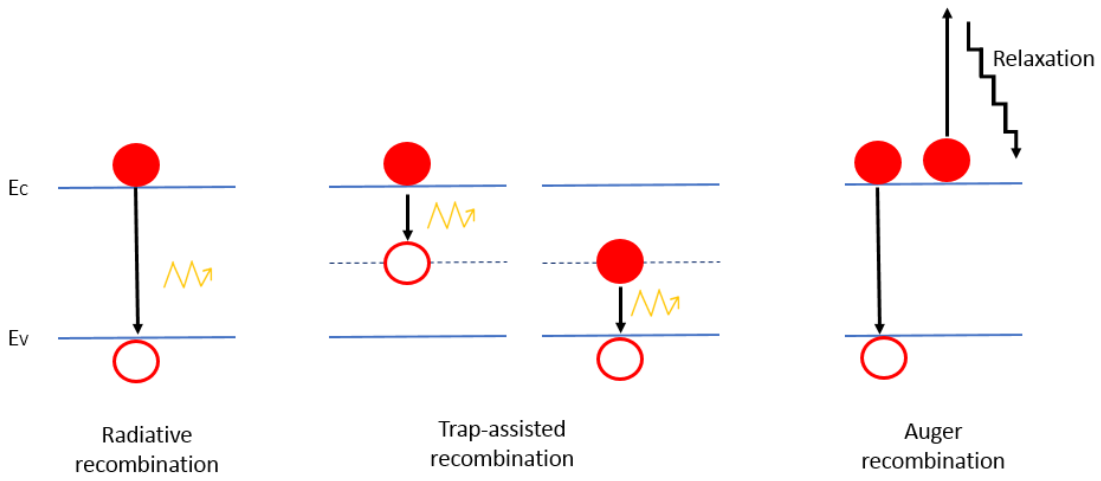

Figure II. 7: Recombination mechanisms

II.2.6.1 Band-to-band or radiative recombination

Radiative recombination occurs when an electron of the conduction band recombines directly with a hole of the valence band by releasing a photon. For a direct bandgap material, the energy of the released photon is almost equal to the bandgap energy Eg. This type of recombination is bimolecular since two charge carriers with different allowed bands (conduction, valance) are involved [77]. Radiative recombination is considered as the reverse process of photogeneration, thus it is the working principle of LED.

II.2.6.2 Trap-assisted recombination or Shockley-Read-Hall (SRH) recombination

trap-assisted recombination is caused by the defects in the crystal lattice, it occurs when a charge carrier (electron or hole) recombines with its opposite charge carrier trapped in an intra-gap energy state. This type of recombination is monomolecular just only one charge carrier from an allowed band is involved [78][79].

II.2.6.3 Auger recombination

Auger recombination occurs when the released energy of recombination is transferred to another charge carrier causing its excitement to a higher energy state, after a while, the excited charge carrier will lose its energy (relaxation) through the thermalization process.

Auger recombination was found insignificant in the context of illumination that follows the AM1.5 norm (100 mW/ cm^2) [80]. Whereas, radiative recombination and trap-assisted recombination take place under these illumination conditions [81].

II.2.7 Equivalent Circuit of a Solar Cell:

The basic physical phenomenons happening inside of a solar cell can be electrically modeled using a simple equivalent circuit as shown in Figure II. 8. The solar cell photogeneration is modeled by a source of current in parallel with a simple diode that represents the PN structure of a solar cell, only these two components can represent an ideal solar cell. Whereas, a real solar cell is not ideal so the different types of electrical losses, such as recombination processes occurring whether in the absorber layer or on the interfaces between the different layers, are modeled by a shunt and a series resistance [82]. A simple equivalent circuit of a solar cell is shown in the Figure II. 8.

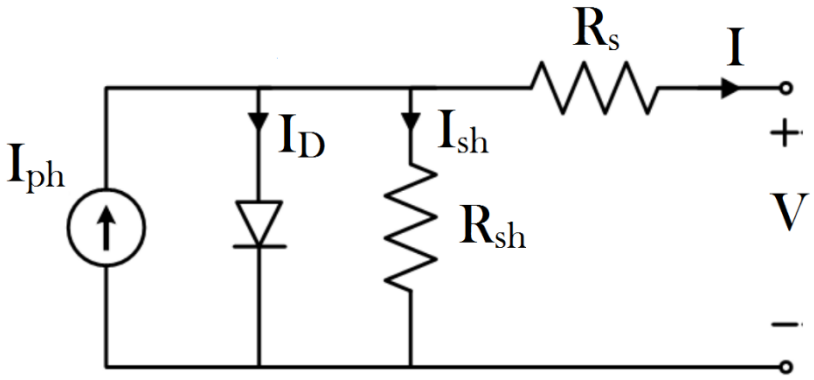

Figure II. 8: Simple solar cell equivalent circuit

From the schematic equivalent circuit, we can notice that the output current I of a solar cell is different from the photogenerated current I_{ph}. The output current I can be calculated from the equivalent circuit as follows:

$$I = I_{ph} - I_D - I_{SH} \qquad (II.6),$$

From Shockely diode equation, the diode current I_D is:

$$I_D = I_0 \left[exp\left(\frac{qV_D}{nkT}\right) - 1 \right] \qquad (II.7),$$

From the ohms law, the flowing current through shunt resistance can be expressed as:

$$I_{SH} = \frac{V_D}{R_{SH}} \qquad (II.8),$$

The voltage across the diode $V_D$is equal to the voltage across the shunt resistance, it can be defined as follows:

$$V_D = V + IR_s \qquad (II.9),$$

Finaly, the equation $(II.6)$ can be expressed as:

$$I = I_{ph} - I_0 \left[exp\left(\frac{q(V + IR_s)}{nkT}\right) - 1 \right] - \frac{V + IR_s}{R_{SH}} \qquad (II.10),$$

The recombination processes occurring in a solar cell can be understood using dark IV measurement (see next section). For this purpose, an equivalent circuit with two diode models is often required as shown in Figure II. 9, the first diode is modeling the trap-assisted (SRH) recombination process, and the second one is modeling the band-to-band

recombination process. Obviously, in this equivalent circuit, there is no current generator since in the dark there is no photogenerated current (Iph = 0).

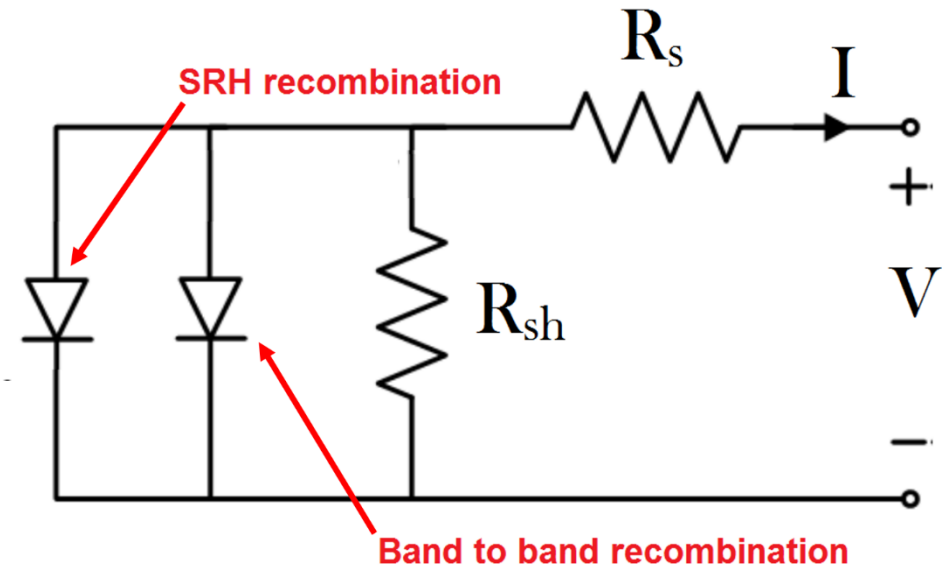

Figure II. 9::Equivalent circuit of a solar cell in the dark

From this equivalent circuit, the current flowing through the solar cell in dark can be defined by the following equation:

$$I = I_{01}\left[exp\left(\frac{q(V+IR_s)}{2kT}\right)-1\right]+I_{02}\left[exp\left(\frac{q(V+IR_s)}{kT}\right)-1\right]+\frac{V+IR_s}{R_{SH}} \qquad (III.2),$$

The VLC requires to put the solar cell under illumination therefore the circuit of is mainly used, however, it could be useful to keep in mind the circuit (in the dark) since it can be helpful to have a more in-depth understanding of the different recombination phenomena occurring inside of the PSC.

II.2.8 Conclusion

In this part, we have seen the basic fundamental aspect of PSCs. Understanding this aspect is crucial for the understanding of the physical origin behind the dynamic behavior of the devices. However, this is not sufficient since these basics must be combined with a deep understanding of the experimental aspect. This part is also crucial since every small experimental detail can make a big difference in the performance of the solar cell or its

dynamic response. Therefore, in the next part, we are giving our fabrication method of efficient solar cells based on triple and double cation PSCs.

II.3 Experimental methods

II.3.1 Device fabrication

In this section, we are presenting the fabrication protocol that we have elaborated in the XLIM laboratory that allows us to have working and efficient mixed cation perovskite solar cells. Especially, most of the recipes can be found in details in the papers published by the ELITE group over the years. [83][84][85][86]

II.3.1.1 Materials:

- *Perovskite material:* Formamidinium iodide (FAI) (≥ 90%, Great cell Solar (Dyesol)), Cesium iodide (CsI) (99.9%, trace metals basis, Sigma Aldrich), lead iodide ($PbI2$) (99%, Sigma Aldrich), lead bromide ($PbBr2$) (≥ 98%, Sigma Aldrich).
- *Transporting layer materials:* Tin oxide nanoparticle colloidal solution ($SnO2$) (15% in $H2O$ colloidal dispersion, Alfa Aesar), Spiro-OMeTAD (99% HPLC, Sigma Aldrich), 4-tert-butylpyridine (96%, Sigma Aldrich), Bis (trifluoromethane) sulfonimide lithium salt (99.95%, Li-TFSI, trace metals basis, Sigma Aldrich).
- *Solvents:* Chlorobenzene (CB, anhydrous, 99.8%, Sigma Aldrich), N-N dimethylformamide (DMF, anhydrous, 99.8%, Sigma Aldrich), dimethyl sulfoxide (DMSO, anhydrous, ≥ 99.9%, Sigma Aldrich), Acetonitrile (anhydrous, 99.8%, Sigma Aldrich) Zinc purum powder (Sigma Aldrich), diethyl ether (DE, ≥ 99.5%, GC, Sigma Aldrich), isopropanol (IPA, anhydrous, 99.5%, Sigma Aldrich), hydrochloric acid (HCl, ACS reagent, 37%, Sigma Aldrich), acetone and ethanol (99%, denature, Lamberty - sarp industries, France).

II.3.1.2 Device architecture:

We used NIP structure for our solar cells, with double or triple cation perovskite as the absorber, SnO_2 as ETL, Spiro-OMeTAD as HTL, FTO as a transparent electrode, and finally gold (Au) as the top electrode. The stacking of the different layers is crucial, each layer should be in contact just with the layer above and or the layer below, (e.g. the SnO_2 layer should be in contact only with FTO and the perovskite layer). Otherwise, unwanted processes, such as short circuits or high recombinations or leakage currents, can take place

and cause a drop in the performances or even completely break down the solar cell. The architecture of our final device is represented in.

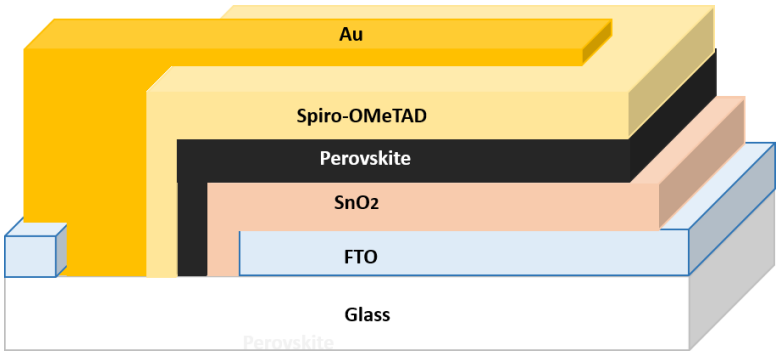

Figure II. 10: A complete perovskite solar cell structure

II.3.1.3 Transparent electrode:

Commercialized FTO (Fluorine-doped Tin Oxide) and ITO (Tin-doped Indium Oxide) substrates were used as transparent electrode, their high visible light transmission, and high conductivity make them perfectly fit this role.

FTO is the electrode that we used most of the time for our devices due to its low price compared to ITO. Furthermore, FTO has shown higher thermal stability which made it more suitable for devices that require high annealing temperature, whereas, the ohmic resistance of FTO is slightly higher than ITO.

The FTO is coated on top of a 12*12 mm glass square, where the thickness of the glass is around 2 mm and the thickness of FTO is around 100 nm. The substrate is etched and cleaned as described in the following paragraphs.

Etching: The etching consists to remove the FTO according to the specific architecture mentioned in Figure II. 11. The arias that we do not want to etch are covered by scotch-adhesive tape, an uncovered band will be exposed to a chemical reaction that includes zinc oxide and HCL, this chemical reaction removes instantly the FTO. To each ITO we cover the unwanted areas for etching with nail polish, thereafter, we put the samples in hot HCL (80°C) mixed with water (volume ratio 1:1) for 5 minutes. The ITO will be removed from the uncovered (HCL exposed) band.

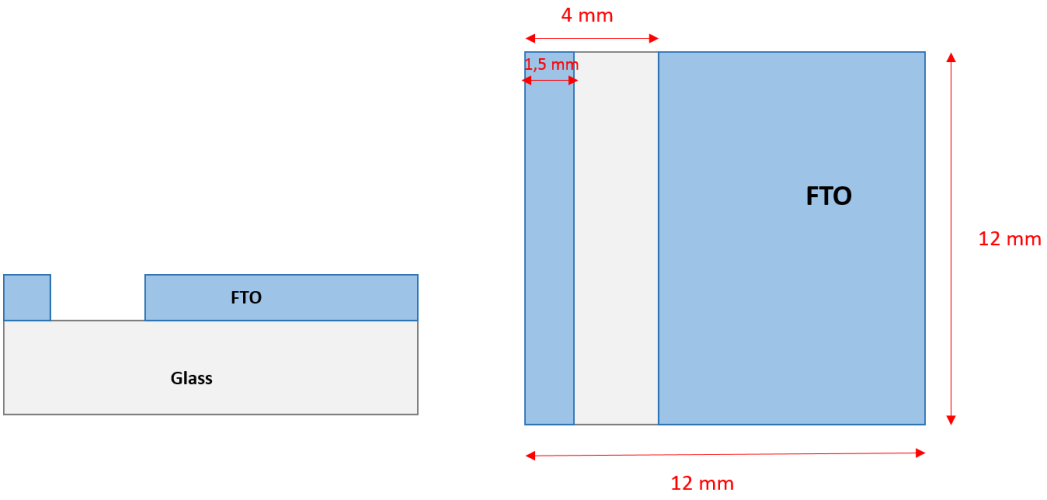

Figure II. 11: The design scheme of etched FTO layer on top of the glass substrate

Cleaning: first we clean the etched substrates with deionized water in order to remove any traces of acid, then we put the substrates in hot acetone (50°C) under the ultrasonic bath for 10 min. Afte, we clean the substrates mechanically to remove any solid dust adhered to the surface using a cotton tissue or cotton swab. Later, we placed our substrates in Acetone, isopropanol, ethanol for 15 min under the ultrasonic bath for each solvent, and we dry the substrates every time we change the solvent using Nitrogen gas flow. Finally, we put the substrates under the UV-ozone for 20 minutes just before the ETL deposition.

II.3.1.4 Electron transporting layer

Titanium dioxide (TiO_2) has been widely used as the electron transporting material for perovskite solar cells, However, TiO_2 has shown some weaknesses such as the low stability (decomposition) under long time exposure to ultraviolet (UV)[87], and the high temperature required for annealing (around 500°C), which represent a constraint for the PSCs commercialization. In contrast, Tin (IV) oxide (SnO_2) is more resistant to UV with excellent chemical stability and it does not require high-temperature annealing. Moreover, SnO_2 has excellent electron extraction properties and high visible light transmission due to its high bandgap of ≈ 3.6 eV against ≈ 3.0 eV for TiO_2[88].

SnO_2 solution preparation:

We mixed 1 ml of a commercial SnO_2 colloidal solution with 10 μl of isopropanol (10% of the SnO_2 volume), afterward we put this solution understeering for 1 hour at least. Before the

deposition, this solution must be filtered using PTFE 2 µm, 1 µm, and 0.45 µm filters respectively.

SnO_2 deposition:

The filtered SnO_2 solution is deposited on top of UV-ozone treated FTO substrate by spin-coating. This simple technic is widely used to obtain uniform thin films by depositing a small drop of the solution onto a flat substrate. The solution is then spread due to the centrifugal force created by the rotation of the substrate. The thickness and the quality of the film depend strongly on the nature of the solution (viscosity, concentration, homogeneity, etc.) and the spin coating parameters (rotation speed, acceleration, etc.).

The following parameters were used to obtain our SnO_2 films with a thickness of ~70nm:

- Solution volume: 70 µL
- Spead of rotation: 4000 rpm
- Acceleration: 1000 rpm/s
- Time: 30 s

After the deposition, we etch the substrates using a cotton swab soaked in deionized water, and according to the design illustrated in Figure II. 12, which must be meticulously respected. Finally, we put immediately the etched substrates onto a hotplate at 150°C for 30 mins in order to dray the spin-coated films and remove any trace of solvents.

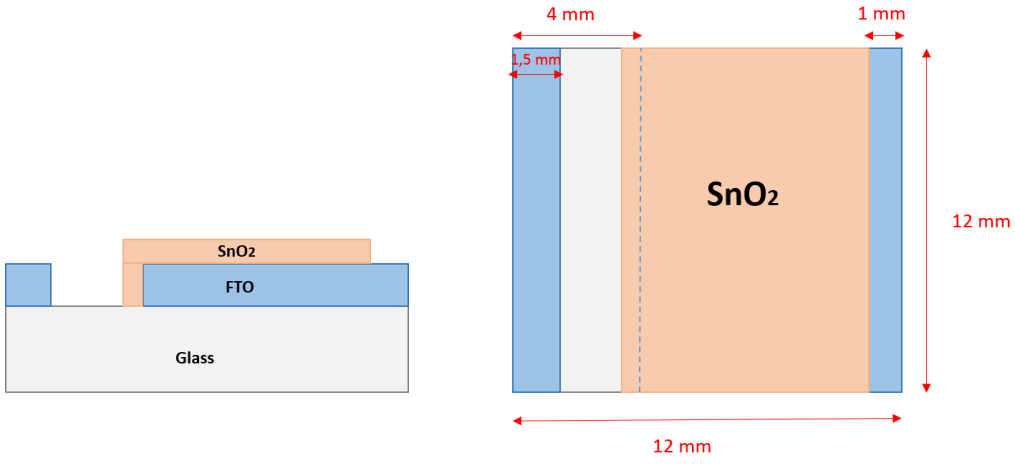

Figure II. 12: The design scheme of etched SnO2 layer on top of FTO

II.3.1.5 Perovskite layer:

During this thesis, we used two different types of perovskites. Double cation perovskite (DCP) where the formula is $FACsPb(IBr)_3$ and triple cation perovskite (TCP) where the formula is $FAMACsPb(IBr)_3$.

Perovskite solution preparation:

Double cation perovskite $FACsPb(IBr)_3$: inside the glove box, we dissolve 146.3 mg of FAI, 392 mg of PbI_2, 39 mg of CsI, and 55.4 mg of $PbBr_2$ in 600 μl of DMF and 78 μl of DMSO in order to have $FA_{0.85}Cs_{0.15}Pb(I_{0.85}Br_{0.15})_3$ perovskite. We put the solution of precursors understeering for at least 2 hours at 65°C.

Triple cation perovskite $FAMACsPb(IBr)_3$: the perovskite solution is obtained by mixing the following two solutions inside the glove box.

- Solution 1: we dissolve 171 mg of FAI, 507 mg of PbI_2, 22 mg of MABr, and 73 mg of $PbBr_2$ in 800 μl of DMF and 200 μl of DMSO.
- Solution 2: we dissolve 78 mg of CsI in 200 μl of DMSO.
- Final solution: we mix 1 ml of solution 1 plus 50 μl of solution 2 in order to obtain $Cs_{0.05}(MA_{0.17}FA_{0.83})_{0.95}PB(I_{0.83}Br_{0.17})_3$ perovskite. Finally, we put the solution of precursors understeering for at least 2 hours at 65°C.

Perovskite deposition: before the deposition, we put the SnO_2 substrates under the UV-ozone for 15 mins. in the same time, we filter the solution using PTFE 0.45 µm filter and we put it back on the hotplate at 65°C. The hot perovskite solution is spin-coated on top of SnO_2 substrates, whether inside or outside of the glove box. After 10 s, we drop 500 µl of the antisolvent (diethyl ether or chlorobenzene) onto the spinning substrate. This step is the same for both double and triple cation perovskites, whereas, the annealing is different. For DCP, immediately after the deposition we put the substrates on the hotplate at 100°C for 5 mins and at 150 °C for 15 mins. For TCP, immediately after the deposition we put the substrates on the hotplate at 100°C for 1 hour and at 150 °C for 15 mins. The following parameters were used to obtain the perovskite film with a thickness of ~450 nm.

- Solution volume: 45 µL
- Spead of rotation: 4000 rpm
- Acceleration: 1000 rpm/s
- Time: 30 s

Finally, we etch the perovskite films using a cotton swab soaked in DMF, and according to the design illustrated in Figure II. 13.

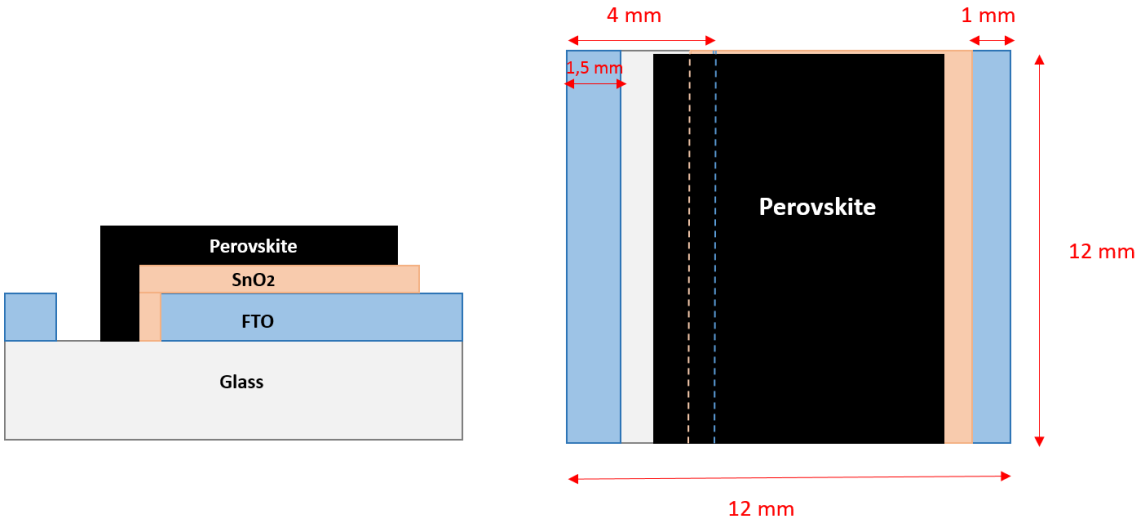

Figure II. 13: The design scheme of the Perovskite layer on top of SnO_2

II.3.1.6 Hole transporting layer (Spiro-OMeTAD)

Spiro is one of the most used HTMs for perovskite solar cells, where its full name is 2,2',7,7'-Tetrakis[N,N-di(4-methoxyphenyl)amino]-9,9'-spirobifluorene, and its molecule is shown in Figure II. 14.

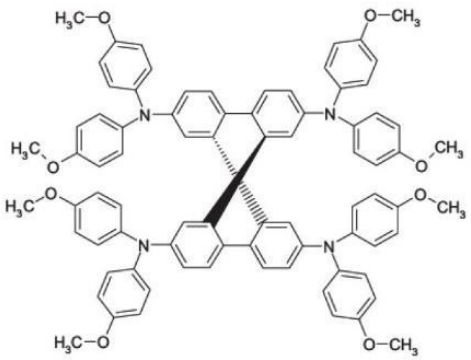

Figure II. 14: Molecular structure of Spiro-OMeTAD

For our devices, we used Spiro-OMeTAD as HTL due to its many advantages, such as the easy processing, good efficiency, or even its stability in ambient conditions which gives a sort of protection for the perovskite layer. However, Spiro-OMeTAD requires doping in order to

improve its charge-transport properties such as the hole mobility and conductivity, it is generally doped by 4-tert-Butylpyridine and bis(trifluoromethane) sulfonimide lithium salt (LiTFSI).

Before preparing the Spiro-OMeTAD solution we need to prepare the lithium salt solution that we called her solution 1.

- Solution 1: Inside the glove box, we dissolve 106 mg of Li-TFSI -Salt in 200 µl of acetonitrile and we leave it understeering for 15 mins.
- Spiro-OMeTAD final solution: Outside of the glove box, we dissolve 73.2 mg of Spiro-OMeTAD powder in 1 ml of chlorobenzene, after that, we add 28.8 µl of tBP (4-tert-Butylpyridine) and 17.5 µl of Solution 1. We leave the solution understeering for at least 3 days.

Spiro-OMeTAD deposition

The Spiro-OMeTAD solution is filtered using PTFE 0.45 µm filter. Then, the solution is deposited, whether inside or outside of the glove box, by spin coating according to the following parameters to obtain a thickness of ∼200 nm :

Solution volume: 25 µL

Spead of rotation: 3000 rpm

Acceleration: 2000 rpm/s

Time: 30 s

The Spiro-OMeTAD layer does not require any annealing, it is etched using a cotton swab soaked in chlorobenzene according to the design shown in Figure II. 15.

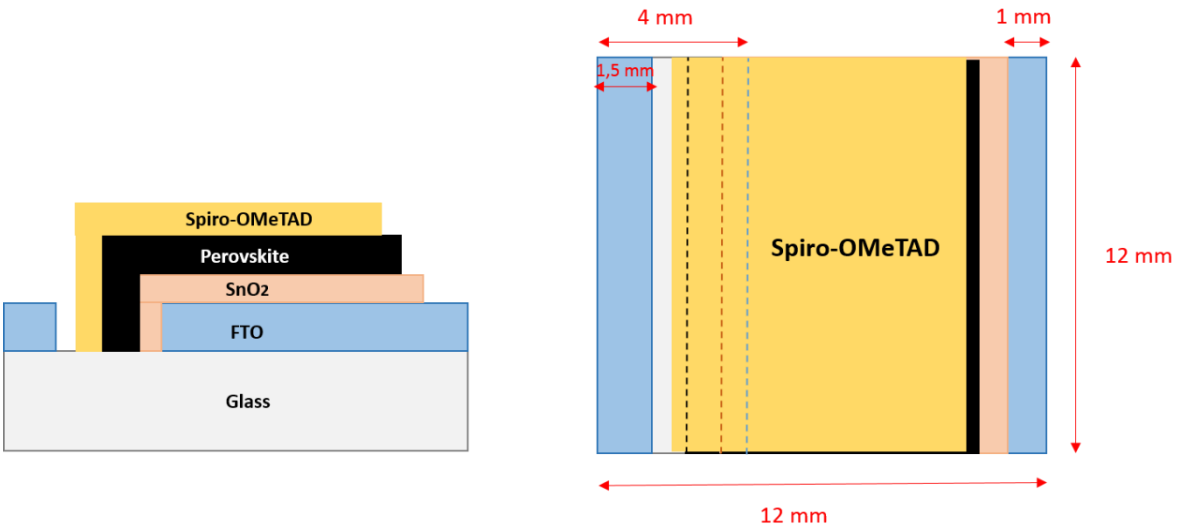

Figure II. 15: The design scheme of the Spiro-OMeTAD layer on top of the perovskite

II.3.1.7 Top electrode (Au)

Finally, the gold electrode with a thickness of 100 nm is deposited on top of the HTL by thermal evaporation. Thermal evaporation is a common technic of physical vapor deposition (PVD), it consists to evaporate a material under a high vacuum, 10^{-6} mbar for our case, using a heating resistive source. Then, the material will be deposited on the bottom of the substrate coating a smooth film. Using thermal evaporation, we are able to control precisely the thickness of the evaporated material.

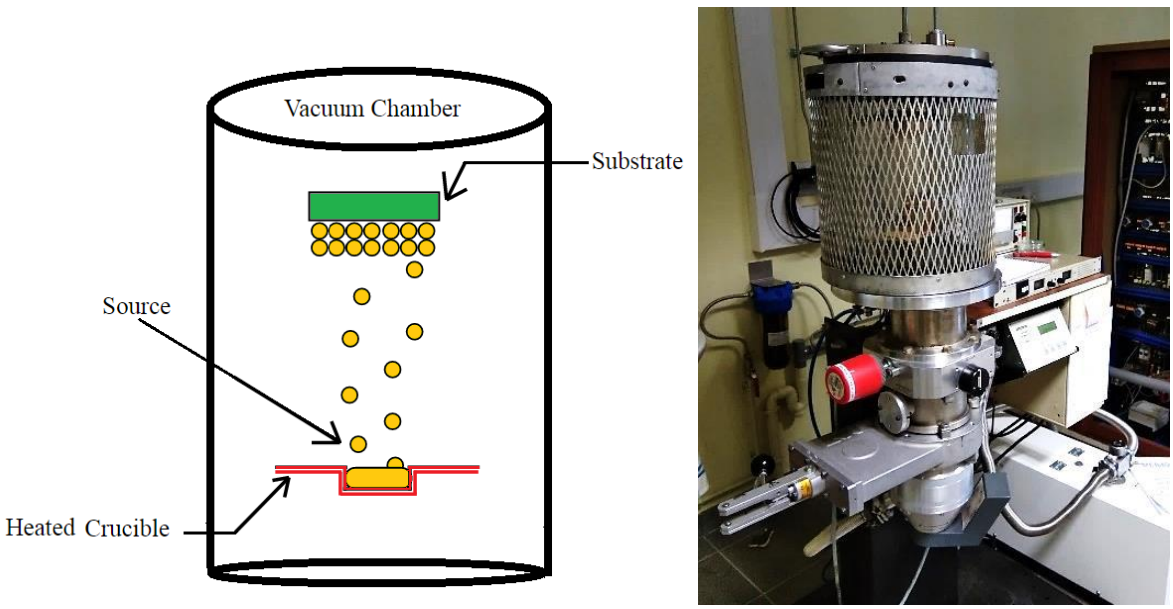

Figure II. 16: The thermal evaporator

In PSC, the speed and the temperature of the deposited gold are crucial, since the gold can defuse inside of the Spiro-OMeTAD layer which creates many defects on the interface, or even touches the perovskite layer which can cause a drastic fall of the solar cell performances.

The gold is evaporated according to the design illustrated in Figure II. 17 and using a Brass mask that covers the unwanted parts (Brass is an alloy of copper and zinc).

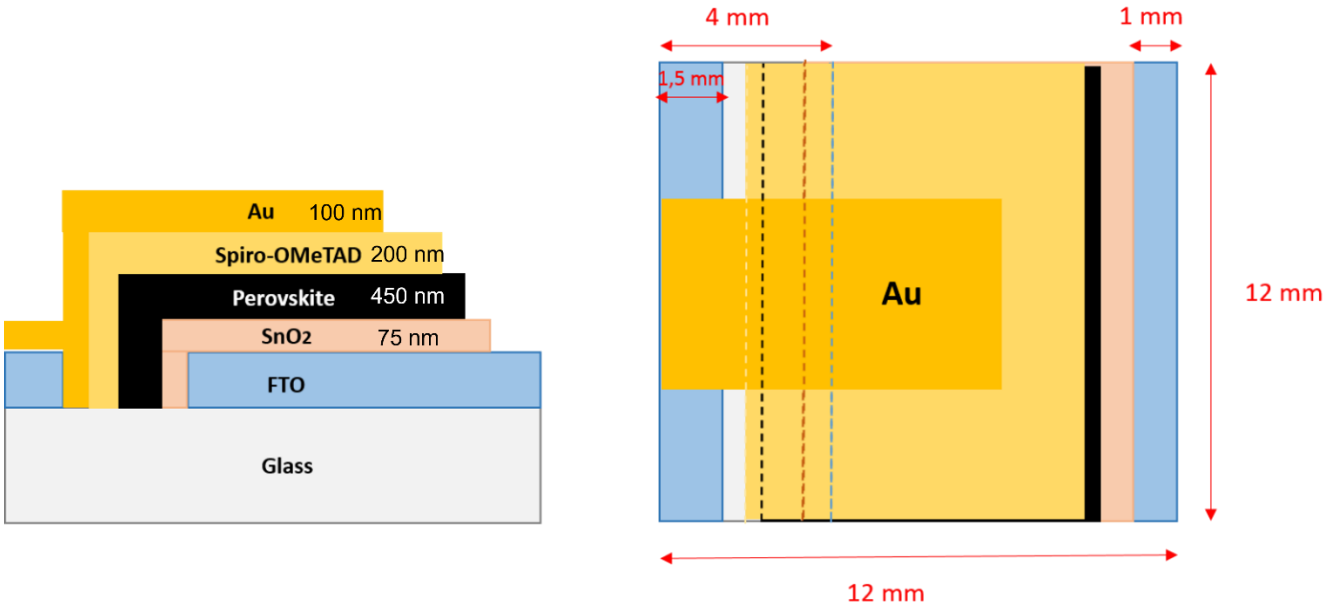

Figure II. 17: The design scheme of the complete solar cell with the gold electrode on top

The active area of the device is around 0.2 cm^2.

II.3.2 Solar cell Current density-Voltage (J-V) measurement

Current density-voltage (JV) measurement is the most fundamental characterization technique for solar cells. It consists to measure the current generated by the solar cell as a function of an applied voltage whether in dark or under exposition to the solar simulator light. The JV measurements are conducted using a computer-controlled Keithley 2400 source-measure that applies a sweeping voltage between the electrodes of the solar cell and measures its density of current. The solar simulator light is provided by a special lamp where the emitted light spectrum follows the AM 1.5 G norm. Figure II. 18 shows the used solar simulator which is a 1600W Newport Solar simulator (class A) . An illumination power density of 100 mW/cm^2 is imposed by the AM1,5G norm. AM1.5G or Air Mass 1.5 Global

refers to the standard solar spectrum, corresponding to the irradiance received on earth at a zenital angle of 48.2°. The air mass corresponds to the length of the optical path traveled by the light across the earth's atmosphere. We must take into consideration that the light spectrum is different from the AMG1.5 solar spectrum as shown in Figure II. 18 therefore it is necessary to implement a mismatch factor to not overestimate or underestimate the solar cell performance.

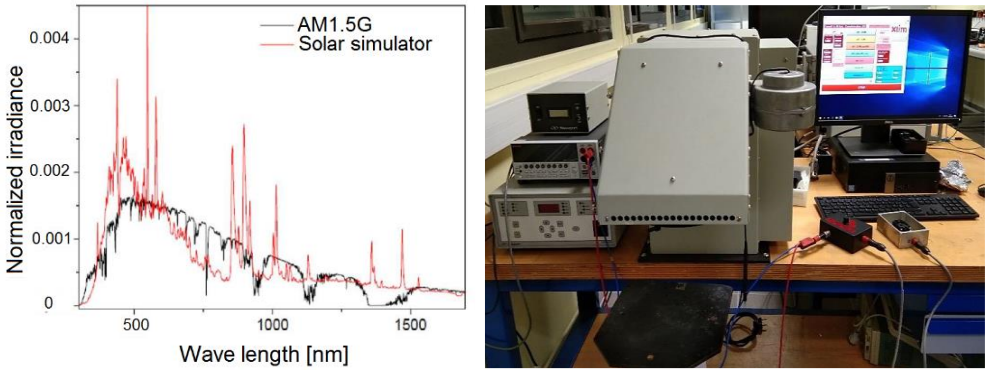

Figure II. 18: AMG1.5 and solar simulator irradiance spectra (left), Solar simulator and experimental set-up (right).

From the current density measurement, we obtain the JV curves that allow us to extract significant electronic parameters that characterize the functioning and the performances of the solar cell.

II.3.2.1 Short circuit current (Jsc)

The Jsc, or the Isc per the solar cell surface, is the maximum current that can flow through the solar cell, it is measured when the value of the load between the electrodes of the solar cell (R_L) is equal to 0, meaning that the solar cell is short-circuited and the voltage equal to 0. The value of Jsc gives us an overview of the charge carrier generation, transport, and collection properties of the solar cell. The Jsc can be easily affected by the power of the light source, therefore we need to do the JV measurement under standard lighting conditions. From the equivalent circuit and the equation $(II.10)$ the Jsc is equal to the photogeneration current (Isc=Iph).

II.3.2.2 Open circuit voltage (V_{oc})

The Voc is the maximum voltage that can be provided by the solar cell. It is measured at $R_L = \infty$ which means that the density of current is equal to 0 and the solar cell is open-circuited. The V_{OC} value depends on the nature of the used materials and their energy band positions.

The different processes of recombination occurring inside of the solar cell can reduce the Voc value. From the equivalent circuit and the equation $(II.10)$ the V_{OC} (at I=0) can be expressed as:

$$V_{oc} = \frac{nkT}{q} ln\left(\frac{I_{ph}}{I_0} + 1\right) \qquad (II.11),$$

Where $I_{ph}$is photo-generated current, I_0 and are reverse saturation current, n is the ideality factor of the diode, and kTq is the thermal voltage.

From this equation, we can see that the Voc is linked to the photogeneration current and the reverse saturation current I_0. The reverse saturation current depends on the recombination occurring inside of the active layer bulk.

II.3.2.3 Fill factor (FF)

The fill factor (FF) characterizes the ideality or the quality of the solar cell. Theoretically, it is defined as the ratio between the solar cell maximum power to the product of V_{OC} and J_{SC} shown below. With P_{max} is the maximum of power that can be generated by a solar cell.

$$P_{max} = V_{max} * J_{max} \qquad (II.12),$$

$$FF = \frac{P_{max}}{V_{oc} * J_{sc}} = \frac{V_{max} * J_{max}}{V_{oc} * J_{sc}} \qquad (II.13),$$

II.3.2.4 Power conversion efficiency

Power conversion efficiency PCE or the efficiency η is the most used parameter to describe the performance of the solar cell. It is defined as:

$$PCE\ (\eta) = \frac{P_{max}}{P_{incident}} = \frac{FF * V_{oc} * J_{sc}}{A * 100} \qquad (II.14),$$

Where A is the area of the solar cell in cm^2 and the light power density for the standard AM1.5 spectrum is 100 mW/ cm^2.

II.3.2.5 Series resistance R_S and the shunt resistance R_{SH}

R_s and R_{sh} represent the parasitic resistances of a solar cell, they have a main impact on the fill factor as demonstrated in Figure II. 19. Moreover, high Rs values can reduce significantly the Jsc since R_s characterize the losses related to the charge carrier transport, the physical origin of these losses can be for example the defects in the interface between two layers. Therefore, It is desirable to have low series resistance. On the other hand, low values of R_{sh}

provided by an alternative current path can reduce the V_{oc} and causes significant power losses. R_{sh} characterize the losses related to the leakage current, where the physical origin of these losses can be for example the structural defaults such as direct contact between the absorber and the electrode, therefore, it is desirable to have high shunt resistance.

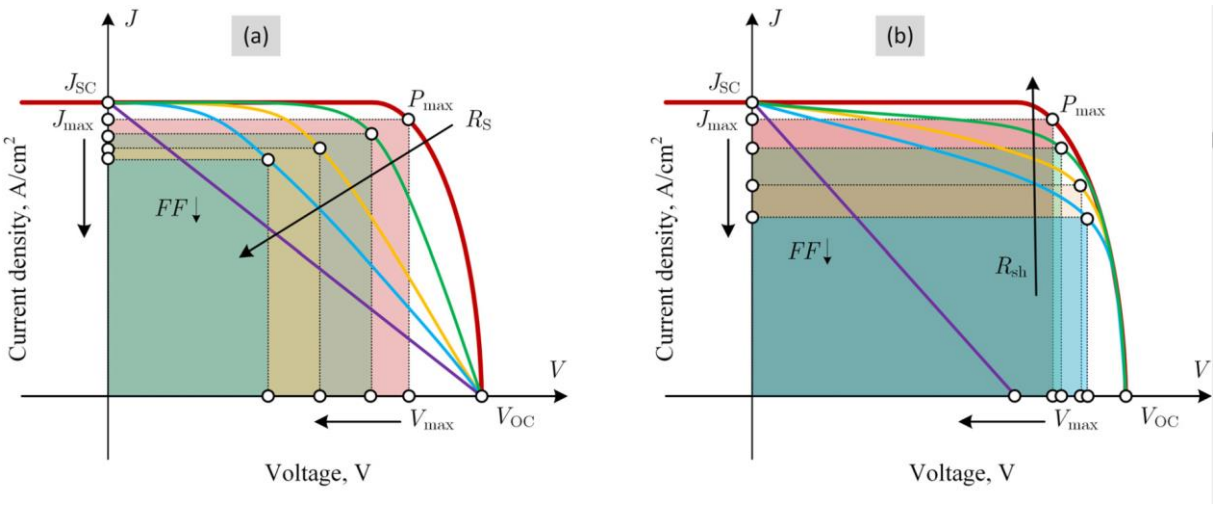

Figure II. 19: (a) Effect of series resistance (Rsh=const), (b) Effect of shunt resistance (Rs =const) [89]

The value of R_s can be graphically obtained from the slop of the J-V curve under illumination at open circuit conditions, it is defined as:

$$R_{series} = \left.\frac{1}{\partial I/\partial V}\right|_{V=V_{oc}} \qquad (II.15),$$

The value of R_{sh} can be graphically obtained from the slop of the JV curve under illumination at open circuit conditions, it is defined as:

$$R_{shunt} = \left.\frac{1}{\partial I/\partial V}\right|_{V=0} \qquad (II.16),$$

II.3.3 The JV characteristics of a perovskite solar cell

Perovskite solar cells are measured under illumination with two directions of a sweeping voltage. From negative to positive voltages is called the forward scan, on the other hand from positive to negative voltages is called the reverse or backward scan.

The typical JV curves measured under illumination for a typically mixed cation perovskite solar cell are given in *Figure II. 20*.

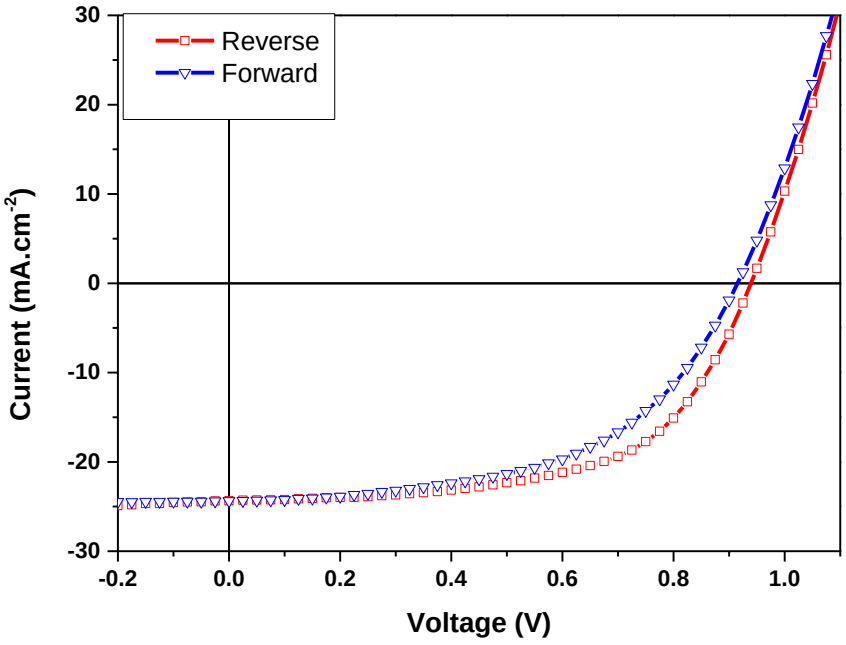

Figure II. 20: J(V) and P(V) curves of a typical double cation perovskite solar cell

Scan direction	Voc(V)	Jsc(mA.cm^{-2})	FF	PCE(%)	Rs(Ω)	Rsh(Ω)
Reverse	0.94±0.01	24.4±1.0	0.60±0.03	13.57±1.33	35±9.8	2808±213
Forward	0.91±0.02	24.3±0.91	0.54±0.03	11.91±1.25	41±10.1	5428±293

Table II. 1: Photovoltaic parameters of a typical mixed cation PSC

The performance of our perovskite solar cell is consistent with the reported literature on similar devices [66][90] (more discussion about these parameters are shown in chapter III and V). However, we emphasize that the spectral correction (use of mismatch factor) was not applied systematically in our study, which can lead to a slight over-estimation of the absolute values of Jsc and PCE in some cases (by a maximum factor of 10%). This slight over-estimation will have no consequence on the general trends which are discussed in this work, as all our comparisons between cells were made using similar experimental conditions and calibrations.

The difference between the backward and reverse J-V scans is named the Hysteresis. This effect is widely addressed in the filled of perovskite solar cells since it can affect its photovoltaic performances. Generally, The hysteresis effect is Associated with the movement of mobile ions (I^-, Pb^+, etc..) or vacancies and [91] the accumulation on the perovskite interfaces (Spiro-OMeTAD / SnO2) this effect will be more discussed in the next chapters. [92][91][93] [94].

The hysteresis index can be introduced to quantify the level of hysteresis in perovskite devices. While several definitions have been proposed, we arbitrary focus on the following expression [90]:

$$HI = \frac{PCE_{reverse} - PCE_{forward}}{PCE_{reverse}}$$

II.3.4 Conclusion

The fabrication protocol shown in this chapter allows us to have state of art working devices. This has required many optimizations that we have gone through to obtain such good performance. However, the reproducibility of these performances was a big concern since even with the same protocol and in the same batch of SCs, we can easily find good and non-working solar cells, in other words, the dispersion of the PCEs was very high meaning the reproducibility was low. Such a problem can highly affect any comparative study conducted later on. In the next chapter, we are showing our pathway to improve the performances of all the solar cells as well as improve their reproducibility.

Chapter III- Toward efficient and reproducible perovskite solar cells

III.1 Introduction

For VLC applications, as discussed in chapter I, we are looking for a low-cost, stable and reproducible perovskite solar cell with high power conversion efficiency. For this purpose, and considering the state of the art, we chose to use a mixed cation perovskite active layer, either a double or a triple cation, due to their many advantages illustrated in chapter II. Moreover, it is important to understand in depth the VLC performances of this emerging kind of PCSs to see if they are good candidates for VLC applications.

In this chapter, we illustrate the optimization process we had to develop to achieve well-performing perovskite solar cells presenting a good level of reproducibility. Such an objective is absolutely a necessity in order to further analyze the dynamic response of the cells by impedance spectroscopy in the next chapters.

During this Ph.D. work, many optimizations were performed in order to optimize a protocol of fabrication of mixed cation PSCs with lower temperature, less time, low dispersion, high repeatability, and good performance.

III.2 Toward efficient and reproducible perovskite solar cells

The choice of SnO_2, as electron transporting layer, was based on its good performance easy processing compared to TiO_2 and its higher stability [95], however, a layer optimization was required in order to have better film quality and good electron-transporting properties. The fabrication protocol of the perovskite solar cells was first developed in the laboratory using triple cation PSCs ($Cs_{0.05}(MA_{0.17}FA_{0.83})_{0.95}PB(I_{0.83}Br_{0.17})_3$), before switching to double cation PSCs ($FA_{0.85}Cs_{0.15}Pb(I_{0.85}Br_{0.15})_3$) due to its easier processing and the reduced fabrication time. The fabrication process basically relay on the what was reported in the literature [96] [66], however specific optimizations are still needed for the elaboration of efficient solar cells.

The strategy of this thesis is to develop a protocol for the fabrication of stable, reproducible, and efficient PSCs that allow us to investigate their dynamic properties towards their application for OWC. In this part, we describe the main developed steps during this thesis towards device optimization, this selection being not exhaustive.

III.2.1 SnO_2 optimization

The TiO_2 with mesoporous or planar structures is widely used as ETL for perovskite solar cells. However, the fact that TiO_2 has low stability under illumination, due to its photocatalytic properties, accelerates the degradation of the PSCs and decreases quickly its performances[95]. This is the main reason that drove us to switch to a higher stability material such as SnO_2. Furthermore, perovskite solar cells based on SnO_2 ETL have recently achieved a power conversion efficiency of 23%[97]. In addition, SnO_2 shows many outstanding advantages compared to TiO_2 such as the lower annealing temperature, the higher bandgap, the higher electron mobility, as mentioned in chapter II [95].

In order to benefit from these advantages, it is required to have a smooth SnO_2 layer with a low thickness that shows fast charge transfer and low charge losses. However, it is known that the wettability and the aggregation issues of the SnO_2 solution are the two major challenges that can be faced during the fabrication of the SnO_2 films[95][98][99].

III.2.1.1 SnO_2 Aggregation

The SnO_2 ETL is generally deposited from a solution of a commercial colloidal SnO_2 suspension. However, the aggregation of SnO_2 nanoparticles makes it challenging to obtain an homogeneous and smooth layer from spin-coating [99]. Large aggregates can be formed with different sizes. Small size aggregate reduces the uniformity of the SnO_2 layer and creates many defects on the interface between SnO_2 and the perovskite, which increases the Rs resistance and by consequence reduces the performance of the solar cell. On the other hand, big-size aggregates can easily drill the perovskite layer, which creates a direct contact between the SnO_2 and the Spiro-OMeTAD layer, which remarkably reduces the shunt resistance and causes a significant drop in V_{OC}, hence strongly limiting the power conversion efficiency of the solar cell. The existing clusters in the colloidal solution can also create pinholes in the SnO_2 film, especially using the spin-coating deposition technic (unlike spray or drop-casting technics), since they stop the continuity and the uniformity of the film during solution evacuation by the rotation process. Moreover, we have noticed that after annealing the deposited film at 150°C, the SnO_2 film tends to shrink around the cluster and make a circle of free SnO_2, or a pinhole, as shown on Figure III. 1.

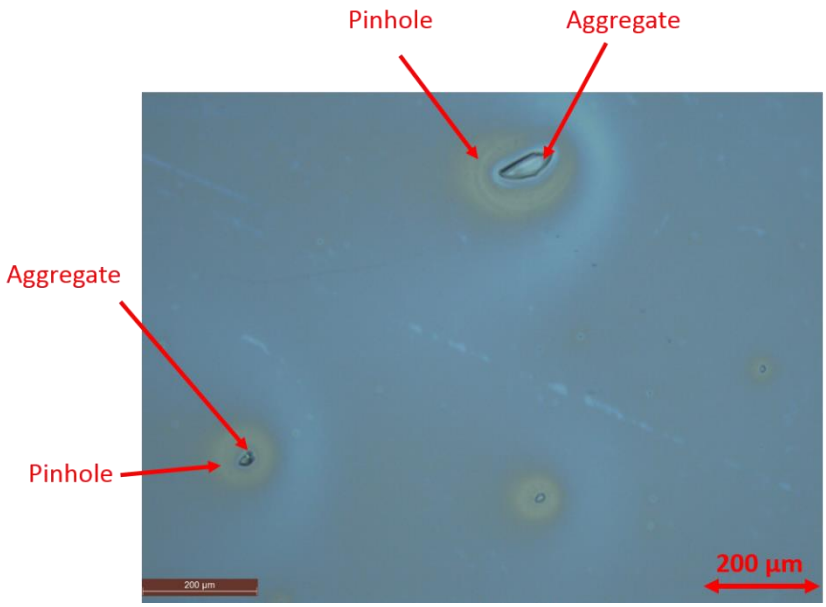

Figure III. 1: Optical microscope image showing the aggregates and pinholes in an SnO_2 film deposited by spin-coating on FTO.

Such pinholes enable a direct contact between the perovskite layer and the FTO electrode which represents a direct path for photogenerated holes. In such a case, the SnO_2 layer is not acting as an efficient hole blocking layer, and huge leakages of current can drastically reduce the solar cell performance.

To overcome these difficulties, we have explored different pathways. Filtering the solution was a good start to discard big size aggregates using three PTFE filters with different sizes 2 µm, 1 µm, and 0.45 µm successively, since it is not possible to filter the solution with the 0.45 µm filter directly because the filter pores can be quickly closed by the big SnO_2 clusters causing a quick stop of the filtration. However, the loss of the quantity of SnO_2 material was considerable, causing a drop in the concentration and the density of the filtered solution. This kind of solution cannot give proper SnO_2 films. Thus, it is necessary to try to break the SnO_2 aggregate before the filtration. Many approaches have been tested but what works the best for us was adding a small volume of ethanol or isopropanol (10% of the SnO_2 solution) and put the mix inside of the ultrasonic bath for 10min, afterwards, the solution is put under steering for at least 1 hour at ambient temperature. A final filtering of the solution is then used using a 0.45 µm PTFE filter.

The ultrasound treatment was performed since it is a widely utilized technic for sol dispersion, especially during the synthesis of nanoparticle colloidal solutions, the ultrasound

waves can help to broke the big clusters of nanoparticles and improve dispersibility[100][101][102].

On the other hand, the adding of isopropanol or ethanol slightly reduces the concentration, however adding a bigger volume can damage or remove the surfactant that surrounds the SnO_2 particles [103]. The adding of isopropanol prevents another type of aggregation which is the aggregation of SnO_2 during the spin-coating, since during this step, the uniformity of the evaporation of the H_2O solvent (The SnO_2 is dispersed in water) leads to an alternation of the concentration of the residual solution on the surface of the substrate that affects the surfactant present in the solution. Consequently, clusters can be formed and the roughness of the film can be increased. However, the presence of IPA leads to more smooth and uniform evaporation of the solvent which reduces the random aggregation of the SnO_2 nanoparticles during the deposition, by consequence a smooth and free-aggregation film is formed [104].

Therefore, this solution treatment eliminates the SnO_2 aggregation and improves the dispersity of the colloidal solution which leads to better film quality as shown in Figure III. 2.

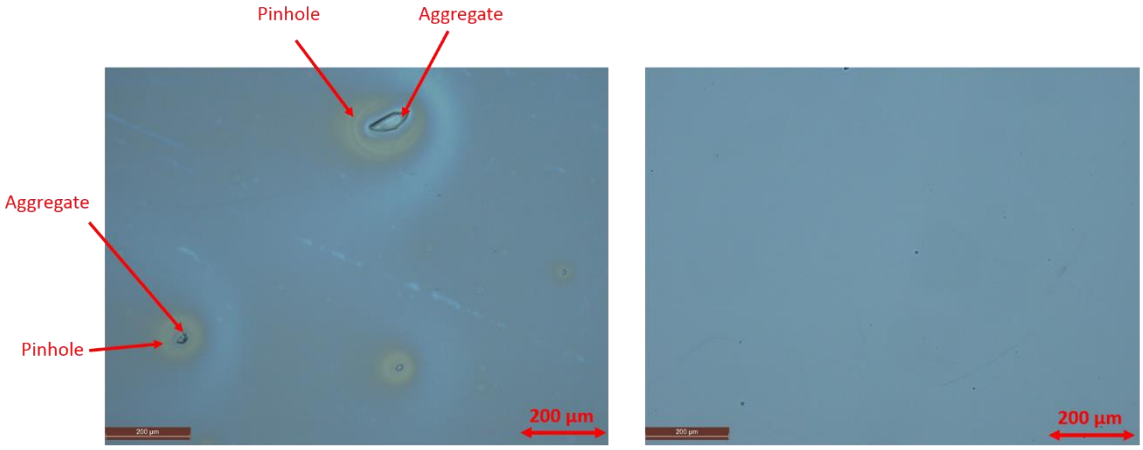

Figure III. 2: Optic microscope image showing the aggregate and pinholes in SnO2 film (left)and a good SnO2 film (right)

To get a better insight into the influence of the procedure on the local morphology of the SnO_2 films, we analyze them using atomic force microscopy (Figure III. 3). More details about this experimental technique are giving in the annex.

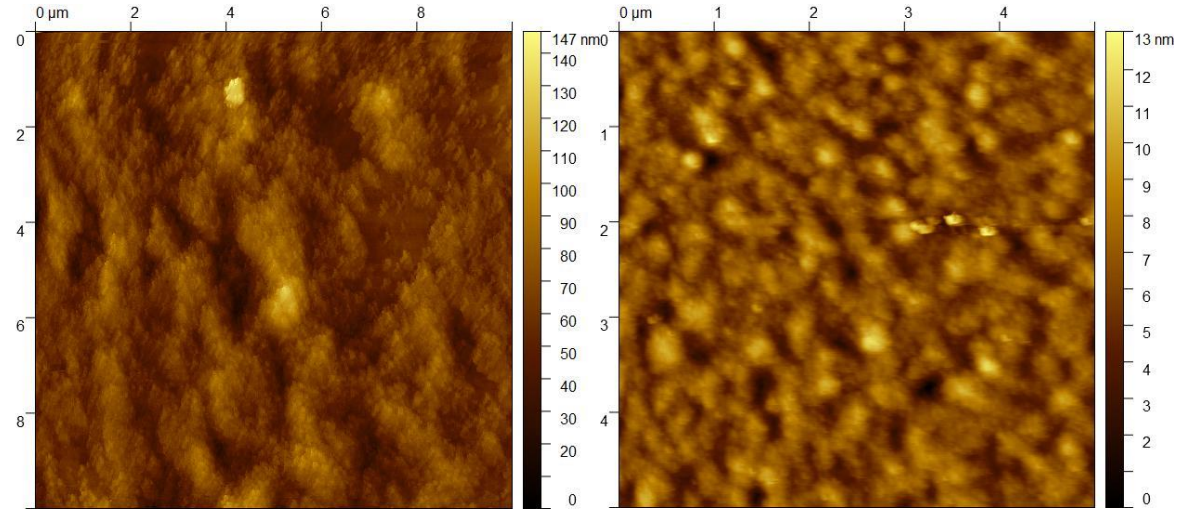

Figure III. 3: AFM images of SnO2 NPs deposited on top of FTO without treatment (left) with treatment (right)

The SnO_2 films without any treatment have shown a high RMS roughness of 12nm in the aggregate free regions, but this value can be much larger in the presence of aggregates. At the opposite, the treated SnO_2 film shows an RMS roughness of only 1.5nm. Reducing the roughness of the ETL layer leads to better contact at the interface, favoring the current flow which is usually associated with lower series resistance. As a consequence, larger Jsc is usually observed which can also reflect the low density of defects at the interface as shown the JV curves and the impedance spectroscopy (IS) curves presented in chapter V. A complete comparative study between treated and untreated SnO_2 is presented in chapter V (XRD, UV, JV, IS), where we discuss more the influence of SnO_2 treatment on the structural properties of the perovskite layer and the performances of the solar cell.

III.2.1.2 SnO_2 wettability

The wettability issues of the SnO_2 film on FTO lead to pinholes or even big uncovered areas as illustrated in Figure III. 4 which create an unwanted contact between the FTO and the perovskite layer therefore the SnO_2 layer is not able to block the photogenerated holes and consequently the huge leakage of current drastically reduce the solar cell performance. Thus, the rheological properties of the deposited solution, as well as the surface energy of the substrate, are the key point to have a good wetting of the substrate before starting the rotation during the spin-coating process.

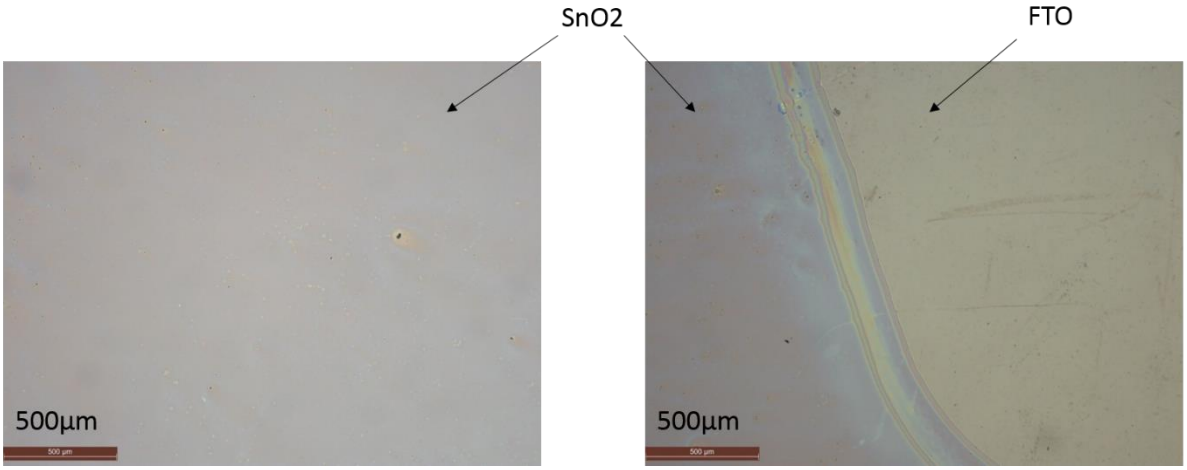

Figure III. 4: Optic microscope image showing FTO covered and uncoverd by the SnO_2 film

To investigate this effect, we used contact angle measurement which consists of to measuring the angle formed by a drop of solution on top of a substrate. Precisely, the value of this angle describes the quality of the wetting since it characterizes the interaction of the solid/liquid interfacial energy (γ^{sl}) with the solid/vapor surface energy (γ^{sv}) and the liquid/vapor surface energy (γ^{lv}) as defined in Young's equation:

$$\gamma^{sv} - \gamma^{sl} - \gamma^{lv}cos\theta = 0$$

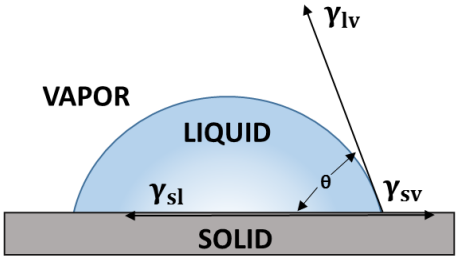

Figure III. 5: The contact angle

If the contact angle θ is higher than 90° the surface is considered as hydrophobic and wetting of the surface is not efficient. If the contact angle θ is lower than 90° the surface is considered hydrophilic. Generally, for high values of θ, the wetting is poor, and we are looking for θ values as low as possible in order to have the better spreading of the drop and by consequence better wetting of the substrate before starting the rotation during the spin-coating process. For SnO_2 solution that suffers from wetting issues, It was demonstrated that adding alcohol such as ethanol or isopropanol can reduce the viscosity and the surface tension

of the SnO_2 nanoparticle solution unlike adding other solvents such as H_2O or DMF[104]. Moreover, the evaporation speed of IPA creates an equilibrium of the three aforementioned energies that finally reduce the contact angle.

On the other hand, the UV ozone (UVO) treatment is commonly used for cleaning the surface of the substrate by effectively removing the organic residue adsorbed and stuck on the surface which reduces the contact angle and improves the wettability[105][95]. Moreover, the UV ozone reduces the defects in the FTO/ SnO_2 interface, which reduces the series resistance value and by consequence improves the solar cell performances.

To investigate the impact of the substrate treatment (IPA/ UVO) we have measured the contact angle of:

a) An SnO_2 drop on top of untreated FTO substrate
b) A mixt of SnO_2 and IPA drop (10V: V) on top of untreated FTO substrate
c) A mixt of SnO_2 and IPA drop (10V: V) on top of FTO substrate treated with UVO for 10 minutes.

The results are shown in Figure III. 6.

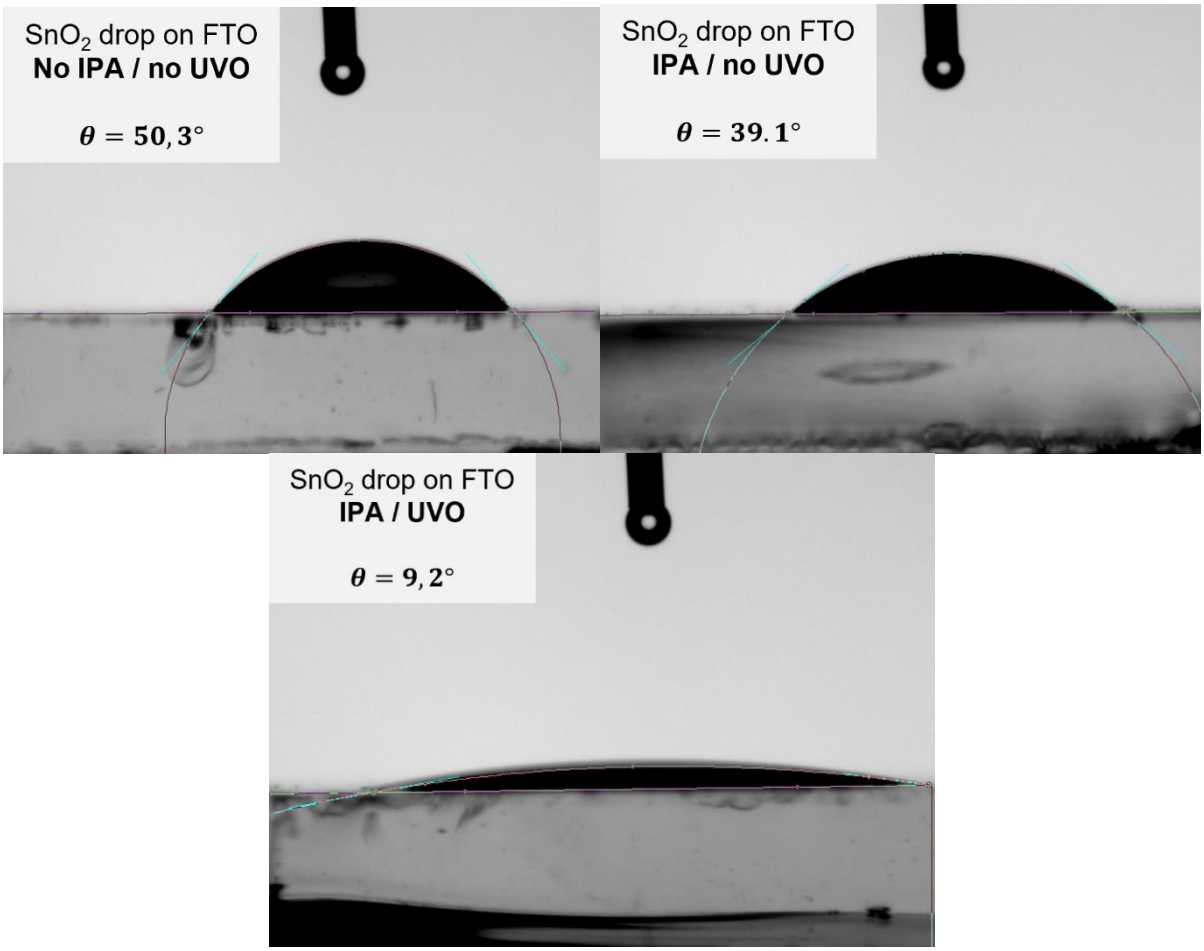

Figure III. 6: The contact angle measurement of : SnO_2 drop on top of FTO substrate (top left), SnO2 +IPA drop on top of FTO substrate (top right), SnO2 + IPA drop on top of FTO substrate treated with UVO (bottom).

Our measurements, shown in Figure III. 6, give evidence that adding IPA to the SnO_2 solution does help to reduce the contact angle value from 50.3° to 39.1°. Furthermore, a preliminary UV ozone (UVO) treatment of the FTO substrate drastically enhances this reduction with a resulting contact angle reaching 9.2°, which takes the wettability of SnO_2 on top of FTO substrate to the next level.

The next issue regarding device fabrication is associated with the affinity of the perovskite active layer with our SnO_2 ETL. Indeed, intrinsically, the perovskite precursor solution, based on DMF solvent, shows a poor wettability on the metal oxide layer of SnO_2, which leads to a low homogeneity of the perovskite film after solvent evaporation. Additionally, considering the crucial influence of the ETL substrate on the crystallization of the perovskite layer, this wettability issue is the first limitation for achieving high-quality perovskite films as it can induce more defects at the interface or even large pinholes in the

resulting perovskite film. The surface coverage by the perovskite is indeed a well-known issue in the field of perovskite optoelectronic devices. An additional UVO treatment is often used to overcome this problem, considering that SnO_2 shows suitable stability under this treatment (unlike TiO_2 for example). Moreover, this UVO treatment was found to improve the energetic configuration at the interface through a significant upward shift of the Fermi energy of the SnO_2, as well as a reduced hysteresis effect [106] [107]. Figure III. 7 illustrates the contact angle of our perovskite precursor solution deposited on top of the SnO_2 layer before and after UVO treatment.

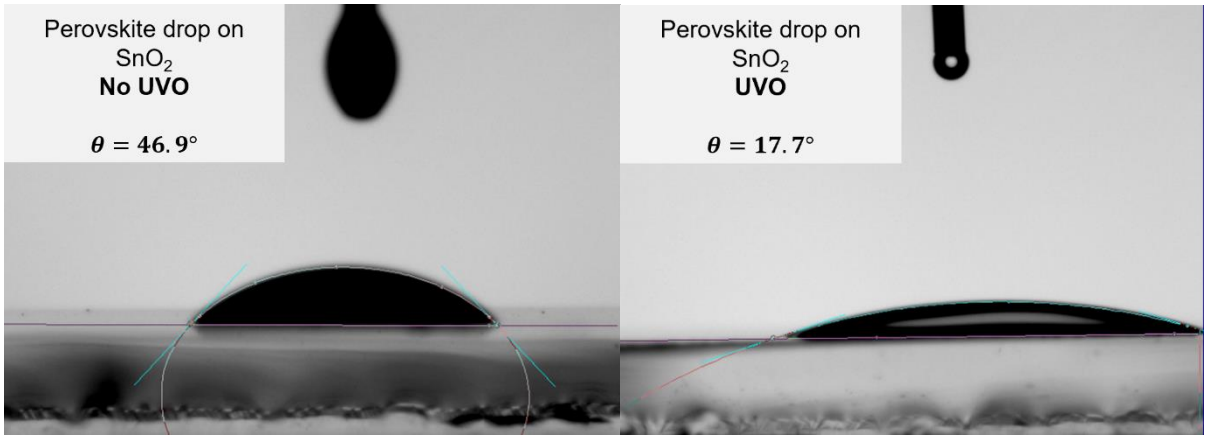

Figure III. 7: The contact angle measurement of: perovskite solution drop on top of SnO2 substrate (left), perovskite solution drop on top of SnO2 substrate treated with UVO (right)

A relatively low angle (46.9°) is already observed without any treatment, indicating a reasonable wettability of the solution on the ETL. The UVO treatment further decreases this value down to 17.7°. This low value enables a very homogeneous coverage of the ETL by the perovskite layer.

Without any specific developments made on the perovskite layer itself (this will be done in the next sections), the optimization of the SnO_2 ETL is already powerful leverage to demonstrate reasonable device performance, as illustrated below.

The current-density / voltage (JV) curves of perovskite solar cells based on the SnO_2 ETL, without and with our optimization protocol, are shown in Figure III. 8.

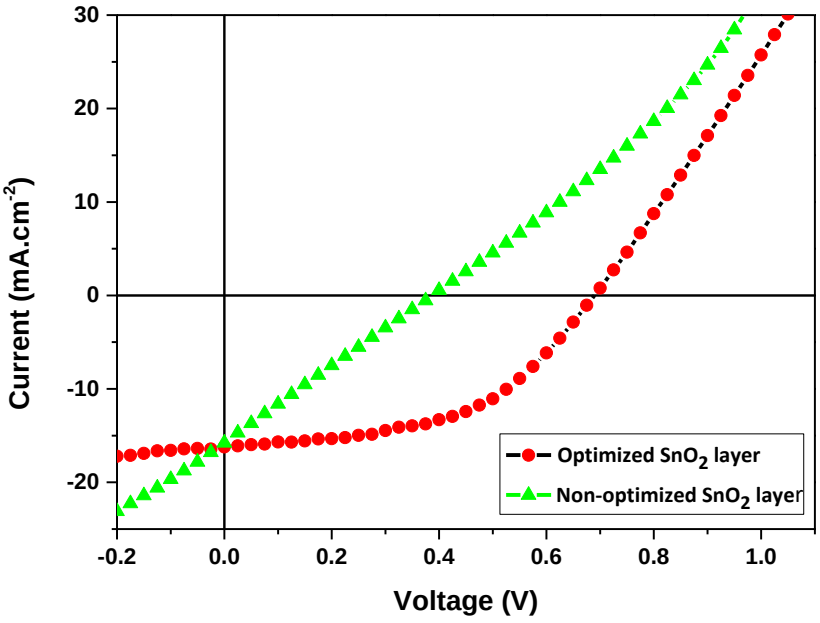

Figure III. 8: JV curves of optimized and non-optimized SnO_2 mixed cation PSCs

	Voc(V)	Jsc($mA.cm^{-2}$)	FF	PCE(%)	Rs(Ω)	Rsh(Ω)
Optimized SnO_2 layer	0.69	16.2	0.50	5.59	66.6	1105
Non-optimized SnO_2 layer	0.38	15.6	0.24	1.49	124	127

Table III. 1:The PV parameters of mixed cation PSC

From these curves and the table of PV performances, we can clearly see that the SnO_2 treatment has improved all the measured parameters of the solar cells notably the PCE has increased by around 4%. this remarkable improvement is mainly due to the elimination of the aggregates and pinholes present in the SnO_2 layer as well as the total coverage of the FTO electrode. The spectral correction (mismatch factor) was not applied to the Jsc performance measurements, leading to a slight overestimation (around 10%) of our short-circuit currents which is acceptable since it does not impact the trend. The shunt resistance of the non-optimized SnO_2 PSC is very low which witnesses a high leakage of current that drastically reduces the value of the Voc. This is typically produced by pinholes that enable direct contact between the perovskite and the FTO, furthermore, the series resistance of the optimized SnO_2

PSC has been reduced this could be due to the low presence of aggregates in the SnO_2 layer and its interfaces.

The following figures show our statistical analysis of more than 40 solar cells studied with and without the SnO2 layer optimization in order to investigate the role of the ETL optimization to improve reproducibility.

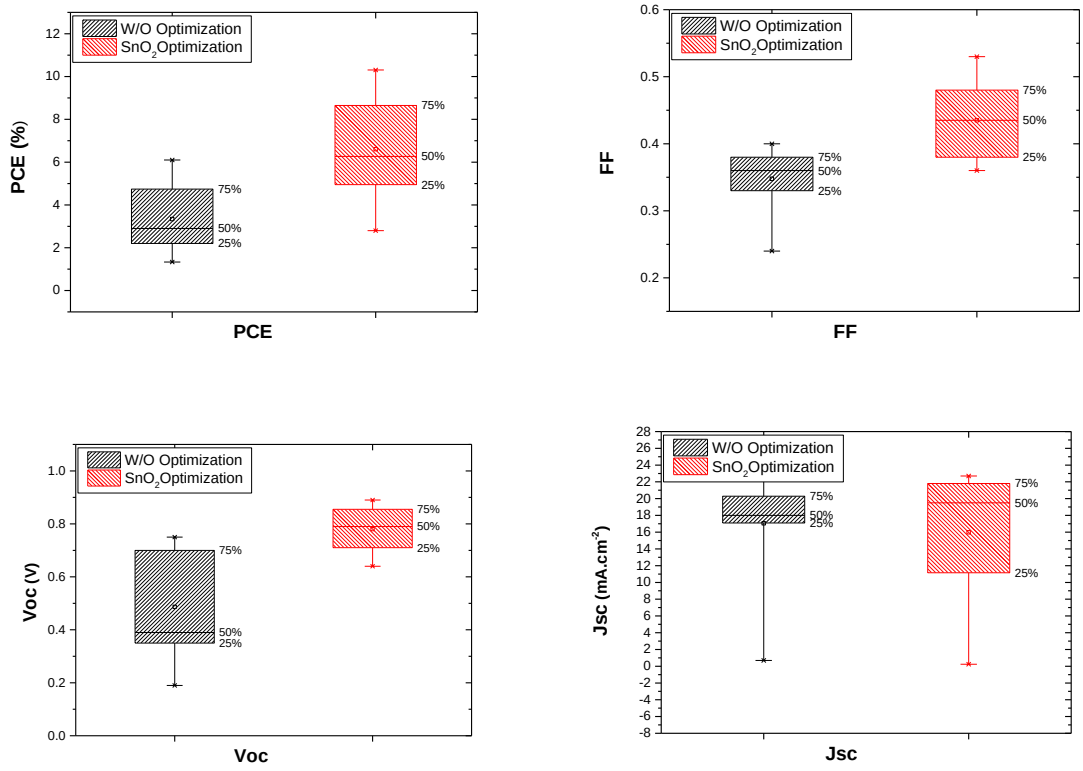

Figure III. 9: Statistical analysis of the reproducibility of the performances of optimized and non-optimized SnO2 PSCs

From these figure, we can see the good impact of the SnO_2 optimization on the PCE and the FF which demonstrate the better quality of the device. The Voc values distinctly improved with this treatment however the Jsc seems to fluctuate. On the other hand, the dispersion of the power conversion efficiencies of the treated solar cells is still high, therefore, the reproducibility of the PSCs is still low and does not allow proper comparison studies that should be conducted further.

Finally, optimizing the ETL layer improves the performances of the solar cell, however, it is still not sufficient to match the trend nor to improve the reproducibility of the performances.

Therefore it is necessary to look more in-depth and conduct more optimization of the perovskite layer.

III.2.2 Perovskite layer optimization

As many groups in the field, we found it very difficult to reproduce the PV performance from a cell to another (even in the same batch), nor from one batch to another. Many factors are known to impact the crystallinity and morphology of the perovskite layer, including precursor solution, ambient moisture, temperature, etc. In this part, we especially present our efforts to improve the reproducibility of the perovskite solar cell performance through careful optimization of the active layer preparation. These developments also impacted the absolute efficiency of the devices. First, we develop our process outside the glovebox, under ambient conditions. We give some tips on specific preparation steps such as layer etching and cleaning, which were found to strongly impact the overall homogeneity of the layer. We then focus on the anti-solvent process which is crucial for the good crystallization of the perovskite, before studying the influence of the ambient atmosphere. In each case, we focus on the reproducibility of the process, by estimating the fraction of working devices among a population of fabricated solar cells.

III.2.2.1 Solvent diffusion

One of the challenges that we faced during the elaboration of the perovskite layer was the diffusion of the solvent used to etch some specific areas of the layer according to our specific design. This solvent diffusion can widely affect the performances and the reproducibility of PSCs. As described in chapter II, the perovskite active layer must be carefully removed just after film deposition, using a perovskite solvent such as DMF or DMSO. Moreover, the back of the substrate and its sides should be cleaned using the same solvent. However, the solvent naturally diffuses through the perovskite layer and removes parts from it that shouldn't be removed (Figure III. 10). In such a case, the perovskite layer does not fully cover the SnO_2 layer, leading to direct contact between the SnO_2 and the Spiro-OMeTAD which highly reduces the performance of the solar cell.

After many tests, we have noticed that DMSO shows a stronger and quicker diffusion through the perovskite compared to DMF. This means that DMSO tends to rapidly alter the borders of the perovskite layer, as shown in Figure III. 10. Both DMF and DMSO are aprotic and polar solvents, however, the higher polarity of DMSO could be the main reason for the observed phenomenon. A fast and efficient redissolution of the perovskite layer is observed

in this case. The slightly higher viscosity of DMSO (1.81 10^{-3} Pa.s) compared to DMF (0.77 10^{-3} Pa.s) does not seem to be the main factor here, as both liquids show a relatively low viscosity. [108][109].

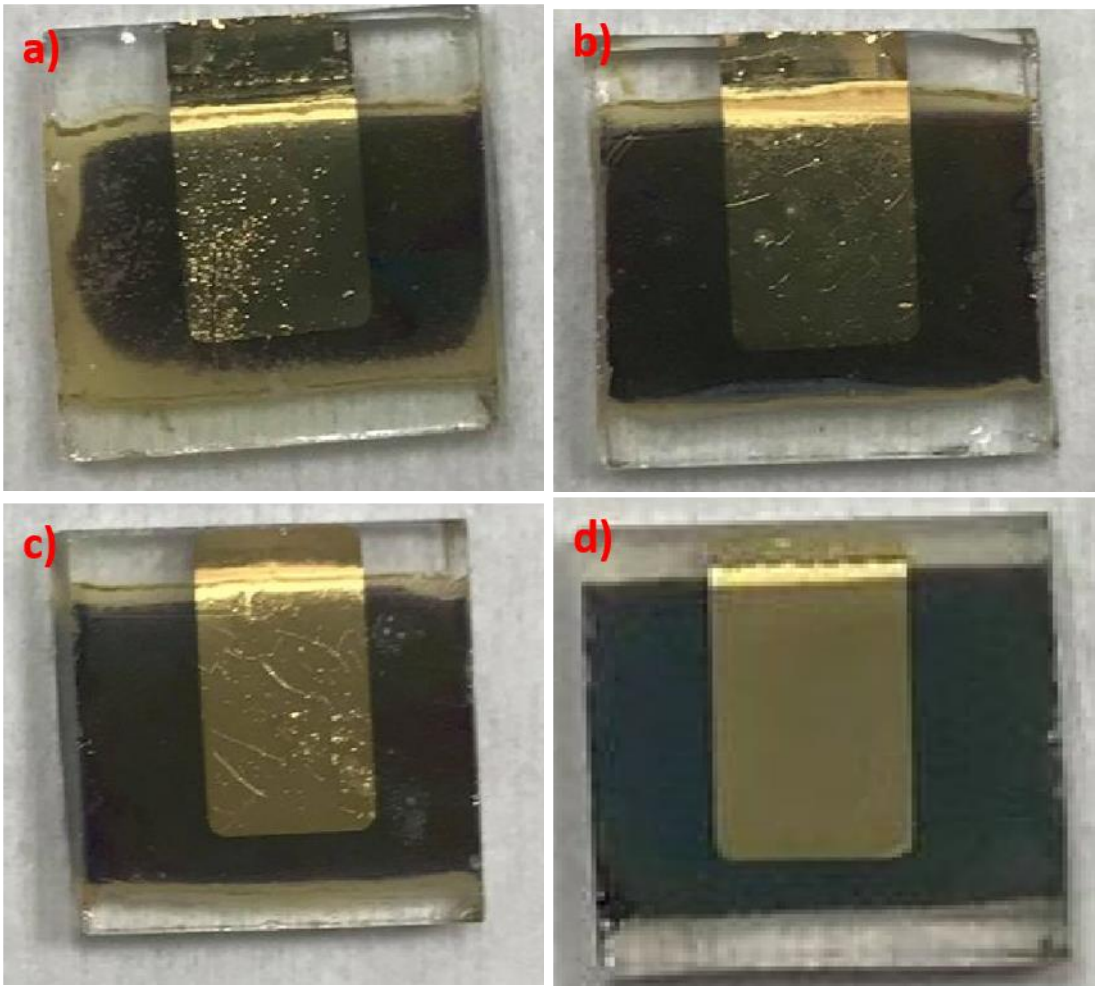

Figure III. 10: Perovskite solar cell etched with: a) DMSO b) DMF c) DMSO during the annealing d) DMF during the annealing

Such very empirical aspects remain of high importance to the final behavior of the device as we show in the following sections. After many tests, the most efficient way to overcome this issue is to use DMF as a solvent, by respecting the following two points:

1) For the reminder, the perovskite layer after the deposition is etched using a cotton swab soaked in DMF. Therefore, we should take a very small quantity of solvent by dipping partially the cotton swab in it, in order to reduce the amount of soaked DMF.
2) Doing the etching directly on hot substrates, which means that we put the substrates on the hot plate for 5 min, under 100°C just before the etching and we put it quickly

back for another 5 min under 100°C as well. Thus, the solvent would remain less on substrate since the heat increases its evaporation. Consequently, the diffusion is immediately stopped which ensures the good quality and well-designed perovskite films as shown in Figure III. 10. This treatment can be performed whether after the perovskite annealing or during its last minutes. This technic reduces the diffusion of DMSO as well (Figure III. 10c) however it is still not good enough as DMF (Figure III. 10 d), this could be related to the lower boiling point of DMF that allows the DMF to be evaporated quickly from the sample. As result, we have approved DMF as the solvent used for perovskite etching.

III.2.2.2 The effect of the antisolvent on the reproducibility of PCS

As reported by many studies in the literature, the anti-solvent dripping step (see chapter II) is crucial for achieving high-quality perovskite layers. Indeed, the anti-solvent treatment, when it is well done after solution spreading on the substrate, increases the crystallization of the perovskite and contributes to the achievement of smooth and uniform perovskite films [110][111]. The following image shows the UV absorption of the triple cation perovskite layer obtained with and without antisolvent.

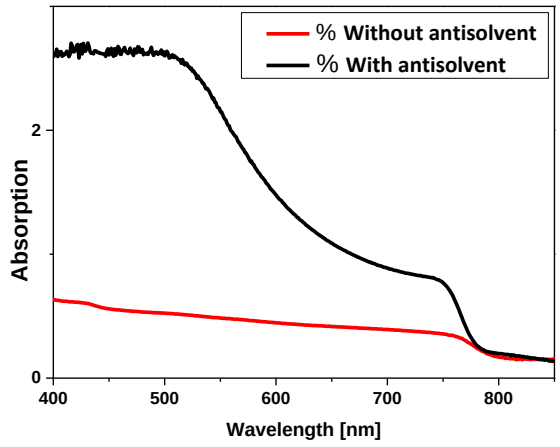

Figure III. 11: Uv-vis absorbance spectra of perovskite solar cell deposited with and without the antisolvent treatment

We notice from Figure III. 11 that the absorption of the untreated film with the antisolvent is extremely low compared to the absorption of the treated perovskite layer where it reflects the

signature of the triple cation perovskite films. Therefore the untreated film is not able to absorb photons and consequently photogenerated charges. Therefore, it seems that without depositing the antisolvent, the gamma dark phase of the perovskite cannot be formed.To investigate the impact of such treatment on the device, we conduct the JV measurement to extract the PV parameters as shown in Figure III. 12. (The spectral correction was not applied to the Jsc performance measurements, leading to a slight overestimation (around 10%) of our short-circuit currents, which is acceptable since it does not impact the trend)

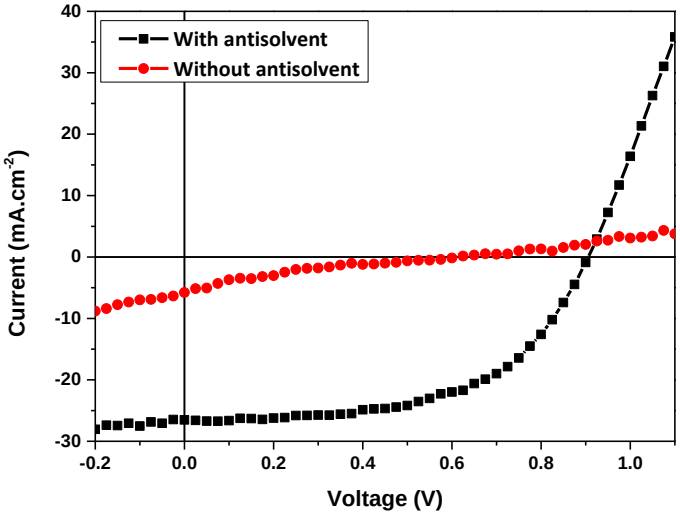

Figure III. 12: JV curves of PSCs obtained with and without the antisolvent treatment

	Voc (V)	Jsc(mA.cm^{-2})	FF	PCE(%)	Rs(Ω)	Rsh(Ω)
With the antisolvent	0.90	26.8	0.56	13.56	27.3	1010
Without the antisolvent	0.61	5.63	0.17	0.6	648	328

Table III. 2: The photovoltaic parameters of PSCs obtained with and without the antisolvent treatment

Noticeably, the PCE of the untreated PCS is extremely low, this is mainly due to the drop of the Jsc, which was expected since the low absorption of the untreated perovskite film

drastically reduces the photogenerated current. Therefore, this kind of perovskite film cannot be used for photovoltaic applications.

Despite such an advantage, the anti-solvent procedure always brings very low efficiency or non-working devices. In other words, the use of antisolvent has a bad impact on the reproducibility of the devices [112]. In our case, we observed many times the formation of pinholes in the perovskite layer as shown in Figure III. 13. This issue is related to the anti-solvent deposition, which is usually done by pouring (using a micropipette) a volume of anti-solvent on top of the perovskite layer, during the spin-coating step.

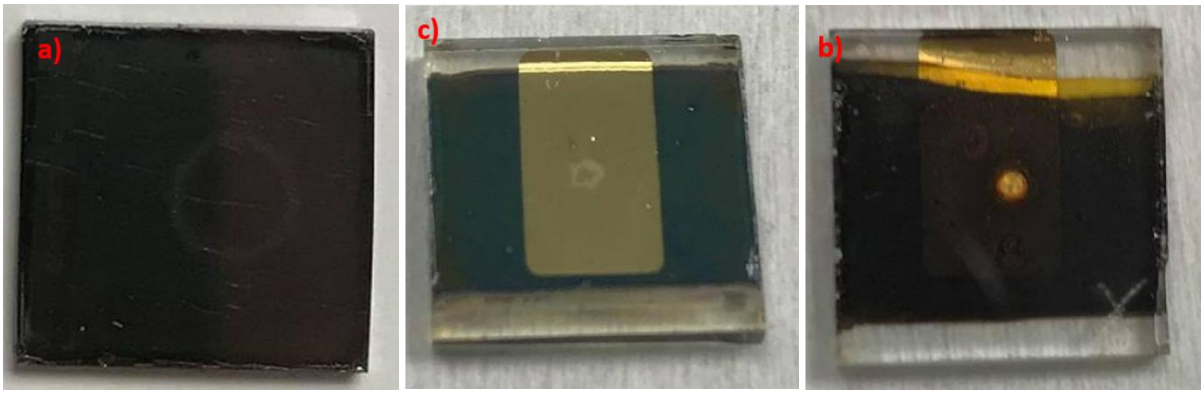

Figure III. 13: Illustration of circles and pinholes in the perovskite layer

The pinholes in the perovskite film allow direct contacts between the HTL and the ETL which reduce the performance of the solar cells, or lead to non-working devices, as illustrated by Figure III. 15.

Moreover, other antisolvent issues can highly affect the solar cell performance (Figure III. 15) such as a circle in the center and the cracks appearing in the perovskite film.

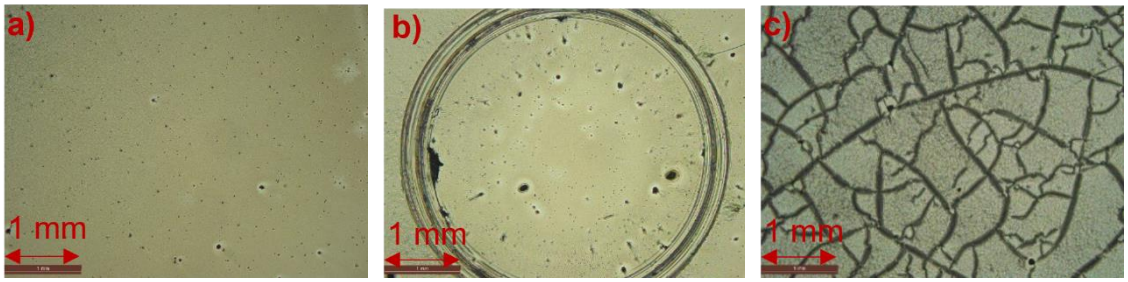

Figure III. 14: Optic microscope image showing a good perovskite film (a) Vs two bad perovskite films (showing a center circle (b) and craks (c))

The following image shows the bad impact of such issues on solar cell performance.

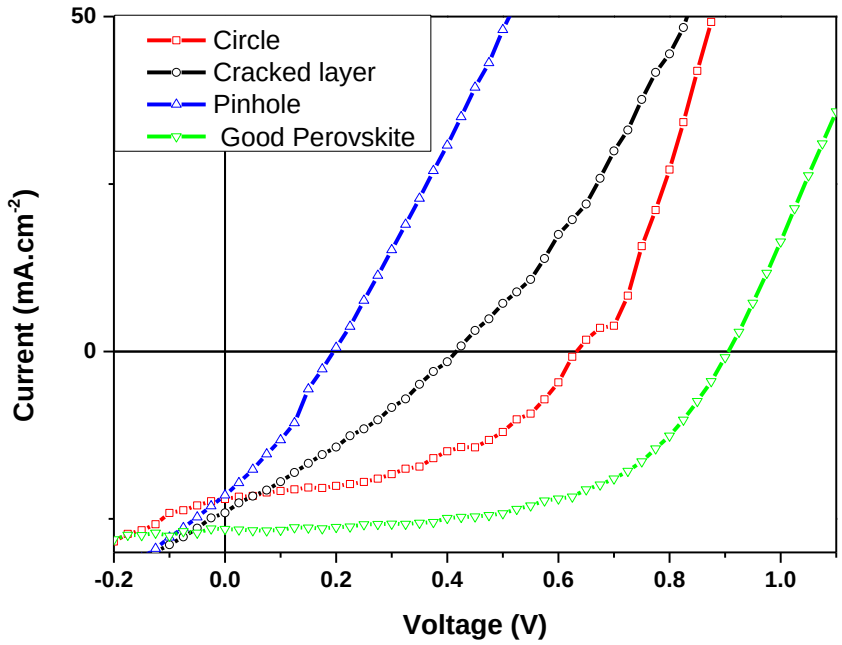

Figure III. 15: JV curves of PSCs

	Voc(V)	Jsc(mA.cm^{-2})	FF	PCE(%)	Rs(Ω)	Rsh(Ω)
Good PSC	0.90	26.8	0.56	13.56	27.3	1010
Pinhole	0.19	20.3	0.34	1.33	39	74
Craked layer	0.41	24.1	0.29	2.89	69	113
Circle	0.64	22.7	0.44	6.44	58	248

Table III. 3: The photovoltaic parameters of PSCs with different layer quality

At very high anti-solvent volume some cracks appear on the surface of the perovskite film which breaks the continuity and reduces the uniformity of the film and leads to low-efficiency PSCs.

From these JV curves and the tables above, we can conclude that the presence of pinholes or cracks in the perovskite layer kills the performance of the PSC, whereas the presence of the central circle can cause less damage but it is still reducing significantly the performance of the solar cell. The spectral correction was not applied to the Jsc performance measurements, leading to a slight overestimation (around 10%) of our short-circuit currents, which is acceptable since it does not impact the trend.

To overcome these issues, we have investigated the effect of various anti-solvents on perovskite film reproducibility. The three anti-solvents that we have chosen are Isopropanol (IPA) chlorobenzene (CBZ) and diethyl ether (DEE), since they are already largely used for their ability to improve the perovskite crystallinity.

We have built preliminary statistics of good perovskite films that can be obtained, thus we have measured the fraction to have **only** good perovskite films (uniform films free from any visible defects such as pinholes, cracks, and circles) for each anti solvents (IPA, DEE, CBZ) and without antisolvent treatment as shown in Figure III. 16. The test was performed on 10 devices for each condition, by dropping 500µl of anti-solvent during the deposition of the perovskite film on top of FTO/SnO_2 substrates and under a controlled environment which means inside of the glove box as described in chapter 2. The anti-solvent was dropped after 10 seconds following the rotation of the spin-coater used for the deposition of the perovskite precursor solution.

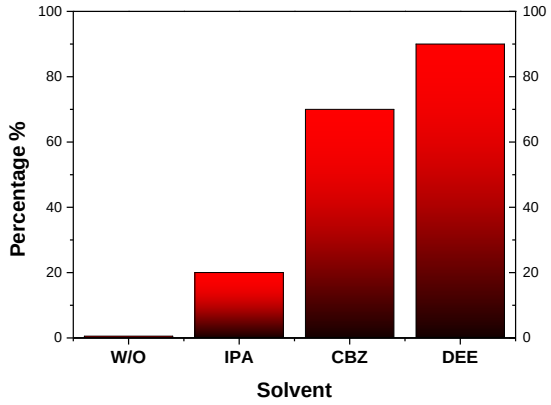

Figure III. 16: The fraction of having good perovskite films via different solvents

From Figure III. 16, we can see that the high probability to have good perovskite films is by using DEE as an anti-solvent, with a probability of 90% to have good films, which strengthens what was reported in the literature that DEE is the most suitable anti-solvent for PSCs since it can efficiently drive the perovskite precursors into the metastable zone rather than the supersaturation zone [112]. The very high volatility of DEE compared to IPA and CBZ (At standard pressure the boiling point of DEE, IPA, CBZ, is 34.6°C, 82.3°C, 131.7°C respectively [113]) can be also a key point to understand this outstanding performance since the high volatility means that the anti-solvent remains less on the substrate and leads to faster crystallization, where the faster crystallization is required for high performance and smooth

perovskite films, meaning a proper speed (not too slow or too fast) and dynamics of nucleation and growth of the crystals that allows having big crystallized grains in the film[110]. IPA is the less suitable anti-solvent which could be related to its higher solubility for the perovskite precursor compared to DEE or CBZ [112]. The CBZ can also be used as an anti-solvent but it is less reproducible in the glove box (see next section).

The volume of the dripped anti-solvent is also a crucial parameter that we evaluated. To do so, we dropped different volumes of DEE on top of perovskite films during its fabrication as described in chapter 2. For each volume, we tested 10 substrates and built preliminary statistics of good perovskite films, in order to illustrate the reproducibility of the process (Figure III. 17).

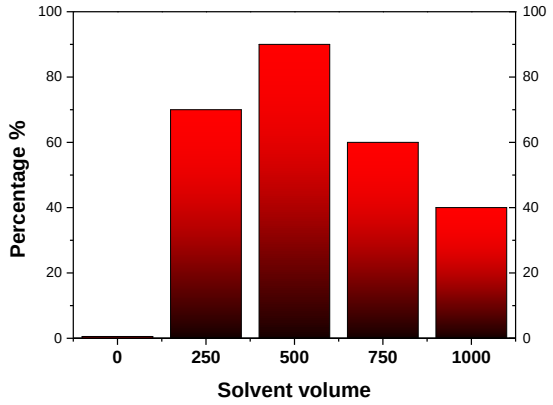

Figure III. 17: Fraction of good perovskite layers as a function of anti-solvent volume (DEE in this case)

From this study, we notice that the best volume of anti-solvent that gives more reproducible perovskite films seems to be 500µl. The ratio of this anti-solvent volume to the deposited perovskite volume is almost 10:1 (v: v) which is similar to what was reported in the literature in some related studies [112].

III.2.2.3 Inside Vs Outside of the glove box

Initially, the process of fabrication was performed outside of the glove box, however, we have switched inside of the glove box (N2 glove box, [O2] and[H2O] < 1ppm) to study the effect of such an environment on the dispersibility of the performances of the solar cells (in the same batch) and the reproducibility in general. The anti-solvents on the perovskite film reproducibility inside and outside of the glove box. Outside of the glove box means in the

fume hood and under ambient conditions (the temperature at ~ 25°C, the humidity between 25% and 50%). This test was done on 12 samples for each solvent.

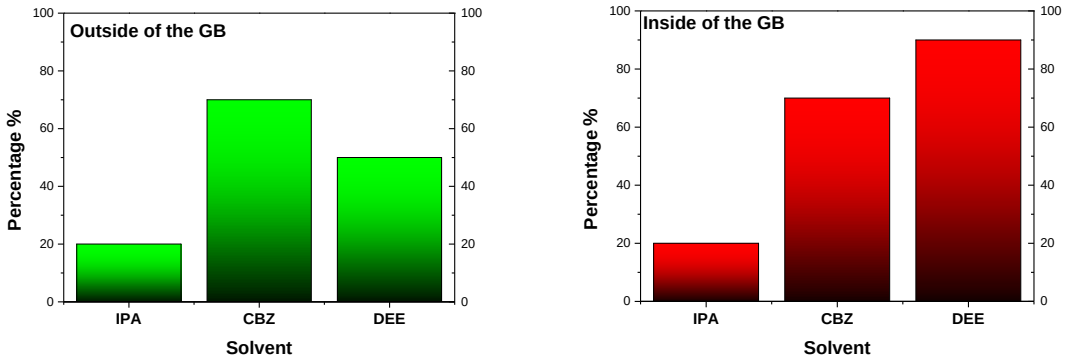

Figure III. 18: The percentage of having good perovskite films from different solvents inside and outside of the glove box

As we can see the probability to have good perovskite films with different solvents can depend on the nature of the environment, inside or outside of the glove box, especially for DEE.

The dripping of DEE outside of the glove box reduces good perovskite films reproducibility. This is could be related to the difference in temperature between the two environments since inside the glove box the temperature is generally higher compared to outside. The presence of the hot plate, at 65°C where the perovskite solution is constantly understeering, in a closed environment as the glove box increases its inter temperature especially with the lack of any cooling or temperature controlling system. This high temperature (around 37°C) favorites the volatility of DEI (boiling point 34.6°C [113]) which changes its interaction with the crystallization process of the perovskite compared to outside. Under the fume hood, the DEE is less volatile because the temperature is generally around 25°C and rarely reaches above 30°C due to the presence of air conditioning. Moreover, the humidity outside can affect the DEE since the Anhydrous DEE used as an anti-solvent can absorb the H_2O which reduces its volatility.

On the other hand, there are no big differences for CBZ (inside and outside the glove box) which could be related to its higher boiling point (131.7°C [113]) compared to DEE, so the crystallization process is less affected.

The statistics of device performance that compare the two environments are included in Figure III. 19**Erreur ! Source du renvoi introuvable.** (the optimized perovskite and deposited outside the GB in blue, the optimized perovskite and deposited inside the GB in pink). Figure III. 19 shows a distinct improvement of the PCE while processing inside of the glove box. Noticeably, the Jsc is increasing (with very low dispersion) this could be related to the nonpresence of moisture, since, uncontrolled moisture can affect the layers, especially at high humidity levels. The effect of moisture is more observed during the characterization of the solar cells where we can see its low electrical performances, and it is hard to distinguish good from bad layers just by observing the perovskite film after the annealing. Unlike the issues related to the anti-solvent where we can see clearly the pinholes or circles or even the yellow phase directly on the films. We could not go further in our analysis since it is not the heart of our work and due to the complexity of such a problem.

Finally, we show the statistics of device performance made through the different optimization stages of the ETL and active layer: optimization of the SnO_2 layer; optimization of the anti-solvent procedure; the influence of the ambient conditions (glovebox or not).

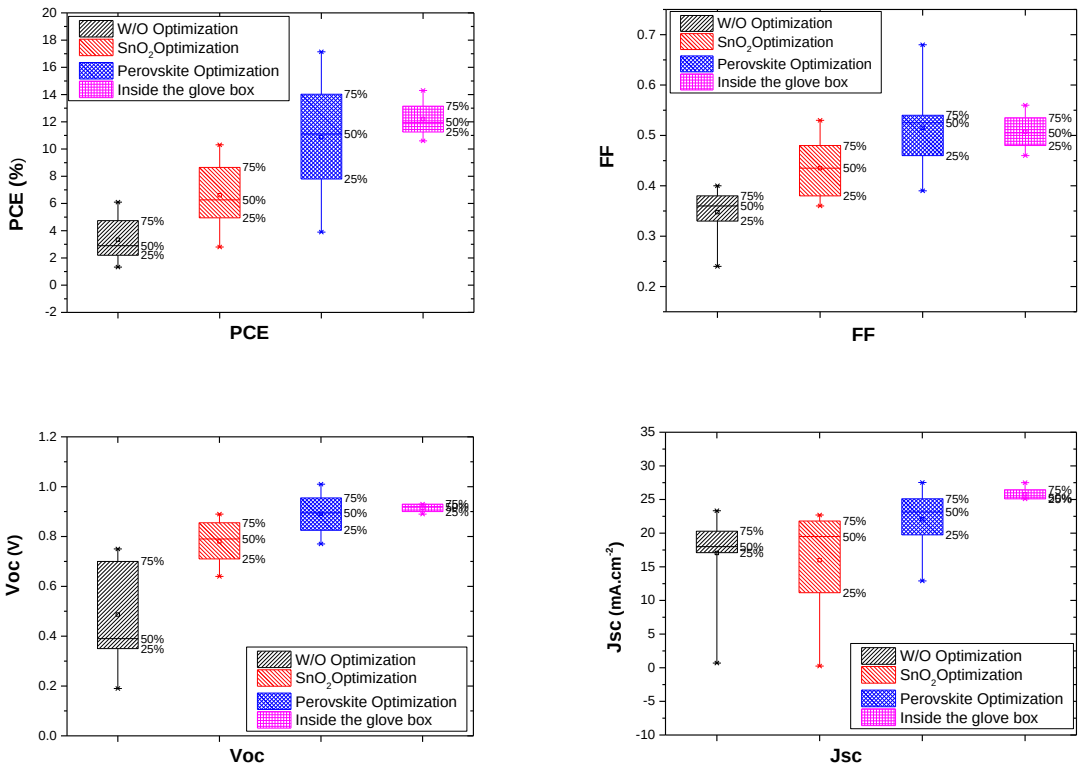

Figure III. 19: statistical analysis of the reproducibility of the PV performances of optimized and non-optimized PSCs

The optimization of the perovskite layer through the anti-solvent procedure made outside the glovebox does improve the performance of the solar cell, however, it increases the non-reproducibility due to the uncontrollable moisture level and temperature. Even if the champion device (showing a power conversion efficiency of nearly 18%) was obtained outside the glovebox, the average performance and reproducibility are largely improved when processing the perovskite layer under an inert atmosphere. On the other hand, fabricating perovskite solar cells inside of the glove box reduces their performances which could be due to the very low rates of oxygen and water [114] however this environment increases the reproducibility of PSCs with acceptable performances.

In our case, the reproducibility of the solar cell is crucial to determine and compare the different parameters by impedance spectroscopy. For this reason, we have approved the fabrication of a perovskite solar cell inside the glove box.

Finally, we can conclude that from a reproducibility point of view it is better to deposit the perovskite inside of the glove box with a volume of 500µl DEE, whereas it is possible to have good PSCs especially if we use CBZ as an anti-solvent. However, the reproducibility is lower, and the performance of the solar cells depends on meteorological conditions such as the humidity and the temperature of the day.

III.3 The stability of perovskite solar cells

One of the big concerns in perovskite solar cells is their stability. Many parameters can affect the PSC stability such as moisture, temperature, oxygen, the degradation of the ETL, the applied bias, the light (UV), etc.[115]. The expected lifetime of the PCS module is estimated to be around 1 year compared to 25 years for Si-based technology, this represents a break of the commercialization of this technology [116] [117]. However, in laboratory scales, and especially in our case, this is not a big concern since we need stable devices only during performing impedance spectroscopy measurements.

One of the main reasons that drove us to choose Cesium-mixed cation perovskite solar cells is their remarkable stability due to their excellent thermal and structural stability. This leads to a stable PCE under illumination and in the presence of moisture [118] [66]. Furthermore, Saliba et al. have demonstrated that adding the cesium as a cation in mixed cation PSCs (the

same perovskite as us) help to stabilize the PCE (21.1%) under operational conditions for more than 250 hours [66]. In our case, We need that the solar cell stays stable for just 20 minutes under illumination during the time of the IS measurement, however, the IS measurements requires putting the solar cell under different DC and AC voltages and the effect of such parameters on the stability of the device is unknown. Therefore, and to be more accurate, we have investigated the stability of our PSC by measuring the JV curves before and after the IS measurement. The spectral correction was not applied to the Jsc performance measurements, leading to a slight overestimation (around 10%) of our short-circuit currents, which is acceptable since it does not impact the trend.

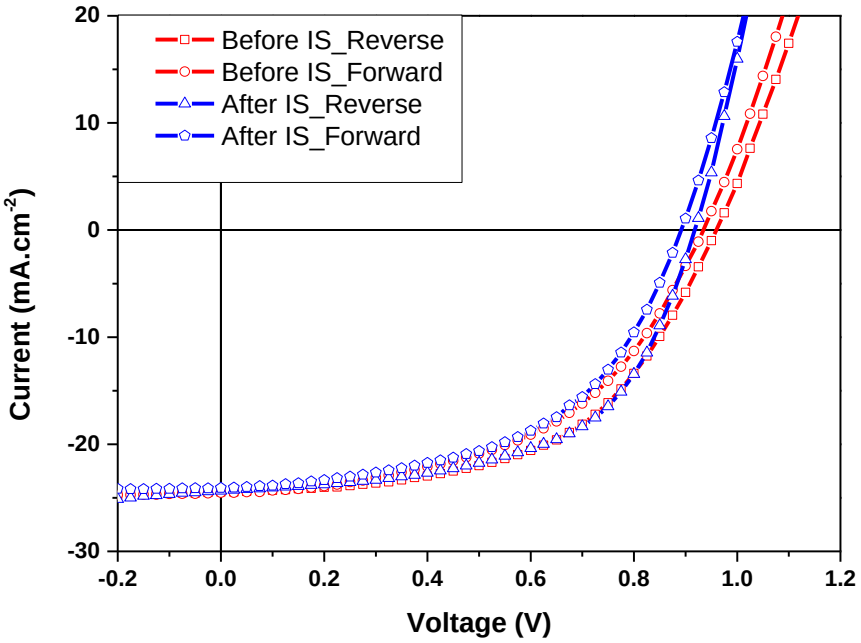

Figure III. 20: JV characteristics off a typical mixed cation PSC before and after IS

	Scan direction	Voc(V)	Jsc(mA.cm^{-2})	FF	PCE(%)
Before IS	Reverse	0.95	24.4	0.55	12.76
	Forward	0.93	24.5	0.51	11.61
After IS	Reverse	0.91	24.4	0.58	12.83
	Forward	0.87	24.0	0.54	11.36

Table III. 4: The photovoltaic parameters of a mixed cation PSC Before and after IS

As expected the PCE remains stable after the impedance spectroscopy measurement meaning that the solar cells do not show any remarkable degradation. The slight variation of the Voc could not impact the IS results (see more details about the stability under IS in chapter IV). It is preferable to conduct JV measurement systematically before and after the IS measurement to be sure of the stability of the device.

III.4 Conclusion

In summary, in this chapter, we have elaborated our protocol toward efficient and especially reproducible mixed cation perovskite solar cells that ensures a firm grounding of the comparative studies conducted thereafter.

We have shown that many parameters can affect the reproducibility of the performance of the perovskite solar cells, we have given special focus on the effect of the nature and volume of antisolvent (DEE, IPA, CBZ) as well as the good impact of depositing the perovskite inside of the glove box in terms of reproducibility and slightly bad impact on the PCE. Moreover, we have demonstrated that our perovskite solar cells are stable enough under IS measurement conditions (outside, under1 sun of illumination, and under different voltages), which allows us to conduct IS in the best conditions. The impedance spectroscopy measurements are presented in the next chapter.

Chapter IV - Principle of impedance spectroscopy and application in the context of visible light communications

IV.1 Introduction

Impedance spectroscopy or IS is a non-destructive electrical characterization technique with a wide range of applications. It can be used to characterize materials or devices that have electronic and/or ionic behaviors such as thin films based on dielectric or semiconducting new materials, electrochemical systems (in solution or solid-state), and complete devices such as batteries, supercapacitors, or solar cells. Over the last decades, IS has been widely used to study the main physical mechanisms occurring in different types of solar cells, especially, dye-sensitized solar cells (DSSCs) and organic solar cells[119][120][121].

The arrival of perovskite solar cells with their outstanding performances and their promising potential has prompted many scientists to use impedance spectroscopy to better understand their physical properties and main limitations. One important advantage of IS compared to other classical characterization techniques is that IS can be implemented on the complete device under working conditions (under illumination and variable applied voltage) which makes it appealing for PV devices. Moreover, IS is known as a high accuracy method that allows researchers to separately analyze the different physical processes involved in a solar cell in the dark or under illumination. However, IS measurements destined to perovskite devices require specific attention, considering the intrinsic electronic and ionic phenomena that are involved at different time scales. In addition, the rapid evolution or degradation of the device performance under ambient conditions or solar illumination makes the analysis complex. Therefore great care must be taken to avoid any misinterpretations.

In this thesis, we are aiming to use IS to evaluate the dynamic properties of perovskite solar cells for the specific OWC application. To do so, we will evaluate the relevant capacitances and resistances of the perovskite solar cells processed at the laboratory scale using the procedures described in the previous chapter. We will mainly focus on the estimation of relaxation times and bandwidth and their relation with device architecture and materials. Before going into the analysis of the device response using IS, we first describe in this chapter our approach to study and characterize perovskite solar cells using impedance spectroscopy and our methodology to get reliable IS measurements. We will also describe the procedures used for data fitting using electrical equivalent circuits, and for the extraction of the main dynamic parameters that can highly affect the OWC.

IV.2 Basics of Impedance spectroscopy

Impedance spectroscopy is a small-voltage perturbation technic that consists to measure the complex impedance of a sample (PSC in our case) which is the ratio between an applied AC sinusoidal voltage (the input) and the resulting sinusoidal current (the output). The applied AC voltage signal can be eventually superimposed to a DC voltage in order to put the probed device in a certain working point condition. The input and the output signals of the system have the same frequency whereas, the amplitude and the phase may differ depending on the impedance of the probed sample as shown in Figure IV. 1. This measured impedance provides information on the resistive, capacitive, and inductive behavior of the device. By varying the frequency, it is then possible to distinguish the specific physical phenomena governing the performance and behavior of the solar cell (contact resistance, recombination and transport resistance, geometric or chemical capacities, etc.).

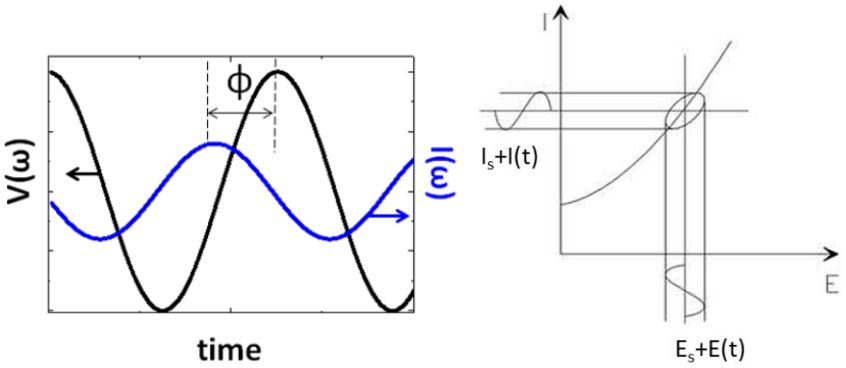

Figure IV. 1 The input and the output signals in impedance spectroscopy [122]

The input voltage signal V(t) is a sinusoidal function defined as:

$$\mathrm{V(t)} = V_0 \sin(\omega t) = V_0 e^{j\omega t} \quad \text{(IV. 1)},$$

Where V_0 is the amplitude and ω is the angular frequency of the perturbation that can be defined as:

$$\omega = 2\pi f$$

Where f is the frequency

The output current signal I(t) is defined as:

$$\mathrm{I(t)} = I_0 \sin(\omega t + \varphi) = I_0 e^{(j\omega t + \varphi)} \quad \text{(IV. 2)},$$

Where I_0 is the amplitude and φ is the phase shift between the input and the output signals.

From (IV. 1)and (IV. 2) the impedance is given by

$$Z(t) = \frac{V(t)}{I(t)}$$

$$Z(t) = Z_0 e^{-j\varphi}$$

$$Z_0 = |z| = \frac{V_0}{I_0}$$

Where Z_0 represents the ratio of input and output signal amplitudes and $e^{-j\varphi}$ is the phase shift between these two signals. It is important to keep in mind that IS is a small-perturbation method where the AC excitation is of low amplitude thus, the operating steady-state of the solar cell is not perturbed. In such a case, IS can relevantly reflect the device dynamic behavior in a specific working point imposed by the DC applied voltage and eventually, the illumination conditions.

The impedance Z is a transfer function that relates the input V(t) to the output I(t) as a frequency function. It is also a complex number of the form :

$$Z = Z' - j\,Z''$$

Where Z' is the real part of Z (at ϕ=0) and Z'' is the imaginary part of Z (at ϕ=90°). The imaginary part Z'' can be considered as a positive or a negative quantity. In physics, Z'' is commonly noted with a negative sign while it is more common for engineers to note it with a positive sign [122].

In a specific frequency point, the Nyquist plot, where -Z'' is plotted as a function of Z', of the impedance can be represented by a vector as shown in Figure IV. 2 where Z_0 is the magnitude and ϕ is the phase angle of Z.

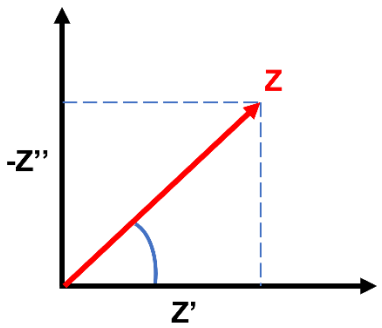

Figure IV. 2: Representation of the impedance Z

Z', the real part of Z, represents physically a simple resistance R that describes the resistance to the flowing current through the device, Z' depends on the Ohm low shown in the following equation:

$$R = \frac{V}{I}$$

Z'', the imaginary part of Z, represents physically a reactance X that describes the resistance to the changes of the flowing current through the device [122].

Z' and Z'' can be defined as:

$$Z' = R = Z_0 \cos(-\phi) = Z_0 \cos(\phi)$$

$$Z'' = X = Z_0 \sin(-\phi) = -Z_0 \sin(\phi)$$

The impedance spectroscopy measurement is performed under different frequency values (from 20 Hz to 1 MHz in our case) which means that for each frequency value there is a corresponding complex impedance Z (ω) with its two components Z'(ω) and Z'' (ω).

IV.3 The impedance of basic circuit elements

The experimental data obtained by impedance spectroscopy, which represents the real and the imaginary values of the impedance (Z'and Z''), are commonly represented by the Nyquist plot that can be fitted using an equivalent electrical circuit. Every component of the equivalent circuit characterizes an electrical property of the device that, in principle, should be linked to its physical origin. For example, if we are measuring a semiconductor layer situated between two electrodes, the series resistance of the equivalent circuit that module this sample could be related to the conductivity of the semiconductor as well as the two electrodes. However, measuring a complete device with multilayers such as solar cells can be complicated in two major ways

1) The difficulty to relate an equivalent circuit component to one specific layer from the device.
2) The defects and non-ideality of the different layers can drive us to use complicated circuits or complicated circuit elements, such as the constant phase element CPE (see next part) rather than a simple capacitor, in order to have a better fit [123].

IV.3.1 Resistor

According to the Ohm law, the current of a simple resistor can be expressed as:

$$I(t) = \frac{V(t)}{R} = \frac{V_0\, e^{j\omega t}}{R}$$

From this equation, the impedance of a resistor is given by:

$$Z_r = \frac{V(t)}{I(t)} = \frac{V_0\, e^{j\omega t}}{\frac{V_0\, e^{j\omega t}}{R}} = R$$

Therefore, the impedance of a resistor has just a real component which is a simple resistance R. The absence of ω in the expression of Z_r means that the impedance of a resistor is frequency-independent. Figure IV. 3 represents the Nyquist plot of the impedance response of a simple resistor (3Ω resistance) measured by impedance spectroscopy under different frequencies. We can see just one real value that does not change with the frequency and represents the resistance value of the resistor.

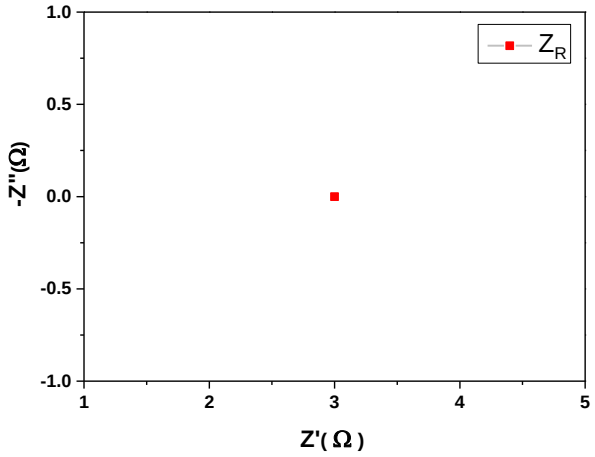

Figure IV. 3: Nyquist plot of the impedance response of the resistor

IV.3.2 Capacitor

The current of a capacitor can be expressed by:

$$Q(t) = C.V(t)$$

$$\int I(t)dt = C.V(t)$$

$$I(t) = C\frac{dV(t)}{dt}$$

And from the equation (IV. 1)

$$I_t = C\frac{d(V_0\, e^{j\omega t})}{dt}$$

$$I_t = jC\omega V_0 e^{j\omega t}$$

Where C is the capacitance of the capacitor.

From the equation above the impedance or a capacitor is given by:

$$Z_C = \frac{V_t}{I_t} = \frac{V_0\, e^{j\omega t}}{jC\omega V_0 e^{j\omega t}} = \frac{1}{jC\omega}$$

$$Z_C = \frac{-j}{C\omega}$$

From this equation, we notice that the impedance of a pure capacitor contains just the imaginary part with a negative sign. The presence of ω in the expression of Z_C means that the impedance of a capacitor depends on the changes in the frequency. Precisely, when the frequency increases the capacitor impedance decreases as illustrated in the Nyquist plot of a capacitor (Figure IV. 4).

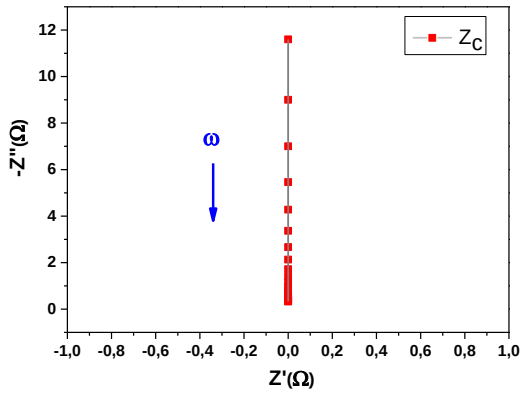

Figure IV. 4: Nyquist plot of the impedance response of the capacitor

IV.3.3 Inductor

The voltage of an inductor can be expressed by:

$$V_t = L\frac{dI_t}{dt} = L\frac{d(I_0\, e^{j\omega t})}{dt}$$

$$V_t = jL\omega I_0 e^{j\omega t}$$

Where L is the inductance of the inductor.

From the equation above, the impedance of an inductor is given by:

$$Z_L = \frac{V_t}{I_t} = \frac{jL\omega I_0 e^{j\omega t}}{I_0\, e^{j\omega t}} =$$

$$Z_C = jL\omega$$

The presence of ω in the expression of Z_L means that the impedance of an inductor depends on the changes in frequency. Precisely, when the frequency increases the inductor impedance increases as illustrated in the Nyquist plot of an inductor (Figure IV. 5).

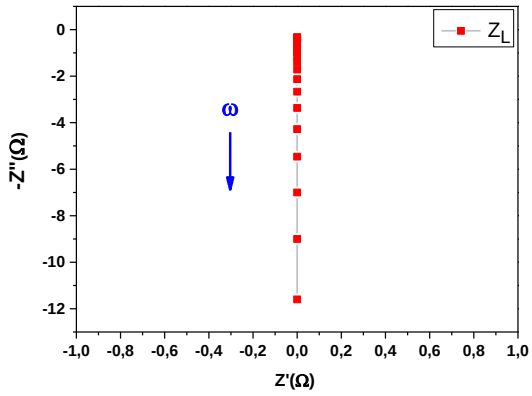

Figure IV. 5: Nyquist plot of the impedance response of the inductor

IV.4 Equivalent circuits

The connection of multiple basic electrical elements (R, C, or L) can form an equivalent circuit presenting a complex response, which can characterize the global impedance response of realistic samples or devices. In this case, the basic associations of elements are applied.

The total impedance of elements assembled in series can be calculated as follows:

$$Z_{tot} = Z_1 + Z_2 + Z_3 + \cdots$$

The total impedance of elements assembled in parallel can be calculated as follows:

$$\frac{1}{Z_{tot}} = \frac{1}{Z_1} + \frac{1}{Z_2} + \frac{1}{Z_3} + \cdots$$

The impedance of resistor and capacitor in series can be calculated as demonstrated in the following equation:

$$Z = Z_R + Z_C = R + \frac{1}{j\omega C}$$

From this equation, we can see that at high frequencies, when ω tends to infinity, the impedance of the capacitor Z_C tends to 0 (short circuit), and consequently, the impedance of the association Z tends to R. Whereas, at low frequencies, when ω tends to 0, the impedance of the capacitor Z_C tends to infinity (open circuit), and consequently, the response of the association Z tends to infinity. Therefore, the total impedance response of the association is dominated by the frequency response of the capacitor. More details about this capacitive behavior are given in the following parts.

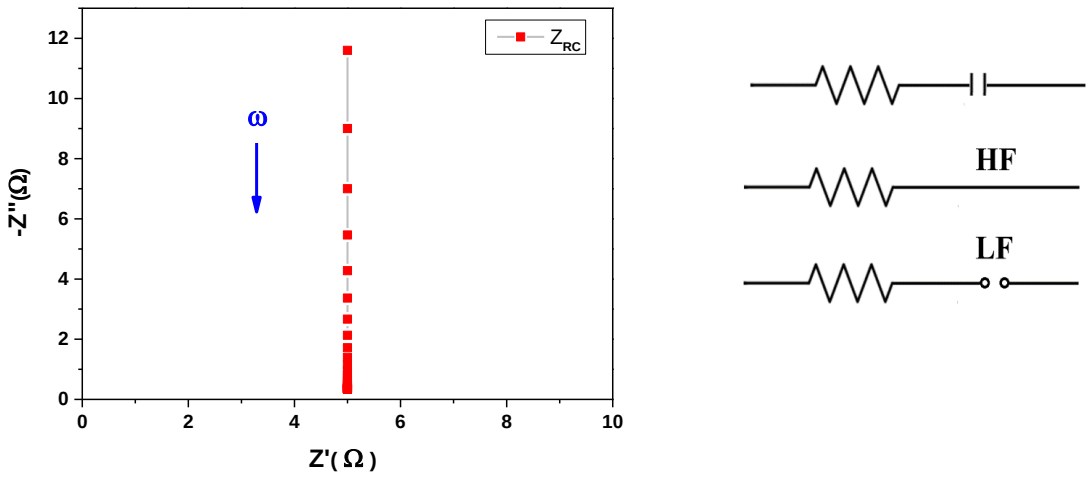

Figure IV. 6: Nyquist plot of RC series circuit

The impedance of resistor and capacitor in parallel can be calculated as demonstrated in the following equation:

$$Z = \frac{1}{\frac{1}{Z_R} + \frac{1}{Z_C}} = R\frac{(1 - j\omega RC)}{(1 + \omega^2 R^2 C^2)}$$

The Nyquist representation of the impedance response of this circuit is a perfect semicircle where the radius is equal to $R/2$ as shown in Figure IV. 7

From this equation, we can see that when ω tends to infinity (high frequencies) the impedance Z tends to 0 due to the capacitor behavior (short circuit) and when ω tends to 0 (very low frequencies) the impedance Z tends to R.

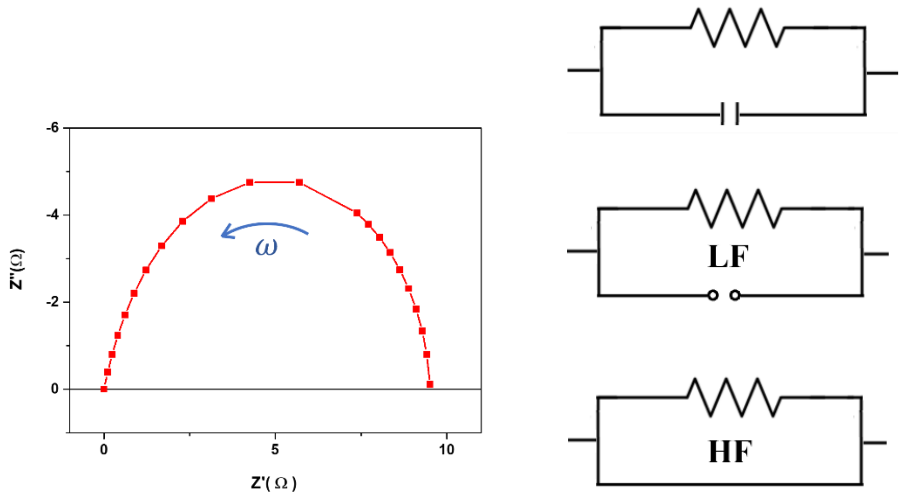

Figure IV. 7: Nyquist plot of R//C circuit

The R//C model is widely used to describe the charge transport and accumulation mechanisms in solar cells. Moreover, adding a series resistance can model the charge losses in the electrodes, this circuit can model the impedance response of some real solar cells, however, such a simple circuit is not able to model the impedance response of our perovskite solar cells as we will see in the following sections.

The extraction of the parameters is done via fitting the Nyquist plots of the impedance response of the sample, the fit is performed using an electrical equivalent circuit and must take into consideration these two points:

- The fit curve, which is based on the nonlinear regression type of fitting, must superimpose the experimental curve by well optimizing the equivalent circuit and its components values.
- Having a good fit is not the only condition since increasing the number of the circuit components gives a better fit, however, there is no relation between each component

and the physics of the solar cell. Therefore it is crucial to have fewer components that each of them can reflect a physical mechanism occurring in the solar cell.

IV.5 Experimental measurements by impedance spectroscopy

IV.5.1 Impedance spectroscopy experimental setup:

We performed the impedance measurements using a Hewlett Packard LCR meter (model 4284A precision LCR meter) in a frequency range between 20 Hz and 1MHz. the LCR meter, controlled through a Labview interface, was connected to our solar cell device using a dedicated sample holder (the same holder is used for the photovoltaic characterization). The solar cell can be indeed measured in dark or under illumination using the solar simulator.

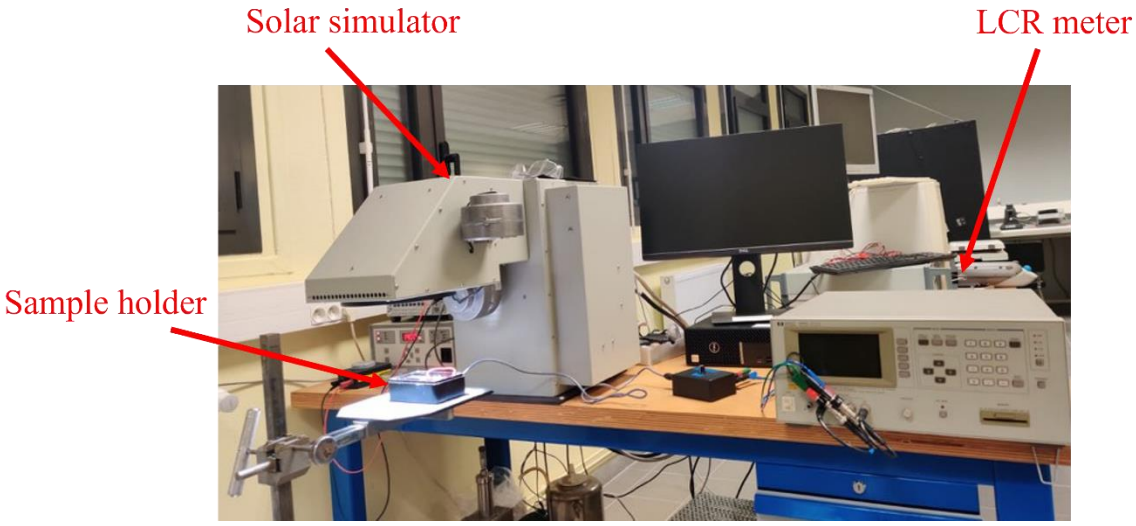

Figure IV. 8: Impedance spectroscopy experimental setup

The experimental setup in itself is simple. However, the real difficulty of IS measurement is associated with the requirement to fulfill the Linear Systems Theory (LST)[124], which defines a set of fundamental conditions to be satisfied and especially Finiteness, causality, linearity, and stability [125]. In this work, we tried to address these criteria that we discuss below.

IV.5.2 Finiteness

Based on the Linear Systems Theory, the impedance values over all the frequencies must be finite which means that there is no singularity in the impedance response. Thus, during the IS

measurements, if some points are undefined or equal to infinity, the whole response of the sample cannot be considered.

IV.5.3 Linearity

The response of the system must be linear which means that the output-input relationship is governed by the superposition principle where the additivity and the homogeneity must be respected. For example, if $V_1 = I_1 \times R$ and $V_2 = I_2 \times R$ where V is the input and I is the output the additivity is respected if $V_1 + V_2 = (I_1 + I_2) \times R$

Assuming that $V = RI$, the homogeneity is respected only if $kV = kRI$, with k is a constant.

For solar cells, the current varies nonlinearly over the applied voltage, however, to obtain a correct IS measurement, the Z response must be linear which means that the AC perturbation of voltage (input) should produce a linear variation of the AC current (output)[125]. This could be possible only if the amplitude of V_{AC} is very small in such a way to drive the amplitude of I_{AC} to vary linearly, this is also called linearization of the current-voltage [126] [125].In this case, the response of the system respects the superposition principle especially the additivity condition:

$$V_{AC} = Z \times I_{AC}$$

$$V_{DC} = Z \times I_{DC}$$

$$V_{AC} + V_{DC} = Z\,(I_{AC} + I_{DC})$$

Where:

- V_{DC} and V_{AC} are two superimposed input signals, and V_{AC} is too small comparing V_{DC}
- $I_{DC}$and I_{AC} are two superimposed output signals
- Z the linear impedance response of the system

The choice of the value of the AC perturbation is not obvious, since it is required to be as small as possible to avoid the nonlinearity issue, however, too small values reduce the signal-to-noise ratio which can affect the impedance response of the solar cell. In other words, the AC perturbation must be also as high as possible to produce noise-free impedance curves.

There is no specific value or a common rule to choose a good AC perturbation value since it depends on the nature of the samples, the measurement equipment, and the environment of each laboratory apart.

To determine the proper AC perturbation value, we have probed the impedance response of our conventional triple cation perovskite solar cell ($Cs_{0.05}(MA_{0.17}FA_{0.83})_{0.95}Pb(I_{0.83}Br_{0.17})_3$). The perovskite solar cell was measured in the dark under an applied DC voltage of 0.7V at different AC perturbation voltages as shown in the figure below.

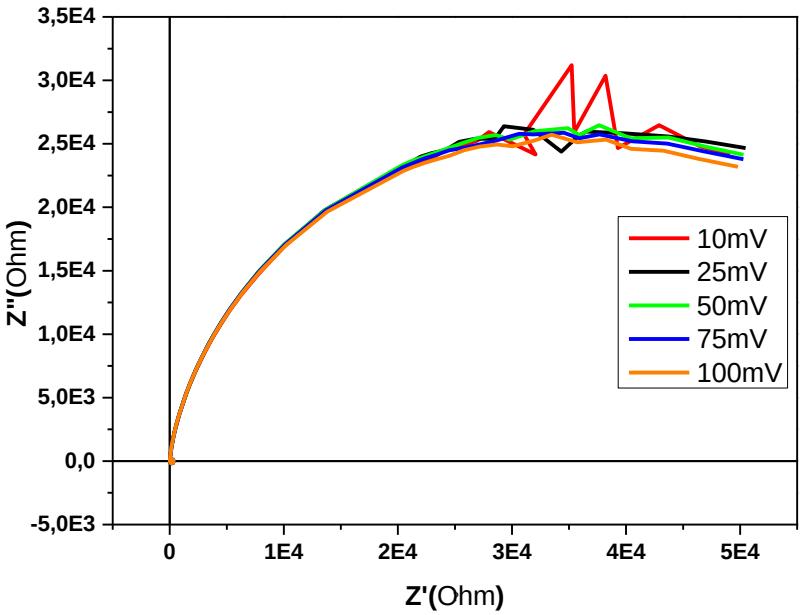

Figure IV. 9:The impedance response of a perovskite solar cell in the dark under different AC perturbation voltages

From the figures, we can see that for small perturbation there is some fluctuation of the spectrum in the low-frequency region, this is due to the low signal-to-noise ratio however from 50 mv and above, the noise is mitigated and the curves are smoother. In such a case, we will choose the smaller value that gives good impedance curves to be far away from any non-linearity issue. Thus we can choose whether 50mV or 75mV, where the 75mv curve is slightly smoother, this result is similar to what was reported in the literature [126].

IV.5.4 Causality

The causality means that the impedance response is exclusively due to the applied stimulus. In other words, the measured sample must be protected from any external source of noise that can affect its impedance response. Thus, the impedance response is only due to the applied parameters (AC and DC voltages, and the frequency). By consequence, the impedance response of the sample only reflects its physical properties and internal mechanisms. In an

ideal case, it is better to measure the samples inside a faraday cage which reduces the external noise. In our case, the connection wires and the experimental setup of the measurement always bring additional contributions to an impedance spectrum. Such contributions must be considered before any data interpretation and simulation, as we will show in this section.

At the beginning of our IS measurement, we have faced many difficulties to achieve good impedance curves. Among these issues associated with our experimental set-up, we have noticed a small inductive circle (corresponding to -Z''< 0) in the high-frequency region while measuring perovskite solar cells in the dark as shown in Figure IV. 10 which shows typical impedance data in the Nyquist plot associated with a reference perovskite device probed in the dark and under varying applied voltage.

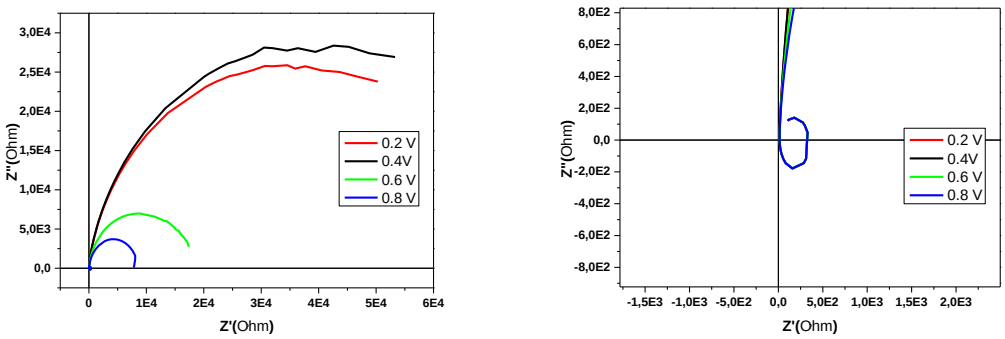

Figure IV. 10:The impedance response of a perovskite solar cell in the dark under different DC voltages with a zoom on the high-frequency region (right)

We clearly observed that this inductive loop was not affected by the applied voltage, nor by the type of the probed solar cell. It obviously indicates an artifact of our measurement.

Although this inductive loop does not seem to strongly affect the IS response in the dark, it largely contributed to the impedance measured under illumination (1 sun) as shown in Figure IV. 11. From Figure IV. 10 and Figure IV. 11, the lateral expansion of this inductive loop is in the order of 3.2 $\times 10^2$ Ω, which is negligible compared to the width of the impedance response of the solar cell in the dark (5×10^4 Ω). However, the impedance of a solar cell decreases significantly under illumination (range of around 60 Ω in our case), this inductive loop appears to be a real issue.

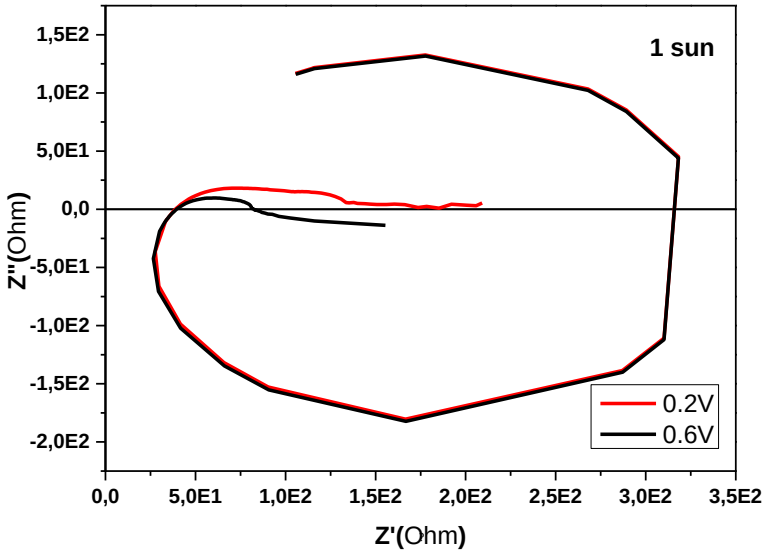

Figure IV. 11: The impedance response of a perovskite solar cell under illumination under two DC voltages

As we can also see, the shape of the inductive loop did not change when varying any experimental parameter (dark, illumination, dc voltages) which proves that it is indeed an external artifact, independent of the solar cell response. Consequently, the causality condition was not fulfilled in this case.

It is hard to exactly assign this kind of artifact to a particular component of the set-up, however, it is reported in the literature that long wires or their unreliable electrical shielding are known to cause such a problem [126][122]. A fine calibration of the LCR equipment should also be performed regularly to avoid any deviations during the short-circuit and open-circuit calibration routines. The device holder can also be a potential contributor to this inductive loop. After several preliminary tests, we succeeded in drastically reducing this inductive artifact mainly by changing our experimental configuration. The configuration of the wires had to be optimized to keep any artifact well below the impedance range of our devices probed in all the tested conditions, and especially under illumination(see Figure IV. 12). All our impedance spectra still show a small residual inductive signature due to the set-up, but this part did not affect our interpretations, as it was systematically taken into consideration during the simulation and the fit of the data using an electrical equivalent circuit, as it will be presented in the following parts.

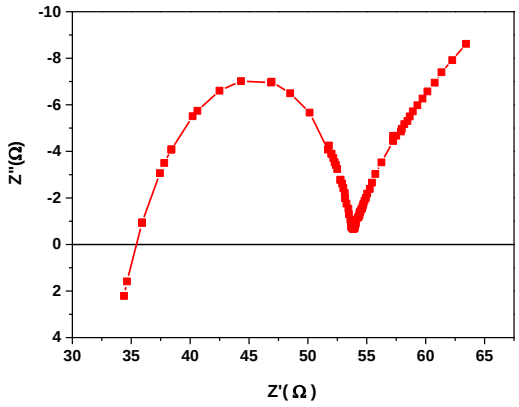

Figure IV. 12: The impedance response of a perovskite solar cell under illumination

IV.5.5 Stability

Performing impedance spectroscopy on solar cells can be time-consuming, it generally takes 1 to 1.5 minutes for measuring a sample at a specific DC applied voltage. However, we often perform IS under 9 different voltages (from 0.1V to 0.9V) which takes around 15 minutes under illumination. Consequently, the stability of the measured sample is crucial in order to have a relevant and robust impedance response. For perovskite solar cells, this condition is particularly challenging since PSCs remain hardly stable in ambient conditions and under solar illumination for a long period of time. Ideally, it is probably more suitable to perform IS under an inert atmosphere (such as in the glove box). However, if this choice is not available, as in our case, the IS can be performed outside of the glove box provided that the solar cells are stable during all the required period. Therefore, the choice of the nature of the perovskite active layer and the interfacial layers are very important in terms of stability. As discussed in the previous chapter, our PSCs show reasonable stability under ambient conditions due to the use of SnO_2 rather than TiO_2 for the ETL, and to the presence of Cesium and Bromide in our double and triple cation mixed halide perovskite active layer. However, for low stability solar cells (which is not the case for us), it is recommended to reduce the measurement time as much as possible by reducing the acquisition time or by reducing the number of points. Nevertheless, this should be done carefully since it can make the system sensitive to noise.

IV.6 Impedance data fitting

As discussed in the first part of this chapter, the impedance data recorded on full devices reflects several relaxation mechanisms related to capacitive and resistive contributions, which can be complex to analyze. It is generally necessary to model the data using an equivalent electrical circuit which should show the relevant physical meaning considering the nature of the tested device. Many equivalent circuits can be found in the literature for perovskite solar cells that can be used to describe a wide range of physical behaviors of solar cells [127] [128][129][130][131]. However, we prefer to explain our methodology to obtain a well-adapted fit of our experimental data curves. This methodology can be used to achieve

Our Impedance data were fitted using the Zview software (from Scribner Associates), which allows us to plot the experimental data (a file containing the frequency, Z', and Z'') in a Bode or Nyquist representation diagrams, and to build the electrical equivalent circuit for the simulation of the frequency-dependent impedance. Thereafter, we module this impedance response by creating an electrical circuit model that shows the same response. We can then compare the two curves directly on the software to see if the fitting matches or not. In Zview interface, there is another window of bode diagrams just to be sure of the accuracy of our fit as shown in Figure IV. 13.

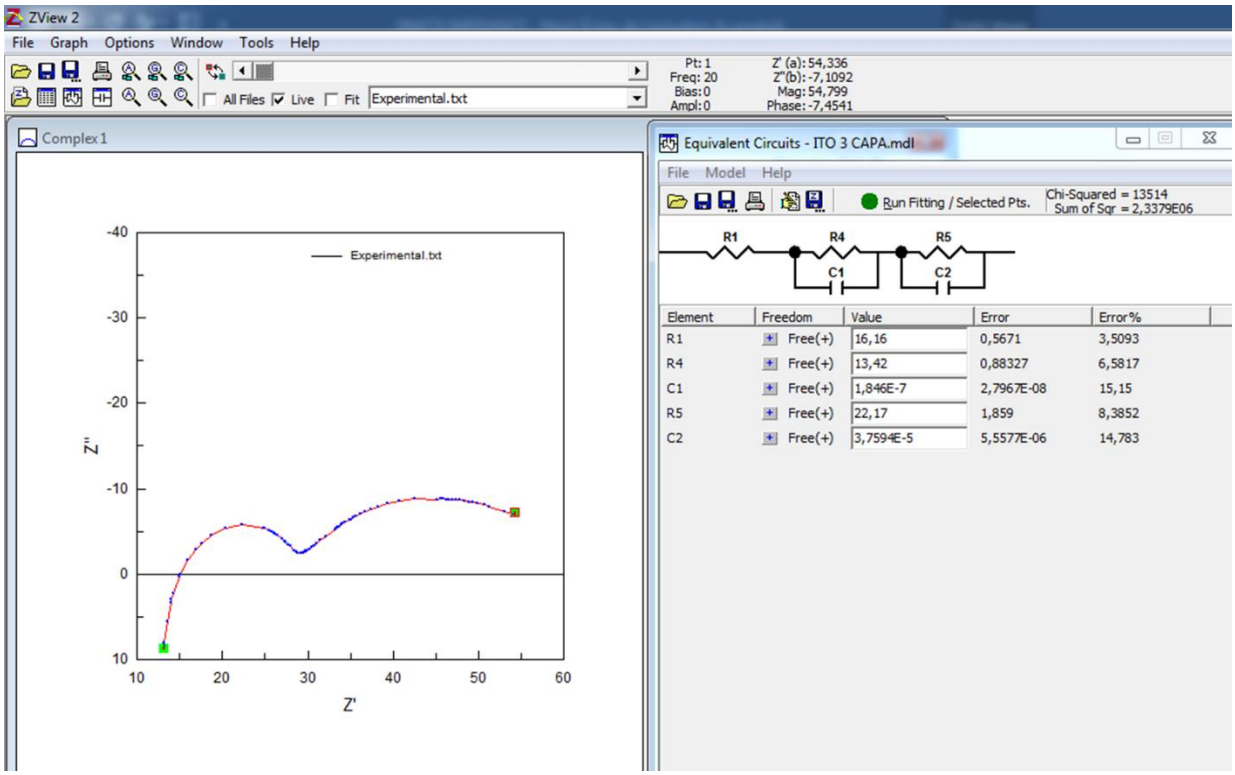

Figure IV. 13: The graphical interface of ZView software. On the left: Nyquist plot. On the right: equivalent electrical circuit built to fit the data.

Such simulation of impedance data can be very tricky. Indeed, fitting spectra using complex circuits is always possible from a mathematic point of view, but the physical meaning of the extracted components should always be the main criteria to assess the relevance of the fit. Typically, preliminary tests on a separate layer can be useful to focus on a specific interlayer or electrode, before going towards more complete architectures. In the following part, we describe our methodology for impedance data fitting, by focusing on the key points that have helped us achieving relevant interpretation of device performance. Notably, starting from a simple equivalent circuit to a more complex circuit that shows a very good level of fit of our experimental data. The experimental impedance response of a typical double cation perovskite solar cell (with the same layers, architecture, thicknesses, etc. as described in chapter II) in ambient conditions and under illumination (~1 sun) with an applied voltage V_{DC} of 0.7V and a perturbation voltage of 50mV is shown in Figure IV. 14. The physical meaning of the circuit component and its relation with the PV performances of the solar cell will be discussed in the following parts.

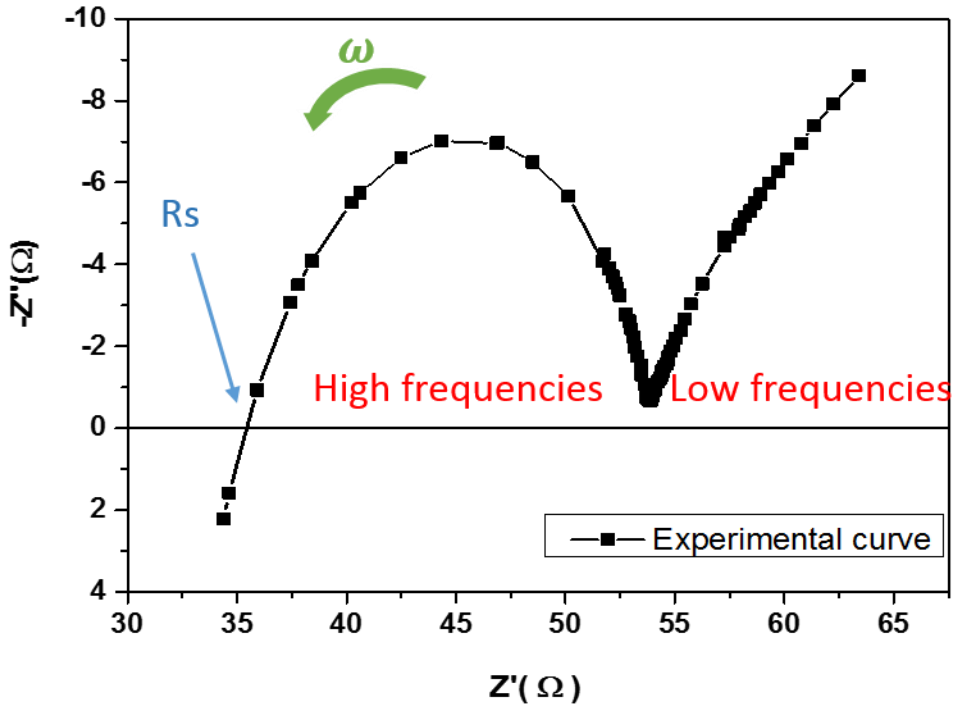

Figure IV. 14: Impedance response of perovskite solar cell

We notice from the IS experimental response of the perovskite solar cell (Figure IV. 14) the presence of two arcs that witness two decoupled relaxation processes. At the intersection point of the graph with the Z' axis at high frequencies, the impedance response is a pure resistance (Z''=0), this resistance is called the series resistance Rs.

To fit the IS response of the perovskite solar cell, it is very important to understand the Nyquist plot of our IS response. Therefore, our graph can be divided into three important regions.

1. Very high-frequency region: Before the Rs point in the Nyquist plot which corresponds to the frequencies between 0.85MHz and 1MHz.
2. High-frequency region: the region characterized by the first arc in the Nyquist plot which corresponds to the frequencies between around 10 kHz and 0.85MHz.
3. Low-frequency region: the region after the high-frequency region, mainly characterized by a second arc in the Nyquist plot which corresponds to the frequencies between 20 Hz and 10 kHz.

To fit this impedance spectrum we have started with a simple type of circuit called Randles circuit as shown in Figure IV. 15. This circuit is composed of a series resistance Rs and two R//C that characterize the two arcs. performing the first optimization of parameters using this model gave the result shown in Figure IV. 15 below.

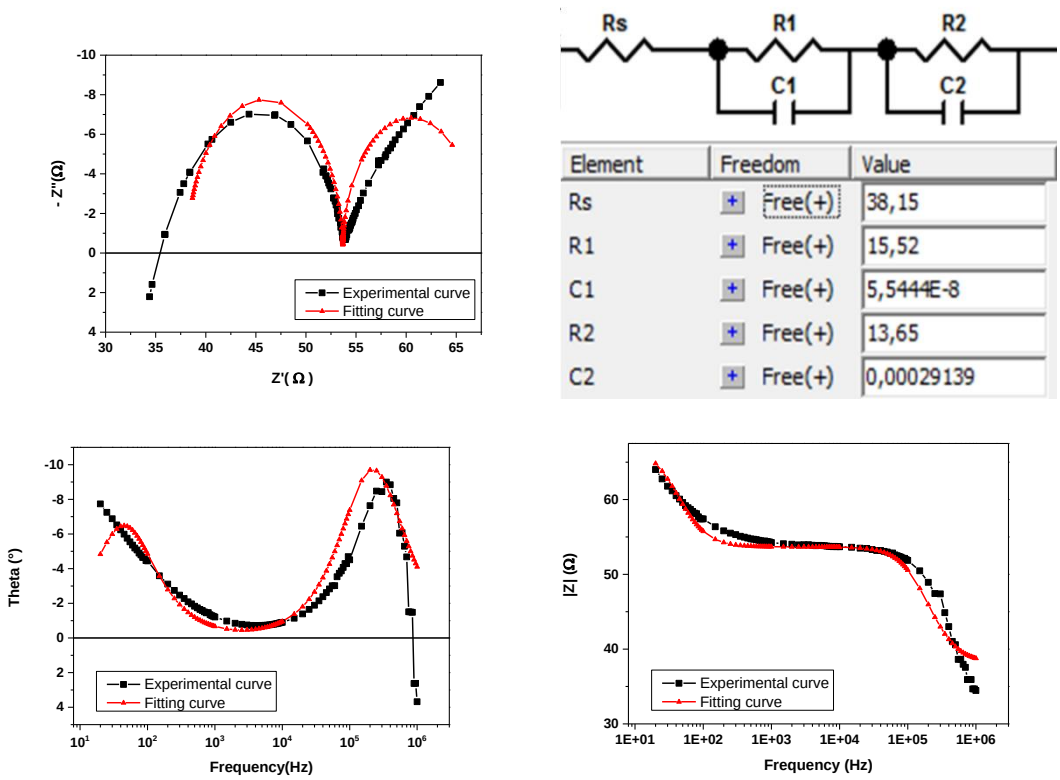

Figure IV. 15: Fitting of impedance response of a perovskite solar cell

From the figures above, we can notice that the fitting is not good and does not reflect the real behavior of the solar cell. Therefore, the electrical model needs to be improved starting by improving and understanding the positive contribution of the imaginary part of the impedance (the inductive part) in the very high-frequency region of the Nyquist plot and trying to model it.

IV.6.1 The inductive part

The intersection point of the graph with the Z' axis at high frequencies (Rs point) characterize a pure resistive behavior of the solar cell, which corresponds to the case where the two capacitances of the Randles model are short-circuited since at high frequencies, Zc = 0 (this capacitive behavior vis-à-vis the frequency is discussed in the following part). The possible two origins of this resistance are whether the resistance of the measured sample or the external resistance due to the measurement set-up components such as the cables, the connection, etc. In our case, the external resistance is removed by the RLC meter during the calibration step before measuring our perovskite solar cells. Therefore this resistance characterizes only the resistance of the sample, specifically, it characterizes the two electrodes of the PSC.

Moreover, our RLC meter can only remove resistive behavior of the external circuit during the calibration, and not inductive or capacitive behavior which means that if the cables or the sample holder have any inductive or capacitive behavior the RLC cannot remove it and it will appear on the impedance spectrum [132] [133]. Furthermore, it was reported in the literature that at very high frequencies the inductive behavior is not related to the measured sample itself but it is an artifact [122] [134] [132]. Therefore this inductive contribution is caused by the same artifact that we have discussed earlier and mainly caused by our old equipment or the connections (cables, sample holder, etc.). Despite the reduction of this artifact, so it won't affect our measurement under illumination as discussed earlier, we were not able to fully remove its contribution and the residual inductive part remains observed in all our IS data. However, while it does not interfere with the solar cell impedance response, we had to account for this contribution in our equivalent electrical circuit by adding an inductance in series in the Randles circuit, as shown in Figure IV. 16 below.

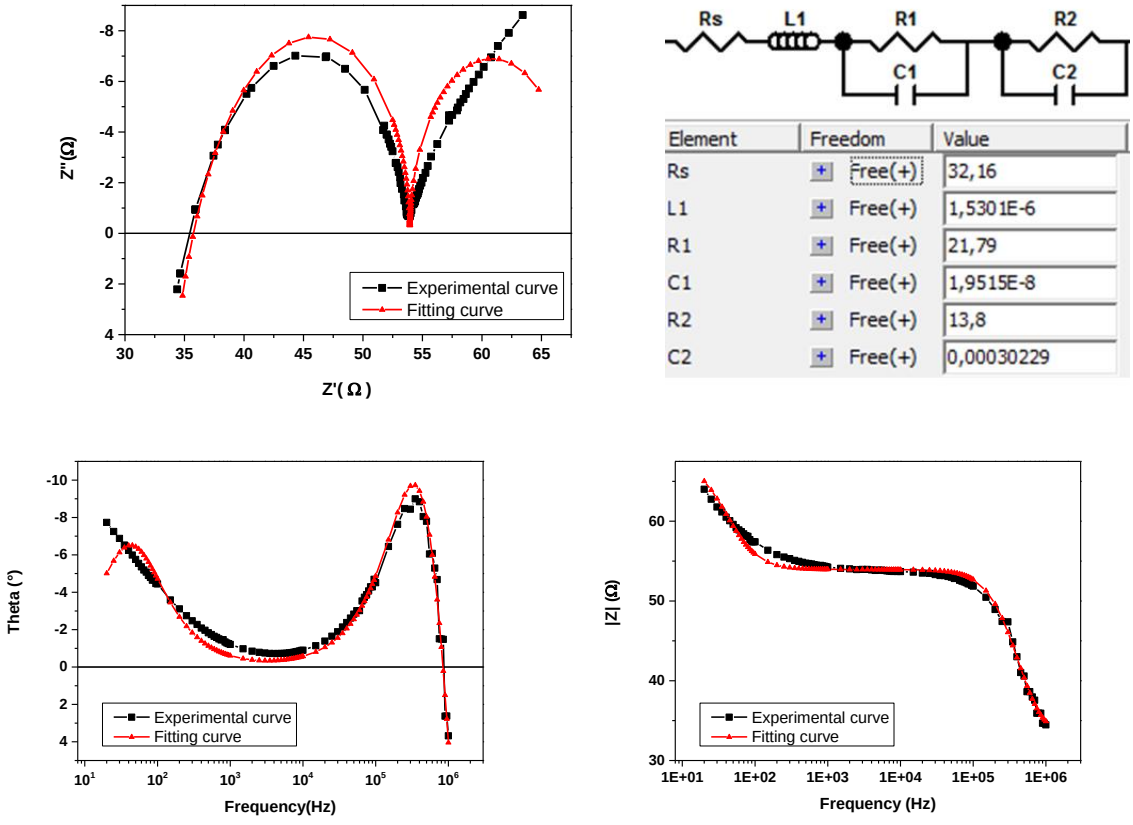

Figure IV. 16: Fitting of impedance response of a perovskite solar cell by adding an inductor

From Figure IV. 16, we can clearly see that adding the inductance improves the fitting in the high-frequency region. The inclusion of this inductance also allows better and accurate extraction of the parameters.

In addition, during this work, we noticed that this inductance value was constant and never changed for different devices or different measurement conditions (especially Vapp), which supports our assumption that it is indeed an artifact.

IV.6.2 Towards a better equivalent circuit for IS data fitting

The last improvements made for the inductive contribution in the Randles circuit presented in the previous section did not enable us to achieve a suitable quality for the fit of the experimental data. Especially, the two relaxation semi-circles are not suitably adjusted by the model, indicating a more complex relation between the components. At this stage, we decided to use another circuit proposed by Garcia-Belmonte's group [135], which is called the Voigt circuit, as shown in Figure IV. 17. This kind of circuit is widely used in the literature to simulate the impedance response of perovskite solar cells [128][127]. This circuit is quite similar to the Randles circuit and can be considered as a special case of the Randles circuit that can improve the of fit non-ideal behaviors (This circuit is generally associated with constant phase element as we well explain in the next part). As shown in Figure IV. 17, C1//R1 model is the high-frequency arc and C2//R2 model is the low-frequency arc.

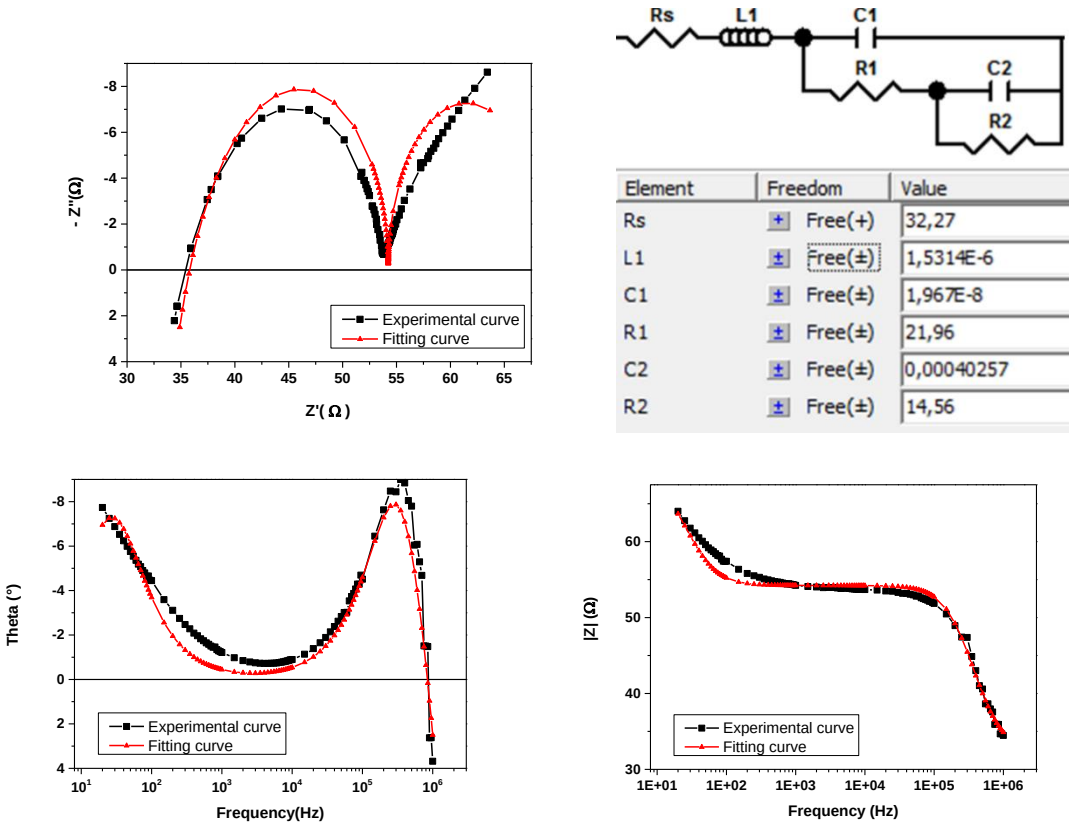

Figure IV. 17: Voigt circuit model

The Voigt circuit model, as its general model (Randles circuit), fails to fit our experimental curves since our solar cells do not show a perfect capacitance behavior. This is a very common feature observed in the field of emerging thin-film solar cells and also in the field of nanostructured materials for electrochemical applications, where real systems behave in a "non-ideal" way.

At this stage, we decided to apply a more complex approach as proposed by Pauporte's group [127], which consists to replace the capacitors of the Voigt circuit model with constant phase elements or CPE.

It is generally admitted that pure capacitances can be replaced by constant phase elements or CPE, which are used to characterize this non-ideal capacitive behavior. From the mathematic point of view, the CPE brings several additional degrees of freedom for the numerical adjustment of the data, and it, therefore, can improve the quality of the fitting. However, it should again be used very cautiously, as we will explain in the next part. Especially, the extraction of real capacitance values from CPE is particularly tricky and should be performed with great care [136].

The CPE, which is a non-intuitive passive circuit element that was created to model non-ideal impedance behavior, has the following impedance expression [137]:

$$Z_{CPE} = \frac{1}{T(j\omega)^P}$$

Where P and T are two parameters.

- If P is equal to 1 the CPE represents an ideal capacitor
- If P is equal to 0 the CPE represents a pure resistor
- If P is equal to -1 the CPE represents an inductor
- If P is equal to 0.5 the CPE represents another element called the Warburg element that models the limitation of the current flow due to the ionic diffusion in a solution (electrolyte). The Warburg element is commonly used in electrochemical impedance spectroscopy to model the impedance response of batteries for example. In our work, we don't need this element.

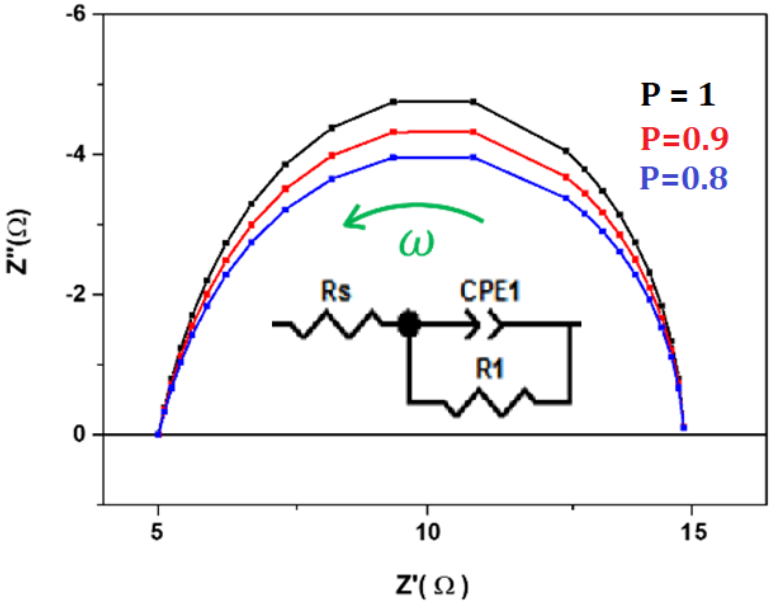

Figure IV. 18: Illustration of the impedance response of a CPE

The capacitance value of CPE called also the effective capacitance can be calculated using Brug's equation [136]:

$$C = \left[T(R_s^{-1} + R_1^{-1})^{(P-1)}\right]^{1/P}$$

Where Rs is the series resistance and R_1 is the resistance in parallel to the CPE as shown in the Figure IV. 18.

The CPE was largely introduced in the simulation of real impedance data of solar cell devices, including dye-sensitized solar cells, organic solar cells, or perovskite solar cells. In all cases, two conditions must be respected while fitting with CPEs:

First, the P of the CPE must have a value between 0.5 and 1 in order to characterize non-ideal capacitors as in solar cells. Sometimes P values above 1 give a very good fitting, however, these values cannot be considered since the CPE does not have any physical signification, such an error can false the capacitance calculation from the CPE.

Second, a large number of CPEs can fit any impedance spectrum, however, this kind of approach does not succeed to describe the physical phenomenon occurring inside the solar cell or any other type of sample in general [138]. Therefore **we should use as few as possible of CPEs to simulate impedance data.**

The non-ideal behavior is mainly due to the nonideal layer morphology such as the surface roughness of the PSC layers or the interface defects and inhomogeneities that lead to inhomogeneous current distribution that can be detected by impedance spectroscopy response [123]. On the Nyquist plot, this phenomenon appears as a “depressed” semicircle that can not be fully represented by an R//C element, however, the CPE is more adapted to model such behavior.

Considering the previous discussioçns, we now present in Figure IV. 19 the optimal IS data fitting using the Voigt circuit based on CPE elements.

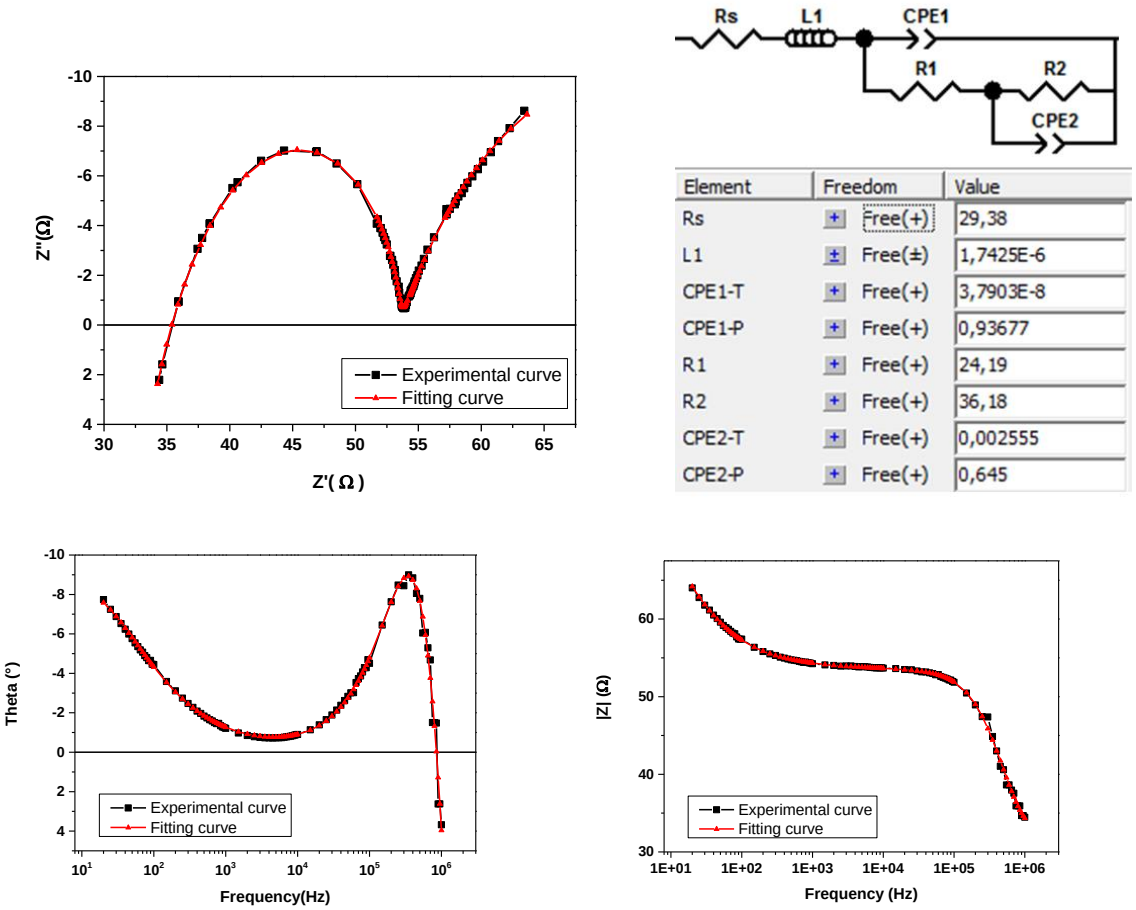

Figure IV. 19: Equivalent circuit employed for fitting the impedance spectra of perovskite solar cells

As we can see in Figure IV. 19, there is an excellent adjustment of our experimental data, both in the Bode representation and in the Nyquist plot. Such high matching was finally observed in all cases presented in this work, and under the different experimental conditions probed. It is indeed crucial to fit the impedance response of all our solar cells, processed using different parameters (see next Chapter) and characterized under different conditions (illumination, applied voltage) with the same electrical model in order to allow relevant comparisons.

IV.7 Understanding the device physics from impedance spectroscopy

From the electrical model, we can extract many parameters that describe the solar cell whether directly, using the extracted circuit components (C, Rs…), or indirectly, by

calculating relaxation times. The electrical model used to fit our solar cells is shown in the figure below:

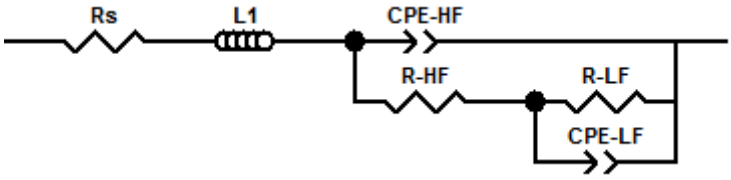

Figure IV. 20: the equivalent circuit used for modeling the impedance response of the PSCs.

The physical origin of all these elements is discussed in the next section, however, we are giving a brief definition of each element as illustrated below.

L1: the inductance related to the high-frequency inductive contribution (measurement artifact not associated with the solar device being tested).

Rs: the series resistance that characterizes the two electrodes

CPE-HF represents the high-frequency capacitive behavior of the device. It allows extracting the high-frequency capacitance (C_{HF}). This non-ideal capacitance is represented by the first arc in the Nyquist diagram. It was reported that this high-frequency capacitance corresponds to the geometrical capacitance of the solar cell [139] [128] [121]. In a first approximation, C_{HF} can therefore be expressed as:

$$C = \frac{\varepsilon_r \varepsilon_0 S}{d}$$

Where $\varepsilon_r$the relative permittivity of the perovskite, ε_0 is the vacuum permittivity (8.85×10^{-12} F/m), S the solar cell surface area and d is the thickness of the perovskite layer.

R-HF: is the high-frequency resistance (R_{HF}), it corresponds to the transport resistance along with the charge transporting layers [139] [128][121].

CPE-LF: is the low-frequency capacitive element that allows extracting the low-frequency capacitance (C_{LF}). In perovskite solar cells, this non-ideal capacitance was found to correspond to the movement of ions in the perovskite layer and their accumulation at the interfaces. This capacitance is intimately associated with the hysteresis phenomenon observed during the JV characterization of perovskite solar cells[140] [128] [121][94].

R2: is the low-frequency resistance (RLF), it represents an estimation of the recombination resistance in the perovskite bulk[140] [128] [121].

Considering the assignment of equivalent circuit elements, we, therefore, can estimate $\tau_{HF,}$ the high-frequency relaxation time and it characterizes a fast relaxation process which is the charge relaxation

$$\tau_{HF} = R_{HF} C_{HF}$$

This relaxation time is, therefore, the most important for VLC, since it can lead to an estimation of the bandwidth. The −3 dB bandwidth ($B_{-3\,dB}$) is given by:

$$B_{-3\,dB} = \frac{1}{2\pi\tau_{HF}}$$

τ_{LF}: This is the low-frequency relaxation time and it characterizes a slow relaxation process which is the ionic relaxation occurring in the perovskite layer. τ_{LF} can be expressed by:

$$\tau_{LF} = R_{LF} C_{LF}$$

The following table shows the different solar cell parameters extracted by impedance spectroscopy under illumination and with a DC voltage of 0.8:

Parameter	L	RS	R_{LF}	C_{LF}	τ_{LF}	R_{HF}	C_{HF}	τ_{HF}	B_{-3db}
Unity	H	Ω	Ω	F	S	Ω	F	S	kHz
Value	$1.7\ 10^{-6}$	29.38	36.16	$6.9\ 10^{-4}$	0.025	24.19	$1.5\ 10^{-8}$	$3.6\ 10^{-7}$	443.6

Table IV. 1: the dynamic parameters of a typical PSC obtained by IS

From Table IV. 1 we can clearly see the big difference between the values of the two relaxation times τ_{LF}, τ_{HF} that reflects the slow relaxation process taking place at low frequencies and the fast relaxation process taking place at high frequencies. This big difference between τ_{LF} and τ_{HF} (4 orders of magnitude) is related to the gap between the values of C_{LF} and C_{HF} (4 orders of magnitude) since R_{LF} and R_{HF} are from the same order of magnitude. The parameters values estimated by IS correspond to what was found in the literature on PSC (see the complete comparison in chapter V). Moreover, the estimated bandwidth also corresponds to the bandwidth reported by Mica et al. [12] therefore this bandwidth can easily give a data rate above 30mbps (see the complete comparison in the Annex).

IV.8 The relation between the bandwidth and equivalent circuit of the solar cell

The equivalent circuit of a solar cell shown in chapter II only models the solar cell under static conditions (constant illumination). However, the equivalent circuit may change due to the presence of the capacitive effect that occurs inside of the SC under dynamic conditions.

It was reported that the solar cell behaves as a low pass filter under a dynamic regime (AC) [3][12], which means that the solar cell let passes only signals with frequencies lower than the cutoff frequency f_c , and attenuate all signals above f_c as shown in Figure IV. 21.

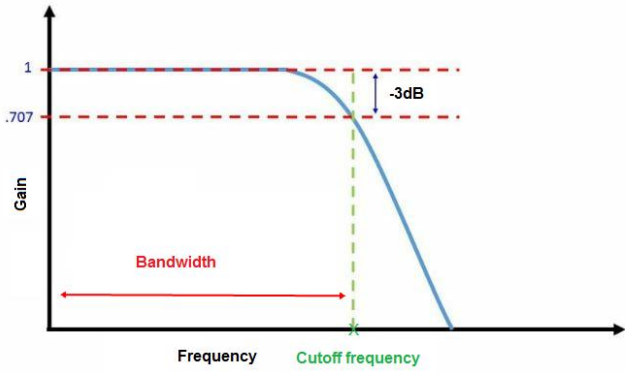

Figure IV. 21: Low pass filter response

It is common for VLC systems to estimate the cutoff frequency and the bandwidth at 3db which means that the frequency for which the gain value of the output reduces by 3 dB from the nominal passband value. In low pass filters, the cutoff frequency is equal to the value of the bandwidth.

For solar cells the bandwidth and the cutoff frequency are dominated by a capacitance C and a resistance R and can be defined as [12]:

$$B_{-3\,dB} = f_c = \frac{\omega_c}{2\pi} = \frac{1}{2\pi R_T C_T} \quad (V.1),$$

From the equation below and as reported in the literature, the bandwidth is limited by the RC time constant. Therefore, it is important to understand the physical origin of R and C and to decouple the resistive and capacitive effects happening inside the solar cell.

The following circuit has been proposed to model the low pass filter behavior of the solar cell under dynamic conditions [141].

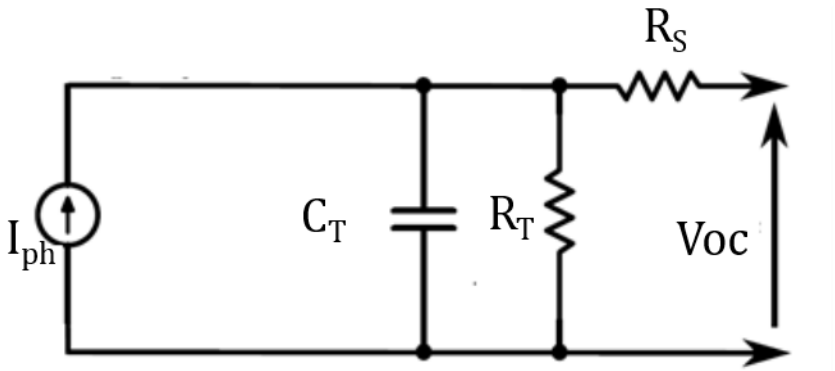

Figure IV. 22: AC simplified equivalent circuit

Where the capacitor C_T characterizes the different capacitive mechanisms occurring inside of the solar cell such as the geometrical capacitance or the chemical capacitance (explained in the next part). The resistor R_T models the different resistive mechanisms occurring in the solar cell under the dynamic regime such as the recombination resistance, or the charge transfer resistance. All these contributions will be defined in the next sections.

As stipulated earlier, impedance spectroscopy is a powerful technic that can allow us to discriminate which type of capacitance dominates the solar cell response, and which type of capacitance and resistance limits the bandwidth.

Bisquert et al. have demonstrated that for perovskite, dye-sensitized, and organic solar cells there are three types of relaxation occurring in solar cells and related to 3 different capacitive effects [121], whereas these three capacitances **don't work in the same range of frequency** as shown in Figure IV. 23.

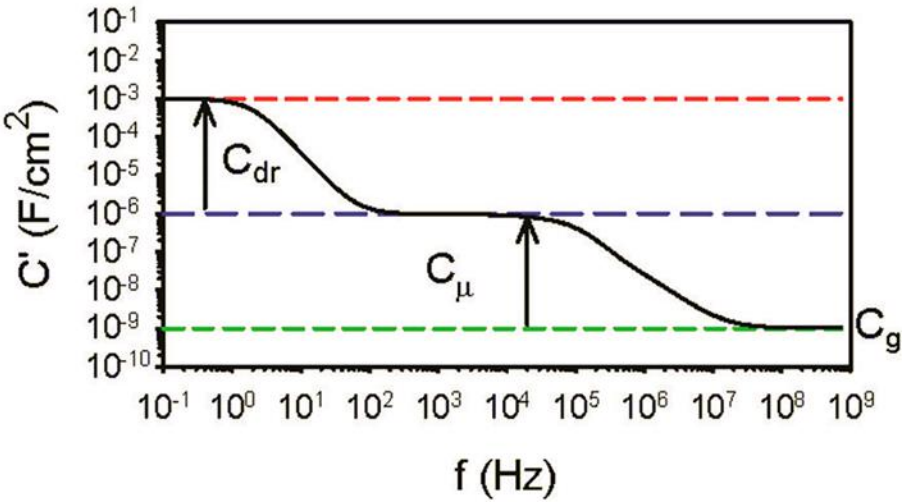

Figure IV. 23: The capacitance of the solar cell as a function of frequency obtained by simulation [121]

Figure IV. 23 represents the capacitive behavior of the solar (or the total capacitance C_T) that can be dominated by three different capacitances: dielectric relaxation capacitance C_{dr}, the chemical capacitance C_{μ}, and the geometric capacitance C_g. From Figure IV. 23, we can see clearly that $C_g << C_{\mu} << C_{dr}$ which causes that the three capacitances don't work in the same frequency domain as we will explain more in the next part.

- At very low frequencies (second timescale), the capacitance of the solar cell is dominated by the capacitance called the dielectric relaxation capacitance C_{dr}. This capacitance (that we can also name C_{VLF}) was introduced, for the first time, by Juan Bisquert works in 2014 [121], however, we don't observe this type of capacitance experimentally in perovskite or organic solar cells, especially that we probe at very low frequencies (we stop only at 20 HZ) therefore this capacitance would not be considered in our equivalent circuit.
- At low frequencies (millisecond to the second timescale): In perovskite solar cells, the low-frequency capacitance has gained a lot of interest since it is responsible for the electrical hysteresis observed during solar cell characterization in reverse and forward scans. The origin of this capacitance was attributed mainly to the migration of ionic species (mainly charged defects such as halide vacations) present in the perovskite layer [131] [94] [140] [128] [121][93]. The capacitance of the solar cell at low frequencies can be dominated by whether the chemical capacitance Cμ or the double layer capacitance C_{dl} (as in our case).

1. The chemical capacitance C_μ (also called diffusion capacitance) is more observed in dye-sensitized solar cells (DSSC) than in perovskite devices. However, this capacitance has been observed in some PSCs with mesoporous TiO_2 ETL. The origin of this capacitance in perovskite solar cells remains uncertain, however, it can be related whether to the movement of ions in the perovskite bulk or to the trapped charge in the mesoporous TiO_2 interface which creates a sort of a depletion region that causes a displacement of the Fermi level in the bandgap [142] [139]. When the solar cell is under a reverse bias, the width of this depletion region gets smaller which decreases C_μ, whereas, under a forward bias and at some point C_μ increase exponentially as shown in Figure IV. 24 [142] [139] [143].
2. The double-layer capacitance C_{dl}: When the ions accumulate on the interface surface of the perovskite layer, they create a sort of layer between the interface and the perovskite layer. This capacitance is called the double layer capacitance or Helmholtz capacitance C_{hz} or even sometimes the surface capacitance C_s. This capacitance can be more present in a planar structure. In our case, we will call it the low-frequency capacitance C_{LF} as we will show that it mainly contributes to the low-frequency regime. Moreover, this capacitance shows a specific feature: the accumulation of charges (ions) on the perovskite interfaces is not homogenous due to defects and the roughness of the interface or even the difference in shape and size of the ionic defects that accumulate randomly on the interface surface. This causes a nonuniformity of the charge distribution, and by consequence. The impedance response of C_{dl} is, therefore, better modeled using a CPE, to account for this non-ideality of the relaxation kinetics. In fact, the CPE has been created to module this kind of double-layer capacitance that accumulates on the electrodes of batteries.

The two capacitances (C_μ and $C_{LF} = C_{dl}$) behave differently as a function of applied voltage. The double-layer capacitance slightly increases near to the Voc (generally one or two orders of magnitude). However, the chemical capacitance increases exponentially and reaches very high values especially around the Voc, in fact, it can increase by 6 orders of magnitude [139] [130][144][127][131], this behavior allows us to differentiate the two types of capacitance while extracting C_{LF} at different voltages[131].

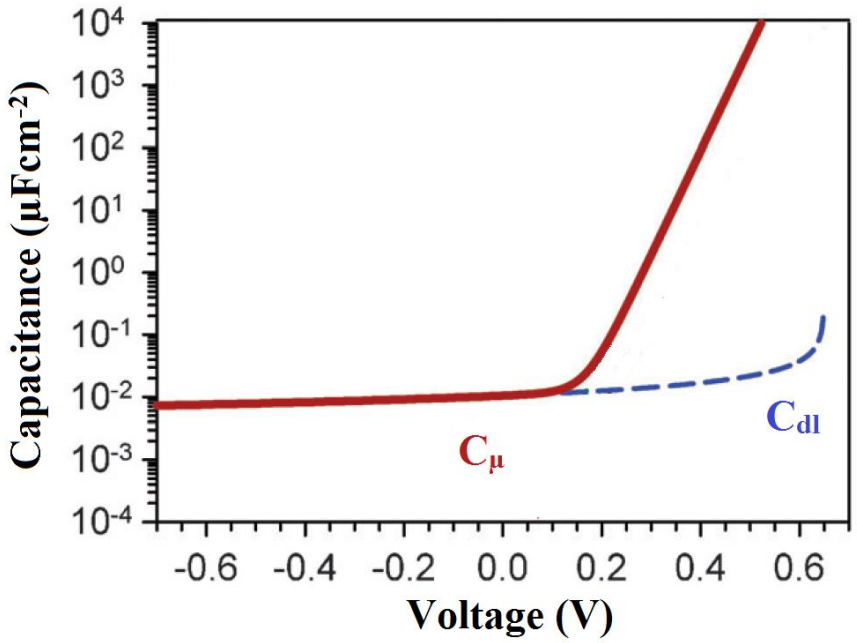

Figure IV. 24: Comparison between the chemical capacitance and the double layer capacitance

The relaxation process associated with C_{LF} is represented by the second arc of the impedance spectrum and characterized by the relaxation time constant τ_{LF}. This process is slow, generally in the millisecond regime.

$$\tau_{LF} = R_{rec}C_{LF}\ (V.2),$$

The resistance associated with this relaxation is called the recombination resistance R_{rec}, it describes the band-to-band recombination mechanism occurring in the perovskite bulk [145]. Therefore, R_{rec} is inversely proportional to the recombination rate which means that the higher R_{rec} is better for the solar cell. R_{rec} also integrates a direct contribution from the shunt resistance, as direct current flow through, leakages can be seen as recombination events.

From a VLC perspective, this low-frequency relaxation is not a limiting factor since these slow mechanisms are not playing any role at high frequencies when the modulation frequency is much faster than their characteristic kinetics. Therefore, the low-frequency relaxation process does not have any direct impact on the bandwidth. However, from a photovoltaic perspective, this relaxation process is very important since it can describe the nature of the perovskite layer such as the ionic movement responsible for the hysteresis effect and the recombination rate that can limit the power conversion efficiency of the PSCs.

- At high frequency (microsecond timescale[131]), the total capacitance of the solar cell is dominated by its geometric capacitance C_g, which is **always the lowest capacitance value** compared to C_μ or C_{dl}. Consequently, the relaxation process related to this capacitance is the fastest one. This relaxation process is also attributed to the charge transfer resistance R_{ct} which is a complex resistance since it gathers many contributions. This resistance can be assigned to the recombination and the losses occurring in the ETL, the HTL, and their interfaces, it is basically related to the nature of the charge transporting layers, their thicknesses, the diffusion length of the electrons and holes, the traps and defects present in the interface, etc. However, this high-frequency resistance can be more complex in mesoporous structures (e.i. mesoporous TiO_2) since it can combine more contributions, such as the nature and the size of the perovskite and its interaction with the mesoporous titania network [127].

At high frequencies, the total capacitance C_T of the solar cell is dominated by the geometric capacitance C_{geo} when its corresponding relaxation process takes place. Consequently, we can conclude that the cutoff frequency and the bandwidth of the perovskite solar cell are determined by this high-frequency relaxation as shown in the following equation:

$$B_{-3\,dB} = f_c = \frac{\omega_c}{2\pi} = \frac{1}{2\pi R_T C_T} = \frac{1}{2\pi R_{HF} C_{HF}} \quad (V.3),$$

Where $\mathbf{R_T = R_{HF} = R_{ct}}$ and $\mathbf{C_T = C_{HF} = C_{geo}}$

This conclusion is supported by the work of Mica et al. [12] where the geometric capacitance was estimated using this equation.

The typical equivalent circuit of a SC that decouples the capacitance and the resistance was reported in the literature as shown in Figure IV. 25 [141]. It dissociates the different types of capacitance and resistance that can contribute to the AC regime. This model should be slightly adjusted to take account of the nature of the capacitive behavior solar cell, in light of our precedent discussion about the different contributions to the resistances and capacitances.

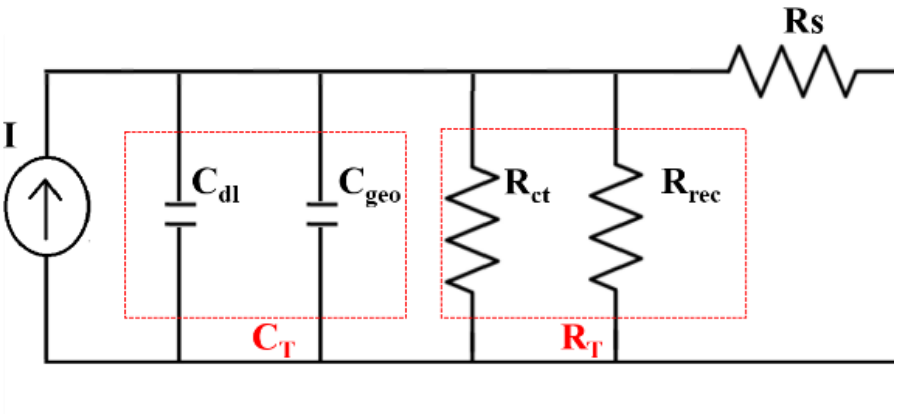

Figure IV. 25: Typical AC equivalent circuit reported in the literature [141]

From a physical viewpoint, we cannot consider this kind of circuit as descriptive for the real behavior of the solar cell under a dynamic regime. In other words, we do not agree with this kind of circuit since the capacitive effects modeled by the two capacitors must be in series and not in parallel for the following two reasons:

The tow capacitances of the solar cell cannot be in parallel due to the big difference between them (3 to 4 orders of magnitude), therefore they are not working in the same frequency domaine (Figure IV. 26), as reported many times in the literature of the impedance spectroscopy [146] [125].

The physical reason behind this behavior is due to the fact that the capacitive behavior of the solar cell is dominated by the capacitive scaling as shown in Figure IV. 26. In other words, the two capacitances do not have the same order of magnitude therefore every capacitance occurs in a specific and different frequency domain. To clarify this behavior, we measure the reactance X, which is the opposition to the current flow of a circuit element, of the two capacitors using our experimental values extracted by IS, (the same behavior is observed using the values reported in the literature):

1. The low-frequency capacitance C_{LF}, represented physically by C_{dl} with a value of around 6.9 10^{-4} F
2. The high-frequency capacitance $C_{HF,}$ represented physically by C_g with a value of 1.5 10^{-8} F

The reactance X of a capacitor is defined by the following equation:

$$X = \frac{1}{C\omega} = \frac{1}{2\pi f C} \ (V.4),$$

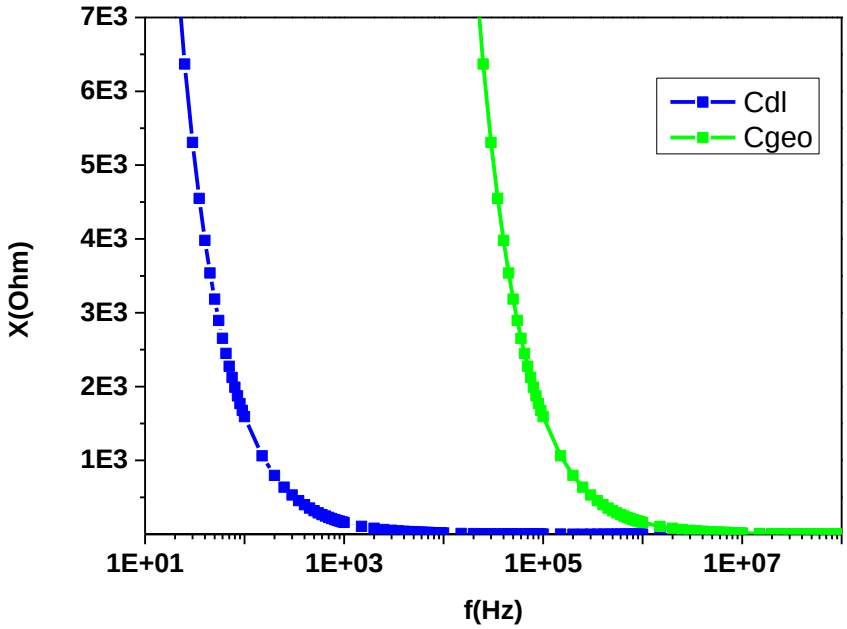

Figure IV. 26:: The simulate reactance of the two capacitances C_{dl} C_{geo} as a function of the frequency

From the graph above we notice that every capacitor work in a specific frequency domain. Lower than this frequency domain, the reactance is getting higher exponentially, which means that X is very high and no current can flow, in other words, the capacitor behaves as an open circuit. At higher frequencies, X will drop exponentially (~ 0) meaning that there is no resistance to the current flow, in other words, the capacitor is short-circuited and behaves as a conductor [147].

This concept is illustrated in Figure IV. 27 where we can see the behavior of the capacitor in a low pass filter at low and high frequencies and at the working frequency domain.

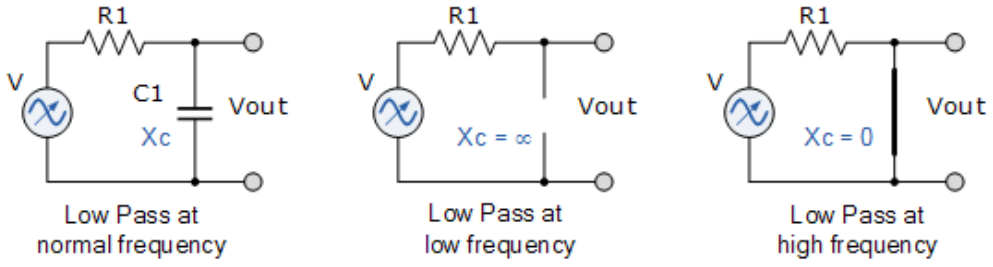

Figure IV. 27: This capacitive behavior in low pass filters with the frequency variation [148]

So we can conclude that every capacitor that models an intern capacitance effect of the solar cell has a specific frequency domain where it is functional, above this frequency, the capacitor behaves as a short circuit, and below this domain, the capacitor behaves as an open circuit. This frequency domain is mainly related to the capacitance value, and when the capacitance gets higher the frequency domain shifts to the low frequencies.

Therefore, the frequency-domain, where the capacitor is operating, is determined by the capacitance value, thus if we want that the capacitor work in higher frequencies we should reduce its capacitance value. Therefore, if we reduce the capacitance value of the C_{geo} we can push the solar cell to work at higher frequencies which will increase the cutoff frequency and the bandwidth.

Based on what said previously, we then conclude that C_{dl} will react as a short circuit at high frequencies since its (X ~0). By consequence, the whole circuit proposed in the literature would be short-circuited as shown in Figure IV. 28. Meaning that this circuit cannot reflect the real behavior of the solar cell in a dynamic regime.

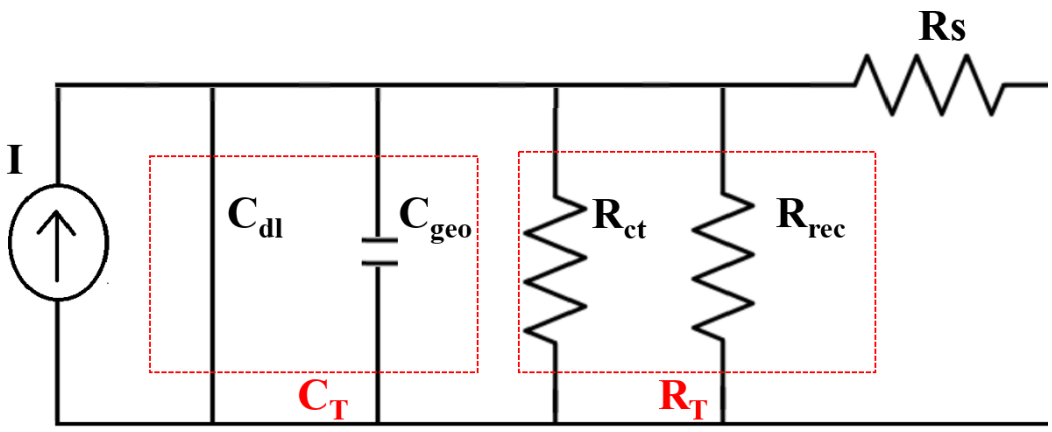

Figure IV. 28: The AC (low signals) parallel circuit of the solar cell at high frequencies

This can be also demonstrated from the equation $(V.3)$ that shows that at high frequencies (where f_c is calculated) C_T =Cg.

And we know from IS theory that $C_{geo} \ll C_{dl}$ [121] [122] (in other words: $C_{HF} \ll C_{LF}$) wich is also confirmed by All our IS mesurment (see chapter V) where our C_{HF} values are from the order of $\approx 10^{-8}$ and C_{LF} are from the order of $\approx 10^{-4}$ (see Table IV. 1), Therefore:

- If the two capacitances are in parallel as in the proposed circuit: $C_T = C_{geo} + C_{dl}$ and knowing that $C_{geo} \ll C_{dl}$ thus $C_T \approx C_{dl}$, (Numerically : $C_T = 10^{-8} + 10^{-4} \approx 10^{-4}$) which is not true since $C_T \approx C_{geo}$ as shown earlier.
- If the two capacitances are in series as it should be:

$$\frac{1}{C_T} = \frac{1}{C_{geo}} + \frac{1}{C_{dl}}$$

- Knowing that $C_{geo} \ll C_{dl}$ $thus$ $C_T \approx C_{geo}$ which is true since $C_T \approx C_{geo}$ as shown earlier.

  (Numerically: $\frac{1}{C_T} = 10^8 + 10^4 \approx 10^8$ so $C_T \approx 10^{-8}$)

In conclusion, the two capacitances (C_{geo} and C_{dl}) **must be put in series not in parallel**, in any proposed equivalent circuit that characterizes the dynamic response of the solar cell, to avoid the shortcircuit of the whole equivalent circuit in the high-frequency region.

Accordingly, we can propose a correction of the initial circuit that respects this conclusion and reflects the dynamic behavior of the solar cell by putting the capacitances in series (see Figure IV. 29).

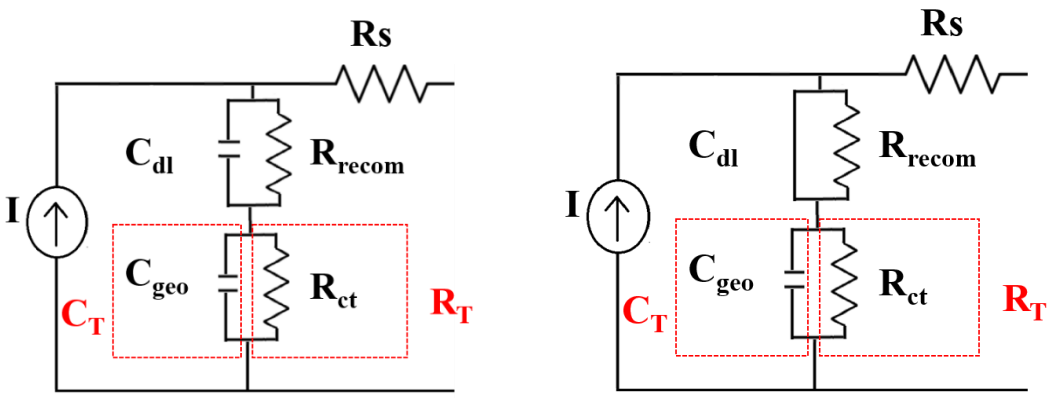

Figure IV. 29: The AC equivalent circuit of the solar cell (left) at high frequencies conditions (right)

Therefore, in high frequencies, C_{dl} behaves as a short circuit however that would not affect the solar cells, and the total capacitance C_T would be equal to C_{geo} as shown in Figure IV. 29 which is in good agreement with the equation $(V.3)$.

Finally, the equivalent circuit that models the solar cell AC behavior at high frequencies, which is relevant for VLC application can be represented as shown in the figure below.

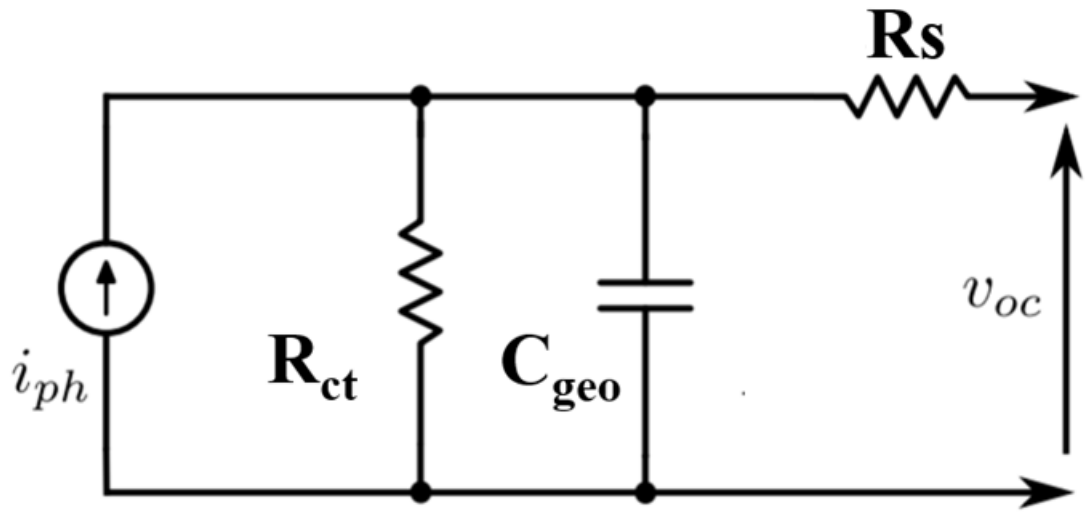

Figure IV. 30: AC equivalent circuit of a solar cell for VLC applications

This circuit is proposed based on our understanding of the dynamic behavior of the PSCs as probed by impedance spectroscopy. Doing so, we were able to identify the physical origin of each component, and we believe that our equivalent circuit is, therefore, more accurate than reported cases, where the series and shunt resistances (Rs, Rsh) are considered even they were also extracted from the curves measured in steady-state conditions (the Rsh is usually neglected in the literature since it is too small compared to Rd [149]). The estimation of these two resistances from static measurements can be quite different than the estimation made from IS (where the Rs is not exactly the series resistance of the solar cells defined in the one-diode model). Noticeably the dynamic resistance Rd that limits the dynamic response of the solar cell (τ = Cd Rd) is the charge transfer resistance that can be measured by IS.

IV.9 Conclusion

In this chapter, we have illustrated our strategy towards reliable impedance spectroscopy measurement that takes into consideration the proper conditions of the experimental measurement as well as the more adapted way to simulate and cautiously interpret the experimental results.

We have illustrated the potential of IS As a strong technique that provides a deeper understanding of the physical properties behind the dynamic behavior of the solar cells. Moreover IS allows measuring the bandwidth of the solar cells via measuring the relaxation time at high frequencies as well as its two resistive and capacitive components which is extremely important for the optical wireless communications field.

Finally, we have also proposed a new equivalent circuit that models the solar cell dynamic behavior. In addition, impedance spectroscopy measurement allows us to estimate the exact values of each component of this circuit therefore this could be useful for the simulation of PSC in a VLC system. All the components of this circuit determine the quality of the signal detection of the solar cell. Therefore all these components can be tuned, via studying and modifying the structural properties of the solar cell, in such a way to improve their VLC performances (bandwidth, S/N, Gain, etc.).

In our case, we are focusing on studying the impact of the structural properties of the PSC, (such as the interfacial layers, the thickness of the absorber, etc.) on the value of the bandwidth as illustrated in the next chapter.

Chapter V - Dynamic response of perovskite solar cells

V.1 The effect of the voltage on the PV and VLC parameters of the solar cell

One of the important concerns in VLC using solar cells is to find the optimal working point to have the maximum energy harvesting and the higher bandwidth. In solar cells used for energy harvesting, the optimal working point is defined under V_{max}, which is the applied potential where the solar cell produces the maximum power (P_{max}) under illumination. To define this point, we calculate the density of power for each voltage using the following equation:

$$P = V * J\ (V.5),$$

The following figure represents the power generated by a double cation perovskite solar cell as a function of voltage and its JV characteristics. The spectral correction was not applied to the Jsc performance measurements, leading to a slight overestimation (around 10%) of our short-circuit currents, which is acceptable since it does not impact the trend.

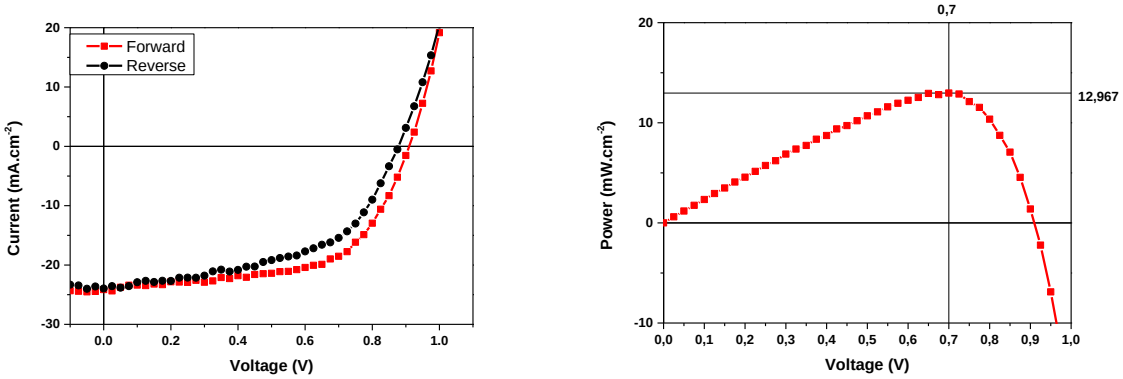

Figure V. 1: J(V) and P(V) curves of a typical double cation perovskite solar cell

Scan direction	Voc(V)	Jsc(mA.cm^{-2})	FF	PCE(%)
Reverse	**0.90**	**24.1**	**0.60**	**12.9**
Forward	**0.87**	**23.3**	**0.54**	**10.9**

Table V. 1: The photovoltaic parameters of a typical mixed cation PSC

An average solar cell gives the performances shown in Figure V. 1 (the standard deviation of this solar cell correspond to what has been reported in chapter III), where the maximum of

power generated by the solar cell is 12.96 mW.cm^{-2}, which correspond to a voltage of 0.7 V. Obviously, around 0 V and Voc, the generated power is very low, whereas the maximum power generated by this PSC can be obtained between 0.6V and 0.75V. It is now important to investigate the dynamic behavior of the device as a function of the applied voltage, in order to assess if a fast modulation bandwidth can be found in the region where the energy harvesting is optimal. Thus, we will estimate the high-frequency time constant τ_{HF} and the bandwidth over different voltages.

To investigate the VLC properties of the perovskite solar cell under different voltages, we perform impedance spectroscopy measurement under the same conditions described in chapter IV (1 Sun, AC perturbation of 50mV, measuring from 20Hz to 1MHz, etc.) and with variating the DC applied voltage (from 0.1 to 0.9V). The IS measurement under different DC voltages is widely used in the IS field since it is extremely useful to study solar cell behavior under dynamic conditions which gives more in-depth information about the different physical mechanisms and processes occurring inside of the solar cell. The impedance spectroscopy response of the double cation PSC under different applied voltages is represented in Figure V. 2.

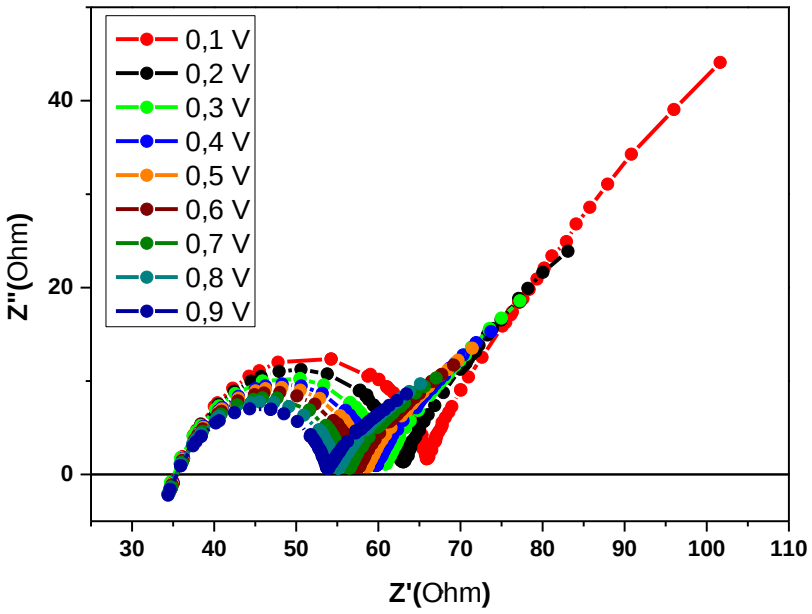

Figure V. 2: The impedance response of a PSC under different applied voltages

As mentioned in chapter IV this graph represents the Nyquist plot of the IS response of the perovskite solar cell under different voltages. Noticeably there is a change in the shape of the curves with the changing of the voltages since we can see the two arcs that characterize the two relaxation processes (see chapter IV). However, they are getting smaller with the increasing voltage. The Rs seems unchanged with the applied voltage, unlike R_{HF} which decreases as the potential increases.

Every impedance spectrum is fitted using the same equivalent circuit mentioned in chapter IV, where all the parameters are extracted (L, R_s, C_{HF}, C_{LF}, R_{HF}, R_{LF}, τ_{HF}, τ_{LF}, BW) for each voltage.

Among the different parameters that can be extracted from impedance spectroscopy (Rs, C_{HF}, C_{LF} …), and considering the scope of this work, we will more focus on the parameters relevant for VLC signal detection, which are C_{HF} and R_{HF} since they represent the two components of the high-frequency relaxation process that limits the bandwidth as explained earlier. However, the other parameters, and especially C_{LF} and R_{LF}, are more in-depth discussed in the following part as they bring more insight into device physics.

The variation of high-frequency capacitance C_{HF} and low-frequency capacitance C_{LF} under different applied voltages are represented in Figure V. 3.

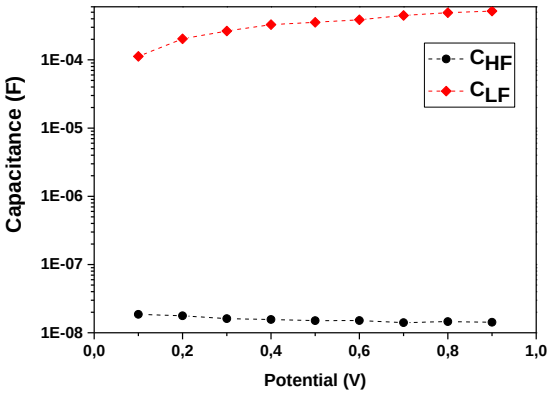

Figure V. 3: The high and low-frequency capacitances of PSCs as a function of the applied voltage

Noticeably, C_{LF} is lower by 4 orders of magnitude than C_{HF} and this difference is preserved for all applied voltages. Therefore, the two capacitances do not operate in the same frequency domain (as explained in chapter IV) no matter the value of the applied voltage. This can be

directly observed in the Nyquist plot where we can see that the two arcs, related to the high and low-frequency relaxations, are present with the same shape under all voltages.

From Figure V. 3 we can notice that the high-frequency C_{HF} capacitance (the geometric capacitance) slightly decreases from 18.6 nF to 14.2 nF with the increasing voltage. On the opposite, the low-frequency capacitance C_{LF} remarkably increases from 0.11 mF to 0.51 mF. The increase of C_{LF} is not pronounced (not an exponential increase) as in the chemical capacitance, hence, this low-frequency capacitance C_{LF} characterize physically the double-layer capacitance C_{dl}.

The low-frequency capacitance is related to the hysteresis behavior of the PSC [94][93] [140] [128] [121], this behavior reduces the PV performances of the solar cell however, it has no direct impact on the data detection performance and does not affect the bandwidth since the only capacitance used for the estimation of the bandwidth is the geometric capacitance. More details about the relation between C_{LF} and hysteresis are given in the following parts.

The resistive parameters extracted by impedance spectroscopy are represented in the graph below.

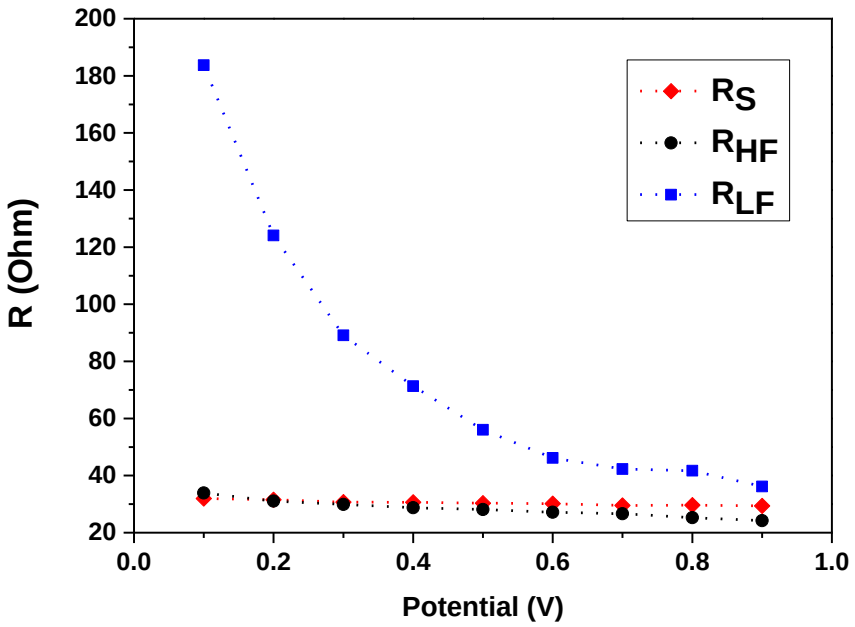

Figure V. 4: The resistive parameters of a PCS as a function of the applied voltage

The Series resistance Rs that can be mainly attributed to the electrodes (gold and FTO) is found almost constant for all applied voltages at approximately 30 Ω. This behavior differs compared to the high-frequency resistance R_{HF} that tends to slightly decrease at high voltages (from 33.9 Ω to 21.1Ω). The low-frequency resistance R_{LF} scales with the applied voltage as shown in Figure V. 4 it decreases with the increasing voltage which is in good agreement with what was found in the literature [150]. The decline of R_{LF} corresponds to the increase of recombination rate which makes sense because at Voc there is no current flowing in the solar cell therefore the generated charges tend to recombine. On the other side, at 0 V (Jsc) the current flow is maximum and the recombination rate is the lowest.

The high-frequency resistance R_{HF} is complex as it gathers many contributions, especially from the charge transporting layers. R_{HF} has been mainly assigned to the charge transfer resistance. Therefore, it has been shown that this resistance can vary by changing the type of HTL used in the PSC (Spiro-OMeTAD, P3HT, etc.), the HTM doping level, the type of ETL (TiO_2, ZnO, Cds…), or even the thickness of the TiO_2 blocking layer and its crystallinity [128][129][130][131]. Moreover, it was demonstrated that changing the nature of the perovskite active layer (MAPI, CsFAMAPbIBr, FAMAPbIBr, etc.) can affect R_{HF} through important contributions from the Perovskite/HTL and perovskite/ETL interfaces [150]. This suggests that all these parameters, which are directly associated with the device architecture, can affect the device bandwidth through the R_{HF} resistance. The origin of the reduction of R_{HF} near Voc can be assigned to the low charge density flowing through the interfacial layers which reduces the charge recombination. The small reduction of R_{LF} resistance near Voc does reflect a high recombination rate in the perovskite bulk (as a lower R_{LF} is compatible with a higher recombination rate, as explained in the previous parts). This makes sense since, under Voc conditions, photo-generated charges can only decay through band-to-band recombination.

The relaxation times of the two relaxation processes (at high and low frequencies) under a variated applied voltage are represented in Figure V. 5.

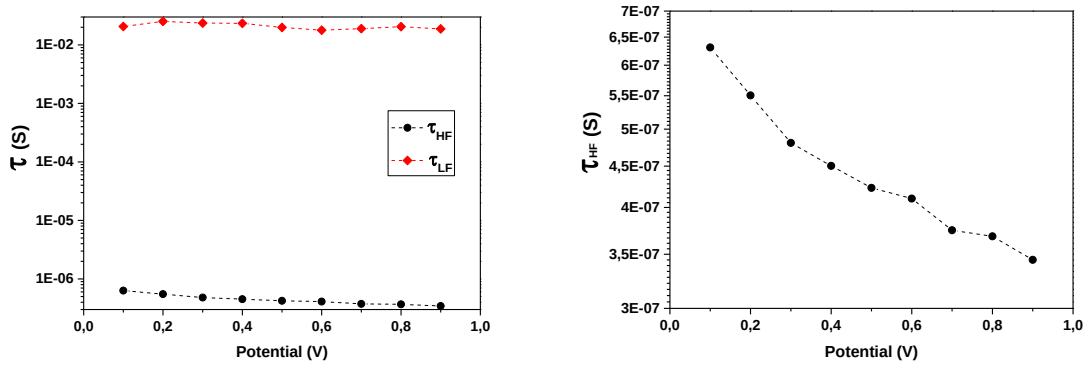

Figure V. 5: The relaxation times at high and low frequencies as a function of the applied voltage

These two physical relaxation processes are occurring in different frequency domains. The high-frequency relaxation time (τ_{HF}) is lower than the low-frequency one (τ_{LF}) by 5 orders of magnitude, which is a direct consequence of the corresponding capacitance values. From the physical point of view, this is expected as the relaxation process of electrons and holes should be much faster than the slow relaxation process associated with ionic species, as discussed earlier.

In fact, τ_{LF} and the two associated elements R_{LF} and C_{LF} are preferentially discussed in the literature since they give more in-depth information about device physics targeting the photovoltaic energy conversion only. This relaxation time is assigned to the ionic diffusion in the perovskite bulk and their accumulation in the interface. On the other hand, high-frequency relaxation is less studied, although it is crucial for VLC applications.

The high-frequency relaxation process is mainly limited by the geometric capacitance of the device. While the geometry is crucial (thicknesses and active area), the effective dielectric response of the sandwich device plays a crucial role in this response as well. Consequently, the intrinsic dielectric relaxation of the perovskite bulk, but also of the different layers and interfaces can contribute to this relaxation process. τ_{HF} is voltage-dependent since it decreases with the increasing voltage from 0.63 µs (at 0.1 V) to 0.34 µs (at 0.9 V). This variation may appear small, however, it is very significant in terms of bandwidth since a simple calculation of bandwidth gives a variation of 252 kHz (at 0.1 V) to 462 kHz (at 0.9 V). One main aspect of device physics towards the OWC application is that the bandwidth is voltage-dependent as shown in Figure V. 6.

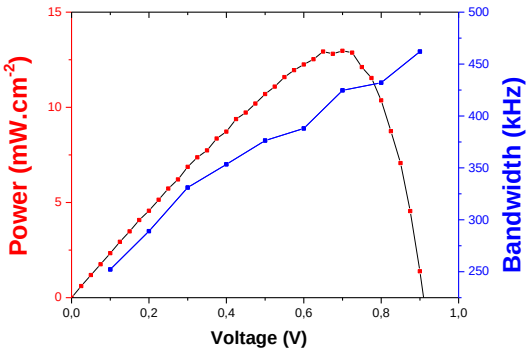

Figure V. 6: The bandwidth and the generated power of a PSC as a function of the applied voltage

It increases almost linearly with the applied voltage. In this figure, the maximum power point of the perovskite solar cell (Vmax = 0.7V) corresponds to a bandwidth of 424 kHz, which appears to be a significant value compared to the bandwidth of devices tested for this application in the literature.

We can conclude that the optimal working point of the solar cell corresponds to a good value of the bandwidth, however, we should avoid making the solar cell work at low voltages since both the generated power and the bandwidth are low. Moreover, we must avoid making the solar cell work at voltages close to the Voc even if it gives the maximum bandwidth since the power that can be generated by the solar cell would be too low. In such a case, the solar cell cannot be used for signal detection and energy harvesting simultaneously (only signal detection), however the influence of a reception circuit (load) is a crucial aspect which is not addressed in the thesis here, but it can be the next logical step of the process [151].

Likewise, other parameters can be probed, for instance, the effect of the intensity of light on the dynamic response of the solar cells. This preliminary study was conducted and shows the light dependency of the charge transfer resistance and the huge impact of the intensity of light on the bandwidth (see annex).

V.2 Perovskite solar cell as a band-pass filter

As shown in the previous sections, at low frequencies, the capacitance of the solar cell is dominated by C_{LF}, which corresponds to the low-frequency relaxation process, no meter the applied voltage. By consequence, this low-frequency relaxation process, associated with the

slow response time τ_{LF}, can limit the response of the solar cell at low frequencies. This means that the perovskite solar cell behaves as a bandpass filter. In this section, we are trying to investigate the impact of this low-frequency contribution on the bandwidth of the perovskite solar cell.

For the remainder, the bandpass filter attenuates the signal above the higher cutoff frequency f_H and below the lower cutoff frequency f_L, as shown in Figure V. 7, it can be seen in a simple way as the combination of a high pass filter and low pass filter. A simple bandpass filter is constituted by two resistors (R1, R2) and two capacitors (C1, C2) where C2<<C1. The frequency response of the bandpass filter is represented in the figure below.

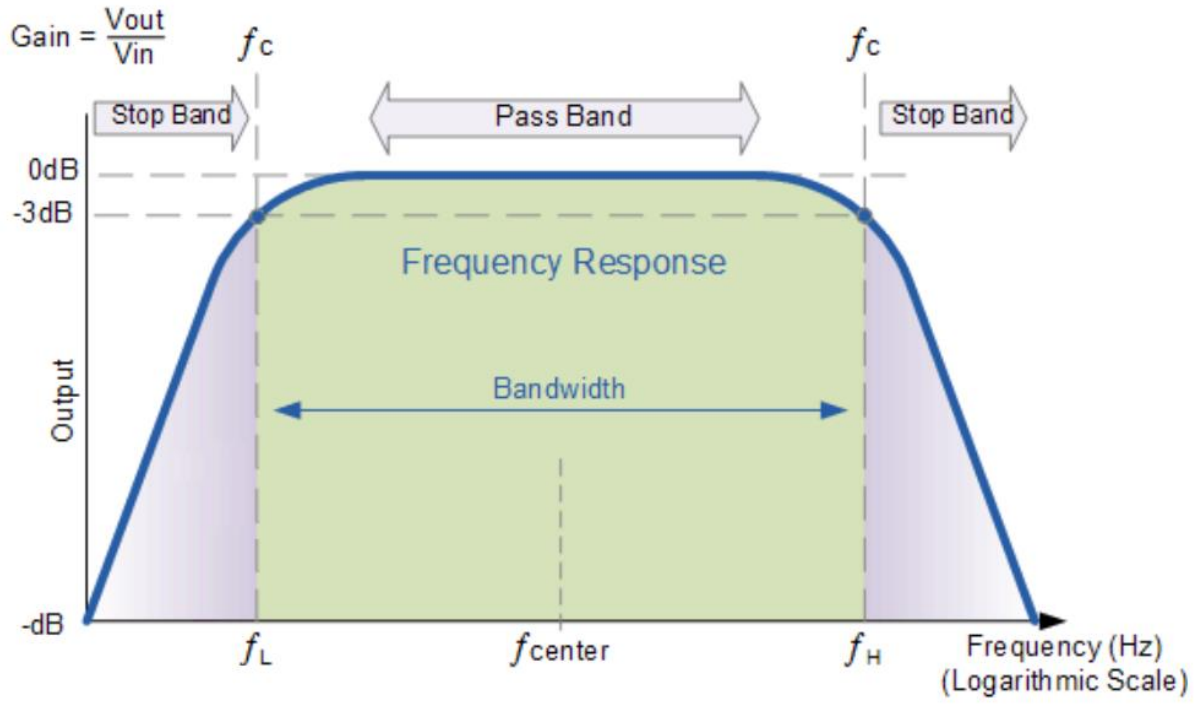

Figure V. 7:: Band-pass filter response [152]

The bandwidth of the band-pass filter is:

$$B_{-3\,dB} = f_H - f_L$$

At high frequencies, the band-pass filter behaves as a low-pass filter and attenuate all the frequencies higher than f_H. f_H is related to R_2 and C_2, which are the dominant capacitance and resistance at high frequencies.

$$f_H = \frac{1}{2\pi R_2 C_2}$$

At low frequencies, the bandpass filter behaves as a highpass filter and attenuate all the frequencies lower than f_L. f_L is related to R_1 and C_2, which are the dominant capacitance and resistance at low frequencies.

$$f_L = \frac{1}{2\pi R_1 C_1}$$

Notice that C_1 and C_2 do not operate in the same frequency domain in order to have a significant bandwidth, in other words, if C_1 and C_2 have the same order of magnitude (and R1, R2 already have the same order of magnitude) the bandwidth will be too small or even insignificant.

In perovskite solar cells, C_{LF} and R_{LF} are similar to C1 and R1, and C_{HF}, R_{HF} are similar to C2 , R2. By consequence, the bandwidth of the PSC will be defined as:

$$B_{-3\,dB} = f_H - f_L$$

Where, f_H is what we called earlier f_c is described for PSCs as:

$$f_H = \frac{1}{2\pi R_{HF} C_{HF}} = \frac{1}{2\pi \tau_{HF}}$$

f_L is described for PSCs as:

$$f_L = \frac{1}{2\pi R_{LF} C_{LF}} = \frac{1}{2\pi \tau_{LF}}$$

We considered previously that $B_{-3\,dB} = f_H$ because we were considering the solar cell as a lowpass filter, however, IS results show another relaxation time τ_{LF} that may limit the bandwidth.

The following graph illustrates the values of f_L and f_H for our double cation perovskite solar cell, which is calculated from our estimation of τ_{LF} and τ_{LF} based on our results of IS.

The values of τ_{LF} are too high compared to τ_{HF} (Figure V. 5) since the relaxation process at high frequencies is way faster than the relaxation process at low frequencies as explained earlier, hence the values of f_L are way smaller than the values of f_H as shown in Figure V. 8.

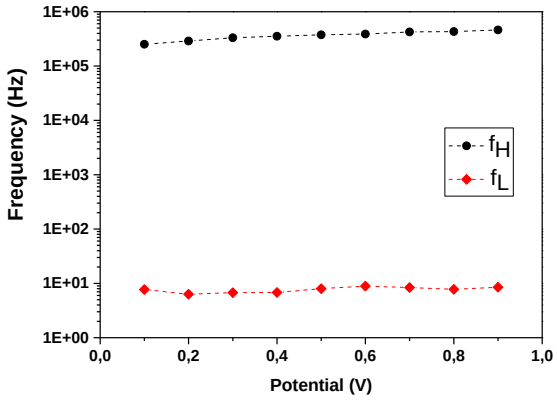

Figure V. 8: the high and low cutoff frequencies of a PSC estimated by IS.

Noticeably the values of f_L are smaller by 5 orders of magnitude than f_H, and this difference is respected over the different values of the applied voltage. Thus, we can neglect f_L in our estimation of the bandwidth.

$$B_{-3\,dB} \approx f_H$$

For instance at 0.7 V $f_L = 8.4\,Hz$ and $f_H = 432 \times 10^3\,Hz$ hence,

$$B_{-3\,dB} = (432 \times 10^3) - 8.4 \approx 432 \times 10^3\,Hz$$

We can conclude that the appearance of the second relaxation in the impedance spectrum signifies that the perovskite solar cell behaves as a band-pass filter under dynamic conditions. However, we still can consider it as a low-pass filter as long as $\tau_{HF} << \tau_{LF}$. This behavior is mainly dominated by the big difference of the capacitance values $C_{HF} << C_{LF}$, hence, if C_{LF} gets too small and has values close to C_{HF} the bandwidth value will be reduced. In such a case, the low-frequency capacitance can have a considerable impact on the value of the bandwidth.

In the case where there is just one arc in the impedance spectrum (as in organic solar cells) the solar cell behaves as a low-pass filter since there is just one relaxation process that can limit the BW.

V.2.1 Conclusion

The PSC behaves as a bandpass filter, therefore, its bandwidth can be affected by the low-frequency contribution. Thus, related physical phenomenons such as the double-layer capacitance or the recombination resistance can affect the bandwidth. However, in our case,

we still consider the PSC as a lowpass filter since the value of the low cutoff frequency f_L is too small and can be neglected.

The bandpass filter behavior of the perovskite solar cells (unlike organic solar cells) can be beneficial for signal detection since it can cut off the low-frequency signal noises which could reduce the N/S ratio. Hence, the value of f_L can be tuned, via changing the structural properties of PSC, to meet an eventual need for specific bandpass filters in the VLC field.

Knowing that all the parameters (C_{HF}, R_{HF}, C_{LF}, R_{LF}) can be affected by the structural properties it is, therefore, possible to improve the signal detection and the PV performances via modifying or improving the device structure.

In our case, we are focusing on studying the impact of the structural properties of the PSC, (such as the interfacial layers, the thickness of the absorber, etc.) on the high-frequency response of the solar cell as illustrated in the next sections.

V.3 Triple cation perovskite solar cells, planar VS mesoporous structure

Considering the outputs of the previous parts, we investigate in this section the potential influence of the nature of the perovskite active layer on the device bandwidth. As explained in chapter II, triple cation perovskite solar cells based for example on the $Cs_{0.05}(MA_{0.17}FA_{0.83})_{0.95}Pb(I_{0.83}Br_{0.17})_3$ composition, are widely studied in the literature due to their excellent photovoltaic performance. This kind of perovskite is usually deposited on top of a TiO_2 mesoporous layer (ETL), leading to a so-called mesoscopic perovskite device. However, Planar PSCs based on Tin (IV) oxide (SnO_2) have shown better advantages (see chapter II).

In this part, we are investigating the dynamic performance of SnO_2 planar PSCs using impedance spectroscopy, and we are trying to make a preliminary comparison with data published on mesoscopic PSCs based on TiO_2, as reported by the Pauporté's group in 2018 (Wang et al.) [127]. Such comparison, even if it has to be considered as preliminary, already gives interesting trends in light of our previous discussion regarding the dynamic limitation of devices at high frequency and the influence of materials and architectures.

Both our solar cells and those of Wang et al. are quite identical, with the same type of perovskite, the same thickness of the layers, etc. The major difference is therefore the nature

of the electron transporting layer as shown in Table V. 2. Our devices are using a planar SnO_2 ETL whereas the Pauporte group is using a mesoporous TiO_2 ETL (mesoporous structure) deposited on top of a thin TiO_2 blocking layer, the role of this layer is to prevent any contact between the perovskite and the FTO.

	Transparent electrode	ETL	Perovskite	HTL	Top electrode
Planar SnO_2 structure	FTO	SnO_2	$CsFAMAPb(IBr)_3$	spiro-OMeTAD	Gold
Mesoporous TiO_2 structure	FTO	TiO_2 mesoporous + TiO_2 compact	$CsFAMAPb(IBr)_3$	spiro-OMeTAD	Gold

Table V. 2: Triple cation perovskite solar cell structure ()

First, we start by comparing the PV parameters of the two types of solar cells obtained by measuring the J(V) curves under the same conditions. The spectral correction was not applied to the Jsc performance measurements, leading to a slight overestimation (around 10%) of our short-circuit currents, which is acceptable since it does not impact the trend.

	Scan direction	Voc(V)	Jsc($mA.cm^{-2}$)	FF	PCE(%)
Planar structure	Reverse	0.90	26.81	0.56	13.56
	Forward	0.86	25.70	0.49	11.11
Mesoporous structure	Reverse	1.01	21.99	0.74	16.51
	Forward	1.01	22.62	0.60	13.90

Table V. 3: The photovoltaic parameters of Triple cation perovskite solar cell with mesoporous and planar structures

As we can see from the table above that the performances of our planner solar cells are lower than the ones reported in the literature (mesoporous). This is mainly due to their higher Voc and FF of the mesoporous devices, which could probably be related to the efficient charge extraction of the TiO2 mesoporous layer. Our Jsc seems to be high which could be partially related to the mismatch factor that has been reevaluated ever since and found to be from the

order of 1.1 which corresponds to an overestimation of the Jsc of around 10% which is acceptable since it does not impact the trend. (the real values of the Jsc can be around 24.13 and 23.13 mA.cm^{-2} for the reverse and forward respectively).

Despite this mismatch issue, the Jsc of the planar structure is still higher than the mesoporous one. This could witness a better charge transfer and lower losses in the planar structure. (IS can help verify this hypothesis)

Next, the IS response of our planar PSC is compared to the response of mesoporous PSCs reported by Wang et al. All the solar cells are measured under the same lighting conditions ~1 sun and under different voltages (from 0.2V to 0.9V). However, the surface of the solar cells are slightly different, our planar PSCs have a surface area of 0.2 cm^2 vs 0.24 cm^2 for the mesoporous PSCs. Both types of solar cells are giving IS response of the same type, with two arcs that characterize the two relaxation processes at high and low frequencies. Thereafter, the IS spectrums are fitted using the same equivalent circuit discussed in chapter V, where the capacitive effects are modeled using constant phase elements CPEs. All the capacitance values are extracted from the CPE using the equation mentioned in chapter IV.

Figure V. 9 shows the variation of the high-frequency capacitance with the applied voltage for the two PSC types. To see if the difference in the surface area can affect the results we have measured the density of capacitance by dividing the capacitance values over the surface area of each device accordingly.

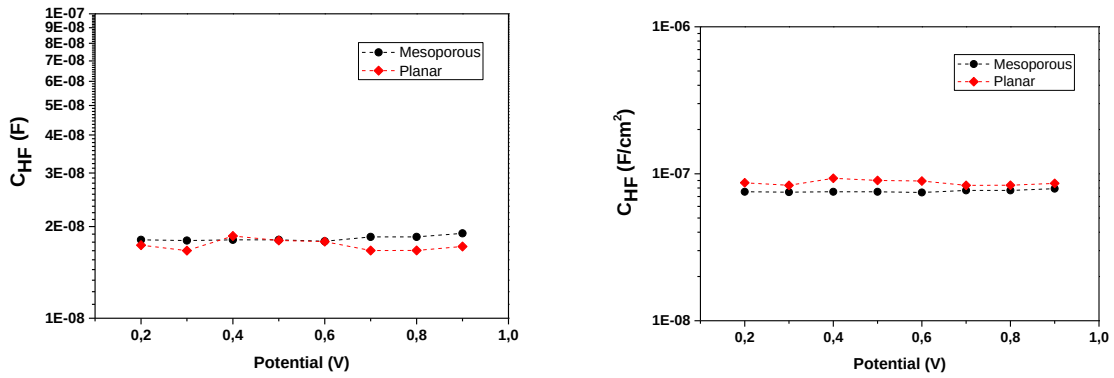

Figure V. 9: The high-frequency capacitance C_{HF} as a function of the applied voltage

At high frequencies, we see a very close capacitance for both types of cells, and for all applied voltage. This observation confirms the fact that the high-frequency capacitance is indeed dominated by geometric capacitance. The values of both mesoporous and planar

structures are quite similar, and they scale with the active area as it is expected from such a geometric contribution to the effective capacitance. The similarity of the geometric capacitance values was expected due to the fact that we are using approximatively the same perovskite surface and the same thickness (~450 nm), and we have the same dielectric constant since we are using the same type of perovskite ($Cs_{0.05}(MA_{0.17}FA_{0.83})_{0.95}Pb(I_{0.83}Br_{0.17})_3$). Noticeably, the geometric capacitance is not affected by the nature of the electron transporting layer (either mesoporous TiO_2 or planar SnO_2 at least), which is not the case for the low-frequency resistance R_{HF}, as shown in Figure V. 10.

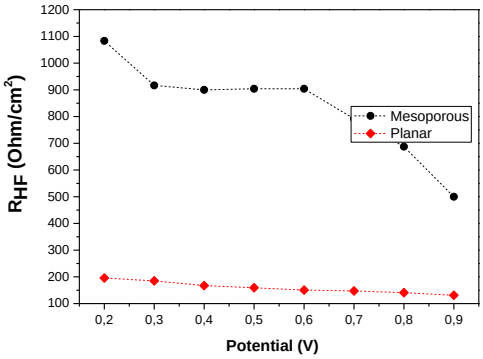

Figure V. 10: The high frequency resistance R_{HF} as a function of the applied voltage

From Figure V. 10 we notice that there is a huge difference in the high-frequency resistance RHF between the planar SnO_2 device (around 100-200 Ω/cm²) and the mesoporous device (between 500 and 1100 Ω/cm²). The R_{HF} of the planar PSC is one order of magnitude lower than that of the mesoporous PCSs. As explained earlier, the R_{HF} is associated with the charge transfer resistance (R_{ct}). The exact origin of this element remains quite complex, as it includes many contributions (recombinations associated with structural defects, trap states, etc.). However, this resistance is generally considered as an indicator of the losses occurring inside the transporting layers and their interfaces with the perovskite active layers (and the contacts). Therefore, the mesoporous TiO_2 ETL is clearly detrimental to this high-frequency resistance, illustrating more intense charge losses. Such behavior is quite expected for mesoporous layers based on nanocrystalline metal oxide layers as their limitation from trapping and de-trapping events were largely discussed in the field of dye-sensitized solar cells for example [153][154]. This could be related to the morphology of mesoporous TiO_2 ETL since in mesoporous TiO_2 there is more contact with the perovskite which is beneficial for the charge extraction however there are more defects and traps in the interface [155]

[156]. In addition, the perovskite penetration in the pores can be not perfect due to the size of the perovskite or the perovskite solution viscosity, or the size of the TiO_2 pores, etc., which can create more defects and nonuniformity on the interface. Moreover, the TiO_2 cannot be used alone, it needs a blocking layer (TiO_2 compact) that prevents the perovskite to have contact with the FTO. This leads to an additional interface between the mesoporous TiO_2 and the compact TiO_2, this additional interface can also increase the charge transfer resistance R_{ct}. The lower R_{HF} (or R_{ct}) of planar SnO_2 can be related to its higher mobility and electron conductivity comparing to TiO_2[95] [98].

The higher R_{HF} (or R_{ct}) of the mesoporous TiO_2 PCSs compared to the planar SnO_2 device supports our previous hypothesis, where, the mesoporous PSC show Jsc around 22 $mA.cm^{-2}$ compared to 24 $mA.cm^{-2}$ for the planar structure. This could be due to the better transport properties of the planar SnO_2 as observed by IS, since the R_{ct} contributes to the total series resistance, and when R_{ct} gets higher the series resistance gets higher and by consequence, the Jsc gets lower.

R_{HF} is decreasing with the applied voltage for both mesoporous structure and planar structures, it goes from 195 Ω/cm² to 131 Ω/cm² for planar structure and from 1083 Ω/cm² to 500 Ω/cm² for mesoporous structure. This tendency does not change while diving on the respective surfaces arias for each device.

Finally, the high-frequency relaxation time (τ_{HF}) is the plot for both cells in Figure V.24, as well as the associated device bandwidth.

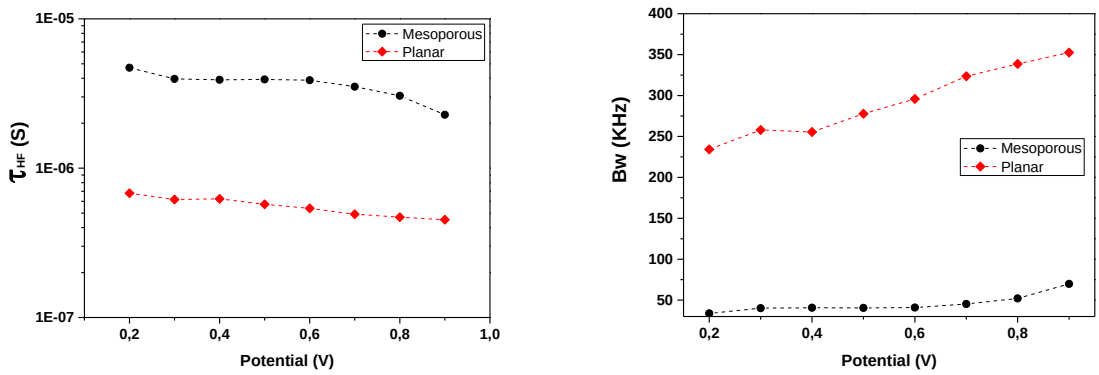

Figure V. 11: The high-frequency relaxation time (left) and the bandwidth (right), as a function of the applied voltage

As expected, the difference between R_{ct} of the planar and mesoporous device is reported by τ_{HF}, as both types of cells share the same high-frequency capacitance values. The planar device shows a relaxation time that is one order of magnitude lower than that of the mesoporous device. Consequently, the bandwidth of the planar device is much larger than that of the mesoscopic cell.

The decreasing of R_{HF} with the applied voltage is the reason behind the decreasing of the high-frequency relaxation time constant τ_{HF} since C_{HF} is quite constant. Hence, the bandwidth gets higher with the increasing voltage.

The bandwidth values for mesoporous PSC start increasing from Voc, going from ~35 kHz to ~70 kHz. In a similar way, the bandwidth of the planar SnO_2 PSC reaches a value of 340 kHz at high applied voltages.

The increase of bandwidth around Voc is mainly related to the drop of the charge transfer resistance. Around Voc, the effective current flowing in the device is close to zero, leading to a minimum impact of charge transport losses at the interfaces and through charge transporting layers.

At low frequencies, the C_{LF} of both types of solar cells is increasing due to the charge accumulation in the perovskite interfaces (with ETL and HTL) (see Figure V.25). We remind that this capacitance is associated with the double layer capacitance C_{dl}, while there is no evidence for a contribution from a chemical capacitance observed, as generally observed in the literature [127]. When the applied voltage increases (at low frequency), more ionic species will migrate towards the active layer interfaces. Their accumulation significantly increases C_{LF}.

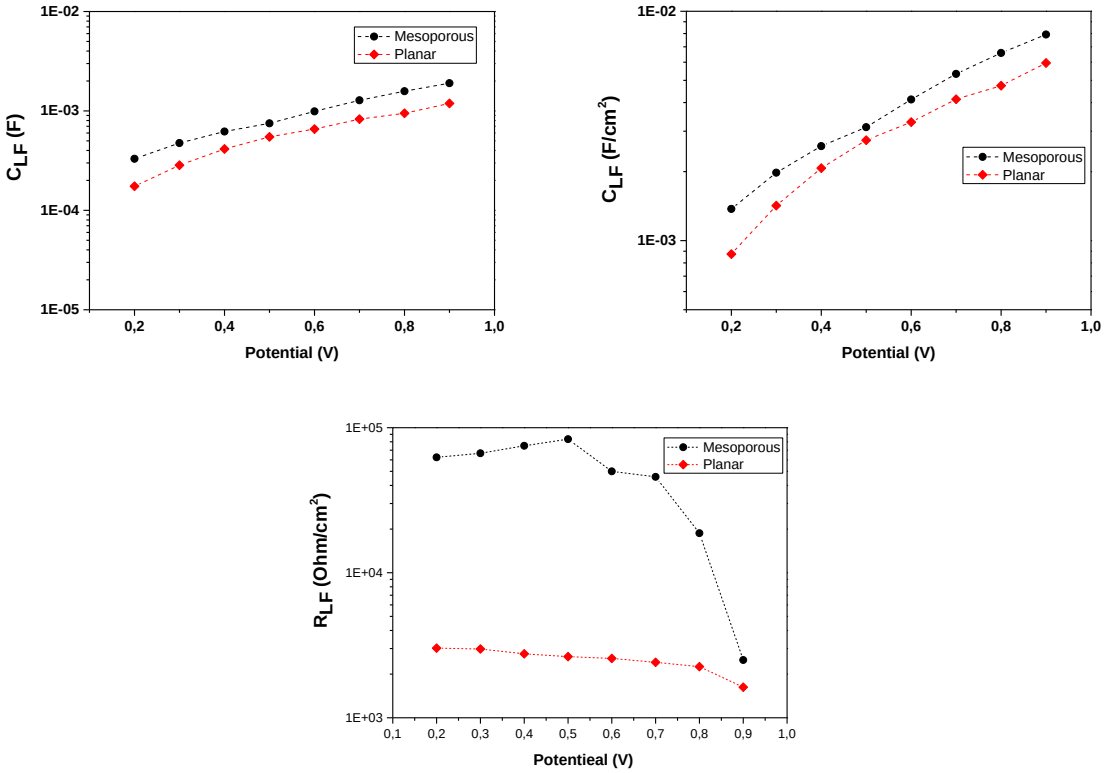

Figure V. 12: C_{LF} and R_{LF} as a function of the applied voltage

The low-frequency capacitance of the planar structure is slightly lower, which generally implies that the hysteresis effect of the planar structure should be slightly lower, as reported in the literature. We cannot verify this hypothesis since we do not have the exact PV parameters of the specific mesoporous PSC that gives this IS response we only have the average PV parameters of many solar cells. The hysteresis index (HI) of the average mesoporous PCSs is 15% which is close to the HI of our planar PSC measured by IS 18%.

At low frequencies, the resistance R_{LF} (which was mainly attributed to the recombination resistance Rrec inside of the perovskite bulk as explained in the previous section) is lower for the planar PSC than for the mesoscopic one. This means that the recombination rate in the planar PSC is higher when probed at low frequencies. This makes sense because the mesoporous TiO_2 has better charge extraction properties, which will reduce the recombination occurring in the perovskite bulk. This could be also the reason why the mesoporous structure has a higher Voc.

Based on the estimated low-frequency parameters, the corresponding relaxation time at low-frequency (τ_{LF}) witnesses the slow relaxation process of the ionic migration in the perovskite

layer. While faster kinetics is observed for the planar device, τ_{LF} remains much smaller than τ_{HF} for both devices. Therefore, it does not affect the bandwidth estimation made previously.

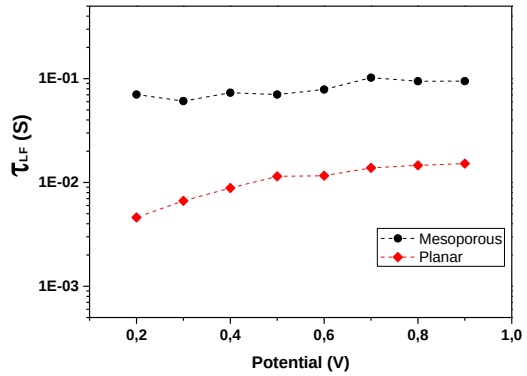

Figure V. 13: the low-frequency relaxation time as a function of the applied voltage

V.3.1 Conclusion

Finally, from this section, we can conclude that the nature of the ETL does not remarkably affect the geometric capacitance probed at high frequency (C_{HF} or C_{geo}) by IS, whereas the charge transfer resistance (R_{ct} or R_{HF}) is significantly impacted by this change. Furthermore, the mesoporous PSCs, and despite their high PV performance, are not adapted for VLC application due to their extremely low bandwidth that is caused by their high charge transfer resistance, whereas planar perovskite structures are more adapted for such an application.

V.4 Double Vs triple cation perovskite solar cells

In this part, we are comparing the PV and the dynamic performances of triple cation PSCs ($Cs_{0.05}(MA_{0.17}FA_{0.83})_{0.95}Pb(I_{0.83}Br_{0.17})_3$ to simplify we call it CsFAMA perovskite) and double cation PSCs ($FA_{0.85}Cs_{0.15}P(I_{0.85}Br_{0.15})_3$ to simplify we call it CsFA perovskite) in order to understand the impact of the intrinsic properties of the perovskite layer on the dynamic response of the solar cells. We remind that both perovskites are deposited on the same substrate (FTO/SnO2) And covered by the same layers (Spiro-OMeTAD /Au) using the same dimensions and architecture, as described in chapter II.

In this section, we tend to emphasize the high-frequency response in light of the aimed application. Whereas, we will discuss the low-frequency response that gives complementary information about the physical nature of the PSC, notably the hysteresis effect which is a

crucial aspect that needs to be reduced in order to have exploitable devices for this application. However, we will not go in-depth addressing this specific point.

V.4.1 XRD

X-ray diffraction (XRD) was conducted to investigate the quality of the perovskite films, we compare the XRD patterns of double and triple cation perovskite layers, deposited on top of SnO_2/FTO substrates, as it is crucial to keep the conditions similar to those of the final devices considering the strong sensitivity of halide perovskite to the growing conditions. The XRD patterns are shown in Figure V. 14.

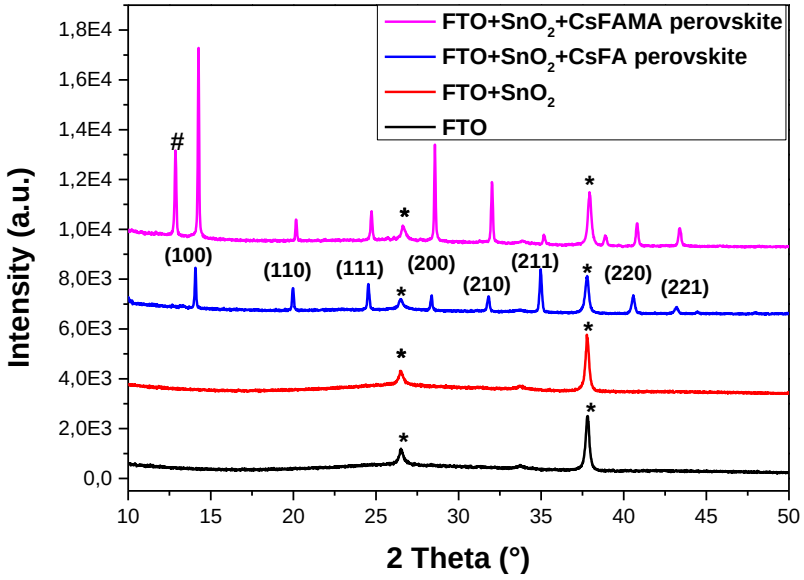

Figure V. 14: XRD patterns of double and triple cations perovskite deposited on top of SnO_2/FTO substrate

The FTO substrate shows only two diffraction peaks at 26.5° and 37.7° whereas the SnO_2 layer does not exhibit any diffraction peak, this could be due to the low thickness of the SnO_2 layer which makes it invisible for XRD.

For both perovskite films, we can observe the typical perovskite peak around 14° that witnesses the black α-phase of the formamidinium-based perovskite. This peak is attributed to the (100) plans [157], whereas we don't see the characteristic peak of the yellow δ-phase centered around 11.6°. Therefore, we conclude that our two perovskite films mainly crystallize in the optically active α-phase.

However, in triple cation perovskite film ($Cs_{0.05}(MA_{0.17}FA_{0.83})_{0.95}Pb(I_{0.83}Br_{0.17})_3$), the typical PbI_2 diffraction peak at 12.8° is clearly observed, which indicates that there is some remaining PbI_2 in the film. The origin of PbI_2 came from the PbI_2 precursor that is not fully dissolved or mixed with the other precursors to form the perovskite crystal structure. This residue can be formed whether in the perovskite solution or more likely during the deposition process of the perovskite. The PbI_2 diffraction peak is not observed in double cation perovskite which can reflect a better quality perovskite layer with fewer residues remaining in the film.

V.4.2 JV characteristics of devices

The photovoltaic performances of the double and triple cation perovskite solar cells have been evaluated from the JV curves measured under standard illumination as shown in Figure V. 15. The spectral correction was not applied to the Jsc performance measurements, leading to a slight overestimation (around 10%) of our short-circuit currents, which is acceptable since it does not impact the trend.

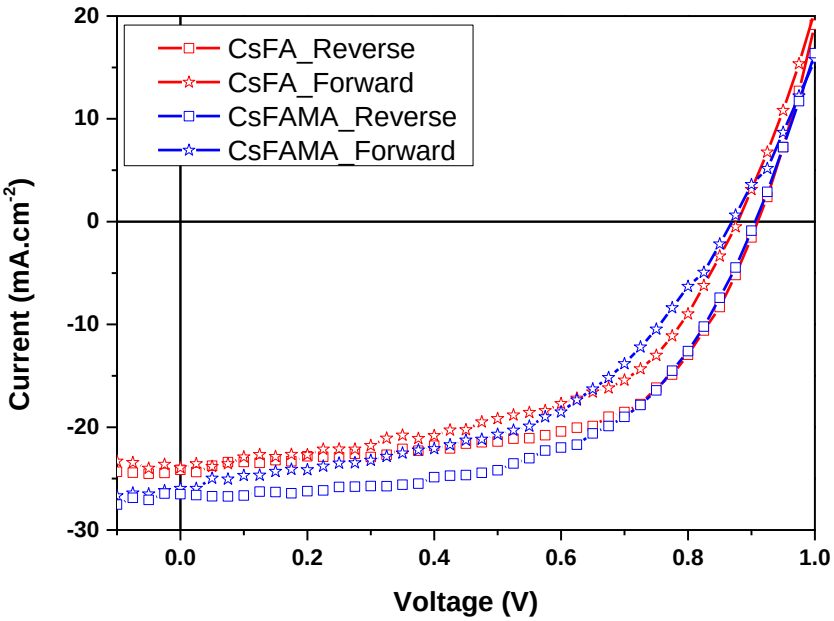

Figure V. 15: JV curves of double (CsFA) and triple (CsFAMA) cation perovskite solar cell

	Scan direction	Voc(V)	Jsc(mA.cm^{-2})	FF	PCE(%)	HI(%)
Triple cation perovskite	Reverse	**0.90**	**26.8**	**0.56**	**13.6**	**18**
	Forward	**0.86**	**25.7**	**0.49**	**11.1**	
Double cation perovskite	Reverse	**0.90**	**24.1**	**0.60**	**12.9**	**15**
	Forward	**0.87**	**23.3**	**0.54**	**10.9**	

Table V. 4: Photovoltaic parameters of double and Triple cation perovskite solar cells

The photovoltaic performances of the two PSC types are found close (the dispersion of the performance corresponds to what was reported in chapter III). We observe a slight increase in Jsc for the triple cation PSC compared to the double cation. This can be considered as an artifact as the spectral mismatch correction was made for both types of cells using the double cation spectral sensitivity. However, this overestimation, which is from the range of 5-10%, does not affect the solar cell behavior. The overestimated Jsc for the triple cation PSC can be the origin of the lower fill factor.

The hysteresis of the triple cation PSC is found to be slightly larger than that of the double cation, as seen from the HI index calculated.

V.4.3 Impedance spectroscopy

To compare the dynamic properties of the double and triple cation perovskite solar cells, we perform impedance spectroscopy measurement under the same conditions described in chapter IV (under 1 sun of illumination, AC voltage 50mV, ambient conditions, etc.) and with varying DC applied voltage (from 0.1 to 0.9V). Both types of solar cells are giving IS response of the same type, with two arcs that characterize two relaxation processes at high and low frequencies (as discussed in the previous chapter). Thereafter, the IS spectrums are fitted using the same equivalent circuit discussed in chapter IV (Page 113).

Figure V. 16 shows the variation of the high-frequency capacitance C_{HF} and high-frequency resistance R_{HF} with the applied voltage for double and triple cation perovskite solar cells.

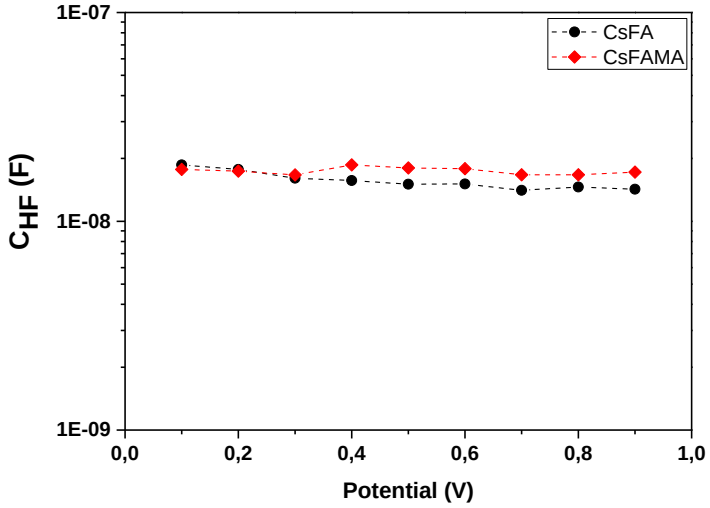

Figure V. 16: The high-frequency capacitance C_{HF} as a function of the applied voltage

The high-frequency capacitance C_{HF} of the double cation PCS is only slightly lower than the C_{HF} of the triple cation PSC. At the optimal working point, (0.7V) C_{HF} of CsFAMA perovskite is 16.7 nF versus 14.1 nF for CsFA perovskite. The origin of the slight difference in C_{HF} (geometric capacitance) value can only be assigned to the lower effective dielectric constant of the double cation perovskite since the thickness and the surface area are the same for both solar cells. Therefore, we can estimate the effective dielectric constant values of double and triple cation perovskite, from C_{HF} (at 0.7 V), using the equation below.

$$C_{HF} = \frac{\varepsilon_r \varepsilon_0 S}{d} \leftrightarrow \varepsilon_r = \frac{d C_{HF}}{\varepsilon_0 S}$$

Where ε_r the relative dielectric permittivity of the perovskite, ε_0 is the vacuum permittivity (8.85×10^{-12} F/m), S the surface of the active area of the solar cell and d is the thickness of the perovskite layer.

This method is already used in the literature to calculate the dielectric constant of the solar cell absorber [158] [159] since at high frequencies the capacitive response of the solar cell is dominated only by the geometric capacitance. By consequence, at high frequency, the ETL and HTL are considered as electrodes (as in a simple capacitor) and the absorber is considered as a dielectric, however, ε_r cannot be estimated at low frequencies.

The dielectric constant (ε_r) calculated from C_{HF} of the triple cation perovskite is around 42 whereas ε_r of the double cation, perovskite is around 36. It seems that the presence of

methylammonium cation in the perovskite seems to increase the dielectric constant, which is consistent with what is reported in the literature by J. Juarez-Perez et al. about the impact of the molecular motion (rotation) of the MA^+ cation: it leads to structural fluctuations that significantly increase the dielectric constant [160]. Thus, the absence of MA^+ in the double cation perovskite may reduce the structural fluctuations and consequently reduce the value of the dielectric constant, and consequently reduce the geometric capacitance.

The variation of the high-frequency resistance R_{HF} with the applied voltage for double cation and triple cation perovskite solar cells is shown in Figure V. 17.

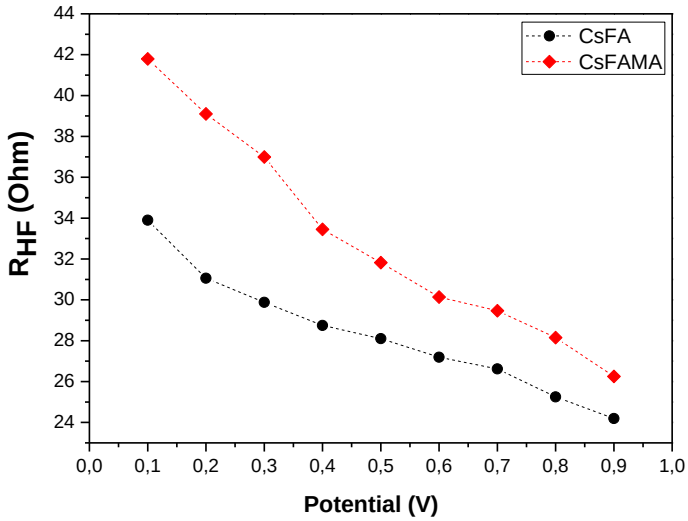

Figure V. 17: The high-frequency resistance R_{HF} as a function of the applied voltage

From Figure V. 17 we notice that the difference in R_{HF} between the double and the triple cation PSC is quite small, where double cation PSC is showing a lower R_{HF} resistance (from 34Ω to 24Ω) compared to the triple cation perovskite (from 41Ω to 26Ω). As explained earlier, this high-frequency resistance is associated with the charge transfer resistance (Rct). Despite the complexity of the physical origin of R_{HF}, we can clearly observe the contribution of the nature of the absorber. However, this contribution is not significant (Around 5 Ω of difference at 0.7V) compared to the contribution of the electron transporting layers as seen earlier between planar SnO_2 and mesoporous TiO_2 (Around 180 Ω of difference at 0.7V). Furthermore, this difference may reflect the nature of the interface between the perovskite/ ETL, and perovskite/HTL.

For triple cation PSC, the higher R_{HF} can be attributed to the presence

It was reported in the literature that the presence of PbI_2, in the perovskite layer, forms PbI_2^- PbI^- traps and I^- ,I_2^-mobile ions that tend to diffuse and segregate in the interface[161]. Therefore, this may explain the higher R_{HF} observed in triple cation PCS.

From C_{HF} and R_{HF}, we calculate the relaxation time at high-frequency (τ_{HF}) and the corresponding device bandwidths as a function of applied voltage (hence operating conditions) as shown in Figure V. 18.

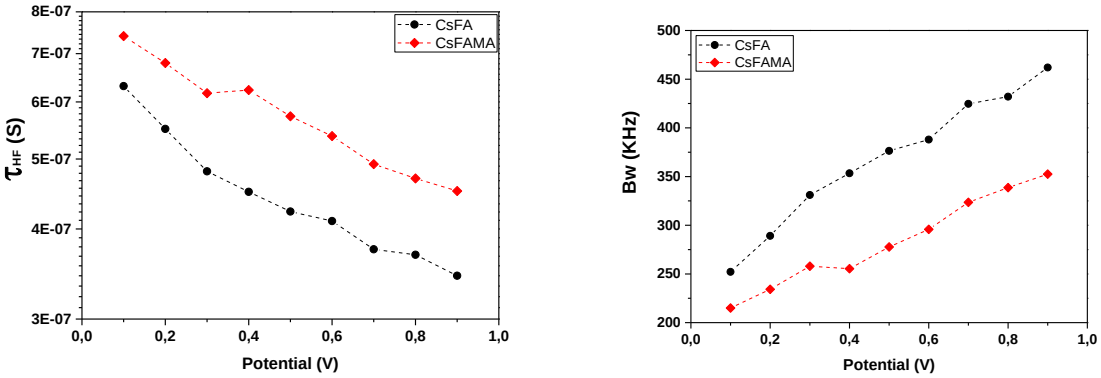

Figure V. 18: The high-frequency relaxation time (left) and the bandwidth (right), as a function of the applied voltage

We notice that there is a considerable difference in relaxation time τ_{HF} between double and triple cation perovskite. The relaxation process of the double cation PSC seems to be slower than the relaxation process of the triple cation PSC. The main origin of this difference is due to the difference in high-frequency capacitance. This can therefore be related to the lower dielectric constant of the double cation (CsFA) perovskite layer that reduces the geometric capacitance of the device. Consequently, the bandwidth of the double cation PSC is higher, it reaches a value of 462 kHz at a higher voltage compared to 352 kHz for the triple cation PSC. These bandwidth values are coherent with what was reported in the literature for perovskite solar cells.

V.4.4 Conclusion

From this simple comparison, we can conclude that the nature of the absorber has a significant impact on the photovoltaic performance of the devices, as well as on their dynamic performance. It strongly affects the bandwidth (increased by 33% from the triple to the double cation active layer) by affecting both the geometric capacitance and the charge transfer resistance. In this context, the double cation perovskite solar cell shows better

dynamic performance than the triple cation device, while their power conversion efficiency (energy harvesting capabilities) are similar. Considering the fact that the processing of double cation perovskite layers is less complex than that of the triple cation (chapter II), we, therefore, focus on the CsFA-based perovskite for the following studies.

V.5 Effect of the perovskite thickness on the dynamic response of the perovskite solar cell

The thickness of the perovskite active layer is an easy and accessible parameter that may allow improving the dynamic response of the solar cells by reducing their geometrical capacitance. However, increasing the active layer thickness can drastically impact the charge transfer resistance. Furthermore, such an approach should not be done at the expense of the PV performance of the solar cells since the thickness of the perovskite active layer is crucial for the PV performances of PSCs.

In this part, we are investigating the impact of the thickness of the double cation perovskite layer ($FA_{0.85}Cs_{0.15}(I_{0.85}Br_{0.15})_3$) on the dynamic behavior of the solar cell. We are using 3 different thicknesses 380nm, 450 nm, and 740 nm that correspond to the spin coating rotation speeds of 6000 rpm, 4000 rpm, 2000 rpm respectively. Besides the perovskite thickness, all the devices are identical (same ETL HTL, same surface area etc.)

V.5.1 XRD

We conduct X-ray diffraction (XRD) to investigate the crystalline quality of the double cation perovskite films with different thicknesses. The perovskite film was deposited on top of SnO_2/FTO substrates in order to be in the same conditions as the solar cell. Figure V. 19 shows the XRD patterns of the three perovskite thicknesses (380 nm, 450 nm, 740 nm), and SnO_2 deposited on top of FTO, and the FTO substrate alone.

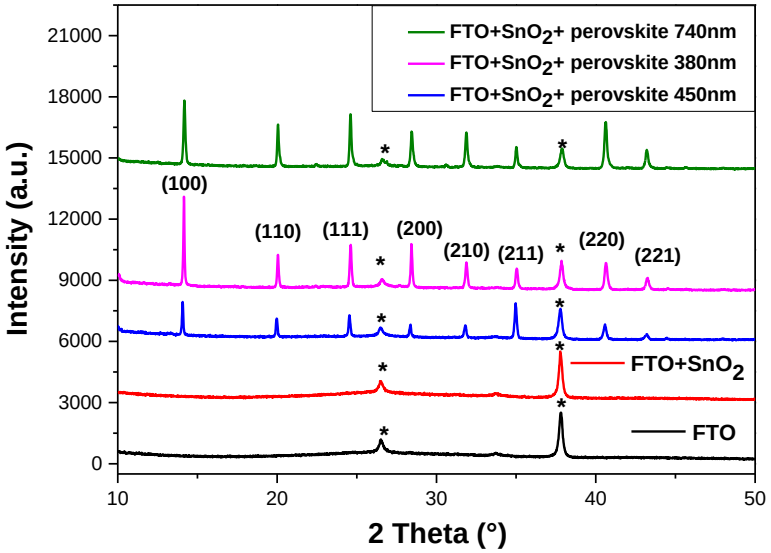

Figure V. 19: XRD patterns of double cation perovskite with three thicknesses deposited on top of SnO_2/FTO substrate

AS mentioned earlier, we can only see the contribution of the two diffraction peaks of FTO at (26.5° and 37.7°) from the SnO_2/FTO substrate due to the low thickness of the SnO_2 layer.

All perovskite films show a proper perovskite crystal structure since we observe all and only the characteristic peaks of $FA_{0.85}Cs_{0.15}P(I_{0.85}Br_{0.15})_3$ perovskite. These peaks characterize the different crystalline plan orientations [157] such as the typical perovskite peak, attributed to the plan (100), around 14° that witnesses the black α-phase of the perovskite. Moreover, we do not see the characteristic peak of the yellow δ-phase mainly centered around 11.6°.

For the three samples, we do not observe any undefined peaks or unwanted peaks such as the typical PbI_2 diffraction peak at 12.8° which means that three thicknesses are giving proper crystal structure. In other words, the thickness seems to not affect the crystal structure of the perovskite layer.

V.5.2 Morphology investigated by SEM

The top view SEM images corresponding to the three perovskite thicknesses (deposited on top of SnO_2/FTO substrate) are shown in Figure V. 20.

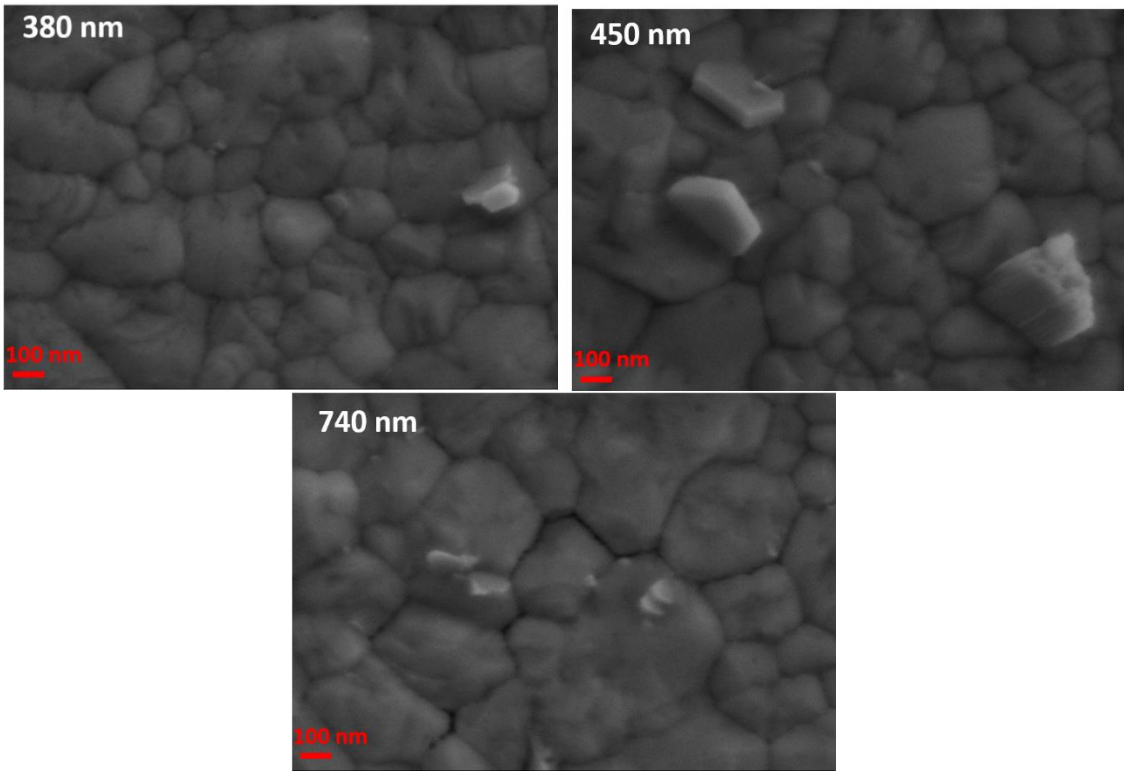

Figure V. 20: SEM images of double cation perovskite film corresponding to the thickness of 380nm, 450nm, and 740nm.

For the three layers, we observe the presence of a distribution of large grains (average diameter of ~200nm) and small grains (~50nm). The contribution of the smaller grains seems to be slightly less important for the 740nm thick film. While the three layers show quite comparable film morphology, such slight differences could be related to the difference in rotation speed used during the film deposition by spin-coating. Especially, the antisolvent treatment made at lower spin-coating speed (2000 rpm) can easily affect the final grain distribution compared to faster rotations, as this process is known to be very sensitive to the evaporation rate of the solvent, as mentioned in chapter III.

V.5.3 UV-visible absorption

We measure the UV-visible absorption of the perovskite films as a function of the thickness (Figure V. 21).

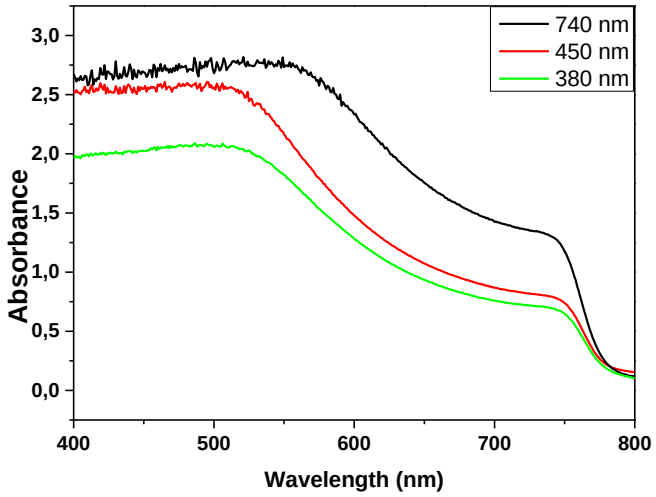

Figure V. 21: Uv-vis absorbance spectra of 380 nm, 450 nm , 740 nm perovskite films.

All perovskite layers show the same characteristic absorption band edge at 780 nm which reflects the absorption signature of the $FA_{0.85}Cs_{0.15}(I_{0.85}Br_{0.15})_3$ perovskite. No optical signature of PbI_6 octahedra, significative of PbI_2 phase (bandgap around 400nm), is observed, which is consistent with the XRD analysis. The higher absorption corresponds to the thicker perovskite film (740 nm), as expected. The optical signature of the films is consistent with what we expect at this stage.

V.5.4 JV

The photovoltaic performances of devices based on the three different thicknesses have been evaluated from the JV measurement under standard illumination. The spectral correction was not applied to the Jsc performance measurements, leading to a slight overestimation (around 10%) of our short-circuit currents, which is acceptable since it does not impact the trend. The electrical characteristics in forward and reverse scans are given in Figure V. 22.

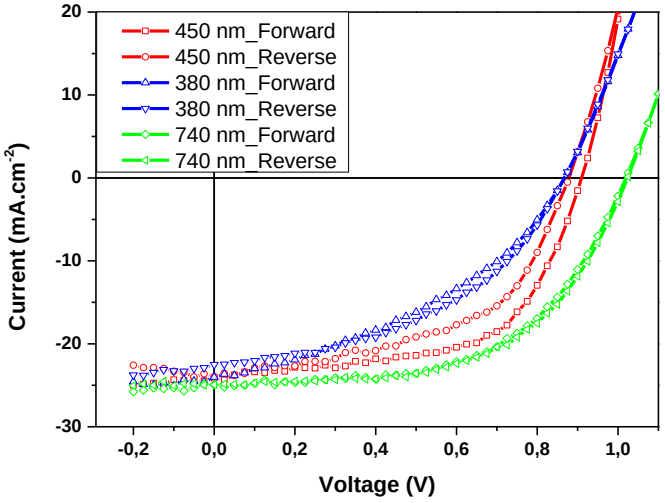

Figure V. 22: JV curves of 380 nm, 450 nm, 740 nm perovskite PSCs

The photovoltaic parameters of the three average PSCs are shown in Table V.4 below.

Thickness	Scan direction	Voc(V)	Jsc(mA.cm^{-2})	FF	PCE(%)	HI(%)
380 nm	Reverse	**0.86**	**22.6**	**0.45**	**8.8**	**8**
	Forward	**0.86**	**23.9**	**0.39**	**8.1**	
450 nm	Reverse	**0.90**	**24.1**	**0.60**	**12.9**	**15**
	Forward	**0.87**	**23.3**	**0.54**	**10.9**	
740 nm	Reverse	**1.02**	**24.8**	**0.58**	**14.6**	**3**
	Forward	**1.01**	**25.1**	**0.56**	**14.2**	

Table V. 5: The photovoltaic parameters of double cation PSC

We can clearly observe the increase of the power conversion efficiency with the increasing thickness, which is mainly due to a significant increase of Voc. The short-circuit current density is also increasing with active layer thickness, but this is less pronounced. The electrical hysteresis is found to be very low for the thicker active layer, which will be discussed in more detail in the following part.

V.5.5 Dynamic properties probed by impedance spectroscopy

To evaluate the impact of the thickness on the dynamic properties of the double cation ($FA_{0.85}Cs_{0.15}(I_{0.85}Br_{0.15})_3$) perovskite solar cell, we perform impedance spectroscopy

measurement under the same conditions described in chapter IV (under 1 sun of illumination, ambient conditions, etc.), as a function of DC applied voltage (from 0.1 to 0.9V). all solar cells are giving IS response of the same type, with two arcs that characterize the two relaxation processes at high and low frequencies (see annex). Thereafter, the IS spectrums are fitted using the same equivalent circuit discussed in chapter IV (Page 113).

High-frequency response:

Figure V. 23 shows the variation of the high-frequency capacitance C_{HF} and high-frequency resistance R_{HF} with the applied voltage for the three PSCs with the three different thicknesses.

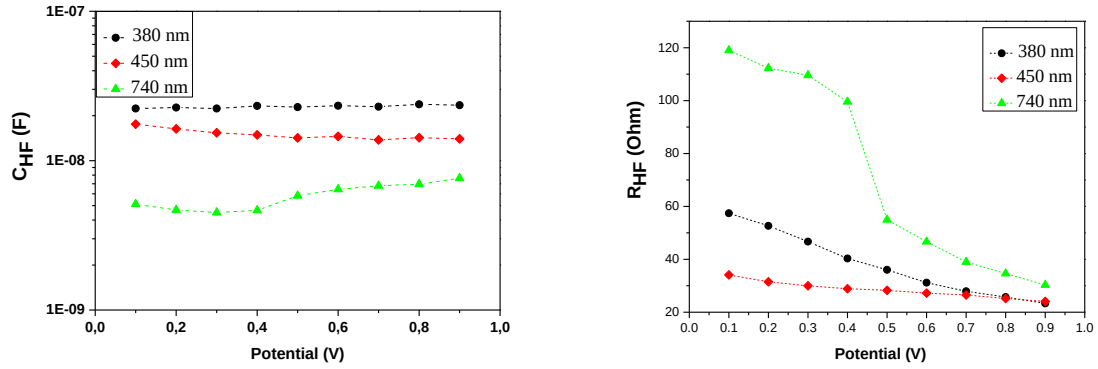

Figure V. 23: The high-frequency capacitance C_{HF} and resistance R_{HF} as a function of the applied voltage

From Figure V. 23 we notice that the high-frequency capacitance values drop with the increasing thickness. At 0.7V, C_{HF} drops from 23nF for 380nm-thick film, to 14nF for 450nm-thick, down to 7nF for 740nm-thick. This drop is therefore significant, and it scales with the inverse of the film thickness, as expected from its theoretical expression.

On the other hand, all high-frequency resistance R_{HF} decreases with the increasing voltage as expected. The difference in R_{HF} for the three thicknesses is very large at low applied voltages (0.1V to 0.4V), while it is much reduced to high voltages which could be related to the improvement of charge transport in the interfacial layers under high voltages (high electric field) which reduces the recombination inside of the ETL/HTL layers. At the working point (0.7V) the R_{HF} of 380nm and 450nm PSC are close ~ 26Ω whereas the R_{HF} of the thicker PSC is higher 39 Ω.

From C_{HF} and R_{HF} we calculate the high-frequency relaxation time τ_{HF} and the corresponding device bandwidth as shown in Figure V. 24.

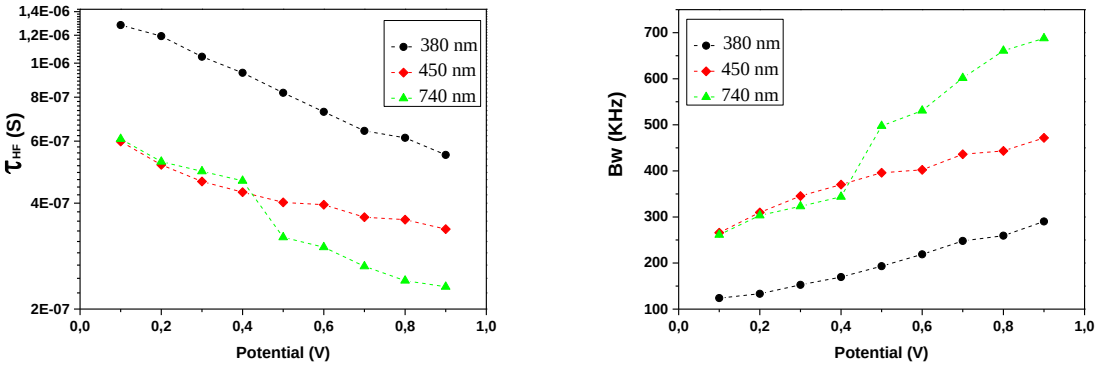

Figure V. 24: The high-frequency relaxation time (left) and the bandwidth (right), as a function of the applied voltage

The thinner perovskite solar cell (350 nm) shows the highest τ_{HF} and the lower bandwidth (247 kHz at 0.7V), this is mainly due to its higher geometric capacitance. On the other hand, the thicker PSC (740nm) shows the lowest τ_{HF} and the highest bandwidth in the high voltage region (601 kHz at 0.7V vs 436 kHz for 450nm PSC). These values are driven by the low C_{HF} values, however, in the low voltages region, the high R_{HF} leads to a significant drop of the bandwidth where the values are close to the 450nm PSC.

Low-frequency response:

In this section, we put a special focus on the low-frequency response since it can bring additional information about the active layer. Notably, the recombination rate occurring inside of the perovskite bulk (characterized by RLF) as well as the hysteresis effect related to the charge accumulation (characterized by CLF). These two pieces of information can give a more in-depth understanding of the nature and the physical properties of the perovskite bulk that mainly affect energy harvesting.

Figure V. 25 illustrates the dynamic behavior of the PSC, with different perovskite thicknesses, at low frequencies.

.

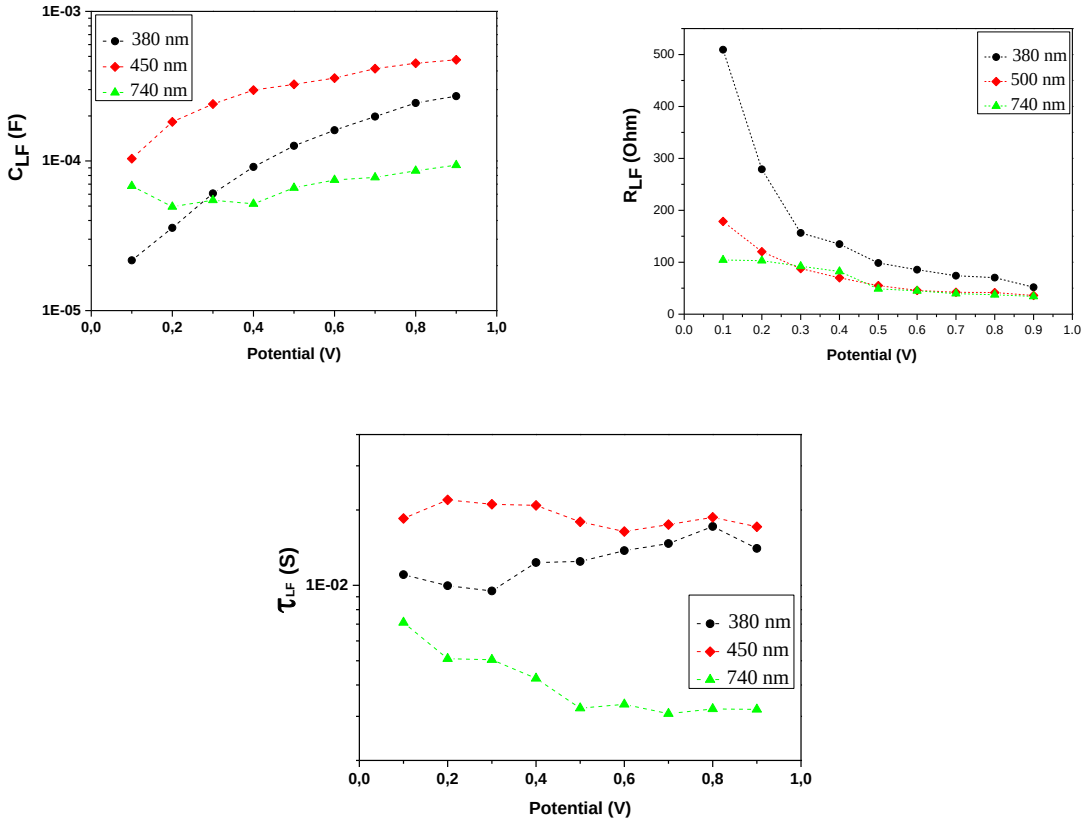

Figure V. 25: C_{LF} and R_{LF} and tauxLF a function of the applied voltage

We remind that the low-frequency capacitance C_{LF} is associated with the double layer capacitance C_{dl}, while there is no evidence for a contribution from a chemical capacitance observed, as generally observed in the literature [127] (see previous parts of this work). At low frequencies, the capacitance C_{LF} of all perovskite solar cells is increasing due to the ionic charge accumulation in the perovskite interfaces with the ETL and the HTL.

At high voltages, C_{LF} of the thicker perovskite layer (740nm) is significantly lower than that of the thinner devices. Interestingly, this observation is consistent with the very low hysteresis observed for this thick device in its JV characteristics (Figure V. 22). The 450nm perovskite shows the higher C_{LF} and the higher hysteresis index which means that the hysteresis effect of the double cation PSC does not variate linearly with the thickness, therefore it is crucial to optimize the thickness of the active layer to find the best performances.

At low frequencies, the resistance R_{LF} (which was mainly attributed to the recombination resistance R_{rec}) is higher for the thinner perovskite film, meaning that the recombination rate

is lower. On the opposite, at higher thicknesses, the recombination rate is higher. This could be related to the defusion length of the charges in the perovskite bulk since increasing the thickness requires for the photogenerated charge to defuse for a longer distance. On the other hand, the recombination rate of the thicker perovskite layer is close to the 450nm perovskite layer, which means that even the 740nm layer absorbs more photons there is the same amount of charges that recombine compared to 450nm PSC. This could be related to the higher grain size and lower grain boundaries since by reducing the grain boundaries we decrease the recombination that can occur inside of the perovskite film. This observation reflects the higher Voc of 740 double cation PSC observed by the JV measurement which witnesses the best quality of the 740nm perovskite.

Based on the estimated low-frequency parameters, the corresponding relaxation time at low-frequency (τ_{LF}) witnesses the slower relaxation process of the 740nm perovskite. This relaxation process reflects also the hysteresis observed by the JV measurement where the faster τ_{LF} corresponds to the higher hysteresis index.

V.5.6 Conclusion

We conclude in this part that the thickness of the active layer is an important lever for controlling the device bandwidth. It increases the absorption with a low recombination rate leading to a significant improvement of Voc of the solar cell, which leads to an improvement of the PCE by around 25% (compared to 450nmPSC). It also increases the bandwidth by 40%, which could significantly improve the data receiving for the OWC systems. Furthermore, increasing the thickness seems to reduce the structural density of defects present in the perovskite bulk leading to a decline of the hysteresis effect.

Likewise, the effect of other geometrical parameters can be probed such as the surface area of the solar cells to find the optimal dimensions of the device.

V.6 Effect of the SnO_2 electron transporting layer

In this part, we are exploring the effect of the quality of the ETL on the photovoltaic and dynamic behavior of the double cation perovskite solar cell (PCE, Voc, BW, etc.). Especially, the final geometry of the device is determined by the whole sandwiched structure, in which charge transport layers can play some role. As no clear study is today reported in the

literature on this aspect, we will try, in this part, to assess the influence of the quality of the ETL layer on the dynamic behavior of the cells.

As mentioned in chapter III, the aggregation of SnO_2 nanoparticles makes it challenging to obtain a homogeneous and smooth layer from spin-coating [100]. We compare a double cation PSC containing an un-optimized SnO_2 layer, with a cell where our optimization treatment has been applied to end up with a smooth and compact layer (the detail of this SnO_2 optimization treatment is described in chapter III).

V.6.1 Structural properties of the perovskite active layer on top SnO_2 ETLs

To investigate the influence of the quality of the SnO_2 layer on the crystalline properties of the deposited perovskite films, we perform the X-ray diffraction on double cation perovskite deposited on top of treated and untreated SnO_2 layers as shown in Figure V. 26 below.

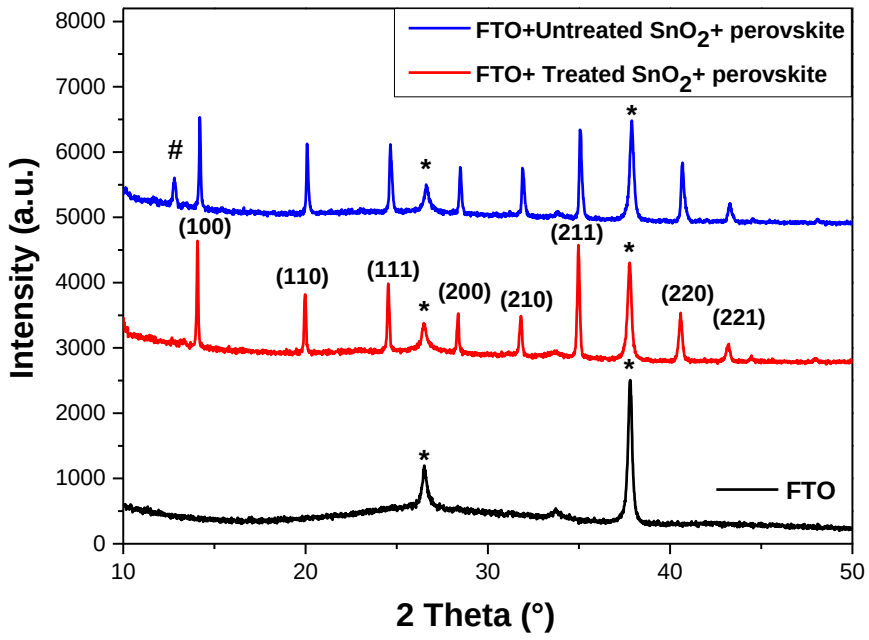

Figure V. 26: XRD patterns of double cation perovskite

Both perovskite films show a proper perovskite crystal structure without the yellow δ-phase as explained earlier, and we observe all the characteristic peaks of $FA_{0.85}Cs_{0.15}P(I_{0.85}Br_{0.15})_3$ perovskite that characterizes the different crystalline plan orientations that witnesses of the black α-phase of the perovskite. However, the perovskite layer deposited on top of the untreated SnO_2 layer shows the typical PbI_2 diffraction peak at 12.8° which witnesses the presence of PbI_2 in the perovskite layer. The origin of this could be related to the

nonuniformity and the roughness of the surface of the untreated SnO_2 as shown in the atomic force microscopy images reported in chapter III. The RMS roughness of the untreated SnO_2 is 12nm compared to 1.5nm for the treated SnO_2. Therefore, during the deposition of the perovskite, the roughness of the SnO_2 and the small aggregate present on the surface may prevent a proper contact between the perovskite precursor solution and the antisolvent which can lead to a sort of small accumulation of the PbI_2 on the perovskite/SnO_2 interface.

Apparently, the quality of SnO_2 film has a direct impact on the quality of the perovskite. Obtaining a compact, homogeneous, and smooth SnO_2 layer leads to much more complete crystallization of the perovskite, without any trace of the presence of PbI_2. In contrast, the untreated SnO_2 layers induce an apparent crystallization difficulty and an incomplete conversion of the precursors. It is also questionable whether the presence of PbI_2 is not linked to premature degradation of the perovskite film on untreated SnO_2 film, since the time between the deposition and the X analyzes are quite large (~2 hours). This assumption can surely not be completely eliminated. In any case, the treatment of SnO_2 is beneficial for obtaining high-quality crystalline perovskite layer

V.6.2 UV-visible absorption

We compare the absorption of the treated and untreated SnO_2 layers and the double cation perovskite layer as shown in Figure V. 27.

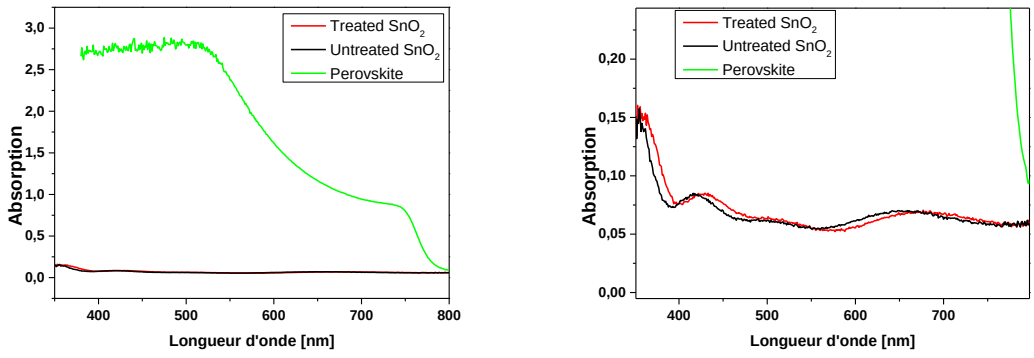

Figure V. 27: Uv-vis absorbance spectra of the treated and untreated SnO_2 films and the double cation perovskite film. Zoom on the Uv-vis spectra (right)

We notice from Figure V. 27 that the absorption of both types of SnO_2 is extremely low compared to the absorption of the perovskite layer, this is normal since the SnO_2 is supposed to be the transparent charge transporting layer that allows the full passage of the light through

it. The zoom of the UV spectrum clearly shows a blue shift for the untreated SnO_2 film. It was reported in the literature that the aggregation of nanoparticles causes this kind of blue shift [162]. Thus, the aggregation of the SnO_2 nanoparticle can be the reason behind this blue shift, in other words, the treatment of the SnO_2 solution reduces the aggregation of the colloidal solution.

V.6.3 JV

The photovoltaic performances of the double cation PSC are compared with the untreated and treated SnO_2 ETL layer. The JV curves under standard illumination are given in Figure V. 28, while the corresponding photovoltaic parameters are given in Table V.6. The spectral correction was not applied to the Jsc performance measurements, leading to a slight overestimation (around 10%) of our short-circuit currents, which is acceptable since it does not impact the trend.

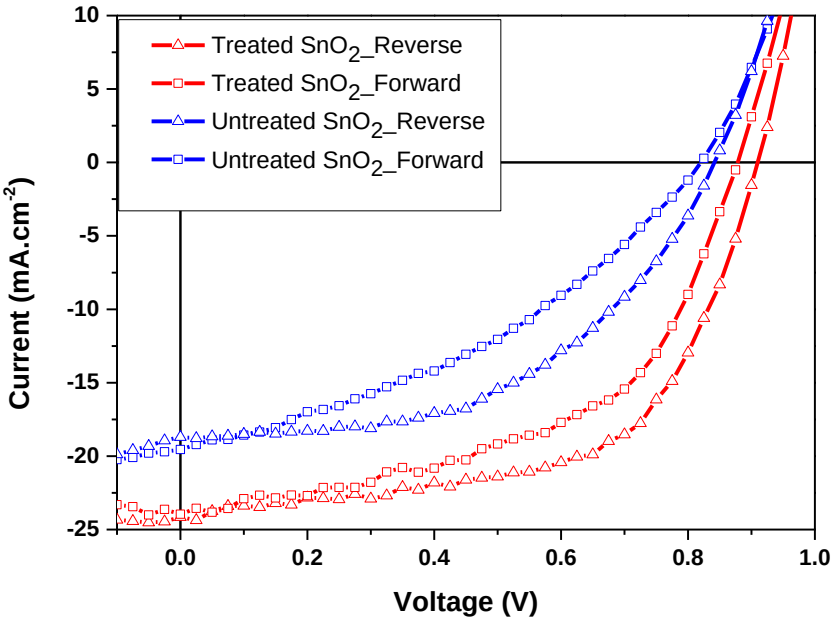

Figure V. 28: JV curves

	Scan direction	Voc(V)	Jsc(mA.cm^{-2})	FF	PCE(%)	HI(%)
Untreated SnO_2	Reverse	0.83	19.1	0.49	7.92	23
	Forward	0.81	19.3	0.38	6.02	
Treated SnO_2	Reverse	0.90	24.1	0.60	12.9	15
	Forward	0.87	23.3	0.54	10.9	

Table V. 6: The photovoltaic parameters of double cation perovskite solar cell with treated and untreated SnO_2 ETL.

The PV performances were extracted from a single cell that reflects the behavior of several independent batches realized using untreated and treated SnO_2.

The notable improvement in the crystalline quality of perovskite, coupled with better surface homogeneity of SnO_2, promotes the optoelectronic properties of the perovskite while ensuring a better quality contact with the ETL layer. These improvements lead to a net increase in all the photovoltaic parameters, and in particular, the short-circuit current, the open-circuit voltage, but also parasitic resistances which lead to much better FF.

Moreover, the quality of the SnO_2 film has a considerable impact on the hysteresis where improving the film quality reduces the hysteresis index. This could make sense because a rough untreated SnO_2 surface deteriorates the quality of the perovskite spreading and deposition during the spin coating process which creates more perovskite mobile defects that would increase the HI.

V.6.4 Impedance spectroscopy

To investigate the influence of the quality of the SnO_2 layer on the dynamic response of the solar cell, we perform impedance spectroscopy measurements under the same conditions as those described in chapter IV, as a function of DC applied voltage (from 0.1 to 0.9V). Both solar cells are giving IS response of the same type, with two arcs that characterize the two relaxation processes at high and low frequencies (see annex). Thereafter, the IS spectrums are fitted using the same equivalent circuit discussed in chapter IV.

Figure V. 29 shows the variation of the high-frequency capacitance C_{HF} and resistance R_{HF} with the applied voltage for solar cells with the treated and the untreated SnO_2 layers.

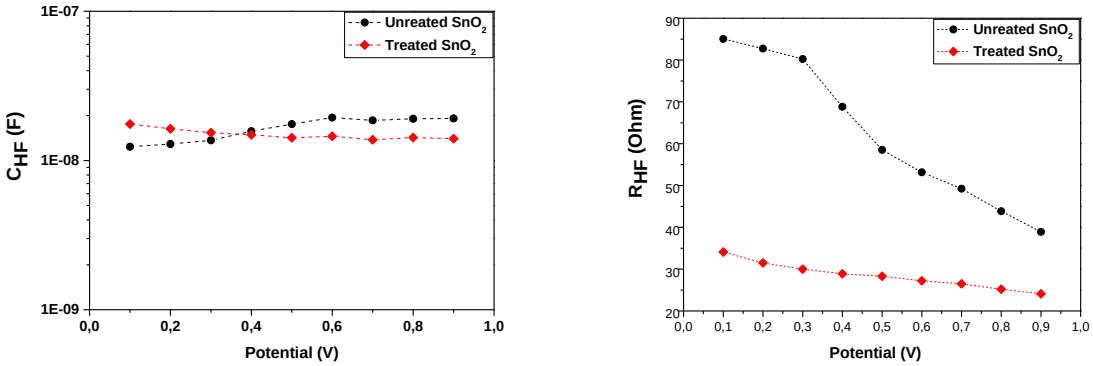

Figure V. 29: The high-frequency capacitance C_{HF} and resistance RHF as a function of the applied voltage

Noticeably, the high-frequency capacitances of the two PSCs are close, 18nF for the untreated SnO_2 PSC at 0.7V compared to 14nF for the conventional PSC. This is due to the use of the same type of perovskite and the same device's geometric dimensions.

However, the small difference between the two capacitance could be related to the indirect impact of the ETL quality on the perovskite layer properties : the presence of large amounts of remaining PbI2, associated with a relatively lower crystalline quality of the perovskite deposited on the untreated ETL, is likely to modify the effective permittivity of the stack, hence slightly changing C_{HF}.

The high-frequency resistance R_{HF}, or the charge transfer resistance, of the two solar cells is significantly different. It is reduced by a factor of 2 after the SnO_2 treatment (from 49Ω to 26Ω). The untreated SnO_2 PSC shows a high charge transfer resistance, which can probably be associated with the presence of aggregates at the perovskite/ETL interface. Such aggregates are likely to present a high density of traps that can act as recombination centers, causing considerable losses of charges.

From C_{HF} and R_{HF}, we calculate the high-frequency relaxation time τ_{HF} and the corresponding device bandwidth as shown in Figure V. 30.

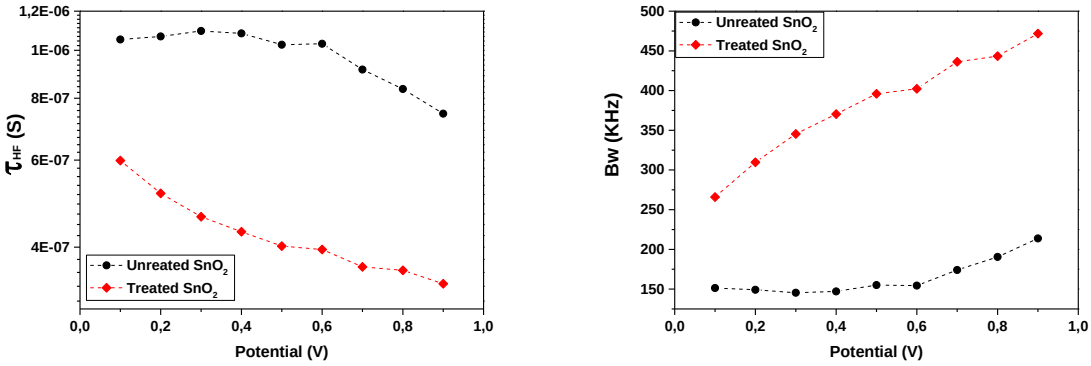

Figure V. 30: The high-frequency relaxation time (left) and the bandwidth (right), as a function of the applied voltage

The high-frequency relaxation process of the untreated SnO_2 PSC is slower than the relaxation process of the conventional PSC. This is caused in the first place by the higher high-frequency resistance of the untreated SnO_2 PSC and by the slight increase of the C_{HF} in the second place. Consequently, the bandwidth of the treated SnO_2 PSC reaches a value of 462kHz at high voltage compared to 213kHz for the untreated device.

V.6.5 Conclusion

Our experimental data demonstrate that the quality of the ETL is an important factor both for the photovoltaic performance of the device, as well as for its dynamic performance. We have demonstrated that treating the SnO_2 film has reduced the value of the R_{HF} (divided by 2) which means that even if the C_{HF} remains the same, the value of the BW would be doubled by 2. Moreover, the quality of the ETL seems to have an impact on the structural properties of the perovskite since it causes the appearance of the PbI_2 residue, this could also change the value of C_{HF}. In our case, the bandwidth decreased by ~54% at high voltages. Thus, we can attribute ~50% of this loss to the rise of the R_{HF} (from 24Ω for the conventional to 39 Ω at 0.9V) and ~4% to the slight increase of C_{HF} (from 14nF for the conventional PSC to 19nF at 0.9V).

In this part, we have shown that a structural issue in the interface layer can drastically reduce the bandwidth of the solar cell. On the other hand, improving the interfacial layer quality can help achieve higher bandwidth and consequently high data rates. Moreover, investigating the dynamic properties of other ETLs may show better performances than SnO_2 the only condition is to stay in a planar structure. In a similar way, other HTMs rather than the Spiro-OMeTAD can be investigated.

General conclusion

In the context of optical wireless communication, perovskite solar cells are a very promising technology that could be used as data receivers and energy harvesters simultaneously. This research project focused on studying the dynamic behavior of mixed cation perovskite solar cells. More specifically, the strategy proposed in this project is to elaborate an efficient and reproducible perovskite solar cell that can be characterized in terms of its dynamic response using impedance spectroscopy.

Firstly, we have addressed some general aspects related to the fabrication of perovskite solar cells in order to control and improve their optoelectronic performance. We have succeeded to improve the power conversion efficiency and reproducibility of the devices by mainly focussing on the perovskite active layer and the SnO_2 electron transporting interface. We proposed several strategies to overcome some of the main issues encountered with perovskite materials processed from solution, such as the appearance of pinholes or cracks at the micro-scale, often associated with the antisolvent treatment. In the end, we have demonstrated a protocol toward efficient and reproducible mixed cation perovskite solar cells presenting high efficiencies, compatible with the expected characterization proposed in the next parts of this work. Several experimental perspectives remain highly relevant, however, in order to get close to state-of-the-art efficiencies of nowadays devices: passivation of interfacial defects using additives (such as methylammonium chloride) or encapsulation of the active layer using perovskite of low dimensionality (2D or quasi-2D layers). Such strategies would be also highly beneficial to the device lifetime in ambient conditions.

Secondly, we have illustrated our methodology towards reliable impedance spectroscopy measurement, by taking into account the necessary conditions of the experimental measurement, as well as by developing the most suitable protocol to simulate the impedance response of equivalent circuits, and by cautiously interpreting the experimental results. This work certainly contributes to demonstrating that impedance spectroscopy is a highly powerful technic to improve our understanding of the different physical phenomena governing the solar cell dynamic response. Based on this understanding, we have shown that the perovskite solar cells behave as bandpass filters, and we have accordingly proposed a new equivalent circuit able to model their dynamic behavior. We have identified the physical origin of the dynamic resistance that we attributed to the charge transfer resistance R_{ct}. This resistance is in

conjunction with the geometric capacitance C_{geo} of the device, these are the two components that limit its bandwidth. We also demonstrated that it is possible to control this bandwidth via a careful optimization of the solar cell architecture and design. The use of a planar architecture and a thick active layer improves the dynamic response of the cell, and bandwidths over 0.6 MHz were achieved. This work opens a door to the use of impedance spectroscopy as a strong characterization tool of solar cells in the OWC field. Our strategy could be easily applied to other types of solar cells, or under a broader range of operating conditions. For instance, we have conducted preliminary studies on the characterization of the dynamic behavior of organic solar cells (OPV) by impedance spectroscopy and we were able to demonstrate high bandwidth obtained using thick active layers of stat-of-the-art organic donor and acceptor blends. Moreover, one of the exciting perspectives of this work would be to investigate the dynamic behavior of devices under low light intensities (indoor lighting conditions), in order to reveal the full potential of third-generation devices for IoT applications inside buildings.

More direct perspectives of this work will have to focus on specific aspects associated with optical wireless communications, such as the assessment of gain, signal-to-noise ratio (SNR), and bit error rate (BER) in specific modulation schemes. Another critical point will be to focus on the trade-off between energy harvesting performance and data reception performance, through the use of dedicated receiver circuits.

In general, the work carried out in this thesis contributes significantly to demonstrate the strong potentialities of perovskite solar cells as data receivers and energy harvesters.

Likewise, more studies can be conducted to evaluate the effect of other parameters such as the electrodes or the HTM, the surface area, etc. on the dynamic response of the solar cell. Such studies can lead to a considerable improvement in the solar cell-based OWC field and consequently lead to a wide deployment of this kind of solar cells in different emerging technologies such as the Internet of Things (IoT), LiFi, and the 5G.

Annex

Comparison between our PSCs and those reported by Mica et al.

Mica et al. have studied the effect of the active layer thickness on the VLC parameters [12], they used the triple cation perovskite CsFAMA in planar SnO_2 perovskite structure, which is similar to our devices. Therefore, we can compare our results as illustrated in the following table.

The thickness of our PCS is 450 nm which is situated between two thicknesses reported in Mica's paper (250nm and 640nm). Our VLC parameters are taken in the Voc point, which is the same point where the bandwidth is estimated in Mica's paper.

	Thickness (nm)	τ_{HF}=RC (ns)	BW (f_C) (kHz)	Data rate (Mbps)	R (Ω)	C (F)
Mica et al. [12]	170	569	280	32±5	138	4.1
	250	385	413	49±4	135	2.9
	640	293	543	43±7	187	1.6
Our PSC	450	451	353	-	26.25	17.2

Table: Comparison between triple cation PSC

From the table, we can see that our PCS gives a bandwidth higher than 170°nm PSC. Therefore, there is a strong probability that our PSC is able to give a data rate higher than 32 Mbps.

The bandwidth of Mica's paper is estimated using two different methods called Transient photo-voltage and bandwidth estimation using a VLC link, these BW values are in good agreement with our bandwidth estimation using impedance spectroscopy.

However, C and R values are quite different, as we can see the capacitance C, which is the geometric capacitance, estimated by Mica's is very low and does not correspond to what was found in the literature for this kind of perovskite (one order of magnitude lower) [127] (see chapter V). This is due to the method used to estimate the capacitance since C was calculated from the bandwidth and as shown In the following equation:

$$C = \frac{1}{2\pi R f_{-3db}}$$

R was estimated by measuring the voltage of the PSC under open-circuit conditions, then putting a load resistor in series, and measuring the voltage again, using the approximation shown below.

$$R = R_0 \frac{V_{oc}}{V_{load} - 1}$$

Where R is the device resistance, R_0 is the load resistance, and V_{load} is the output voltage of the solar cell when the load resistor is connected.

We don't totally agree with this method since it measures the solar cell resistance under a static regime which means that this static resistance gathers many resistive contributions that are not necessarily present at high frequencies (such as Rs). However, we know that only the high-frequency resistance must be used to estimate f_{-3db}.

Impedance spectroscopy allows us to decouple the R_{HF} from R_S and R_{LF} which is more accurate. Hence, the resistance measured by Mica et al. is over-estimated which causes by consequence an under-estimation of the geometric capacitance C.

Finally, impedance spectroscopy seems to be a more accurate technique to measure the capacitance and resistance that limit the dynamic response of the solar cell.

Preliminary study on the influence of the light intensity

The light intensity has a direct impact on the data rate of the VLC system since the bandwidth of the photodetector improves with the increasing light intensity as reported by Ghassemlooy et al. [163]. In this part, we are trying to first verify if the bandwidth of the solar cell increases with the increasing light intensity and second to determine the physical origin of such behavior (C_{HF} or R_{HF}). Thereby, we conduct impedance spectroscopy on our conventional double cation perovskite solar cell under a DC voltage of 0.7V which is the optimal working point for our PSC (maximum power point). Afterward, we extract the dynamic parameters of the solar cell in the dark (0 sun) and under the illumination of 0.5 sun, 0.8 sun, and 1sun.

The figure below shows the variation of the high-frequency capacitance C_{HF} and resistance R_{HF} as a function of light intensity.

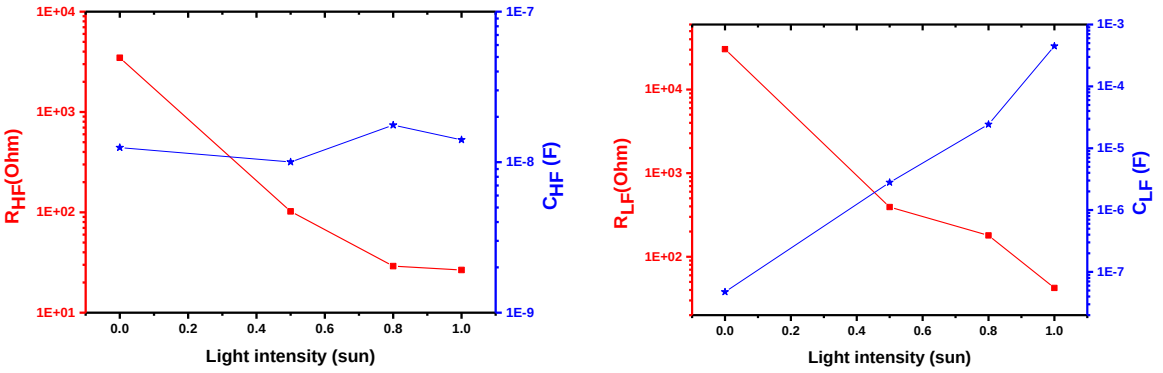

Figure A. 1: dynamic parameters as a function of light intensity

The high-frequency capacitance C_{HF} is independent of incident DC light intensity, which is expected since C_{HF} is a geometric capacitance that is light intensity independent. On the other hand, the high-frequency resistance R_{HF} highly increases with the decreasing light intensity it goes from 26 Ω under 1sun to 3469 Ω in the dark. This behavior is mainly due to the drop of the charge density of the solar cell with the decreasing of illumination intensity.

From C_{HF} and R_{HF} we calculate the high-frequency relaxation time τ_{HF} and the bandwidth as shown in Figure

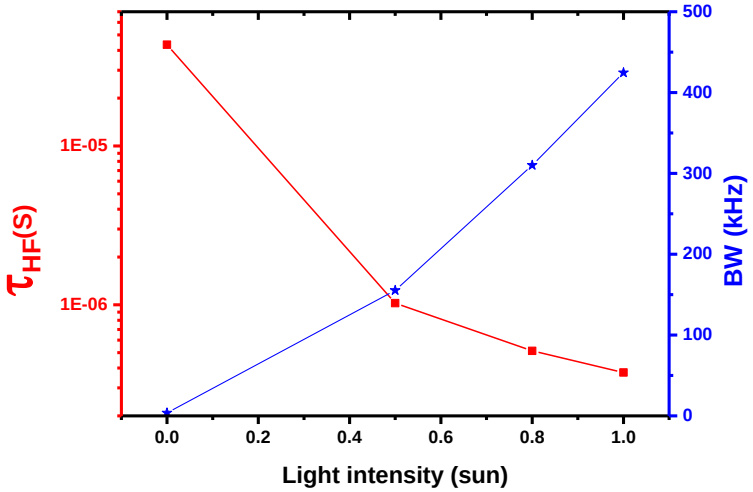

Figure A. 2: The high-frequency relaxation time and the bandwidth as a function of light intensity

The high-frequency relaxation process of the perovskite solar cell is getting slower with the decrease of the light intensity which causes a significant drop of the bandwidth it goes from

424 kHz at 1 sun to 155kHz at 0.5 sun which is a big loss in the bandwidth caused by the behavior of the high-frequency resistance.

We can conclude that the bandwidth of the solar cell is light intensity-dependent due to the light dependency of R_{HF}, this behavior may present a serious limitation for the VLC systems especially in low light intensity applications (indoor for example). Therefore, perovskite solar cells must be under a high-intensity illumination to have a good data rate. The origin of the incident light is not important, whether it can come from the intense modulated source (LED, laser) or the environment that provides static light intensity such as the sun or the other sources of artificial illumination. Moreover, reducing R_{HF} by optimizing the ETL and HTL can reduce the impact of the light intensity.

[1] G. Forecast, “Cisco visual networking index: global mobile data traffic forecast update, 2017–2022,” *Update*, vol. 2017, p. 2022, 2019.

[2] Cisco, “Cisco Vision: 5G – THRIVING INDOORS,” *Cisco White Pap.*, pp. 1–6, 2017, [Online]. Available: https://www.cisco.com/c/dam/en/us/solutions/collateral/service-provider/ultra-services-platform/5g-ran-indoor.pdf.

[3] S. Zhang *et al.*, “Organic solar cells as high-speed data detectors for visible light communication,” *Optica*, vol. 2, no. 7, pp. 607–610, 2015, doi: 10.1364/OPTICA.2.000607.

[4] V. W. S. Wong, R. Schober, D. Wing, K. Ng, and L. Wang, *Key Technologies for 5G Wireless Systems*. 2017.

[5] H. Haas, L. Yin, Y. Wang, and C. Chen, “What is lifi?,” *J. Light. Technol.*, vol. 34, no. 6, pp. 1533–1544, 2015.

[6] W. Iarc, “IARC Classifies Radiofrequency Electromagnetic Fields as Possibly Cancinogenic to Humans. International Agency for Research on Cancer,” Lyon, Tech Rep, 2011.

[7] A. E. Ibhaze, P. E. Orukpe, and F. O. Edeko, “High capacity data rate system: Review of visible light communications technology,” *J. Electron. Sci. Technol.*, vol. 18, no. 3, p. 100055, 2020, doi: https://doi.org/10.1016/j.jnlest.2020.100055.

[8] A. S. G. Andrae and T. Edler, “On global electricity usage of communication technology: trends to 2030,” *Challenges*, vol. 6, no. 1, pp. 117–157, 2015.

[9] Z. Wang, D. Tsonev, S. Videv, and H. Haas, “Towards Self-powered Solar Panel Receiver for Optical Wireless Communication,” *IEEE Int. Conf. Commun.*, pp. 3348–3353, 2014.

[10] Z. Wang, D. Tsonev, S. Videv, and H. Haas, “On the Design of a Solar-Panel Receiver for Optical Wireless Communications With Simultaneous Energy Harvesting,” *IEEE J. Sel. AREAS Commun. VOL.*, vol. 33, no. 8, pp. 1612–1623, 2015.

[11] H. Zheng *et al.*, “Emerging organic/hybrid photovoltaic cells for indoor applications: recent advances and perspectives,” *Sol. RRL*, vol. 5, no. 7, p. 2100042, 2021.

[12] N. Mica *et al.*, “Triple cation perovskite solar cells for visible light communications,” *Photonics Res.*, vol. 8, no. 8, pp. 16–24, 2020, doi: 10.1364/prj.393647.

[13] I. Mathews, S. N. Kantareddy, T. Buonassisi, and I. M. Peters, “Technology and market perspective for indoor photovoltaic cells,” *Joule*, vol. 3, no. 6, pp. 1415–1426, 2019.

[14] J. Dagar, S. Castro-Hermosa, G. Lucarelli, F. Cacialli, and T. M. Brown, “Highly efficient perovskite solar cells for light harvesting under indoor illumination via solution processed SnO2/MgO composite electron transport layers,” *Nano Energy*, vol. 49, pp. 290–299, 2018.

[15] C. H. Sterling, *Military communications: from ancient times to the 21st century*. Abc-clio, 2008.

[16] P. A. Clayton, “The Pharos at Alexandria,” *Seven Wonders Anc. World*, pp. 138–157, 1988.

[17] “The Pharos of Alexandria.” https://www.dkfindout.com/us/history/seven-wonders-world/lighthouse-at-alexandria/.

[18] “Man holds two signal fire SOS signal with hand flare.” https://depositphotos.com/188081476/stock-video-man-holds-two-signal-fire.html.

[19] A. G. Bell, “ART. XXXIV.--On the Production and Reproduction of Sound by Light,” *Am. J. Sci.*, vol. 20, no. 118, p. 305, 1880.

[20] A. A. Huurdeman, *The worldwide history of telecommunications*. John Wiley & Sons, 2003.

[21] A. M. Noll, *Principles of modern communications technology*. Artech House, 2001.

[22] Z. Ghassemlooy, W. Popoola, and S. Rajbhandari, *Optical wireless communications: system and channel modelling with Matlab®*. CRC press, 2019.

[23] S. A. Townes *et al.*, “The Mars laser communication demonstration,” in *2004 IEEE Aerospace Conference Proceedings (IEEE Cat. No. 04TH8720)*, 2004, vol. 2, pp. 1180–1195.

[24] Z. Sodnik, B. Furch, and H. Lutz, “Free-space laser communication activities in Europe: SILEX and beyond,” in *LEOS 2006-19th Annual Meeting of the IEEE Lasers*

and Electro-Optics Society, 2006, pp. 78–79.

[25] “Visible Light Communication Consortium (VLCC).” http://vlcc.net.

[26] “Li-Fi Consortium.” .

[27] G. Pang, T. Kwan, C.-H. Chan, and H. Liu, “LED traffic light as a communications device,” in *Proceedings 199 IEEE/IEEJ/JSAI International Conference on Intelligent Transportation Systems (Cat. No. 99TH8383)*, 1999, pp. 788–793.

[28] “Visible Light Communications Consortium (VLCC) Released Visible Light Communication Standard Based on IrDA Core Specification.” http://www.vlcc.net/pr/090312_e.pdf.

[29] “Standardization Committee VLCC ‘Visible optical communication system’ and ‘Visible light ID system.’” http://www.vlcc.net/modules/xpage2/index.php?id=6&ml_lang=en.

[30] S. Kim, J. Won, and A. O. C. Efficiency, “Simultaneous Reception of Visible Light Communication and Optical Energy using a Solar Cell Receiver,” pp. 896–897, 2013.

[31] P. A. Haigh, Z. Ghassemlooy, S. Rajbhandari, I. Papakonstantinou, and W. Popoola, “Visible light communications: 170 Mb/s using an artificial neural network equalizer in a low bandwidth white light configuration,” *J. Light. Technol.*, vol. 32, no. 9, pp. 1807–1813, 2014.

[32] D. Tsonev *et al.*, “A 3-Gb / s Single-LED OFDM-Based Wireless VLC Link Using a Gallium Nitride μ LED,” vol. 26, no. 7, pp. 637–640, 2014.

[33] Y. Wang, L. Tao, X. Huang, J. Shi, and N. Chi, “8-Gb/s RGBY LED-based WDM VLC system employing high-order CAP modulation and hybrid post equalizer,” *IEEE Photonics J.*, vol. 7, no. 6, pp. 1–7, 2015.

[34] H. Chun *et al.*, “LED based wavelength division multiplexed 10 Gb/s visible light communications,” *J. Light. Technol.*, vol. 34, no. 13, pp. 3047–3052, 2016.

[35] X. Liu *et al.*, “Gbps long-distance real-time visible light communications using a high-bandwidth GaN-based micro-LED,” *IEEE Photonics J.*, vol. 9, no. 6, pp. 1–9, 2017.

[36] R. Bian, I. Tavakkolnia, and H. Haas, “15 . 73 Gb / s Visible Light Communication with,” *J. Light. Technol.*, vol. PP, no. c, p. 1, 2019, doi: 10.1109/JLT.2019.2906464.

[37] H. Chun, A. Gomez, C. Quintana, W. Zhang, G. Faulkner, and D. O. Brien, “OPEN A Wide-Area Coverage 35 Gb / s Visible Light Communications Link for Indoor Wireless Applications,” pp. 4–11, 2019, doi: 10.1038/s41598-019-41397-6.

[38] I. Tavakkolnia *et al.*, “Organic photovoltaics for simultaneous energy harvesting and high-speed MIMO optical wireless communications,” *Light Sci. Appl.*, vol. 10, no. 1, pp. 1–11, 2021.

[39] J. Fakidis, H. Helmers, and H. Haas, “Simultaneous wireless data and power transfer for a 1-Gb/s GaAs VCSEL and photovoltaic link,” *IEEE Photonics Technol. Lett.*, vol. 32, no. 19, pp. 1277–1280, 2020.

[40] “The National Highway Traffic Safety Administration (NHTSA) Moving Ahead With Car-to-Car Communication.” https://www.autoguide.com/auto-news/2014/02/nhtsa-moving-ahead-car-car-communication.html.

[41] B. A. Vijayalakshmi and M. N. Sudha, “A Novel Approach to Using Energy-Efficient LED-Based Visible Light Communication in Hospitals,” in *Intelligent and Efficient Electrical Systems*, Springer, 2018, pp. 197–204.

[42] Y. Zhou *et al.*, “Common-anode LED on a Si substrate for beyond 15 Gbit/s underwater visible light communication,” *Photonics Res.*, vol. 7, no. 9, pp. 1019–1029, 2019, doi: 10.1364/PRJ.7.001019.

[43] C. Shen *et al.*, “20-meter underwater wireless optical communication link with 1.5 Gbps data rate,” *Opt. Express*, vol. 24, no. 22, pp. 25502–25509, 2016, doi: 10.1364/OE.24.025502.

[44] Unios Australia PTY LTD, “Driving the Flicker-Free Effect Whitepaper,” 2019, [Online]. Available: https://unios.com/wp-content/uploads/2019/02/UN_Driving-the-Flicker-Free-Effect_White-Paper-190205.pdf.

[45] C. Hsu, C. Chow, I. Lu, Y. Liu, C. Yeh, and Y. Liu, “High Speed Imaging 3 × 3 MIMO Phosphor White-Light LED Based Visible Light Communication System,” *IEEE Photonics J.*, vol. 8, no. 6, pp. 1–6, 2016, doi: 10.1109/JPHOT.2016.2633395.

[46] I.-C. Lu, C.-H. Lai, C.-H. Yeh, and J. Chen, “6.36 Gbit/s RGB LED-based WDM MIMO Visible Light Communication System Employing OFDM Modulation,” in *Optical Fiber Communication Conference*, 2017, p. W2A.39, doi:

10.1364/OFC.2017.W2A.39.

[47] N. Sharan, S. K. Ghorai, and A. Kumar, “Peak-to-Average Power Ratio (PAPR) Reduction Using Combination of Precoding and Companding Techniques for VLC OFDM Systems,” in *2019 TEQIP III Sponsored International Conference on Microwave Integrated Circuits, Photonics and Wireless Networks (IMICPW)*, 2019, pp. 149–153, doi: 10.1109/IMICPW.2019.8933194.

[48] Y. Zhao and J. Vongkulbhisal, “Design of visible light communication receiver for on-off keying modulation by adaptive minimum-voltage cancelation,” *Eng. J.*, vol. 17, no. 4, pp. 125–130, 2013.

[49] S. Biswas and H. Kim, “Solar Cells for Indoor Applications: Progress and Development,” *Polymers* , vol. 12, no. 6. 2020, doi: 10.3390/polym12061338.

[50] R. Cheng *et al.*, “Tailoring triple-anion perovskite material for indoor light harvesting with restrained halide segregation and record high efficiency beyond 36%,” *Adv. Energy Mater.*, vol. 9, no. 38, p. 1901980, 2019.

[51] E. Bialic, L. Maret, and D. Kténas, “Specific innovative semi-transparent solar cell for indoor and outdoor LiFi applications,” *Appl. Opt.*, vol. 54, no. 27, pp. 8062–8069, 2015.

[52] B. Malik and X. Zhang, “Solar Panel Receiver System Implementation for Visible Light Communication,” pp. 502–503, 2015.

[53] W.-H. Shin, S.-H. Yang, D.-H. Kwon, and S.-K. Han, “Self-reverse-biased solar panel optical receiver for simultaneous visible light communication and energy harvesting,” *Opt. Express*, vol. 24, no. 22, pp. A1300–A1305, 2016.

[54] J. Wu, C. Chow, Y. Liu, C. Hsu, and C. Yeh, “Performance enhancement technique of visible light communications using passive photovoltaic cell,” *Opt. Commun.*, vol. 392, no. February, pp. 119–122, 2017, doi: 10.1016/j.optcom.2017.01.052.

[55] H.-Y. Wang *et al.*, “Using pre-distorted PAM-4 signal and parallel resistance circuit to enhance the passive solar cell based visible light communication,” *Opt. Commun.*, vol. 407, pp. 245–249, 2018.

[56] A. Kojima, K. Teshima, Y. Shirai, and T. Miyasaka, “Organometal halide perovskites as visible-light sensitizers for photovoltaic cells,” *J. Am. Chem. Soc.*, vol. 131, no. 17,

pp. 6050–6051, 2009.

[57] H.-S. Kim *et al.*, "Lead iodide perovskite sensitized all-solid-state submicron thin film mesoscopic solar cell with efficiency exceeding 9%," *Sci. Rep.*, vol. 2, no. 1, pp. 1–7, 2012.

[58] M. M. Lee, J. Teuscher, T. Miyasaka, T. N. Murakami, and H. J. Snaith, "Efficient hybrid solar cells based on meso-superstructured organometal halide perovskites.," *Science*, vol. 338, no. 6107, pp. 643–7, Nov. 2012, doi: 10.1126/science.1228604.

[59] NERL, "Best research-cell efficiencies," 2020. https://www.nrel.gov/pv/cell-efficiency.html.

[60] M. Kim, "Perovskite photovoltaics: the road ahead," *Opt. Photonics News*, vol. 31, no. 11, pp. 32–39, 2020.

[61] Z. Yi, N. H. Ladi, X. Shai, H. Li, Y. Shen, and M. Wang, "Will organic–inorganic hybrid halide lead perovskites be eliminated from optoelectronic applications?," *Nanoscale Adv.*, vol. 1, no. 4, pp. 1276–1289, 2019.

[62] Z. Li, M. Yang, J.-S. Park, S.-H. Wei, J. J. Berry, and K. Zhu, "Stabilizing perovskite structures by tuning tolerance factor: formation of formamidinium and cesium lead iodide solid-state alloys," *Chem. Mater.*, vol. 28, no. 1, pp. 284–292, 2016.

[63] A. A. Bakulin *et al.*, "Real-time observation of organic cation reorientation in methylammonium lead iodide perovskites," *J. Phys. Chem. Lett.*, vol. 6, no. 18, pp. 3663–3669, 2015.

[64] W. Travis, E. N. K. Glover, H. Bronstein, D. O. Scanlon, and R. G. Palgrave, "On the application of the tolerance factor to inorganic and hybrid halide perovskites: a revised system," *Chem. Sci.*, vol. 7, no. 7, pp. 4548–4556, 2016.

[65] M. R. Filip, G. E. Eperon, H. J. Snaith, and F. Giustino, "Steric engineering of metal-halide perovskites with tunable optical band gaps," *Nat. Commun.*, vol. 5, no. 1, pp. 1–9, 2014.

[66] M. Saliba *et al.*, "Cesium-containing triple cation perovskite solar cells: improved stability, reproducibility and high efficiency," *Energy Environ. Sci.*, vol. 9, no. 6, pp. 1989–1997, 2016.

[67] S. Mahesh *et al.*, “Revealing the origin of voltage loss in mixed-halide perovskite solar cells,” *Energy Environ. Sci.*, vol. 13, no. 1, pp. 258–267, 2020.

[68] M. Grundmann, “The Physics of Semiconductors. Graduate Texts in Physics.” Springer-Verlag Berlin Heidelberg, 2010.

[69] T. S. Moss, G. J. Burrell, and B. Ellis, *Semiconductor Opto-Electronics Chapter 3 - ABSORPTION PROCESSES IN SEMICONDUCTORS*. 1973.

[70] F. Urbach, “The Long-Wavelength Edge of Photographic Sensitivity and of the Electronic Absorption of Solids,” *Phys. Rev.*, vol. 92, no. 5, p. 1324, Dec. 1953, doi: 10.1103/PhysRev.92.1324.

[71] S. Sindhu, S. Sanghi, A. Agarwal, V. P. Seth, and N. Kishore, “Effect of Bi2O3 content on the optical band gap, density and electrical conductivity of MO· Bi2O3· B2O3 (M= Ba, Sr) glasses,” *Mater. Chem. Phys.*, vol. 90, no. 1, pp. 83–89, 2005.

[72] M. Shirayama *et al.*, “Optical transitions in hybrid perovskite solar cells: ellipsometry, density functional theory, and quantum efficiency analyses for CH 3 NH 3 PbI 3,” *Phys. Rev. Appl.*, vol. 5, no. 1, p. 14012, 2016.

[73] S. Rühle, “Tabulated values of the Shockley–Queisser limit for single junction solar cells,” *Sol. Energy*, vol. 130, pp. 139–147, 2016, doi: https://doi.org/10.1016/j.solener.2016.02.015.

[74] X. Chen, H. Lu, Y. Yang, and M. C. Beard, “Excitonic effects in methylammonium lead halide perovskites,” *J. Phys. Chem. Lett.*, vol. 9, no. 10, pp. 2595–2603, 2018.

[75] M. Saba, F. Quochi, A. Mura, and G. Bongiovanni, “Excited state properties of hybrid perovskites,” *Acc. Chem. Res.*, vol. 49, no. 1, pp. 166–173, 2016.

[76] Y. Xie and H. Wu, “Balancing charge generation and voltage loss toward efficient nonfullerene organic solar cells,” *Mater. Today Adv.*, vol. 5, p. 100048, 2020.

[77] C. L. Davies *et al.*, “Bimolecular recombination in methylammonium lead triiodide perovskite is an inverse absorption process,” *Nat. Commun.*, vol. 9, no. 1, pp. 1–9, 2018.

[78] W. Shockley and W. T. Read Jr, “Statistics of the recombinations of holes and electrons,” *Phys. Rev.*, vol. 87, no. 5, p. 835, 1952.

[79] W.-J. Yin, T. Shi, and Y. Yan, “Unusual defect physics in CH3NH3PbI3 perovskite solar cell absorber,” *Appl. Phys. Lett.*, vol. 104, no. 6, p. 63903, 2014.

[80] R. L. Milot, G. E. Eperon, H. J. Snaith, M. B. Johnston, and L. M. Herz, “Temperature-dependent charge-carrier dynamics in CH3NH3PbI3 perovskite thin films,” *Adv. Funct. Mater.*, vol. 25, no. 39, pp. 6218–6227, 2015.

[81] M. B. Johnston and L. M. Herz, “Hybrid perovskites for photovoltaics: charge-carrier recombination, diffusion, and radiative efficiencies,” *Acc. Chem. Res.*, vol. 49, no. 1, pp. 146–154, 2016.

[82] P. Landsberg, “An introduction to the theory of photovoltaic cells,” *Solid. State. Electron.*, vol. 18, no. 12, pp. 1043–1052, 1975.

[83] S. Karthick, H. Hawashin, N. Parou, S. Vedraine, S. Velumani, and J. Bouclé, “Copper and Bismuth incorporated mixed cation perovskite solar cells by one-step solution process,” *Sol. Energy*, vol. 218, pp. 226–236, 2021.

[84] S. Karthick, S. Velumani, and J. Bouclé, “Experimental and SCAPS simulated formamidinium perovskite solar cells: A comparison of device performance,” *Sol. Energy*, vol. 205, pp. 349–357, 2020.

[85] R. Belchi *et al.*, “One-step synthesis of TiO2/graphene nanocomposites by laser pyrolysis with well-controlled properties and application in perovskite solar cells,” *ACS omega*, vol. 4, no. 7, pp. 11906–11913, 2019.

[86] A. Gheno *et al.*, “Toward highly efficient inkjet-printed perovskite solar cells fully processed under ambient conditions and at low temperature,” *Sol. RRL*, vol. 2, no. 11, p. 1800191, 2018.

[87] T. Leijtens, G. E. Eperon, S. Pathak, A. Abate, M. M. Lee, and H. J. Snaith, “Overcoming ultraviolet light instability of sensitized TiO 2 with meso-superstructured organometal tri-halide perovskite solar cells,” *Nat. Commun.*, vol. 4, no. 1, pp. 1–8, 2013.

[88] J. Kim, K. S. Kim, and C. W. Myung, “Efficient electron extraction of SnO 2 electron transport layer for lead halide perovskite solar cell,” *npj Comput. Mater.*, vol. 6, no. 1, pp. 1–8, 2020.

[89] M. Plakhotnyuk, “Nanostructured Heterojunction Crystalline Silicon Solar Cells with

Transition Metal Oxide Carrier Selective Contacts," 2018.

[90] P. Wang, M. Ulfa, and T. Pauporte, "Effects of Perovskite Monovalent Cation Composition on the High and Low Frequency Impedance Response of Efficient Solar Cells Effects of Perovskite Monovalent Cation Composition on the High and Low Frequency Impedance Response of Efficient Solar Cells," 2018, doi: 10.1021/acs.jpcc.7b11010.

[91] B. Chen, M. Yang, S. Priya, and K. Zhu, "Origin of J–V hysteresis in perovskite solar cells," *J. Phys. Chem. Lett.*, vol. 7, no. 5, pp. 905–917, 2016.

[92] H. J. Snaith *et al.*, "Anomalous hysteresis in perovskite solar cells," *J. Phys. Chem. Lett.*, vol. 5, no. 9, pp. 1511–1515, 2014.

[93] H. S. Kim *et al.*, "Control of I-V Hysteresis in CH3NH3PbI3 Perovskite Solar Cell," *Journal of Physical Chemistry Letters*, vol. 6, no. 22. pp. 4633–4639, 2015, doi: 10.1021/acs.jpclett.5b02273.

[94] O. Almora, I. Zarazua, E. Mas-Marza, I. Mora-Sero, J. Bisquert, and G. Garcia-Belmonte, "Capacitive dark currents, hysteresis, and electrode polarization in lead halide perovskite solar cells," *J. Phys. Chem. Lett.*, vol. 6, no. 9, pp. 1645–1652, 2015.

[95] Q. Dong *et al.*, "Improved SnO2 electron transport layers solution-deposited at near room temperature for rigid or flexible perovskite solar cells with high efficiencies," *Adv. Energy Mater.*, vol. 9, no. 26, p. 1900834, 2019.

[96] A. Gheno, S. Vedraine, B. Ratier, and J. Bouclé, "π-Conjugated Materials as the Hole-Transporting Layer in Perovskite Solar Cells," *Metals (Basel).*, vol. 6, no. 3, p. 21, Jan. 2016, doi: 10.3390/met6010021.

[97] Q. Jiang *et al.*, "Surface passivation of perovskite film for efficient solar cells," *Nat. Photonics*, vol. 13, no. 7, pp. 460–466, 2019.

[98] Q. Jiang *et al.*, "Enhanced electron extraction using SnO 2 for high-efficiency planar-structure HC (NH 2) 2 PbI 3-based perovskite solar cells," *Nat. Energy*, vol. 2, no. 1, pp. 1–7, 2016.

[99] J. Wei *et al.*, "SnO2-in-polymer matrix for high-efficiency perovskite solar cells with improved reproducibility and stability," *Adv. Mater.*, vol. 30, no. 52, p. 1805153, 2018.

[100] S. S. Barkade *et al.*, “Ultrasound assisted synthesis of polythiophene/SnO2 hybrid nanolatex particles for LPG sensing,” *Chem. Eng. Process. Process Intensif.*, vol. 74, pp. 115–123, 2013.

[101] T. Q. Bui, H. T. M. Ngo, and H. T. Tran, “Surface-protective assistance of ultrasound in synthesis of superparamagnetic magnetite nanoparticles and in preparation of mono-core magnetite-silica nanocomposites,” *J. Sci. Adv. Mater. Devices*, vol. 3, no. 3, pp. 323–330, 2018.

[102] C. Yang, G. Wang, Z. Lu, J. Sun, J. Zhuang, and W. Yang, “Effect of ultrasonic treatment on dispersibility of Fe 3 O 4 nanoparticles and synthesis of multi-core Fe 3 O 4/SiO 2 core/shell nanoparticles,” *J. Mater. Chem.*, vol. 15, no. 39, pp. 4252–4257, 2005.

[103] C. Liu *et al.*, “Hydrothermally treated SnO2 as the electron transport layer in high-efficiency flexible perovskite solar cells with a certificated efficiency of 17.3%,” *Adv. Funct. Mater.*, vol. 29, no. 47, p. 1807604, 2019.

[104] C. Xu, Z. Liu, Q. Sun, and E.-C. Lee, “Morphology control of SnO2 layer by solvent engineering for efficient perovskite solar cells,” *Sol. Energy*, vol. 214, pp. 280–287, 2021.

[105] W. Ke *et al.*, “Efficient hole-blocking layer-free planar halide perovskite thin-film solar cells,” *Nat. Commun.*, vol. 6, no. 1, pp. 1–7, 2015.

[106] K. Jung *et al.*, “Influence of a UV-ozone treatment on amorphous SnO2 electron selective layers for highly efficient planar MAPbI3 perovskite solar cells,” *J. Mater. Sci. Technol.*, vol. 59, pp. 195–202, 2020.

[107] P. F. Méndez, S. K. M. Muhammed, E. M. Barea, S. Masi, and I. Mora-Sero, “Analysis of the UV–Ozone-Treated SnO2 Electron Transporting Layer in Planar Perovskite Solar Cells for High Performance and Reduced Hysteresis,” *Sol. RRL*, vol. 3, no. 9, p. 1900191, 2019.

[108] F. Yang and P. Feng, “Densities and Viscosities of Ionic Liquid with Organic Solvents,” *Appl. Sci.*, vol. 10, no. 23, p. 8342, 2020.

[109] V. Martin *et al.*, “Harnessing polarity and viscosity to identify green binary solvent mixtures as viable alternatives to DMF in solid-phase peptide synthesis,” *Green*

Chem., 2021.

[110] M. Xiao *et al.*, "A fast deposition-crystallization procedure for highly efficient lead iodide perovskite thin-film solar cells," *Angew. Chemie Int. Ed.*, vol. 53, no. 37, pp. 9898–9903, 2014.

[111] B.-E. Cohen, S. Aharon, A. Dymshits, and L. Etgar, "Impact of antisolvent treatment on carrier density in efficient hole-conductor-free perovskite-based solar cells," *J. Phys. Chem. C*, vol. 120, no. 1, pp. 142–147, 2016.

[112] M. Xiao *et al.*, "Selection of an anti-solvent for efficient and stable cesium-containing triple cation planar perovskite solar cells," *Nanoscale*, vol. 10, no. 25, pp. 12141–12148, 2018.

[113] I. BrandTech Scientific, "Solvent Boiling Points Chart," 2020. https://www.brandtech.com/solventboilingpointschart/.

[114] H. Gao *et al.*, "Nucleation and crystal growth of organic–inorganic lead halide perovskites under different relative humidity," *ACS Appl. Mater. Interfaces*, vol. 7, no. 17, pp. 9110–9117, 2015.

[115] Q. Wali, F. J. Iftikhar, M. E. Khan, A. Ullah, Y. Iqbal, and R. Jose, "Advances in stability of perovskite solar cells," *Org. Electron.*, vol. 78, p. 105590, 2020.

[116] Q. Wang, N. Phung, D. Di Girolamo, P. Vivo, and A. Abate, "Enhancement in lifespan of halide perovskite solar cells," *Energy Environ. Sci.*, vol. 12, no. 3, pp. 865–886, 2019.

[117] L. Meng, J. You, and Y. Yang, "Addressing the stability issue of perovskite solar cells for commercial applications," *Nat. Commun.*, vol. 9, no. 1, pp. 1–4, 2018.

[118] J. Lee, D. Kim, H. Kim, S. Seo, S. M. Cho, and N. Park, "Formamidinium and cesium hybridization for photo-and moisture-stable perovskite solar cell," *Adv. Energy Mater.*, vol. 5, no. 20, p. 1501310, 2015.

[119] F. Fabregat-Santiago, J. Bisquert, G. Garcia-Belmonte, G. Boschloo, and A. Hagfeldt, "Influence of electrolyte in transport and recombination in dye-sensitized solar cells studied by impedance spectroscopy," *Sol. Energy Mater. Sol. Cells*, vol. 87, no. 1–4, pp. 117–131, 2005.

[120] G. Garcia-Belmonte, A. Guerrero, and J. Bisquert, “Elucidating operating modes of bulk-heterojunction solar cells from impedance spectroscopy analysis,” *J. Phys. Chem. Lett.*, vol. 4, no. 6, pp. 877–886, 2013.

[121] J. Bisquert, L. Bertoluzzi, I. Mora-Sero, and G. Garcia-Belmonte, “Theory of impedance and capacitance spectroscopy of solar cells with dielectric relaxation, drift-diffusion transport, and recombination,” *J. Phys. Chem. C*, vol. 118, no. 33, pp. 18983–18991, 2014.

[122] E. Von Hauff, “Impedance spectroscopy for emerging photovoltaics,” *J. Phys. Chem. C*, vol. 123, no. 18, pp. 11329–11346, 2019.

[123] J.-B. Jorcin, M. E. Orazem, N. Pébère, and B. Tribollet, “CPE analysis by local electrochemical impedance spectroscopy,” *Electrochim. Acta*, vol. 51, no. 8–9, pp. 1473–1479, 2006.

[124] D. D. Macdonald, “Reflections on the history of electrochemical impedance spectroscopy,” *Electrochim. Acta*, vol. 51, no. 8–9, pp. 1376–1388, 2006.

[125] V. F. Lvovich, *Impedance spectroscopy: applications to electrochemical and dielectric phenomena*. John Wiley & Sons, 2012.

[126] D. Pitarch-Tena, T. T. Ngo, M. Vallés-Pelarda, T. Pauporté, and I. Mora-Seró, “Impedance spectroscopy measurements in perovskite solar cells: device stability and noise reduction,” *ACS Energy Lett.*, vol. 3, no. 4, pp. 1044–1048, 2018.

[127] P. Wang, M. Ulfa, and T. Pauporté, “Effects of Perovskite Monovalent Cation Composition on the High and Low Frequency Impedance Response of Efficient Solar Cells,” *J. Phys. Chem. C*, vol. 122, no. 4, pp. 1973–1981, 2018, doi: 10.1021/acs.jpcc.7b11010.

[128] P. Wang, Z. Shao, M. Ulfa, and T. Pauporté, “Insights into the hole blocking layer effect on the perovskite solar cell performance and impedance response,” *J. Phys. Chem. C*, vol. 121, no. 17, pp. 9131–9141, 2017.

[129] E. J. Juarez-Perez *et al.*, “Role of the selective contacts in the performance of lead halide perovskite solar cells,” *J. Phys. Chem. Lett.*, vol. 5, no. 4, pp. 680–685, 2014.

[130] M. Ulfa, T. Pauporté, T.-T. Bui, and F. Goubard, “Impact of organic hole transporting material and doping on the electrical response of perovskite solar cells,” *J. Phys.*

Chem. C, vol. 122, no. 22, pp. 11651–11658, 2018.

[131] A. Pockett, G. E. Eperon, N. Sakai, H. J. Snaith, L. M. Peter, and P. J. Cameron, "Microseconds, milliseconds and seconds: deconvoluting the dynamic behaviour of planar perovskite solar cells," *Phys. Chem. Chem. Phys.*, vol. 19, no. 8, pp. 5959–5970, 2017.

[132] Research solutions &resources, "Inductance and Inductive Loops and Instrumental Artifacts." http://www.consultrsr.net/resources/eis/induct1.htm#ref1.

[133] C. M. J.-P. Diard, B. Le Gorrec, *Handbook of Electrochemical Impedance Spectroscopy, CIRCUITSmade of RESISTORS, INDUCTORS and CAPACITORS*, Bio-Logic. 2011.

[134] B. W. Veal, P. M. Baldo, A. P. Paulikas, and J. A. Eastman, "Understanding artifacts in impedance spectroscopy," *J. Electrochem. Soc.*, vol. 162, no. 1, p. H47, 2014.

[135] I. Zarazua *et al.*, "Operating mechanisms of mesoscopic perovskite solar cells through impedance spectroscopy and J–V modeling," *J. Phys. Chem. Lett.*, vol. 8, no. 24, pp. 6073–6079, 2017.

[136] G. J. Brug, A. L. G. van den Eeden, M. Sluyters-Rehbach, and J. H. Sluyters, "The analysis of electrode impedances complicated by the presence of a constant phase element," *J. Electroanal. Chem. interfacial Electrochem.*, vol. 176, no. 1–2, pp. 275–295, 1984.

[137] J. Bisquert, G. Garcia-Belmonte, P. Bueno, E. Longo, and L. O. S. Bulhoes, "Impedance of constant phase element (CPE)-blocked diffusion in film electrodes," *J. Electroanal. Chem.*, vol. 452, no. 2, pp. 229–234, 1998.

[138] C. H. Hsu and F. Mansfeld, "Technical Note : Concerning the Conversion of the Constant Phase Element Parameter Y 0 into a Capacitance," vol. 57, no. 9, pp. 747–748, 2001.

[139] H.-S. Kim *et al.*, "Mechanism of carrier accumulation in perovskite thin-absorber solar cells," *Nat. Commun.*, vol. 4, no. 1, pp. 1–7, 2013.

[140] R. S. Sanchez *et al.*, "Slow dynamic processes in lead halide perovskite solar cells. Characteristic times and hysteresis," *J. Phys. Chem. Lett.*, vol. 5, no. 13, pp. 2357–2363, 2014.

[141] P. A. Cotfas, D. T. Cotfas, P. N. Borza, D. Sera, and R. Teodorescu, “Solar cell capacitance determination based on an RLC resonant circuit,” *Energies*, vol. 11, no. 3, p. 672, 2018.

[142] J. Bisquert, “Chemical capacitance of nanostructured semiconductors: its origin and significance for nanocomposite solar cells,” *Phys. Chem. Chem. Phys.*, vol. 5, no. 24, pp. 5360–5364, 2003.

[143] F. Fabregat-santiago and J. Bisquert, “Characterization of nanostructured hybrid and organic solar cells by impedance spectroscopy w,” pp. 9083–9118, 2011, doi: 10.1039/c0cp02249g.

[144] F. Fabregat-Santiago, G. Garcia-Belmonte, I. Mora-Sero, and J. Bisquert, “Characterization of nanostructured hybrid and organic solar cells by impedance spectroscopy,” *Phys. Chem. Chem. Phys.*, vol. 13, no. 20, pp. 9083–9118, 2011.

[145] J.-P. Correa-Baena *et al.*, “Changes from bulk to surface recombination mechanisms between pristine and cycled perovskite solar cells,” *ACS Energy Lett.*, vol. 2, no. 3, pp. 681–688, 2017.

[146] E. Von Hau, “Impedance Spectroscopy for Emerging Photovoltaics,” *J. Phys. Chem. C*, 2019, doi: 10.1021/acs.jpcc.9b00892.

[147] C. Rawlins, *Basic AC circuits, CHAPTER 6 - Capacitance*. Elsevier, 2000.

[148] “Capacitive Reactance for Low Pass Filter and High Pass Filter.” https://www.electronics-tutorials.ws/filter/filter_1.html.

[149] N. Lorrière *et al.*, “Photovoltaic solar cells for outdoor LiFi communications,” *J. Light. Technol.*, vol. 38, no. 15, pp. 3822–3831, 2020.

[150] P. Wang, M. Ulfa, and T. Pauporté, “Effects of perovskite monovalent cation composition on the high and low frequency impedance response of efficient solar cells,” *J. Phys. Chem. C*, vol. 122, no. 4, pp. 1973–1981, 2018.

[151] N. Lorrière, “Cellules photovoltaïques pour la récupération d’énergie et la communication de données.” Aix-Marseille Université (AMU); IM2NP-Aix Marseille Université, 2019.

[152] Electronics-tutorials, “Passive Band Pass Filter.” https://www.electronics-

tutorials.ws/filter/filter_4.html.

[153] A. J. Frank, N. Kopidakis, and J. Van De Lagemaat, “Electrons in nanostructured TiO2 solar cells: transport, recombination and photovoltaic properties,” *Coord. Chem. Rev.*, vol. 248, no. 13–14, pp. 1165–1179, 2004.

[154] M. Wang, P. Chen, R. Humphry-Baker, S. M. Zakeeruddin, and M. Grätzel, “The influence of charge transport and recombination on the performance of dye-sensitized solar cells,” *ChemPhysChem*, vol. 10, no. 1, pp. 290–299, 2009.

[155] R. Long, W.-H. Fang, and O. V Prezhdo, “Strong interaction at the perovskite/TiO2 interface facilitates ultrafast photoinduced charge separation: A nonadiabatic molecular dynamics study,” *J. Phys. Chem. C*, vol. 121, no. 7, pp. 3797–3806, 2017.

[156] R. Long and O. V Prezhdo, “Dopants control electron–hole recombination at perovskite–TiO2 interfaces: ab initio time-domain study,” *ACS Nano*, vol. 9, no. 11, pp. 11143–11155, 2015.

[157] S. Prathapani, P. Bhargava, and S. Mallick, “Electronic band structure and carrier concentration of formamidinium–cesium mixed cation lead mixed halide hybrid perovskites,” *Appl. Phys. Lett.*, vol. 112, no. 9, p. 92104, 2018.

[158] A. Guerrero *et al.*, “Properties of contact and bulk impedances in hybrid lead halide perovskite solar cells including inductive loop elements,” *J. Phys. Chem. C*, vol. 120, no. 15, pp. 8023–8032, 2016.

[159] A. Guerrero, E. J. Juarez-Perez, J. Bisquert, I. Mora-Sero, and G. Garcia-Belmonte, “Electrical field profile and doping in planar lead halide perovskite solar cells,” *Appl. Phys. Lett.*, vol. 105, no. 13, p. 133902, 2014.

[160] E. J. Juarez-Perez *et al.*, “Photoinduced giant dielectric constant in lead halide perovskite solar cells,” *J. Phys. Chem. Lett.*, vol. 5, no. 13, pp. 2390–2394, 2014.

[161] R. K. Gunasekaran, D. Chinnadurai, A. R. Selvaraj, R. Rajendiran, K. Senthil, and K. Prabakar, “Revealing the self-degradation mechanisms in methylammonium lead iodide perovskites in dark and vacuum,” *ChemPhysChem*, vol. 19, no. 12, pp. 1507–1513, 2018.

[162] L. Zhu, C. Yang, and J. Qin, “An aggregation-induced blue shift of emission and the self-assembly of nanoparticles from a novel amphiphilic oligofluorene,” *Chem.*

Commun., no. 47, pp. 6303–6305, 2008.

[163] Z. Ghassemlooy *et al.*, "Visible light communications: 3.75 Mbits/s data rate with a 160 kHz bandwidth organic photodetector and artificial neural network equalization," *Photonics Res.*, vol. 1, no. 2, pp. 65–68, 2013.

LIST OF FIGURES

Figure I.1: Cisco forecast for mobile data traffic by 2022 [1] 12
Figure I.2: Share of communication technology of global electricity usage 2010–2030 [8] .. 14
Figure I.3: Left, The Pharos of Alexandria[14]. Right, Man holds two signal fire SOS signal with hand flare [15] 17
Figure I. 4: Alexander Graham Bell Photophone 18
Figure I.5: Vehicle-to-vehicle technology [37] 22
Figure I.6: Li-Fi technology in offices (left) and hospitals (right)[38] 23

Figure I.7: Illustration of human activities underwater demanding long-distance, high transmission speed, and large data rate wireless communications [40].....23
Figure I.8: Block diagram of a visible light communication (VLC) system where is the LED is the light-emitting diode and the PD is the photodetector.....24
Figure I.9: Phosphor-Converted and Red-Green-Blue LED.....27
Figure I.10: On-Off Keying data modulation 28
Figure I.11: a) Single carrier modulation, b) FDM, c) OFDM.....29
Figure I.12: I-V characteristic of the photodiode (the photoconductive and the photovoltaic modes).....31
Figure I.13: A simplified electrical equivalent circuit of a solar cell under a dynamic regime 34

Figure II.1: Evolution of the world record efficiencies of the different photovoltaic SCs technologies obtained in laboratory conditions [59].....40
Figure II. 2: Structure of ideal ABX3 perovskites[60] 41
Figure II. 3: Correlations between tolerance factor and crystal structure of perovskite materials [11] 43
Figure II. 4: Perovskite solar cell direct structure NIP (on the left), inverse structure PIN (on the right).....45
Figure II. 5: Electron transitions after light absorption in (a) direct bandgap semiconductors, and (b) indirect bandgap semiconductors [67].....46
Figure II. 6: Absorption coefficient (α) spectra of various solar cell materials [18] 48
Figure II. 7: Recombination mechanisms 49
Figure II. 8: Simple solar cell equivalent circuit.....51
Figure II. 9::Equivalent circuit of a solar cell in the dark.....52
Figure II. 10: A complete perovskite solar cell structure.....54
Figure II. 11: The design scheme of etched FTO layer on top of the glass substrate.....55
Figure II. 12: The design scheme of etched SnO2 layer on top of FTO.....56
Figure II. 13: The design scheme of the Perovskite layer on top of SnO_2.....58
Figure II. 14: Molecular structure of Spiro-OMeTAD 58
Figure II. 15: The design scheme of the Spiro-OMeTAD layer on top of the perovskite.....60
Figure II. 16: The thermal evaporator.....60
Figure II. 17: The design scheme of the complete solar cell with the gold electrode on top ..61
Figure II. 18: AMG1.5 and solar simulator irradiance spectra (left), Solar simulator and experimental set-up (right).....62
Figure II. 19: (a) Effect of series resistance (Rsh=const), (b) Effect of shunt resistance (Rs =const) [84].....64
Figure II. 20: J(V) and P(V) curves of a typical double cation perovskite solar cell 65

Figure III. 1: Optical microscope image showing the aggregates and pinholes in an SnO_2 film deposited by spin-coating on FTO.....70
Figure III. 2: Optic microscope image showing the aggregate and pinholes in SnO2 film (left)and a good SnO2 film (right).....71
Figure III. 3: AFM images of SnO2 NPs deposited on top of FTO without treatment (left) with treatment (right) 72

Figure III. 4: Optic microscope image showing FTO covered and uncoverd by the SnO_2 film 73
Figure III. 5: The contact angle.....73
Figure III. 6: The contact angle measurement of : SnO_2 drop on top of FTO substrate (top left), SnO2 +IPA drop on top of FTO substrate (top right), SnO2 + IPA drop on top of FTO substrate treated with UVO (bottom).....75
Figure III. 7: The contact angle measurement of: perovskite solution drop on top of SnO2 substrate (left), perovskite solution drop on top of SnO2 substrate treated with UVO (right) 76
Figure III. 8: JV curves of optimized and non-optimized SnO_2 mixed cation PSCs.....77
Figure III. 9: Statistical analysis of the reproducibility of the performances of optimized and non-optimized SnO2 PSCs 78
Figure III. 10: Perovskite solar cell etched with: a) DMSO b) DMF c) DMSO during the annealing d) DMF during the annealing 80
Figure III. 11: Uv-vis absorbance spectra of perovskite solar cell deposited with and without the antisolvent treatment 81
Figure III. 12: JV curves of PSCs obtained with and without the antisolvent treatment.....82
Figure III. 13: Illustration of circles and pinholes in the perovskite layer.....83
Figure III. 14: Optic microscope image showing a good perovskite film (a) Vs two bad perovskite films (showing a center circle (b) and craks (c)).....83
Figure III. 15: JV curves of PSCs 84
Figure III. 16: The fraction of having good perovskite films via different solvents 85
Figure III. 17: Fraction of good perovskite layers as a function of anti-solvent volume (DEE in this case) 86
Figure III. 18: The percentage of having good perovskite films from different solvents inside and outside of the glove box 87
Figure III. 19: statistical analysis of the reproducibility of the PV performances of optimized and non-optimized PSCs.....88
Figure III. 20: JV characteristics off a typical mixed cation PSC before and after IS.....90

Figure IV. 1 The input and the output signals in impedance spectroscopy 94
Figure IV. 2: Representation of the impedance Z.....96
Figure IV. 3: Nyquist plot of the impedance response of the resistor 97
Figure IV. 4: Nyquist plot of the impedance response of the capacitor 98
Figure IV. 5: Nyquist plot of the impedance response of the inductor.....99
Figure IV. 6: Nyquist plot of RC series circuit.....100
Figure IV. 7: Nyquist plot of R//C circuit.....101
Figure IV. 8: Impedance spectroscopy experimental setup 102
Figure IV. 9:The impedance response of a perovskite solar cell in the dark under different AC perturbation voltages.....104
Figure IV. 10:The impedance response of a perovskite solar cell in the dark under different DC voltages with a zoom on the high-frequency region (right) 105

Figure IV. 11: The impedance response of a perovskite solar cell under illumination under two DC voltages.....106
Figure IV. 12: The impedance response of a perovskite solar cell under illumination 107
Figure IV. 13: The graphical interface of ZView software. On the left: Nyquist plot. In the middle: Bode plots of the real and imaginary part of the impedance. On the right: equivalent electrical circuit built to fit the data. 109
Figure IV. 14: Impedance response of perovskite solar cell.....109
Figure IV. 15: Fitting of impedance response of a perovskite solar cell 111
Figure IV. 16: Fitting of impedance response of a perovskite solar cell by adding an inductor 112
Figure IV. 17: Voigt circuit model 114
Figure IV. 18: Illustration of the impedance response of a CPE 115
Figure IV. 19: Equivalent circuit employed for fitting the impedance spectra of perovskite solar cells 117
Figure IV. 20: the equivalent circuit used for modeling the impedance response of the PSCs. 118
Figure IV. 21: Low pass filter response.....120
Figure IV. 22: AC simplified equivalent circuit 121
Figure IV. 23: The capacitance of the solar cell as a function of frequency obtained by simulation [106].....122
Figure IV. 24: Comparison between the chemical capacitance and the double layer capacitance.....124
Figure IV. 25: AC equivalent circuit left reported in the literature [119].....126
Figure IV. 26:: The simulate reactance of the three capacitance CDR C_μ C_g as a function of the frequency.....127
Figure IV. 27: This capacitive behavior in low pass filters with the frequency variation [128] 127
Figure IV. 28: The AC (low signals) parallel circuit of the solar cell at high frequencies....128
Figure IV. 29: The AC equivalent circuit of the solar cell (left) at high frequencies conditions (right) 129

Figure V. 1: J(V) and P(V) curves of a typical double cation perovskite solar cell 133
Figure V. 2: The impedance response of a PSC under different applied voltages 134

Figure V. 3: The high and low-frequency capacitances of PSCs as a function of the applied voltage....135
Figure V. 4: The resistive parameters of a PCS as a function of the applied voltage....136
Figure V. 5: The relaxation times at high and low frequencies as a function of the applied voltage....138
Figure V. 6: The bandwidth and the generated power of a PSC as a function of the applied voltage....139
Figure V. 7:: Band-pass filter response [145]....140
Figure V. 8: the high and low cutoff frequencies of a PSC estimated by IS. 142
Figure V. 9: The high-frequency capacitance C_{HF} as a function of the applied voltage 145
Figure V. 10: The high frequency resistance R_{HF} as a function of the applied voltage....146
Figure V. 11: The high-frequency relaxation time (left) and the bandwidth (right), as a function of the applied voltage 147
Figure V. 12: C_{LF} and R_{LF} as a function of the applied voltage....149
Figure V. 13: the low-frequency relaxation time as a function of the applied voltage....150
Figure V. 14: XRD patterns of double and triple cations perovskite deposited on top of SnO_2/FTO substrate 151
Figure V. 15: JV curves of double (CsFA) and triple (CsFAMA) cation perovskite solar cell 152
Figure V. 16: The high-frequency capacitance C_{HF} as a function of the applied voltage....154
Figure V. 17: The high-frequency resistance R_{HF} as a function of the applied voltage 155
Figure V. 18: The high-frequency relaxation time (left) and the bandwidth (right), as a function of the applied voltage 156
Figure V. 19: XRD patterns of double cation perovskite with three thicknesses deposited on top of SnO_2/FTO substrate....158
Figure V. 20: SEM images of double cation perovskite film corresponding to the thickness of 380nm, 450nm, and 740nm. 159
Figure V. 21: Uv-vis absorbance spectra of 380 nm, 450 nm , 740 nm perovskite films. 160
Figure V. 22: JV curves of 380 nm, 450 nm, 740 nm perovskite PSCs 161
Figure V. 23: The high-frequency capacitance C_{HF} and resistance R_{HF} as a function of the applied voltage....162
Figure V. 24: The high-frequency relaxation time (left) and the bandwidth (right), as a function of the applied voltage 163
Figure V. 25: C_{LF} and R_{LF} and tauxLF a function of the applied voltage....164
Figure V. 26: XRD patterns of double cation perovskite 166
Figure V. 27: Uv-vis absorbance spectra of the treated and untreated SnO_2 films and the double cation perovskite film. Zoom on the Uv-vis spectra (right)....167
Figure V. 28: JV curves 168
Figure V. 29: The high-frequency capacitance C_{HF} and resistance RHF as a function of the applied voltage....170
Figure V. 30: The high-frequency relaxation time (left) and the bandwidth (right), as a function of the applied voltage 171